Modelling and Measurement of the Land Mobile Satellite MIMO Radio Propagation Channel

P.R. King

Submitted for the Degree of Doctor of Philosophy from the University of Surrey



Centre for Communication Systems Research School of Electronics and Physical Sciences University of Surrey Guildford, Surrey GU2 7XH, UK

April 2007

© P.R King 2007

ProQuest Number: 27610193

All rights reserved

INFORMATION TO ALL USERS

The quality of this reproduction is dependent upon the quality of the copy submitted.

In the unlikely event that the author did not send a complete manuscript and there are missing pages, these will be noted. Also, if material had to be removed, a note will indicate the deletion.



ProQuest 27610193

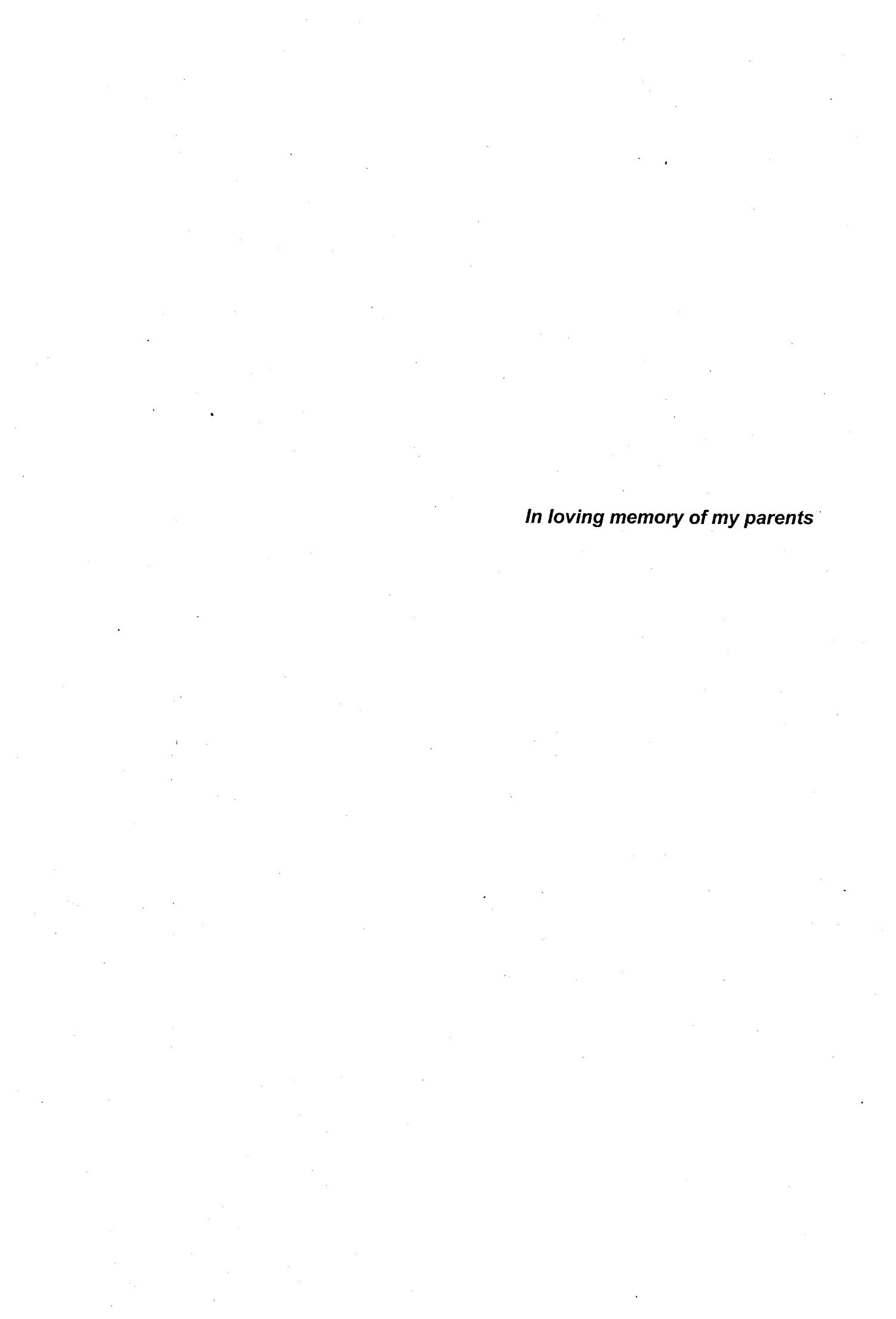
Published by ProQuest LLC (2019). Copyright of the Dissertation is held by the Author.

All rights reserved.

This work is protected against unauthorized copying under Title 17, United States Code

Microform Edition © ProQuest LLC.

ProQuest LLC. 789 East Eisenhower Parkway P.O. Box 1346 Ann Arbor, MI 48106 – 1346



Abstract

Three crucial factors in land mobile satellite (LMS) communication systems are the quality of service (QoS), spectral efficiency and cost. The QoS in a LMS system often suffers due to high link path loss due to the vast distances covered, signal shadowing and blockage, and a high link delay. Spectral efficiency can also be fairly low in LMS systems due to small received signal to noise ratios disabling the adoption of high order modulation techniques. Setup cost is also a major factor influencing the business case for LMS communication systems, which often makes single satellite systems more attractive than multiple satellite constellations. This thesis advances a technique for increasing QoS and spectral efficiency, without any increase in total transmit power, antenna gain or bandwidth by using multiple-input multiple-output (MIMO) techniques, which is then investigated thoroughly by theoretical and experimental means.

To investigate the benefit from satellite-MIMO techniques, work began with the design of a satellite-MIMO physical-statistical channel model, which enables computer simulation of the LMS-MIMO channel. Although the single-input single-output (SISO) channel, a subset of the MIMO channel was validated partially to previously published measurement data, there was no measurement campaign data or literature that informed about the LMS-MIMO channel. The model was used to carry out an initial estimation of capacity and diversity gain available from LMS-MIMO systems.

Work moved onto the wideband characterization of the satellite-MIMO channel. A measurement campaign was carried out in Guildford, U.K., where a terrestrially based artificial platform, representing two low elevation satellites in a cluster communicated with a mobile van, situated in three environments: tree-lined road, suburban and urban. Each emulated satellite contained a right and left hand circularly polarized (R/LHCP) directional antenna mounted next to each other. The vehicle contained four spatially separated omnidirectional antennas: two RHCP and two LHCP. A complete analysis was performed on the dual polarization single satellite 2x2 MIMO channel data. The data was characterized in terms of narrowband and wideband first and second order statistics for both large and small scale channel fading. The large and small scale correlation statistics were also extracted from the data across the delay and MIMO domains. The data was used to estimate the capacity and diversity gain that could be achieved from a low elevation LMS-MIMO channel.

This analysis also resulted in the derivation of empirical-statistical narrowband and wideband satellite-MIMO channel models, which have been validated against the experimental measurement data. The models can be used by the global research community to help design advanced PHY and MAC layer techniques, and some interest has already been shown.

Key words: Land Mobile Satellite (LMS), Radio Propagation, MIMO Systems, Channel Modelling, Channel Characterization

Acknowledgements

Firstly, I wish to thank Professor Barry Evans for giving me the opportunity to study for a research degree, and the Engineering and Physical Sciences Research Council and the European Union's 6th framework Satellite Communications Network of Excellence (SatNEx) project for providing funding. Sincere and utmost gratitude are due to my supervisors Professor Barry Evans and Dr. Stavros Stavrou (no longer with the University of Surrey), both for their initial guidance, continual support and encouragement.

I also wish to thank the Centre for Communication Systems Research for providing excellent facilities for carrying out the research. In particular, access to sophisticated channel measurement equipment, provision of a significant budget for ancillary equipment and excellent computing facilities. In addition, thanks are due to the School of Electronics and Physical Sciences for use of the school van made available during the measurement campaign.

For interesting discussions about mobile satellite propagation, I would like to thank Prof. István Frigyes and Péter Horváth from Budapest University of Technology and Economics, Hungary, and Prof. Fernando Pérez-Fontán from the University of Vigo, Spain. For useful discussions about previous measurement campaigns, I would like to thank Prof. Erich Lutz and Núria Riera Díaz of Deutsches Zentrum für Luft- und Raumfahrt eV (German Aerospace Centre), Germany.

A number of staff and students in the School of Electronics and Physical Sciences have been exceptionally helpful. In particular, I would like to thank Dave Fishlock and Terry Roberts for help with equipment and vehicle modification for the measurement campaign.

Finally, I would like to express thanks to my friends and family for their unyielding support, especially and necessarily through the difficult times, and for putting up with me throughout the whole research project.

Abbreviations

3GPP Third Generation Partnership Project 16QAM 16 point Quadrature Amplitude Modulation

ADC Analogue to Digital Converter
AGC Automatic Gain Control
AFD Average Fade Duration
ALC Automatic Level Control
AoA Angle of Arrival

AoD Angle of Departure
BS Base Station

BUTE Budapest University of Technology and Economics

CDF Cumulative Distribution Function
DAC Digital to Analogue Converter
DARS Digital Audio Radio Service

dBi decibels relative to an isotropic antenna

DLR Deutsches Zentrum für Luft- und Raumfahrt eV (German Aerospace Centre)

ERS Empirical Roadside Shadowing FDD Frequency Division Duplex

FSL Free Space Loss

GEO Geostationary Earth Orbit

GWSSUS Gaussian Wide Sense Stationary Uncorrelated Scattering

HAP High Altitude Platform IF Intermediate Frequency

IID Independent and Identically Distributed ISM Industrial, Scientific and Medical IST Information Society Technologies

LCR Level Crossing Rate
LEO Low Earth Orbit

LHCP Left Hand Circular Polarization

LMS Land Mobile Satellite
LOS Line Of Sight

MAC Medium Access Control Layer

MARECS Maritime European Communications Satellite

MED Modified Exponential Decay

MEO Medium Earth Orbit

MIMO Multiple-Input Multiple-Output
MISO Multiple-Input Single-Output
MRC Maximum Ratio Combining

MS Mobile Station

MSPS Mega Samples per Second NLOS Non Line Of Sight

PDF Probability Density Function

PHY Physical Layer

PTC Polarization Time Coding
QoS Quality of Service

Quality of Service

QPSK Quadrature Phase Shift Keying

RF Radio Frequency

RHCP Right Hand Circular Polarization

RMS Root Mean Square
RMSE Root Mean Square Error
SCM Spatial Channel Model
SDMA Space Division Multiple Access

SFIR Spatial Filtering for Interference Reduction

SISO Single-Input Single-Output
SIMO Single-Input Multiple-Output
SNR Signal to Noise Ratio
STC Space Time Coding
TDD Time Division Duplex
TDM Time Division Multiplex

ToA Time of Arrival

VSAT Very Small Aperture Terminal
WLAN Wireless Local Area Network
XPD Cross Polar Discrimination
XPI Cross Polar Isolation

Table of Contents

1	Introduc	tion	13
	1.1 Mo	tivations	14
	1.2 Ain	ns and objectives	15
		thodology	
		nievements and contributions	
		sis structure	
	110		10
2	Mobile S	Satellite Systems and Channel Modelling	19
	2.1 Mol	bile satellite systems	20
	2.1.1	Introduction	20
	2.1.2	Satellite spectrum	
	2.1.3	Multiple satellite coverage improvement	
	2.1.4	Role of terrestrial repeaters and time diversity	
	2.1.5	Geostationary orbit satellite systems	
	2.1.6	Highly elliptic orbit satellite systems	. 23
	2.1.7	Medium Earth orbit satellite systems	. 23
	2.1.8	Low Earth orbit satellite systems	. 23
	2.2 Mol	oile satellite channel modelling	. 24
	2.3 Sur	vey of channel models	. 25
	2.3.1	Empirical models	
	2.3.2	Statistical models	
	2.3.3	Deterministic (or physical) modelling	
	2.3.4	Physical-statistical modelling	
	2.3.5	Multiple-State models	. 32
	2.3.6	Wideband models	. 33
3	Terrestria	al MIMO Channel Modelling and Capacity	3/1
_	3.1 Intro	oduction	. 2 4 25
		MIMO channel	
		·	
	3.3.1	y gain, diversity gain and spatial multiplexing	
	3.3.2	Array gain Diversity gain	
	3.3.3	Spatial multiplexing gain	
	3.4.1	acity principles	. 40
	3.4.2	Eigenanalysis of channel	
	3.4.3	Capacity of SIMO and MISO channels	. 4Z . 42
	3.4.4	Frequency selective channel	
	3.4.5	Causes of sub-optimal capacity	. 43
	3.5.1	enna arrays and correlation	
	3.5.2	Antenna pattern	
	3.5.3	Angle of arrival	
		estrial MIMO channel models	
	J.O Tem	csulal lyllylo channel models	. 55

_			
	3.6.1	FLOWS channel model	56
	3.6.2		
	3.7	Interim conclusions	71
4	Phys	ical-Statistical Model of the LMS-MIMO Channel	70
7			
	4.1.1	Multiple satellite MIMO channel model	
	4.1.1		
	4.1.2		/0
	4.2.1	Single satellite MIMO channel model	80
	4.3 J	Multiple satellite capacity predictions	
	4.3.1	Method	
	4.3.3	,	
	4.4.1	Multiple satellite diversity predictions	
	4.4.2		
	4.4.3		os 86
	4.5	Limitations of models	
		Interim conclusions	
	7.0	micrim conclusions	0 /
5	Meas	suring the LMS-MIMO Channel	88
		Measurement campaign planning	
	5.1.1	Introduction	
	5.1.2	Equipment	
	5.1.3	Antenna characterization	92
	5.1.4	Environment	96
	5.1.5	Link budget and calibration	97
		The Wideband MIMO channel sounder	
	5.2.1	Introduction	
	5.2.2	*	
	5.3	Campaign procedure and data capture	. 104
6	Chara	acteristics of the LMS-MIMO Channel	106
		Narrowband LMS-MIMO characteristics	
	6.1.1	Initial observations	
	6.1.2	Large scale characteristics	
	6.1.3	Small scale characteristics	
	6.1.4	Combined large and small scale characteristics	
	6.2 \	Wideband LMS-MIMO characteristics	
	6.2.1	Large scale characteristics	. 132
	6.2.2	Small scale characteristics	. 138
	6.2.3	Combined large and small scale characteristics	. 145
	6.3 N	Measurement data limitations	. 164
		Capacity predictions	
	6.4.1	Method	

l		
	.4.2 Results	
6	.4.3 Observations	167
6.5	=	168
	.5.1 Method	
	.5.2 Results	
6	.5.3 Observations	171
7 E	mpirical-Statistical Model of the LMS-MIMO Channel	172
7.1	Introduction	173
7.2	Narrowband model	174
7.3	Narrowband model output	
7.4	Limitations of narrowband model	
7.5	Wideband model	181
7.6	Wideband model output	184
7.7	Limitations of wideband model	
7.8	Using the models	
8 C	onclusions and Further Investigation	186
8.1	Introduction	
8.2	Review of literature survey	187
8.3	Review of physical-statistical channel model	
8.4	Review of experimental findings	188
8.5	Review of resultant empirical-statistical channel model	
8.6	Implications of the research	
8.7	Further investigation	
8.	7.1 Further processing of measurement campaign data	
8.	7.2 Combined LMS and repeater MIMO channel modelling	
8.	7.3 LMS-MIMO channel modelling with shadowing diversity	190
8.	7.4 Effect of satellite elevation on the LMS-MIMO channel	
8.	7.5 Characterizing the HAP-MIMO channel	191
9 Bi	ibliography	192
10	Annendiy	207

List of Figures

Fig. 1-1 Methodology	16
Fig. 2-1 Optimum position of two satellites for maximizing satellite visibility (courtesy of [Gki02]).21
Fig. 2-2 Mobile satellite channel mechanisms (courtesy of [Gki02])	24
Fig. 2-3 Excess attenuation distributions versus elevation at 2.45GHz and 5.25GHz	26
Fig. 2-4 Level crossings and fade durations	30
Fig. 2-5 Lutz two state simulation model	32
Fig. 3-1 Basic Channel Model	36
Fig. 3-2 MIMO used for Spatial Multiplexing Gain	39
Fig. 3-3 Example comparison of capacity increase from a 2x2 MIMO system over a SISO system	41
Fig. 3-4 Channel capacity for n coupled channels versus correlation	46
Fig. 3-5 Uniform Linear Array	48
Fig. 3-6 Antenna Factor as a function of number of elements (left) and element separation (right)	49
Fig. 3-7 Figure showing location of scatterers	51
Fig. 3-8 Diagram showing single ring model	52
Fig. 3-9 Correlation coefficient at basestation antennas	52
Fig. 3-10 correlation coefficient at mobile antennas	53
Fig. 3-11 Antenna azimuth plot showing Gaussian and Laplacian distributions	54
Fig. 3-12 Contribution of s ^{ull} scatterer on channel response $h_{n,m}(\tau,f)$	57
Fig. 3-13 Normalised power versus Path delay	59
Fig. 3-14 Diagram showing nomenclature used in channel model	61
Fig. 3-15 Shadow fading distribution	61
Fig. 3-16 AoD at BS and AoA at MS distribution over all m subpaths and n paths	62
Fig. 3-17 BS and MS Array element gain versus azimuth angle	62
Fig. 3-18 Example small scale fading and envelope distribution for a MS at 3km/hr	63
Fig. 3-19 Time domain tapped delay line model of a multipath channel	65
Fig. 3-20 Frequency domain tapped Doppler-shift model of a multipath channel	66
Fig. 3-21 Relationship between system functions	67
Fig. 3-22 Example of 3GPP spatial channel model Input Delay Spread Function	68
Fig. 3-23 Examples of 3GPP spatial channel model Time Variant Transfer Function	68
Fig. 3-24 Example of 3GPP spatial channel model Delay-Doppler Spread Function	69
Fig. 3-25 Example of 3GPP spatial channel model Output Doppler Spread Function	69
Fig. 3-26 Relationship between channel correlation functions	70
Fig. 4-1 Cluster environment around mobile	73
Fig. 4-2 3D Point-line geometry	74
Fig. 4-3 Time series data of model	76
Fig. 4-4 First order statistics of model	76
Fig. 4-5 Antenna separation nomenclature	77
Fig. 4-6 Required antenna separation at satellite	78
Fig. 4-/ Required antenna separation at HAP	79
Fig. 4-8 Cluster environment around mobile vehicle	80
Fig. 4-9 Contrasting cumulative distribution functions of capacity for SISO and 2x2 MIMO system	s in
urban and highway environments with 20dB average receive SNR	83
Fig. 4-10 Bit error rate curves showing the effect of large and small scale diversity improvements	for
the urban environment	85
Fig. 4-11 Bit error rate curves showing the effect of large and small scale diversity improvements	for
the highway environment	85
Fig. 5-1 Propsound transmitter	.90
Fig. 5-2 Propsound receiver and disk drive	.90
Fig. 5-3 Measurement vehicle showing roof-mounted antenna rack	.90
Fig. 5-4 Hill-mounted artificial platform showing antenna mast and sounder	.91
Fig. 5-5 Clockwise from top left: front view of patch antenna; antenna on turntable; reference anter	nna
	.92
Fig. 5-6 Patch antenna pattern in vertical axis	.93
Fig. 5-7 Patch antenna in horizontal axis	.93

Fig. 5-8 Omnidirectional mobile antenna during characterization	0/
Fig. 5-9 Omnidirectional azimuth radiation pattern	25
Fig. 5-10 Omnidirectional elevation radiation pattern	93
Fig. 5-11 Map of Guildford showing measurement routes in each environment	93
Fig. 5-12 Cross-section of environment showing elevation and Fresnel clearance	9U
Fig. 5-13 Levels plan referred to antenna connector	<i>27</i>
Fig. 5-14 Elektrobit wideband MIMO channel sounder transmitter architecture	ソ/ 101
Fig. 5-15 Elektrobit wideband MIMO channel sounder receiver architecture	101
Fig. 5-16 Timing diagram	102
Fig. 5-16 Timing diagram	103
Fig. 6-1 Example narrowband received powers relative to FSL in the tree-lined road environment	104 • for
dual polarization single satellite case.	. 101 107
Fig. 6-2 Example narrowband received powers relative to FSL in the tree-lined road environment	for
dual satellite cluster case	. 101 108
Fig. 6-3 Large scale fading co-polar distribution and model fit for tree-lined road environment	100
Fig. 6-4 Large scale fading autocorrelation model fit to measured data for urban environment	111
Fig. 6-5 Rice K factor conditioning on large scale fading level for road environment	113
Fig. 6-6 Rice K factor conditioning on large scale fading level for suburban environment	113
Fig. 6-7 Rice K factor conditioning on large scale fading level for urban environment	114
Fig. 6-8 Cumulative distribution of Rice K factor in road environment (normalized to median)	115
Fig. 6-9 Cumulative distribution of Rice K factor in suburban environment (normalized to median)	116
Fig. 6-10 Cumulative distribution of Rice K factor in urban environment (normalized to median)	116
Fig. 6-11 Tree-lined road small scale fading multipath Doppler spectrum	117
Fig. 6-12 Cumulative distributions of MIMO channel correlation coefficients in tree-lined re-	oad
environment	119
Fig. 6-13 Cumulative distributions of MIMO channel correlation coefficients in suburban environm	ient
	119
Fig. 6-14 Cumulative distributions of MIMO channel correlation coefficients in urban environments	ient
	120
Fig. 6-15 Cumulative distributions of co-polarized and cross-polarized components in e	ach
environment	121
Fig. 6-16 Definitions of XPD and XPI	122
Fig. 6-17 Cumulative distributions of XPD and XPI for road environment (normalized to median).	123
Fig. 6-18 Cumulative distributions of XPD and XPI for suburban environment (normalized to medi	an)
Fig. 6.10 G. 1.1. No. 11. Carry 1.	123
Fig. 6-19 Cumulative distributions of XPD and XPI for urban environment (normalized to median)	124
Fig. 6-20 Normalized level crossing rate in tree-lined road environment	126
Fig. 6-21 Normalized level crossing rate in suburban environment.	126
Fig. 6-22 Normalized level crossing rate in urban environment	127
Fig. 6-23 Normalized average fade duration in tree-lined road environment	128
Fig. 6-24 Normalized fade duration cumulative distributions in tree-lined road environment	128
Fig. 6-25 Normalized average fade duration in suburban environment	129
Fig. 6-26 Normalized fade duration cumulative distributions in suburban environment	129
Fig. 6-27 Normalized average fade duration in urban environment.	130
Fig. 6.28 Normalized fade duration cumulative distributions in urban environment	130
Fig. 6.29 Large scale fading cross-polar distribution and model fit for tree-lined road environment. 1	.32
Fig. 6-30 Mean power versus excess delay profile and standard deviation for large scale fading in translational deviation for large scale fading in translation for large scale fading in the scale fading in translation for large scale fading in translation fading in translation for large scale fading in translation for large scale fading in translation fading in translatio	ee-
lined road environment	. 34
suburban environment	; m
Fig. 6-32 Mean power versus excess delay profile and standard deviation for large scale fading	. ;
urban environment	, III 3.5
Fig. 6-33 Large scale fading correlation versus delay separation	36
Fig. 6-34 Large scale MIMO channel correlation coefficient over delay domain	37
Fig. 6-35 Rice K factor conditioning on large scale fading for direct path in tree-lined ro	nad.
environment	39
Fig. 6-36 Rice K factor conditioning on large scale fading for direct path in suburban environment. 1	39

Fig. 6-37 Example Doppler spectrums in temporal domain in tree-lined road environment	14
Fig. 6-38 Small scale fading average correlation coefficient over delay separation	142
Fig. 6-39 Small scale correlation coefficient 10/50/90% distribution points versus excess del	av fo
channels emanating from the same and different vehicle antennas in the tree-lined	roa
environment	
Fig. 6-40 Small scale correlation coefficient 10/50/90% distribution points versus excess del	ou fo
channels emanating from the same and different vehicle antennas in the suburban environmen	ay 10
Fig. 6-41 Small scale correlation coefficient 10/50/90% distribution points versus excess del	.l . 144
channels emanating from the same and different vehicle antennas in the urban environment	ay 10
Fig. 6.42 Average power delay profile in road environment	144
Fig. 6-42 Average power delay profile in road environment	140
Fig. 6-43 Cumulative distribution of RMS delay spread in road environment	146
Fig. 6-44 Average power delay profile in suburban environment	147
Fig. 6-45 Cumulative distribution of RMS delay spread in suburban environment	147
Fig. 6-46 Average power delay profile in urban environment	148
Fig. 6-47 Cumulative distribution of RMS delay spread in urban environment	148
Fig. 6-48 Input delay-spread function of co-polarized channel in tree-lined road environment	149
Fig. 6-49 Input delay-spread function of cross-polarized channel in tree-lined road environment	149
Fig. 6-50 Input delay-spread function of co-polarized channel in suburban environment	150
Fig. 6-51 Input delay-spread function of cross-polarized channel in suburban environment	150
Fig. 6-52 Input delay-spread function of co-polarized channel in urban environment	151
Fig. 6-53 Input delay-spread function of cross-polarized channel in urban environment	151
Fig. 6-54 Delay Doppler-spread function of co-polarized channel in tree-lined road environment.	153
Fig. 6-55 Delay Doppler-spread function of cross-polarized channel in tree-lined road environment	nt153
Fig. 6-56 Delay Doppler-spread function of co-polarized channel in suburban environment	154
Fig. 6-57 Delay Doppler-spread function of cross-polarized channel in suburban environment	154
Fig. 6-58 Delay Doppler-spread function of co-polarized channel in urban environment	155
Fig. 6-59 Delay Doppler-spread function of cross-polarized channel in urban environment	155
Fig. 6-60 Time-variant transfer function of co-polarized channel in tree-lined road environment	157
Fig. 6-61 Time-variant transfer function of cross-polarized channel in tree-lined road environmen	157 + 157
Fig. 6-62 Time-variant transfer function of co-polarized channel in suburban environment	1.157
Fig. 6-63 Time-variant transfer function of cross-polarized channel in suburban environment	150
Fig. 6-64 Time-variant transfer function of co-polarized channel in urban environment	150
Fig. 6-65 Time-variant transfer function of cross-polarized channel in urban environment	150
Fig. 6-66 Example frequency response of co-polarized tree limit and read about 1	139
Fig. 6-7 Output Domler arread function of co-polarized tree-lined road channel	160
Fig. 6-68 Output Doppler-spread function of co-polarized channel in tree-lined road environment	161
Fig. 6-68 Output Doppler-spread function of cross-polarized channel in tree-lined road environ	•
Eig 6 60 Outsut David and 10 0 0 1 1 1 1 1 1 1 1 1	161
Fig. 6-69 Output Doppler-spread function of co-polarized channel in suburban environment	162
Fig. 6-70 Output Doppler-spread function of cross-polarized channel in suburban environment	162
Fig. 6-71 Output Doppler-spread function of co-polarized channel in urban environment	163
Fig. 6-72 Output Doppler-spread function of cross-polarized channel in urban environment	163
Fig. 6-73 Channel dynamic range validity	164
Fig. 6-74 Contrasting complementary cumulative distribution functions of capacity for SISO and	1 2x2
dual polarization MIMO systems in the tree-lined road, suburban and urban environments	with
15dB FSL SNR	167
Fig. 6-75 Bit error rate curves for road environment	169
Fig. 6-76 Bit error rate curves for suburban environment	170
Fig. 6-77 Bit error rate curves for urban environment	.170
Fig. 7-1 Example of simulated co- and cross-polar channels	. 178
Fig. 7-2 Tree-lined road cumulative distribution comparison between modelled and measured data	179
Fig. 7-3 Level crossing rate and average fade duration model validation	179
Fig. 7-4 LMS-MIMO channel model outline	181
Fig. 7-5 Example input delay-spread function	18/
Fig. 8-1 Methodology	197
8	.10/

List of Tables

Table 1 Large scale fading log-normal model parameters	110
Table 2 Average large scale correlation coefficients between MIMO channels	111
Table 3 Rice K factor polynomial parameters for narrowband data	114
Table 4 Rice K factor statistics in road environment	115
Table 5 Rice K factor statistics in suburban environment	
Table 6 Rice K factor statistics in urban environment	
Table 7 Average small scale correlation coefficients between MIMO channels	118
Table 8 XPD and XPI statistics for road environment	123
Table 9 XPD and XPI statistics for suburban environment	
Table 10 XPD and XPI statistics for urban environment	
Table 11 Maximum level crossing rate	
Table 12 Level crossing rate at maximum signal level	127
Table 13 Maximum average fade duration	131
Table 14 Average fade duration at -20dB level	131
Table 15 Rice K factor polynomial parameters	140
Table 16 Markov state and transition matrices for tree-lined road environment	175
Table 17 Markov state and transition matrices for suburban environment	175
Table 18 Markov state and transition matrices for urban environment	175
Table 19 Frequency band terminology	207

Chapter One

1 Introduction

This thesis is submitted for the partial fulfilment of the degree of Doctor of Philosophy, which has been carried out at the Centre for Communication Systems Research at the University of Surrey, United Kingdom. The personal research has been performed on "Modelling and Measurement of the Land Mobile Satellite MIMO Radio Propagation Channel".

1.1 Motivations

Personal wireless communications is a true success story and has become part of people's everyday lives. Whereas in the early days of mobile communications QoS was often poor, nowadays it is assumed the service will be ubiquitous, of high speech quality and the ability to watch and share streaming video for example is driving operators to offer even higher uplink and downlink data-rates, whilst maintaining appropriate QoS.

Terrestrial mobile communications infrastructure has made deep inroads around the world. Even rural areas are obtaining good coverage in many countries. However, there are still geographically remote and isolated areas without good coverage, and some countries do not yet have coverage in towns and cities. On the other hand, satellite mobile communications offers the benefits of true global coverage, reaching into remote areas as well as populated areas. This has made them popular for niche markets like news reporting, marine, military and disaster relief services. However, until now there has been no wide-ranging adoption of mobile satellite communications to the mass market.

Current terrestrial mobile communication systems are inefficient in the delivery of multicast and broadcast traffic, due to network resource duplication (i.e. multiple base stations transmitting the same traffic). Satellite based mobile communications offers great advantages in delivering multicast and broadcast traffic because of their intrinsic broadcast nature. The utilization of satellites to complement terrestrial mobile communications for bringing this type of traffic to the mass market is gaining increasing support in the standards groups, as it may well be the cheapest and most efficient method of doing so.

Current mobile satellite communication systems however often suffer from poorer QoS due to high path loss, shadowing, blockage, limited satellite power and high link delay. Unfortunately, even with state of the art high power satellites with narrow spot beams or multiple satellite constellations, link availability is not always possible when the signal is blocked by buildings, and indoor coverage is often poor. With future satellites providing substantially more radiated power and possibly using diversity techniques, users may someday perceive the same QoS from a satellite or terrestrial communication systems. However there is a long way to go before this is achieved. Satellite communication system operators are always trying to achieve adequate QoS with the minimum fade margin (and therefore cost). A figure of 16.5dB was used in the Iridium constellation system [EvJ98]. However, signal blockage can easily be 30dB or more, and the link would be dropped. Even with multiple satellites offering satellite diversity, signal availability is not guaranteed.

Some improvements to land mobile satellite communication systems are available by using the technique of satellite-MIMO between the satellite and mobile in both directions, and this is the subject of this piece of research. Satellite-MIMO, where channels can be separated by space or polarization, can offer improvements to QoS by providing diversity gain using spatial/polarization time block coding techniques, and increases to spectral efficiency by using spatial/polarization multiplexing or a combination of both. It is assumed that the link between the Earth station and satellite can be designed with excellent QoS, and that it is the satellite to mobile link that often suffers poor QoS.

An Earth station could transmit two channels to a repeating down-converting satellite, where they could be transmitted back to Earth, either by using a single satellite with two orthogonal polarizations, or by using two satellites with one polarization, or a combination of both. Multiple satellites can be placed in a cluster to create an effective 'antenna array in the sky', or can be placed widely apart, which benefits from additional large scale fading diversity gain.

This piece of research was driven to understand the satellite-MIMO channel, and quantify the available diversity and capacity gain benefits.

1.2 Aims and objectives

The main aims of this research were to characterize the land mobile satellite-MIMO channel between a satellite and a mobile, and estimate the available diversity and capacity gains from satellite-MIMO communication systems. Additionally, in order for PHY layer researchers to take advantage of the channel characterization, another aim of the research was to produce satellite-MIMO channel models.

The approach used in this research followed a serial path of objectives, as follows:

- Review in detail the literature on land mobile satellite SISO channel modelling and measurements, gain a good understanding of terrestrial MIMO channel modelling and measurements, and gain an understanding of diversity and capacity enhancements through multiple antenna systems.
- ◆ To gain some initial understanding of the LMS-MIMO channel, prior to the arrival of sophisticated MIMO channel sounding equipment, it was decided to develop a physical-statistical mobile satellite-MIMO channel model, based in part on terrestrial MIMO channel models, and SISO land mobile satellite channel models. This was initially coded in Matlab, but required recoding in C++ to accelerate performance. As a key member of the satellite propagation activities in the EU IST FP6 project SatNEx: Satellite Communications Network of Excellence, a personal exchange mission to DLR in Munich, Germany was organized, where the analysis and practical aspects of a well cited LMS measurement campaign was retraced, that led to Prof. Lutz' two state Markov LMS channel model. Together with a PhD student colleague at DLR, test runs were taken down the actual roads used in the campaign. Therefore notes could be made about the environment. This enabled the physical-statistical model to be more accurately constructed.

However the MIMO aspects of the LMS model could not be validated necessitating the requirement for real LMS-MIMO channel data.

- ♦ The next objective was to characterize the wideband LMS-MIMO channel. After six months of planning and setting up the experiment, the measurement campaigns were carried out in the summer of 2005. Around 100GBytes of channel data was generated between a terrestrially based artificial platform based on a hilltop, to represent the satellite and a vehicle situated in three environments: tree-lined road, suburban and urban.
- This led to the quantification of the narrowband and wideband first and second order statistics as well as the correlation statistics of the LMS-MIMO channel. From the channel data and their statistics, the capacity and diversity gain from a LMS-MIMO system was studied.
- Finally the development of a valid empirical-statistical LMS-MIMO channel model was explored which could be used in software simulation or hardware emulation.

1.3 Methodology

The methodology can best be described with the aid of the following diagram:

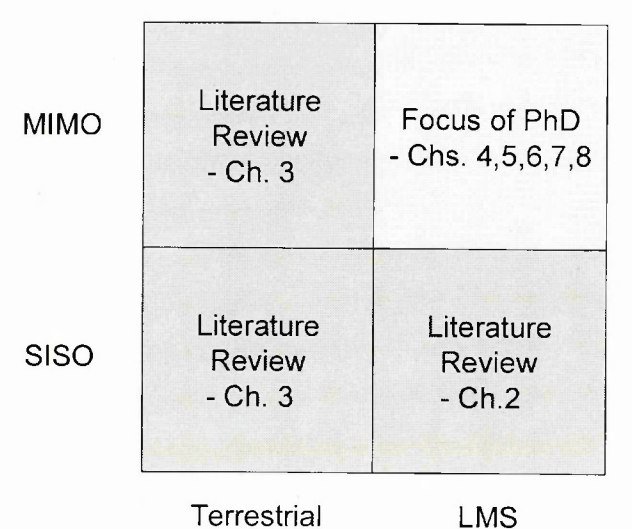


Fig. 1-1 Methodology

The diagram clearly shows how the research arrived at the focus area. Terrestrial mobile systems are already well researched for SISO and MIMO channels. Land mobile satellite systems are well covered by researchers in the SISO case. However MIMO applied to the LMS case is new research and is the subject of this thesis.

1.4 Achievements and contributions

The major achievements and novelty in this work are:

- Design and construct a novel physical-statistical land mobile satellite-MIMO channel model.
- Design and carry out a LMS-MIMO measurement campaign and provide a thorough analysis of the captured data. Use this data to predict available diversity and capacity improvements. To the author's knowledge, no narrowband or wideband MIMO mobile-satellite channel measurement campaign had been carried out prior to the present work.
- Design and implement a narrowband and a wideband empirical-statistical LMS-MIMO channel model, which is novel.

The results of this work have been published in learned journals and international conferences. The work was defended personally at two conferences.

Journals

- ♦ Kasparis C, King PR, Evans BG, "Doppler spectrum of the multipath fading channel in mobile satellite systems with directional terminal antennas", *IET Communications*, in Press.
- Horvath P, Karagiannidis GK, King PR, Stavrou S, Frigyes I, "Investigations in satellite MIMO channel modeling: accent on polarization", EURASIP Journal on Wireless Communications and Networks, in Press.
- ♦ King PR, Stavrou S, "Low elevation wideband land mobile satellite MIMO channel characteristics", *IEEE Transactions on Wireless Communications*, in Press.
- ♦ King PR, Stavrou S, "Capacity improvement for a land mobile single satellite MIMO system", *IEEE Antennas and Wireless Propagation Letters*, vol.5, Dec.2006, pp.98-100.
- ♦ King PR, Stavrou S, "Land mobile-satellite MIMO capacity predictions", *IEE Electronics Letters*, vol. 41, no.13, June 2005, pp.749-751.

Conferences

- ◆ Kasparis C, King PR, Evans BG, "Doppler spectrum of the multipath fading channel in mobile satellite systems with directional terminal antennas", *Ka and Broadband Communications Conference*, Sep.2006.
- ◆ King PR, Stavrou S, "Characteristics of the land mobile satellite MIMO channel", *IEEE Vehicular Technology Conference*, Sep.2006.

- ♦ King PR, Stavrou S, "Tree obscured mobile satellite channel characteristics and mitigation", *IST Mobile Summit*, June 2006.
- ♦ King PR, Horváth P, Pérez-Fontán F, Frigyes I, Stavrou S, "Satellite channel impairment mitigation by diversity techniques", *IST Mobile Summit*, June 2005.
- ♦ King PR, Evans BG, Stavrou S, "Physical-statistical model for the land mobile-satellite channel applied to satellite/HAP-MIMO", 11th European Wireless Conference, vol.1, Apr.2005.

Book Contribution

• King PR, a co-author in e-book, 'Influence of the propagation channel on satellite communications - channel dynamics effects on mobile, fixed and optical multimedia applications', written as final deliverable for joint activity group on satellite propagation during EU IST FP6 SatNEx project: Satellite Communications Network of Excellence.

1.5 Thesis structure

Chapter 2 provides a review of land mobile satellite systems and SISO channel modelling and measurements. Key well known empirical, statistical, deterministic, physical-statistical, state and wideband models are reviewed.

Chapter 3 focuses on the MIMO channel and channel capacity theory, as well as causes of non-ideal channels for MIMO capacity. An overview of antenna array theory and some important terrestrial MIMO channel models are presented.

Chapter 4 describes in detail the construction of a physical-statistical satellite MIMO channel model and its partial validation against measurement data in the literature. MIMO capacity and diversity gain are estimated from the model. The need for LMS-MIMO channel data is highlighted.

Chapter 5 provides details about the measurement campaign design and planning, and also about the operation and theory of the channel sounder.

Chapter 6 provides a thorough analysis of the LMS-MIMO channel data. This included narrowband and wideband first and second order statistics and correlation properties over the delay domain and over the MIMO channel domain. The data was also analysed quantitatively for diversity gain and capacity gain. Measurement limitations are discussed.

Chapter 7 uses the measurement data to derive a narrowband and a wideband empirical-statistical LMS-MIMO channel model. Model limitations are also discussed.

Finally, the last chapter draws conclusions on the work, and provides scope and direction for further work.

Ch	an	40	r T	wo
	ap	ILE	,	WU

2 Mobile Satellite Systems and Channel Modelling

2.1 Mobile satellite systems

2.1.1 Introduction

Mobile satellite services have been around since the 1980s, in a similar time frame to terrestrial cellular communications. Improvements to launch capabilities, payload technology, antennas and advanced modulation/coding techniques have enabled mobile terminals to become increasingly smaller with better quality of service (QoS) and much improved roaming capabilities. (The appropriate QoS required for speech is an uncoded bit error rate (BER) of around $10^{-2} - 10^{-3}$ and for data is around $10^{-5} - 10^{-7}$.) Terrestrial cellular development has also seen major advances in technology, and offer a more cost-effective, better QoS solution in many situations. However mobile satellite communication systems offer some key advantages bringing communications to sparsely populated or barren areas, in addition to maritime and aeronautical services. Satellites also offer key advantages in multicast and broadcast services to mobile devices due to efficient delivery, and can well complement terrestrial cellular communications in this area.

There are four main types of satellite orbit: geostationary orbit (GEO – a useful geosynchronous orbit), highly elliptic orbit (HEO), medium Earth orbit (MEO) and low Earth orbit (LEO), each with various benefits and drawbacks.

2.1.2 Satellite spectrum

Although most current mobile satellite services operate in the L and S bands (see Appendix for a description of frequency bands), greater demand for bandwidth has meant some services are now operating from VHF up to Ka bands. The link between satellite and mobile at higher frequencies poses many difficulties. For example, the problems associated with noise, path loss, shadowing, Doppler effect are all more challenging at high millimetre wave frequencies. Smaller wavelengths are also more likely to be scatterered when reflected by rough surfaces; this wave spreading reduces multipath power compared with lower frequencies [PaD92].

Higher frequency channels therefore require more directional mobile (tracking) antennas due to link budget constraints and therefore tend to provide enhanced distinct 'on/off' states, whereas multipath is more pronounced at the lower L and S band frequencies when using omnidirectional antennas. For this reason, the benefits of satellite-MIMO are more likely to improve at lower frequencies, although the benefits of satellite-MIMO at higher frequencies may become possible in the future with higher radiated power satellites.

2.1.3 Multiple satellite coverage improvement

Much work was carried out in [Gki02] to simulate the satellite visibility and multiple satellite diversity probabilities for various constellation orbit architectures and various mobile terrestrial environments. The target design aim is to ensure at least one satellite is visible to the mobile for the highest amount of time. The geographical mobile/population density is also accounted for in that constellation orbits are often optimized around mid-latitudes. When more than one satellite is visible to a mobile, signals can be combined in a diversity arrangement.

For the case of two satellites, the following diagram [Gki02] shows the correlation coefficient between satellite visibilities as a function of azimuth separation at various elevations, street widths (W=12m shown here), mobile position from buildings (d [m]) and building height (Hb=15m shown here). The optimum azimuth separation is 90°, where a negative cross correlation coefficient occurs (meaning when one satellite is blocked there is a higher probability that the other satellite is visible). This is also intuitively correct, as when a mobile is moving along a street, one satellite is more likely to be visible if the other is blocked when separated in azimuth by 90°. When satellites are close together, as they would be in a satellite cluster, the shadowing will be highly correlated. Similarly if satellites are positioned at either side of the mobile at 180° azimuth, blockage is also likely to be highly correlated.

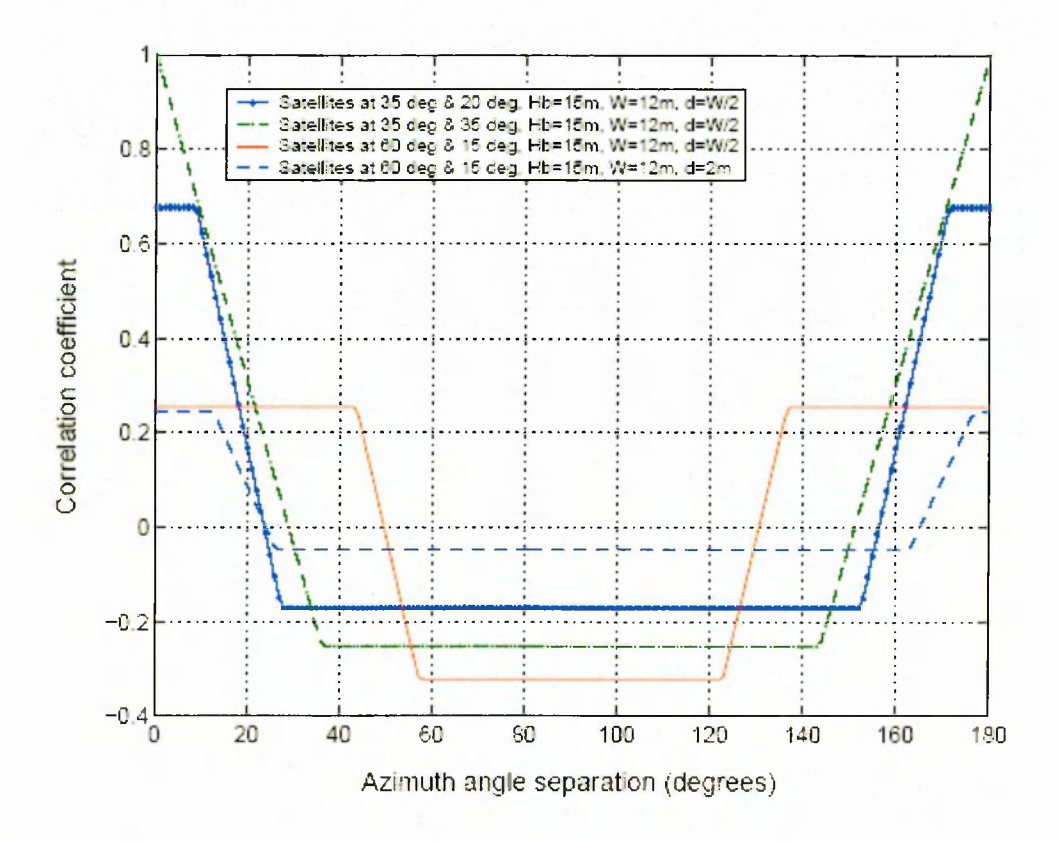


Fig. 2-1 Optimum position of two satellites for maximizing satellite visibility (courtesy of [Gki02])

2.1.4 Role of terrestrial repeaters and time diversity

When designing a land mobile satellite system, it is found that a large shadowing fade margin is necessary. For example in [Dav02] it is reported that 29dB fade margin is required in downtown Athens for 99% availability with a satellite at 60° elevation operating at 1.8GHz. This would be uneconomical and technically challenging with current payload and handset technology. Systems such as a digital audio radio service (DARS) system called Sirius Satellite Radio use many techniques to overcome large and small scale fading. Firstly, two satellites are used in a HEO, which ensures a high likelihood of high satellite elevation from at least one satellite, thus improving coverage [Dav02]. However this does not help reception indoors or under bridges for example. To counter this, time diversity is used, where one satellite broadcasts with 4 second delay. When buffered and coherently combined using MRC in the receiver, this clearly improves the chance of a non blocked signal. Whereas these two techniques deal with shadowing fading, small scale fading at speeds of several fades per second, are dealt with by interleaving, and concatenated convolutional and Reed-Solomon coding.

However, even with all these forms of diversity, it is found that in order to achieve the target of 99% availability in built up areas and in tunnels, inside buildings, shopping malls, etc, further signal strength is required. In many systems like Sirius Satellite Radio and other satellite digital multimedia broadcasting systems, like those researched in EU projects such as SATIN and MAESTRO, terrestrial gap-fillers or repeaters are used. The requirement is to minimize the system cost whilst maintaining a required QoS, which usually means optimizing the satellites' orbit and diversity schemes to minimize the number of gap-fillers.

In the Sirius Satellite Radio system [Dav02], a separate VSAT receiver system at the terrestrial gap-filler is used, where signals are re-broadcast within the operators 12.5MHz of S band spectrum using COFDM, a modulation/coding scheme that provides resilience to wideband multipath echoes, and allows each gap-filler to use the same piece of spectrum. The signals from the terrestrial paths and the two satellite paths are all coherently combined using MRC in the receiver.

Another United States DARS system XM Radio, which uses GEO satellites, has recently (2007) announced plans to merge with Sirius Satellite Radio.

2.1.5 Geostationary orbit satellite systems

GEO satellites are placed above the equator at an altitude of 35786km and always appear in the same place (azimuth and elevation) from Earth. One satellite can provide continental size coverage, and a minimum of three satellites can provide global coverage. Satellite visibility becomes increasingly worse at higher latitudes due to reduced elevation angle. Visibility in built up areas is poor. Unlike terrestrial cell-based architectures or systems based on satellites in lower orbits, no

handover is required during a connection, which simplifies the network architecture. A single hop transmission delay is around 250ms to 280ms depending on path length.

The past 20 years of GEO mobile satellite systems has seen a vastly improved satellite effective isotropic radiated power (EIRP), by means of higher onboard power amplifiers and narrower spotbeams; mobile terminal antennas are now able to provide a link with much wider antenna beamwidths, enabling users to be much more mobile whilst in a call.

Land mobile satellite services from GEO satellite systems are offered in Europe, North America, Australia, the Middle East and South East Asia, by companies such as Inmarsat, Euteltracs, Emsat, Optus, N-Star, Msat, Aces and Thuraya.

2.1.6 Highly elliptic orbit satellite systems

HEO satellite systems offer many benefits for mobile satellite communications. With an apogee of 40000 to 50000km and a perigee of 1000 to 20000km, transmission delay is variable. However orbits can be chosen to provide a high guaranteed satellite elevation angle to mid-latitude regions with two to four satellites. Handover is required three to four times a day, so may not be necessary during a call.

Sirius Satellite Radio in the United States offers and Europe's Ondas Media aims to offer digital radio services using HEO satellites.

2.1.7 Medium Earth orbit satellite systems

MEO constellation satellite systems require between 10 and 20 satellites for global coverage at an altitude of 10000 to 20000km. Transmission delay and path losses are reduced compared to GEO systems and good visibility can be obtained and satellite diversity techniques used. Handover is required between satellites more frequently than HEO systems but much less than LEO systems.

Examples of MEO satellite systems are GPS (owned by United States military), Glonass (Russia) and Galileo (Europe) navigation systems. MEO satellite systems for mobile satellite communication services are few, with ICO as the best known proposed commercial system for communications.

2.1.8 Low Earth orbit satellite systems

LEO satellite systems, with an altitude between 750 and 2000km, offer much improved transmission delay and path loss. Multiple satellite constellations require more than 30 satellites for global coverage. Multiple satellite diversity can greatly enhance the link availability, where either selection diversity or maximum ratio combining diversity techniques are often used. In order to guarantee visibility of at least one satellite above a certain satellite elevation, more satellites are

required in the constellation. Handover can frequently occur within a call, and adds great complexity to the network.

Many attempts at providing a mobile satellite voice/data service business from LEO systems were made during the 1990s. Some examples are Orbcomm, Iridium, Globalstar, Constellation Communications. However most were unsuccessful financially due to major inroads from terrestrial mobile communications, which offered a cheaper service of higher quality. LEO systems are still in use for special applications such as for barren regions and military communications.

2.2 Mobile satellite channel modelling

The land mobile satellite channel can be partitioned into ionospheric effects, tropospheric effects and local effects [Mar00], [EvB99]:

Ionospheric effects involve the interaction between layers of charged particles around the Earth and the radio waves. It includes ionospheric refraction, Faraday rotation, group delay, dispersion and ionospheric scintillation.

Tropospheric effects involve the interaction between the lower layer of the Earth's atmosphere (including the air and hydrometeors such as rain) and the radio waves. It includes attenuation, rain attenuation, gaseous absorption, tropospheric refraction, tropospheric scintillation, depolarisation and sky noise. Cross-polar discrimination, as defined in [ITU-R618-8], is negligible below 4GHz.

Local effects involve radio wave interaction with the features in the vicinity of the mobile terminal. The terrain, vegetation, buildings, other structures, and vehicles can all interact with the radio wave by the mechanisms of reflection, diffraction, transmission and scattering [Sau99], [Kar99].

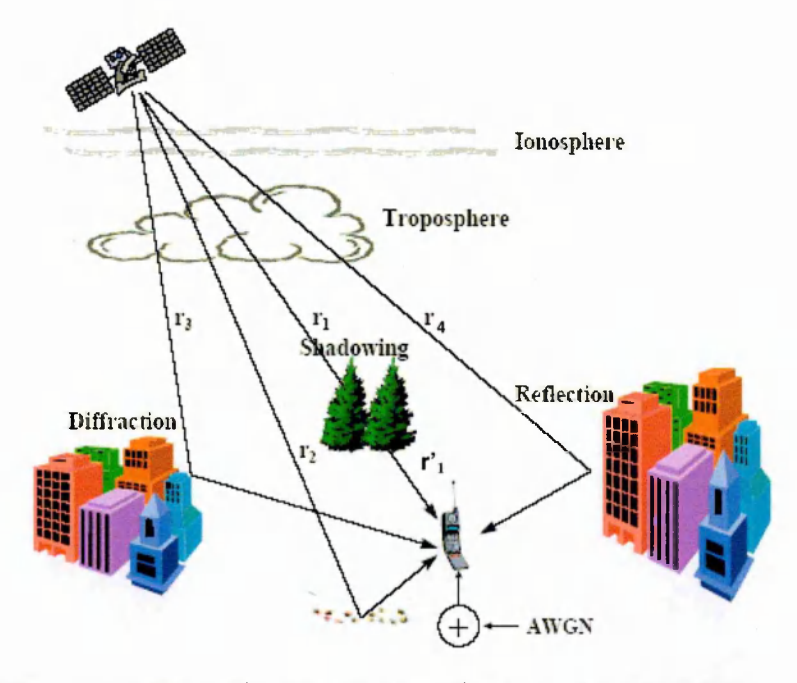


Fig. 2-2 Mobile satellite channel mechanisms (courtesy of [Gki02])

The direct component, r_l or line of sight path (LOS) is subjected to all the ionospheric and tropospheric components listed above, in addition to free space loss (FSL), given by:

$$FSL = 20\log\left[\frac{4\pi d}{\lambda}\right], dB$$
 (2-1)

where d is the distance between the satellite and mobile and λ is the wavelength. At L and S bands, Faraday rotation in the ionosphere is significant, increasing with lower frequencies. For this reason circularly polarized antennas are often used. When the LOS path is obstructed by trees, buildings, hills or other obstacles, large scale fading or shadowing occurs, and causes severe signal attenuation, which must be accounted for in the link budget.

The specular component r_2 reaches the mobile by reflection from the ground. Its strength depends on the constitutive parameters and roughness of the ground. Since this ray normally arrives with a negative elevation, it is not always received by a directional terminal antenna [Kar99]. The diffuse components $(r_3 \text{ and } r_4)$ account for the small scale fading in the received signal, which occurs due to the vector addition of reflections, diffractions and scattering from local objects. All the channel effects are multiplicative; however additive white Gaussian noise (AWGN) is also present in the system, as shown.

2.3 Survey of channel models

Signal fading is often separately described by path loss, large scale and small scale fading effects. Various methods and models have been proposed to model the LMS channel. This section provides an overview of some of the well cited SISO models in the literature that describe the large scale and small scale fading effects.

2.3.1 Empirical models

Modified exponential decay (MED) model

In order to compute the mean path loss through vegetation, knowledge of the path length, D_{ν} through vegetation and the frequency, f can be used in the following formulas:

$$L_{\nu} = a_{\nu} D_{\nu} \tag{2-2}$$

The value of a_v has been calculated by various research studies. The ITU define this as [Kar99]:

$$a_{v} = 0.2 f^{0.3} D_{v}^{-0.4} \tag{2-3}$$

valid for the range $0 \le D_v \le 400$ m, and $200 \le f \le 95000$ MHz. Therefore, at 2450MHz, for example the attenuation through 1m of vegetation is 2dB. This model is built around a large database of measurements with foliage in-leaf and out-of-leaf and in wet and dry conditions.

Researchers Vogel and Goldhirsh also formulated roadside tree attenuation at different satellite elevations, based around extensive measurement campaigns [Vog88].

Empirical roadside shadowing (ERS) model

The ERS model, along with its revisions, developed by Vogel and Goldhirsh, enables calculation of shadowing fades beyond free space loss as a function of percentage (P), satellite elevation (θ) and frequency (f). The original model, valid for f = 1.5GHz, $1\% \le P \le 20\%$, and $20^{\circ} \le \theta \le 60^{\circ}$, is given by [Vog90]. Here, L is the channel attenuation:

$$L(P, \theta) = -A\ln(P) + B$$
where A = 3.44 + 0.0975 \theta - 0.002 \theta^2
and B = -0.443 \theta + 34.76

To extend the model percentage range to $20\% < P \le 80\%$, the following scaling is used [Vog88]:

$$L(P,\theta) = \frac{L(20\%,\theta)}{\ln 4} \ln \left(\frac{80}{P}\right)$$
 (2-5)

To extend the model frequency range, where $0.8 \text{GHz} \le f \le 20 \text{GHz}$, the following is used [Gol93]:

$$L(f_2) = L(f_1) \exp \left[1.5 \left(\frac{1}{\sqrt{f_1}} - \frac{1}{\sqrt{f_2}} \right) \right]$$
 (2-6)

In Fig. 2-3, the excess attenuation is given for a range of satellite elevations, at 2.45GHz and 5.25GHz. These frequencies are of interest because they are representative of commercial LMS bands. Additionally, the channel sounder can operate at these two frequencies and it useful to see the impact on attenuation, for measurement campaign planning purposes: 2.45GHz was chosen due to lower loss. Note there is an 80% chance of fading in this model for all satellite elevations.

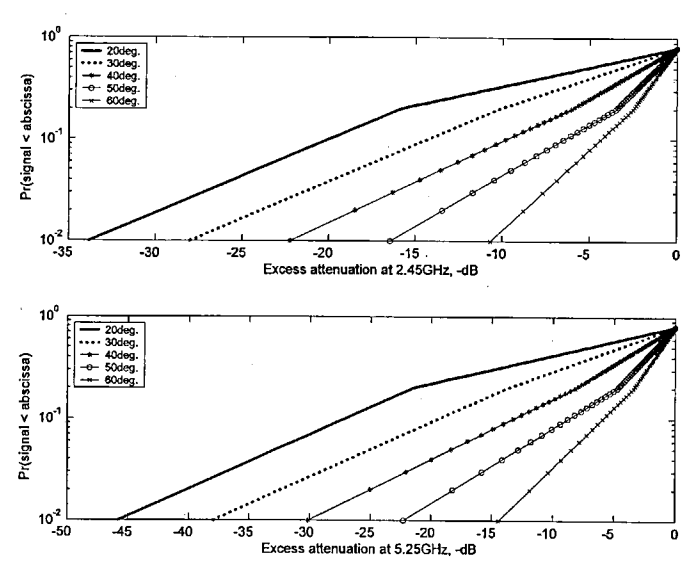


Fig. 2-3 Excess attenuation distributions versus elevation at 2.45GHz and 5.25GHz

2.3.2 Statistical models

First order statistics

First order statistics are described by their probability density function or cumulative distribution function. However they say nothing about how the signal level changes with time.

Shadowing model

Shadowing probability can be reduced by positioning the satellites at higher elevations (eg. HEO systems) and using multiple satellite diversity (eg. LEO systems) [Gki02]. However, at all elevations, shadowing can occur reducing the signal level substantially, which necessitates the addition of a large scale fade margin to the link budget.

The change from shadowed to non-shadowed signal conditions is often modelled using a state approach, which also better accounts for signal temporal variations. Two, three and four state models have gained popularity. Each state can be separately described by large scale and small scale fading statistics. The large scale fading is usually modelled using a log-normal approach. This can be justified if the signal attenuation contributions along the shadowing path act independently. In this case the total attenuation is the multiplication of signal attenuation power ratios. Expressed in dB, this is the sum of attenuation contributions in dB. If these contributions are taken as random variables, then the central limit theorem holds and hence the shadowing follows a log-normal (Gaussian) distribution [Sau99]. Additionally, many 'mixture' models use the Gaussian shadowing model as a component. The Gaussian shadowing distribution is normal in decibels, and is therefore also known as log-normal. The normal distribution is defined as follows [Sau99], [Vuc92]:

$$p(L_s) = \frac{1}{\sigma_L \sqrt{2\pi}} exp\left(-\frac{L_s^2}{2\sigma_L^2}\right)$$
 (2-7)

where σ_L is the shadowing standard deviation and L_S is the shadowing loss in decibels. Typical values of σ_L range from 4dB to 12dB, and is dependent on satellite elevation and environment.

Rayleigh model

The Rayleigh distribution [Jak74] is a very often used small scale fading narrowband model for non-line-of-sight (NLOS) channels. It is also commonly used in 'mixture' distributions. The Rayleigh distribution can be seen from the magnitude of complex Gaussian independently and identically distributed random numbers with zero means. The first order probability density is given as follows:

$$p_{R}(r) = \frac{r}{\sigma^{2}} exp\left(-\frac{r^{2}}{2\sigma^{2}}\right)$$
 (2-8)

where r is the fading magnitude, $r = |\alpha| = \sqrt{x^2 + y^2}$, x and y being the real and imaginary Gaussian random variables, and α being the complex fading multiplier. The parameter σ is the standard deviation of either the real or imaginary part of the complex fading α and σ^2 is the power in α .

Ricean model

The Ricean distribution [Ric48] is a commonly used narrowband model for LOS or partial LOS conditions. Whereas in the Rayleigh case the fading is due to reflected, diffracted and scattered multipath energy, the Ricean case has an additional LOS component. The ratio between the LOS power and the multipath power is known as the Rice K factor. When $K \to \infty$, the channel is purely LOS with no multipath and the signal level does not fluctuate, and when $K \to 0$, the channel is purely multipath and the fading becomes Rayleigh. Typical K values in a mobile satellite channel range from -15dB to +15dB. The Ricean distribution is given by:

$$p_R(r) = \frac{r}{\sigma^2} exp\left(-\frac{r^2 + s^2}{2\sigma^2}\right) I_0\left(\frac{rs}{\sigma^2}\right)$$
 (2-9)

where σ is the standard deviation of the real or imaginary components, and s is the magnitude of the LOS component. The function I_0 is the modified Bessel function of the first kind and zeroth order. The Rice K factor is given by:

$$K = \frac{power\ in\ constant\ part}{power\ in\ random\ part} = \frac{s^2/2}{\sigma^2} = \frac{s^2}{2\sigma^2}$$
 (2-10)

Ricean channels can be simulated by adding a real component representing the LOS signal magnitude to the complex Gaussian random number generator, or alternatively by using a sum of sinusoids approach [Pat98].

Suzuki model

The Suzuki model [Suz77] is a multiplicative mixture distribution that describes the distribution of large and small scale fading in terrestrial urban environments. It combines the Rayleigh small scale and log-normal large scale distributions. His distribution is formulated as follows:

$$p_{R}(r) = \int_{0}^{\infty} \frac{r}{\sigma^{2}} exp\left(-\frac{r^{2}}{2\sigma^{2}}\right) \frac{1}{\sqrt{2\pi\sigma}d} exp\left(\frac{(\ln\sigma - \mu)^{2}}{2d^{2}}\right) d\sigma$$
 (2-11)

where r is the fading envelope, $2\sigma^2$ is the average Rayleigh power, d is the standard deviation of the normal shadowing variable and μ is the mean value of the normal shadowing variable.

Loo model

The Loo process [Loo85] is the sum of a log-normal random phasor and a Rayleigh phasor:

$$r = z \exp(j\phi_0) + w \exp(j\phi)$$
 (2-12)

where z is log-normally distributed and w is Rayleigh distributed. The phases φ_0 and φ are uniformly distributed between $[0, 2\pi]$. If z is temporarily held constant, then r is simply the Ricean vector:

$$p(r \mid z) = \frac{r}{b_0} exp\left(-\frac{(r^2 + z^2)}{2b_0}\right) I_0\left(\frac{rz}{b_0}\right)$$
 (2-13)

where b_0 is the multipath power, and I_0 is the modified Bessel function of zeroth order. Combining this probability density with that of the log-normal density, the envelope of the Loo density is defined as:

$$p(r) = \frac{r}{b_0 \sqrt{2\pi d_0}} \int_0^\infty \frac{1}{z} exp \left[-\frac{(\ln z - \mu)^2}{2d_0} - \frac{r^2 + z^2}{2b_0} \right] I_0 \left(\frac{rz}{b_0} \right) dz$$
 (2-14)

where $\sqrt{d_0}$ is the standard deviation and μ is the mean of the log-normal process. It can be shown that r is log-normal for small values of multipath, and Rayleigh for large values of multipath power $\sqrt{b_0}$.

Rice-log-normal model

The RLN model, developed by Corazza and Vatalaro [Cor94], [Vat95] can be described by the multiplication of the log-normal phasor and the Ricean phasor:

$$r = RS \exp(j\phi) \tag{2-15}$$

where R is Ricean distributed and S is log-normally distributed. The phase φ is uniformly distributed between $[0, 2\pi]$. The PDF of the Ricean phasor is conditioned on the log-normal amplitude:

$$p(r|S) = 2(K+1)\frac{r}{S^2} exp\left[-(K+1)\frac{r^2}{S^2} - K\right] I_0\left(2\frac{r}{S}\sqrt{K(K+1)}\right)$$
(2-16)

where K is the Rice K factor. Combining the conditioned Ricean phasor and the log-normal phasor:

$$p_{R}(r) = 2(K+1)\frac{r}{\sqrt{2\pi}hd_{0}}\int_{0}^{\infty}\frac{1}{S^{2}}\exp\left[-\frac{1}{2}\left(\frac{\ln S - h\mu}{hd_{0}}\right)^{2}\right]\exp\left[-(K+1)\frac{r^{2}}{S^{2}} - K\right]I_{0}\left(2\frac{r}{S}\sqrt{K(K+1)}\right)dS$$
(2-17)

where $h=(\ln 10)/20$ and $(hd_0)^2$ is the variance and μ is the mean of the normal distribution associated with the log-normal fading process. The Rice factor K is defined as $r_S^2/(2\sigma^2)$, where $r_S^2/2$ is the power of the LOS component and σ^2 is the power of the multipath. As $K\to\infty$, the PDF of the Ricean process tends to the Dirac pulse located at R=1 and the RLN PDF becomes log-normal. As

 $K \to 0$, the Ricean process becomes Rayleigh and the RLN PDF becomes the Suzuki PDF As $K \to \infty$ and $d_0 \to 0$, fading is absent. The RLN PDF is defined fully by the parameters K, μ and d_0 , and lends itself well to software simulators and hardware emulators.

Second order statistics

Second order statistics are a measure of the rate at which the signal level changes with time. They are important in the choice of bit-rate, frame length and the design of interleavers, channel estimators, channel coding to name some examples. Common methods to describe the rate of change of the signal level are by autocorrelation, Doppler spectrum, levels crossings per second and fade durations in seconds. Usually, we refer to the average level crossing rate (LCR) and the average fade duration (AFD), as shown in Fig. 2-4.

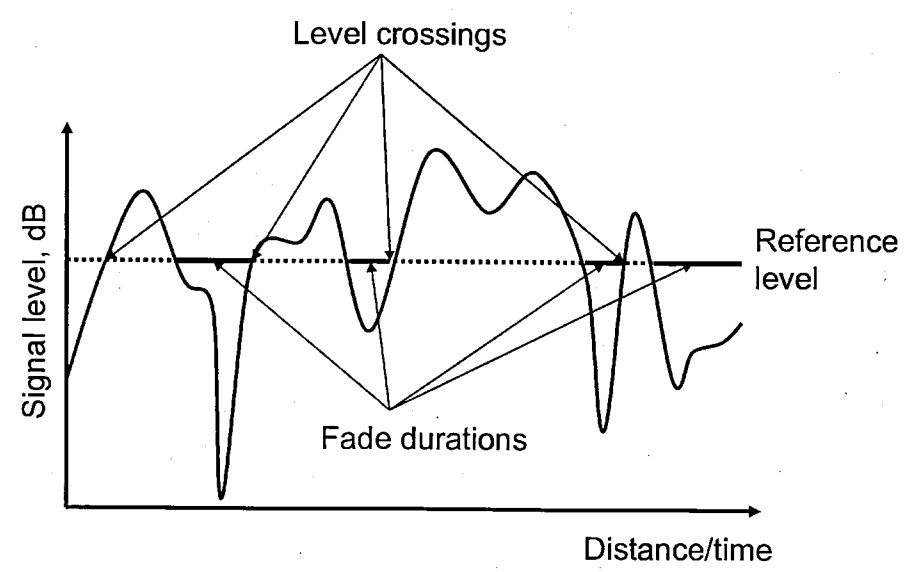


Fig. 2-4 Level crossings and fade durations

Models have been derived for large scale shadow fading, small scale fading and a combination of the two.

Shadowing model

Work in [Has91] used measured data to describe the CDF of fade and non-fade durations, measured in metres. Whilst in fade conditions, with a threshold ranging from 2 - 8dB, the best-fit curve was log-normal. The probability of a fade duration lasting more than x metres is given by:

$$P(d_F > x) = \frac{1}{2} \left[1 - erf \left(\frac{\ln x - \ln a}{\sigma_F \sqrt{2}} \right) \right]$$
 (2-18)

where a and σ_F were computed from the measurement data. Whilst in non-fade conditions, the CDF curve followed a power law:

$$P(d_{nF} > x) = bx^{-c} (2-19)$$

where b and c are derived from the measurement data.

A study [Taa97], based on measurements with elevations ranging from 60° to 80°, found the shadow fading to be log-normally distributed, and suggested an autocovariance formulation:

$$C_S(\tau) = \sigma_S^2 \exp(-v|\tau|/X_C) \tag{2-20}$$

where σ_S is the standard deviation of the log-normal shadow fading, v is the velocity and X_C is the effective correlation distance, defined as the distance when the correlation falls to e^{-l} , and is found to be 9-17m in wooded areas and 16-20m in suburban areas.

Rayleigh model

For the classical Doppler spectrum, theoretical derivations of LCR and AFD for a Rayleigh channel are given in [Jak74]. The LCR, N_R in crossings per second is given as:

$$N_R = \sqrt{2\pi} f_m \bar{r} \exp(-\bar{r}^2) \tag{2-21}$$

where f_m is the maximum Doppler frequency and $\bar{r} = r/r_{rms}$ is the signal level relative to the mean. The AFD, τ in seconds is given as:

$$\tau_{\bar{r}} = \frac{\exp(\bar{r}^2) - 1}{\bar{r}f_{-}\sqrt{2\pi}} \tag{2-22}$$

Note that the LCR and AFD are directly related to the Doppler spectrum. However they are much easier to measure, due to the small shifts in frequency with respect to the carrier frequency in the Doppler spectrum.

2.3.3 Deterministic (or physical) modelling

Due to the global area coverage of satellites, deterministic modelling is not often used in the mobile satellite scenario, as the range of environments to cover are vast. However, if a particular application is required, for example satellite to indoor propagation, then 2D, 2.5D or 3D ray tracing can be used to estimate the wideband shadowing and small scale fading. Some details of applying ray tracing to the mobile satellite environment is given in [Dot01].

2.3.4 Physical-statistical modelling

Whilst physical or deterministic models can provide accurate and detailed electrical channel characteristics, they are impractical for a mega-cell environment. On the other hand purely empirical channel models, based on measurement data, can provide excellent statistical accuracy. However their application is limited to similar environments and frequencies. A compromise between these approaches, known as physical-statistical modelling, was developed in [Sau01]. They combine the statistical accuracy, ease-of-use and low computational requirements of empirical models, yet with the physical insights of deterministic models. The approach uses geometrical optics and the geometrical theory of diffraction, known as ray-tracing, on statistically accurate environment parameters. Different environments can be categorized by a set of these environment statistics – for example the sporadic nature of buildings and their height distributions, and vegetation statistics can be inputted into ray tracing simulations. Physical-statistical channel modelling also lends itself well to obtaining Markov state and transition matrices in multiple-state models. Some examples of physical-statistical modelling are given in [Oes99], [Oes99b], [Sau96], [Sau01] and [Tza98].

2.3.5 Multiple-State models

Markov multiple-state models have gained popularity for LMS channel modelling as they can account for the rapid change in signal level between LOS and NLOS conditions. Two well cited models are now briefly described.

Lutz two state Markov model

Lutz et al [Lut91], [Lut96], [Lut98], [Lut00] conducted a Europe wide measurement campaign from the MAREC B2 satellite at an elevation of 13° to 43°. They derived a two state model from their data. When in a 'good' state, a state with no shadowing, the envelope of the fading was modelled as Ricean with a different Rice K factor for each environment and vehicle antenna. When in a shadowed 'bad' state, the envelope was modelled as a Rayleigh process with log-normal mean distribution. They proposed the following model for simulation, as shown in Fig. 2-5.

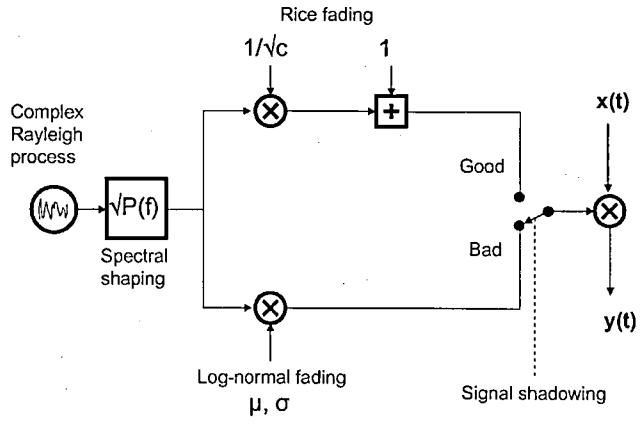


Fig. 2-5 Lutz two state simulation model

The time share of shadowing A is defined by the state transition and probability matrices. The parameters c, μ , and σ were derived from the measured data and presented for various elevations, environments and vehicle antenna. Parameter c defines the Rice K factor, μ is the log-normal process mean and σ is the log-normal process standard deviation.

Three state Markov model

Fontan et al, [Per97], [Per97b], [Per98], [Per01], proposed a three state Markov model, where:

- ◆ State 1: line of sight (LOS) conditions
- ♦ State 2: moderate fading conditions
- ♦ State 3: deep fading conditions

The measured data was low pass filtered into 'very slow' fading, which is used to calculate the Markov state and transition matrices, **W** and **P**. Log-normal fading was used to model the 'slow' fading within each state, and the small scale fading in each state was dependent on the large scale fading level using the Loo approach.

Many measurement campaign datasets were used to derive the parameters for their three state model. 3x1 state and 3x3 transition Markov matrices were derived for each measurement campaign, and therefore given as a function of elevation and environment. The Loo parameters were also calculated separately for each state.

Attempts were also made to derive a wideband model addition to this narrowband SISO model, but were not fully validated due to lack of wideband measurement data.

2.3.6 Wideband models

Most research on LMS channel modelling has created narrowband models as the transmitted bandwidths are usually small compared with the channel coherence bandwidths. At higher elevations associated more often with LMS systems, the coherence bandwidths are usually wider than low elevation terrestrial systems. However, with future broadband systems like the Inmarsat BGAN system, wideband channel modelling becomes increasingly important, to model intersymbol interference for example.

Mobile-satellite wideband channel modelling usually takes the form of a time-variant impulse response, which is often modelled as a delay-line with each tap defined by different weights and distributions. Empirical wideband modelling, based on extensive measurement campaigns, has been carried out in [Par96], [Bel00], [Jah96] and [Jah01].

Chapter Three

3 Terrestrial MIMO Channel Modelling and Capacity

3.1 Introduction

Multiple-input multiple-output (MIMO) systems, where more than one antenna is available at each end of the communication link, has become a highly researched area since ground-breaking work during the nineties showed that large increases in capacity over the Shannon limit were available without increase in power or bandwidth [Fos98].

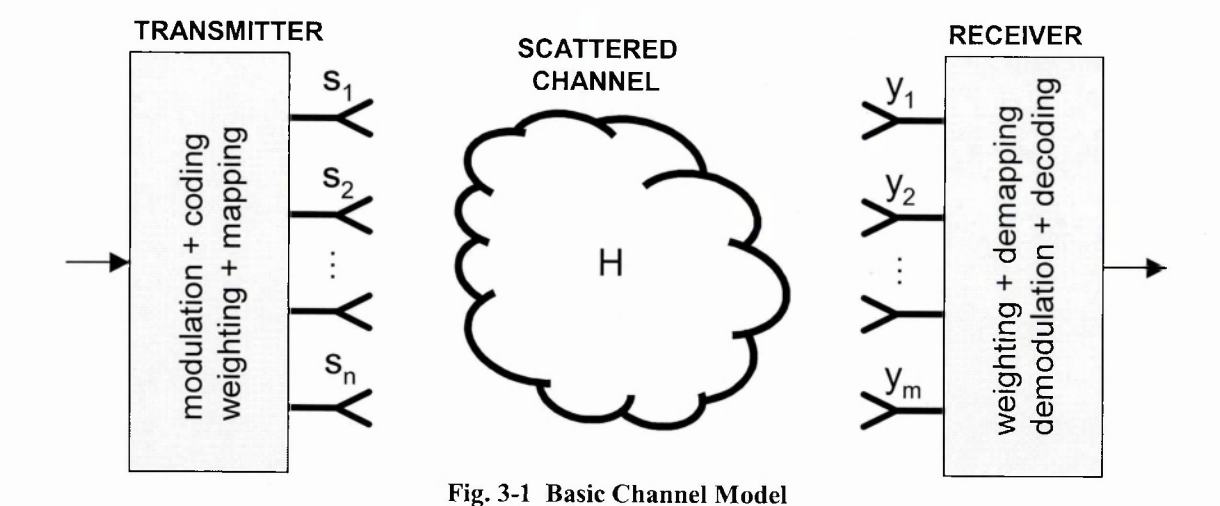
Single-input multiple-output (SIMO) and multiple-input single-output (MISO) systems have been used in mobile communications for many years in order to offer diversity gain. In addition, receiving and transmitting from multiple antennas (known as 'smart antennas') has been used to reduce interference in an interference limited cellular environment and for space division multiple access (SDMA) by providing array gain toward the wanted mobile and array nulling toward unwanted emissions. However this required accurate instantaneous channel information, which is not always available in a scattered environment with incoming rays arriving with significant delay and spatial angular spreads. Using multiple mobile antennas in a LMS-SIMO system can also be achieved [Bea89].

MIMO technology can provide increased diversity and array gain previously associated with SIMO and MISO systems, but also adds a new dimension of capacity gain by spatial multiplexing, where a highly scattered (NLOS) environment is a benefit instead of a hindrance. Here, different data is transmitted simultaneously from each antenna element at the same time and frequency. Advanced receiver algorithms are able to separate each channel because the scattered environment causes these channels to be partially orthogonal; this orthogonality is a random variable as the channel parameters are fluid and hence capacity is also a random variable.

In future land mobile satellite systems, data-rate improvement may also be possible in resource limited allocated spectrum by using satellite-MIMO. Whereas using a higher order modulation scheme can also increase data-rates in the same allocated spectrum, only satellite-MIMO can achieve this for the same required average receive signal to noise ratio (SNR). For land mobile satellite systems, the link budget often prohibits the use of higher order modulation schemes, and satellite-MIMO may be able to offer an improvement.

3.2 The MIMO channel

To explain the principle of MIMO, we start with a single-user, frequency-flat channel with n transmit antennas and m receive antennas [Pau03]:



The input-output relation is given by:

$$y = \mathbf{H}.\mathbf{s} + \mathbf{w} \tag{3-1}$$

where the $n \times 1$ transmit vector is $\mathbf{s} = [\mathbf{s}_1 \ \mathbf{s}_2 \ \dots \ \mathbf{s}_n]^T$, the $m \times n$ channel transfer matrix is:

$$\mathbf{H} = \begin{bmatrix} h_{11} & h_{12} & \cdots & h_{1n} \\ h_{21} & h_{22} & \cdots & h_{2n} \\ \vdots & \vdots & \ddots & \vdots \\ h_{m1} & h_{m2} & \cdots & h_{mn} \end{bmatrix}$$
(3-2)

, the $m \times 1$ receive vector is given by $\mathbf{y} = [y_1 \ y_2 \ ... \ y_m]^T$ and the $m \times 1$ noise vector is given by $\mathbf{w} = [\mathbf{w}_1 \ \mathbf{w}_2 \ ... \ \mathbf{w}_m]^T$. The available capacity, is highly dependent on the variation of \mathbf{H} , the MIMO channel, in addition to the number of transmit and receive antennas and SNR.

In the time domain, the output from a SISO link can be expressed as the convolution of input and channel (dropping the noise contribution for clarity):

$$y(t) = h(\tau, t) * s(t) = \int_{0}^{\tau_{\text{max}}} h(\tau, t) \ s(t - \tau) d\tau$$
 (3-3)

In computer simulation, it is convenient to work with a sampled system and this becomes:

$$y[k] = \sum_{l} h[k-l] s[l]$$
 (3-4)

where s[I] (l=0,1,2,...) are the transmitted data and h[I] (l=0,1,2,...,L-1) is the channel and L is the channel length measured in sampling periods. The received signal sample is therefore:

$$y[k] = [h[L-1]...h[1]h[0]] \begin{bmatrix} s[k-L+1] \\ \vdots \\ s[k-1] \\ s[k] \end{bmatrix}$$
(3-5)

In the MIMO case, we represent the channel by an (n by m) matrix H[k] and so:

$$\mathbf{y}[k] = \begin{bmatrix} \mathbf{h}_{11} & \cdots & \mathbf{h}_{1n} \\ \vdots & \vdots & \vdots \\ \mathbf{h}_{m1} & \cdots & \mathbf{h}_{mn} \end{bmatrix} \begin{bmatrix} s_1[k-L+1] \\ \vdots \\ s_1[k] \\ \vdots \\ s_n[k-L+1] \\ \vdots \\ s[k-1] \\ s_n[k] \end{bmatrix}$$

$$(3-6)$$

where y is the (m by 1) receive vector and the channel vector is given by:

$$\mathbf{h}_{ii} = \left[h_{ii}[L-1] \cdots h_{ii}[0] \right] \tag{3-7}$$

3.3 Array gain, diversity gain and spatial multiplexing

MIMO channels offer many advantages over SISO channels such as array gain, diversity gain and spatial multiplexing gain. Whereas SIMO and MISO systems can offer array gain and diversity gain, only MIMO can offer multiplexing gain with its associated increase in capacity beyond the Shannon limit. Space-time coding and receiver algorithms can trade-off these gains, maintaining adequate bit-error-rate at all times in a noise and interference limited system, but maximising throughput in favourable conditions. Optimising the trade-off between array gain, diversity gain and multiplexing gain is a highly active research area and beginning to gain strength in standardization for cellular, indoor and fixed wireless access environments.

3.3.1 Array gain

Array gain or beamforming has been heavily researched over the last fifteen years under the heading 'smart antennas' or 'adaptive antennas'. In a cellular environment, smart antennas offer increased range, reduced interference and therefore increased capacity, longer mobile battery life due to reduced transmit power, reduced channel delay spread and reduced average human radio emission exposure. In spatial filtering for interference reduction (SFIR), weights are applied to each antenna to direct the beam toward the wanted mobile and null out interference, and results in the one wanted output. However, with more complex signal processing, each mobile in a cell can be extracted and interference nulled simultaneously in a system known as space division multiple access (SDMA) [Sau99].

3.3.2 Diversity gain

A SISO system in a Rayleigh channel can experience –40dB below mean fades with 0.01% probability increasing to –20dB fades with 1% probability. Time diversity, frequency diversity or spatial diversity techniques are often used to greatly reduce the chance of a deep fade. 10dB of diversity gain can be achieved for dual diversity at 1% fade probability increasing the fade depth to – 10dB.

In time diversity, data is retransmitted after a delay of at least the channel coherence time (therefore being an uncorrelated channel). However, this reduces the data rate as copies of the data are sent.

In frequency diversity, data is transmitted simultaneously at different frequencies at least the coherence bandwidth apart (therefore ensuring an uncorrelated channel). However, again this is often undesirable as it wastes valuable bandwidth. Selecting good sub-carriers in OFDM systems is a form of frequency diversity.

Spatial diversity where two or more antennas are used at the transmitter (MISO), receiver (SIMO) or both (MIMO) does not use extra bandwidth, but adds complexity and cost to the base station, mobile or both. However it is often preferable and base station spatial diversity has been in general deployment for over a decade.

To combine signals from two or more antennas, a trade-off between complexity, cost and performance is made [Sau99]. Selection combining merely selects the antenna with highest instantaneous SNR. The drawback is that each antenna SNR must be monitored simultaneously. Switched combining, where a new antenna is switched-in when the SNR falls below a pre-defined threshold level is a lot simpler, particularly since only one RF transceiver is required. In order to gain energy from all antennas, each channel can be co-phased and added and this is known as equal gain combining. However, a channel with low SNR can affect the other channels and so the ideal

combining method known as maximum ratio combining, can be used to maximise overall SNR by weighting each channel in amplitude and phase. Optimum combining refers to maximum ratio combining that maximises signal to interference plus noise ratio (SINR).

3.3.3 Spatial multiplexing gain

Multiplexing gain increases the bit-rate without using more power or bandwidth, and requires multiple antennas at both ends of the link. Data is multiplexed over each transmit antenna as shown below [Ges03], [Bea01]:

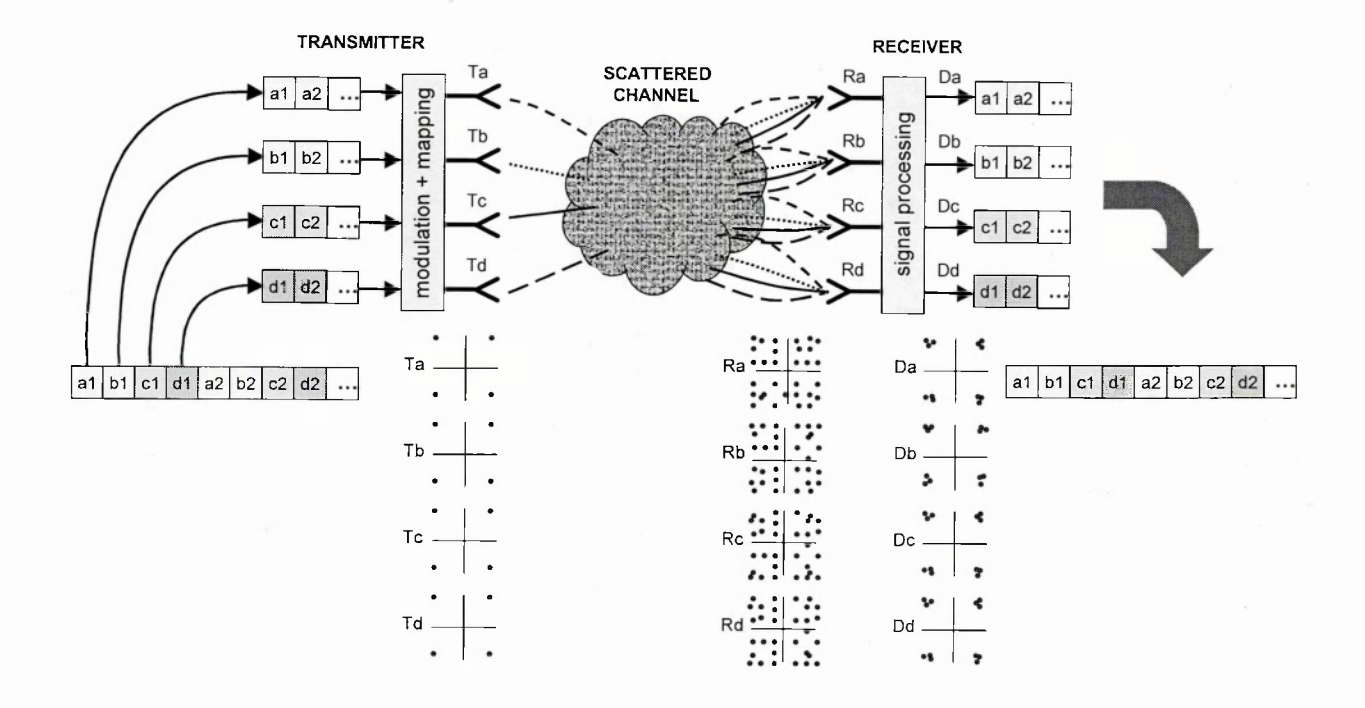


Fig. 3-2 MIMO used for Spatial Multiplexing Gain

3.4 Capacity principles

3.4.1 Capacity of SISO and MIMO channels

The Shannon upper bound limit on capacity is given by the following equation:

$$C = \log_2[1 + SNR] \text{ bps/Hz}$$
 (3-8)

Or, when including a SISO channel, it can be expressed as:

$$C = \log_2 \left| 1 + SNR \left| h \right|^2 \right| \text{ bps/Hz}$$
 (3-9)

where h is a normalized ($E[|\mathbf{h}|^2]=1$) channel power complex scalar. In this case, 3dB more SNR gives one more bps/Hz capacity.

This capacity can be approached with advanced modulation and channel coding techniques, however, (3-8) was seen as an upper bound until half a century later, when pioneering work at Bell-Labs changed the course of communications research. In 1987, J.Winters published the concept of a new technique using multiple antennas at both the transmitter and receiver [Win87], now known as MIMO. In 1995, I.E.Teletar published derivations of capacities in Gaussian and fading channels for MIMO systems [Tel95]. In 1996, G.Foschini presented his derivation for the upper bound capacity for MIMO channels [Fos96]:

$$C = \log_2 \det \left[\mathbf{I}_m + \left(\frac{SNR}{n} \right) \mathbf{H} \mathbf{H}^H \right] \text{ bps/Hz}$$
 (3-10)

where det is the determinant, I_m is the m by m identity matrix, m is the number of receive antenna elements and n is the number of transmit antenna elements. It is assumed that the receiver but not the transmitter has knowledge of the channel and that the channel is frequency non-selective (flat fading) over the signal bandwidth. H is the channel matrix and H^H is the complex conjugate transpose or Hermitian adjoint:

$$\mathbf{H} = \begin{bmatrix} h_{11} & h_{12} & \cdots & h_{1n} \\ h_{21} & h_{22} & \cdots & h_{2n} \\ \vdots & \vdots & \ddots & \vdots \\ h_{m1} & h_{m2} & \cdots & h_{mn} \end{bmatrix} \quad \mathbf{H}^{H} = \begin{bmatrix} h_{11}^{*} & h_{21}^{*} & \cdots & h_{m1}^{*} \\ h_{12}^{*} & h_{22}^{*} & \cdots & h_{m2}^{*} \\ \vdots & \vdots & \ddots & \vdots \\ h_{1n}^{*} & h_{2n}^{*} & \cdots & h_{mn}^{*} \end{bmatrix}$$
(3-11)

In [Fos98], graphs of 99 percentile capacities as a function of number of antennas (m=n) and average receive SNR, Γ are presented. If, which is often the case in NLOS conditions, each of the

elements of the matrix \mathbf{H} , denoted by h_{mn} are independent identically distributed (i.i.d.), complex, zero mean, unit-variance random variables given by:

$$h_{nm} = Normal(0, 1/\sqrt{2}) + \sqrt{-1} \ Normal(0, 1/\sqrt{2}),$$
 (3-12)

it was shown that, for a SISO link with $\Gamma = 12 dB$, the maximum capacity achievable is 4.1 bps/Hz. However, for a 16x16 MIMO system, the same SNR provides approximately 45bps/Hz. This is gained without increases in total transmit power and is attributed to the orthogonality of rich multipath scattering.

For example, the following plot in Fig. 3-3 shows the cumulative distribution of capacity of a 2x2 MIMO system compared to a SISO system. In the SISO case, a zero mean, unit variance complex Gaussian channel is used with a received SNR of 10dB. In the MIMO case, four independent instances of the SISO channel are used with an average receive SNR of 10dB.

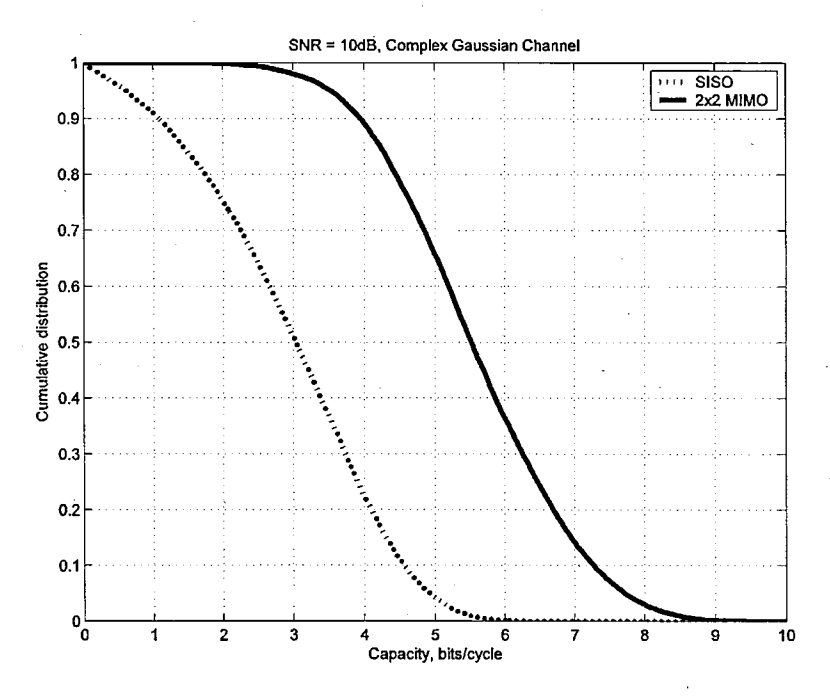


Fig. 3-3 Example comparison of capacity increase from a 2x2 MIMO system over a SISO system

It can be seen that a significant increase in capacity is possible for the same power and bandwidth. Capacity units are given in bits/cycle, which is identical to bits/s/Hz.

3.4.2 Eigenanalysis of channel

The MIMO channel can also be interpreted as a set of min(n, m) parallel eigen-channels [Ker02], where the amplitude of each sub-channel is given by λ_i , the i^{th} eigenmode of \mathbf{HH}^H . To find the eigenvalues, either \mathbf{HH}^H can be diagonalized using eigenvalue decomposition (EVD) to find λ_i or \mathbf{H} can be diagonalized using singular value decomposition (SVD) to find σ_i noting that $\sigma_i = \sqrt{\lambda_i}$. When \mathbf{H} is unknown at the transmitter, equal power is transmitted from each antenna element. Capacity can be formulated as:

$$C = \sum_{i=1}^{k} \log_2 \left[1 + \frac{SNR}{n} \lambda_i \right] \text{ bps/Hz}$$
 (3-13)

where k is the rank of \mathbf{H} , which is at most $\min(m, n)$. The rank of a matrix is the number of linearly independent rows or columns of a matrix. By using signalling feedback or in a TDD system, \mathbf{H} is known at the transmitter as well as the receiver. The transmitter can use this information by increasing the power to the strongest sub-channels. In this case, the capacity:

$$C = \sum_{i=1}^{k} \log_2 \left[1 + \frac{p_i}{\sigma^2} \lambda_i \right] \text{bps/Hz}$$
 (3-14)

where p_i is the power in the i^{th} sub-channel and σ^2 is the noise power and $SNR = \frac{P_T}{\sigma^2}$ where

$$P_T = \sum_{i=1}^k p_i = \sum_{i=1}^k \left(v - \frac{1}{\lambda_i} \right)^+$$
. This technique is known as waterfilling and means: start with the

strongest sub-channel, allocate power: $p_i = v - \frac{1}{\lambda_i}$, where v is a fixed threshold level. Then repeat the process for the next strongest sub-channel, and so on.

3.4.3 Capacity of SIMO and MISO channels

In a receive diversity SIMO (single input multiple output) case, when the receiver uses optimum combining (maximum ratio combining), the capacity can be given by [Fos98]:

$$C = \log_2 \left[1 + SNR \sum_{i=1}^m \left| h_i \right|^2 \right]$$
 bps/Hz (3-15)

When using selection diversity, where the strongest channel is selected, the capacity is given by:

$$C = \max_{m} \log_{2} \left[1 + SNR \left| h_{m} \right|^{2} \right] = \log_{2} \left[1 + SNR \max_{m} \left| h_{m} \right|^{2} \right] \text{ bps/Hz}$$
 (3-16)

For a transmit diversity MISO (multiple input single output) system, if it is assumed that the total transmit power across all antennas is constant, then the capacity becomes:

$$C = \log_2 \left[1 + \frac{SNR}{n} \sum_{i=1}^n \left| h_i \right|^2 \right] \text{ bps/Hz}$$
 (3-17)

3.4.4 Frequency selective channel

When the coherence bandwidth << 1 / symbol duration or the coherence time << symbol duration, the channel can be described as frequency selective. An expression for capacity can be obtained by channelizing the bandwidth into small bins, working out the capacity in each bin and adding them together [Mol02]. Frequency flat fading can then be applied to each bin. In the limit as the bin bandwidth becomes very small, it is the same as integrating over the bandwidth, B:

$$C = \frac{1}{B} \int \log_2 \det \left(\mathbf{I} + \frac{SNR}{n} \mathbf{H}(f) \mathbf{H}^H(f) \right) df \text{ bps/Hz}$$
 (3-18)

The steepness of a capacity cumulative distribution graph will increase with a more frequency selective channel thus improving outage performance. In practice this can be realized taking advantage of the multipath using a diversity technique like a Rake receiver [Sau99], or by using OFDM modulation.

3.4.5 Causes of sub-optimal capacity

In practice, the optimal capacity achieved above is not possible due to a number of factors: no multipath or limited scatterers, a LOS component (Ricean fading), keyholes, antenna element correlation at the Tx, Rx or both due to low angular spread, small element separation and antenna geometry.

Effect of no multipath

Where there is a single LOS component only, there is the free space loss propagation scenario with attenuation:

$$FSL = \frac{G_1 G_2 \lambda^2}{(4 \pi R)^2}$$
 (3-19)

[Dri99] derives a formula relating the channel coefficients to the antenna element spacing:

$$h_{ik} = (T_1 - R_1) \exp \left[\frac{(-j2\pi |T_i - R_k|/\lambda)}{|T_i - R_k|} \right], \tag{3-20}$$

where T_i , R_i are coordinate vectors for the i^{th} element of T, R and h_{ik} is normalized between T_1 , R_1 so that $h_{11} = 1$ and n=m.

Since there is no rich multipath scattering, capacity is reduced. In the case where the antenna elements at both ends are spaced less than half a wavelength apart, the phases become nearly equal therefore the channel coefficients become all equal: $\mathbf{HH}^H \approx \mathbf{n}$ and \mathbf{H} is of rank 1 and the capacity gain is essentially due to an n-fold array gain and becomes: $C = \log_2(1 + n \ SNR)$. When the array spacing is wider, the complex scalars h_{ik} all have magnitude near one but with different phases so that: $\mathbf{HH}^H \approx \mathbf{n} \ \mathbf{I}_n$. In this case \mathbf{H} is of rank n and $C = n \log_2(1 + SNR)$.

Effect of limited scatterers

In [Bur02], [Bur03], capacity derivations are given for channels with finite scattering, using ray tracing methods. In [Bur03] the finite scatterer model shows that for the case when n, $m\rightarrow\infty$, for $\lambda/2$ spaced antenna elements:

$$C = \sum_{i=1}^{n_s} \log_2 \left[1 + SNR \ m \left| \xi_i \right|^2 \right]$$
bps/Hz (3-21)

where n_s is the number of scatterers and ξ_i is the power gain of the i^{th} scatterer, where λ_i , the i^{th} eigenmode equals $m.n.|\xi_i|^2$. The rank of **H** is limited to min (n, m, n_s) .

In [Bur02], a simple ray tracing approach is used to derive the elements of H as:

$$h_{ik} = \sum_{p} \left[\gamma_{p} \exp \left(\frac{2 \pi j i l}{\lambda} \sin(\phi_{R,p}) \right) \exp \left(\frac{2 \pi j k l}{\lambda} \sin(\phi_{T,p}) \right) \right]$$
(3-22)

where p is the multipath index, $\varphi_{R,p}$ is the angle of arrival at the receiver and $\varphi_{T,p}$ is the angle of departure at the transmitter, l denotes the antenna element spacing and γ_p is the complex path propagation. Capacity simulations are shown for a perfectly conducting corridor and an imperfect conducting corridor.

Effect of Ricean fading

The Ricean MIMO channel can be modelled as the sum of a LOS matrix and a fading matrix:

$$\mathbf{H} = \sqrt{\frac{K}{1+K}} \,\overline{\mathbf{H}} + \sqrt{\frac{1}{1+K}} \,\mathbf{H_w} \tag{3-23}$$

where $\mathbf{H}_{\mathbf{w}}$ are statistically independent unit variance complex Gaussian random variables, while $\overline{\mathbf{H}} = \mathbf{a}(\theta_t) \mathbf{a}(\theta_r)^{\mathsf{T}}$, where $\mathbf{a}(\theta_t)$ and $\mathbf{a}(\theta_r)$ are the specular array responses at the transmitter and receiver respectively. When K=0, we have Rayleigh fading and when $K\to\infty$, we have a non-fading case. [Dri99] shows capacity results for 0 < K < 20, with two different specular array geometries and shows ergodic capacity can increase or decrease depending on K and the geometry.

Effect of keyholes

Keyholes describe a reduced capacity scenario due to a rank deficient yet uncorrelated channel matrix [Loy02], [Chi02]. Theoretically this situation arises when there is a metal screen between the Tx and Rx with a small hole through which all the rays pass. In practice this might be caused when the mobile goes through a tunnel or for an indoor environment, when the rays propagate down a hallway.

The electric field incident on the keyhole is:

$$E_{inc} = \begin{bmatrix} a_1 & a_2 \end{bmatrix} \begin{bmatrix} s_1 \\ s_2 \end{bmatrix}$$
 (3-24)

, where s_1 and s_2 are the transmitted signals and a_1 , a_2 are the channel coefficients before the keyhole. Assuming rich scattering around the transmitter, a_1 , a_2 are independent Gaussian random variables. The field transmitted through the keyhole is: σE_{inc} . Denoting the scattering around the receive array b_1 , b_2 , also independent Gaussian random variables, the received electric field strength is:

$$E_{rec} = \begin{bmatrix} b_1 \\ b_2 \end{bmatrix} \sigma E_{inc} \tag{3-25}$$

The channel matrix **H** is therefore:

$$\mathbf{H} = \begin{bmatrix} b_1 \\ b_2 \end{bmatrix} \sigma \begin{bmatrix} a_1 & a_2 \end{bmatrix} = \sigma \begin{bmatrix} a_1 b_1 & a_2 b_1 \\ a_1 b_2 & a_2 b_2 \end{bmatrix}$$
(3-26)

Writing $\mathbf{v} = \mathbf{H} \mathbf{x}$, we have:

$$\begin{bmatrix} y_1 \\ y_2 \end{bmatrix} = \sigma \begin{bmatrix} a_1b_1 & a_2b_1 \\ a_1b_2 & a_2b_2 \end{bmatrix} \begin{bmatrix} x_1 \\ x_2 \end{bmatrix} = \begin{bmatrix} \sigma b_1 (a_1 x_1 + a_2 x_2) \\ \sigma b_2 (a_1 x_1 + a_2 x_2) \end{bmatrix}$$
(3-27)

Therefore **H** is uncorrelated yet has one degree of freedom and capacity is reduced.

Effect of correlation

In (3-10) the assumption is made that each H matrix element h_{mn} is independent and therefore any two elements are uncorrelated. However in practice, different environments cause different amounts of channel matrix correlation. Channel correlation is the result of small angular spread at the Tx or Rx or both, small antenna element separation and antenna geometry. The effect of correlation on capacity was studied analytically in [Loy01a], [Loy01b]. He considered n equal rate and equal power parallel sub-channels (with n=m), where the correlation coefficient, r is between any two channels. Capacity as a function of SNR, n and r is given as:

$$C_{nn}(r) = n \log_2 \left(1 + \frac{SNR}{n} (1 - r) \right) + \log_2 \left(1 + \frac{n \ SNR \ r}{n + SNR(1 - r)} \right)$$
(3-28)

This shows for example that r=0.7 is equivalent to a 3dB reduction in SNR. When r=0, the channel matrix **H** becomes equal to **I** and reduces to:

$$C_{nn} = n \log_2 \left(1 + \frac{SNR}{n} \right) \text{ bps/Hz}$$
 (3-29)

In cases where r<0.6, (3-28) can be approximated by:

$$C_{nn} \approx n \log_2 \left(1 + \frac{SNR}{n} (1 - r) \right) \text{ bps/Hz}$$
 (3-30)

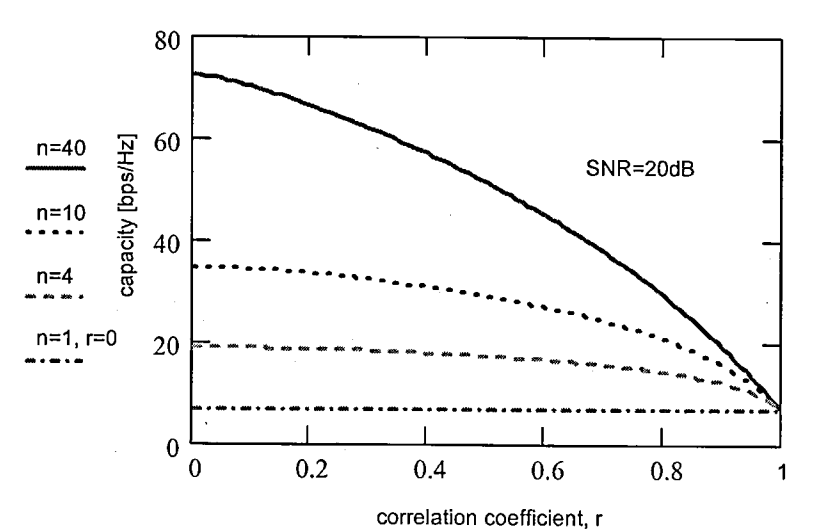


Fig. 3-4 Channel capacity for n coupled channels versus correlation

In order to maximise capacity, the sub-channels must be kept independent, which is the role of adaptive space-time coding.

Correlated channels, which imply elements of **H** are correlated, can be modelled by:

$$vec(\mathbf{H}) = \mathbf{R}^{(1/2)} vec(\mathbf{H}_{w})$$
(3-31)

where H_w is the spatially white (ie all ray AoA and AoD equally likely) $m \times n$ channel matrix. R is the covariance matrix of the channel:

$$\mathbf{R} = E(vec(\mathbf{H}) \ vec(\mathbf{H})^{\mathbf{H}}) \tag{3-32}$$

If **R** is the identity matrix, **H** is spatially white.

Alternatively, a simpler and less generalized model is often adequate, which can be expressed as the product of transmit and receive correlation matrices [Chiz03]:

$$\mathbf{H} = \mathbf{R}_{Tx}^{(1/2)} \mathbf{H}_{w} \mathbf{R}_{Rx}^{(1/2)}$$
 (3-33)

where \mathbf{R}_{Tx} and \mathbf{R}_{Rx} are the transmitting and receiving correlation matrices, which could be the function of angle of arrival (AoA), power azimuth spectrum (PAS), the antenna spacing and the radiation pattern of the antenna elements and distance between transmitter and receiver. $\mathbf{H}_{\mathbf{w}}$ can be modelled as a matrix of independent zero mean, unit variance, complex Gaussian random variables.

Effect of polarization

For a 2×2 MIMO channel, the channel matrix **H** is formulated as [Erc02]:

$$\mathbf{H} = \mathbf{H}_{LOS} + \mathbf{H}_{NLOS} = \left(\sqrt{\frac{K}{K+1}} \mathbf{H}_{F} + \sqrt{\frac{1}{K+1}} \mathbf{H}_{V} \right)$$

$$= \left(\sqrt{\frac{K}{K+1}} \begin{bmatrix} e^{j\phi_{11}} & \alpha_{1}e^{j\phi_{12}} \\ \alpha_{1}e^{j\phi_{21}} & e^{j\phi_{22}} \end{bmatrix} + \sqrt{\frac{1}{K+1}} \begin{bmatrix} X_{11} & \alpha_{2}X_{12} \\ \alpha_{2}X_{21} & X_{22} \end{bmatrix} \right)$$
(3-34)

where X_{ij} (i^{th} transmitting antenna and j^{th} transmitting antenna) are uncorrelated zero-mean, unit variance, complex Gaussian random variables as coefficients of the variable (Rayleigh) matrix \mathbf{H}_{ν} , $\exp(j\phi_{NM})$ are the elements of fixed matrix \mathbf{H}_{F} , K is the Rice K-factor, and α_{i} represents the cross-polarization discrimination (XPD). If K=0, then

$$H = \left(\sqrt{\frac{K}{K+1}} \begin{bmatrix} e^{j\phi_{11}} & \alpha_{1}e^{j\phi_{12}} \\ \alpha_{1}e^{j\phi_{21}} & e^{j\phi_{22}} \end{bmatrix} + \sqrt{\frac{1}{K+1}} \begin{bmatrix} X_{11} & \alpha_{2}X_{12} \\ \alpha_{2}X_{21} & X_{22} \end{bmatrix} \right) = \begin{bmatrix} X_{11} & \alpha_{2}X_{12} \\ \alpha_{2}X_{21} & X_{22} \end{bmatrix}$$
(3-35)

and becomes a pure Rayleigh fading channel.

3.5 Antenna arrays and correlation

3.5.1 Antenna pattern

Antenna arrays enable more control over the antenna pattern that would not be possible with a single antenna. By changing the amplitude, phase and alignment to a quantity of antenna elements, it is possible to create a vast amount of antenna patterns, increasing with a higher quantity of elements. This has the advantage of increasing directivity and nulling interference in a SDMA system for example. In this case, the amplitude and phase weights become time-variant, as the antenna pattern adapts to the changing mobile environment.

For an antenna array, the antenna pattern can be found by pattern multiplication:

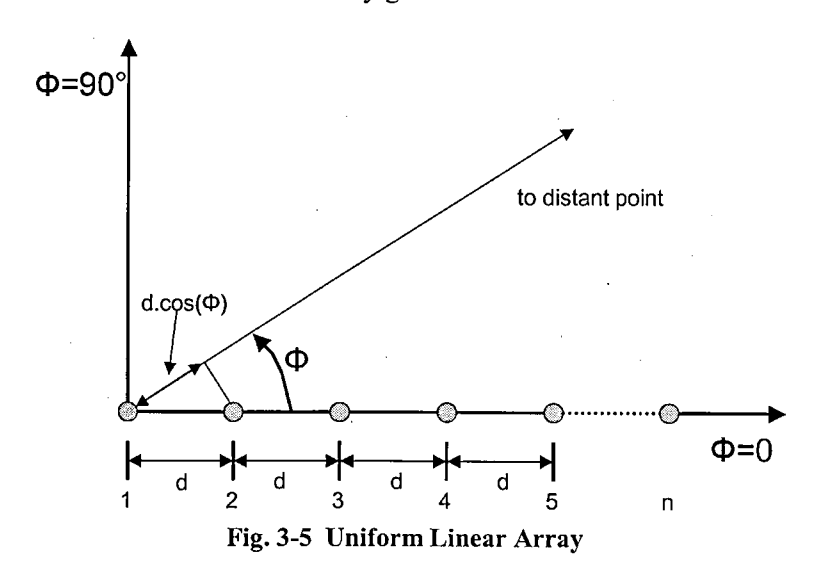
Antenna array pattern
$$(\theta, \Phi)$$
 = Antenna element pattern (θ, Φ) x Antenna array factor (θ, Φ) (3-36)

Assuming no mutual coupling between the antenna elements, the Antenna array factor(θ, Φ) is given by:

$$AF(\theta,\phi) = \exp(j k r_0) \sum_{n} A_n \exp(j \alpha_n) \exp(-j k r_n(\theta,\phi))$$
(3-37)

where $k=2\pi/\lambda=$ the wavenumber, $r_0=$ phase centre reference point in antenna structure, $A_n=$ element weighting amplitude, $\alpha_n=$ element weighting phase and $r_n(\theta,\Phi)=$ distance to imaginary sphere in the far field centred on r_0 in (θ,Φ) direction.

Starting with a uniform linear array consisting of n isotropic radiators, the far field antenna factor is derived by summing the excitations at each element. As the angle of incidence Φ increases, the phase shift between each element decreases; when the angle of incidence is broadside (Φ =90°), all elements are in phase and there is an n-fold array gain.



Making the assumption that electric field amplitudes arriving at each antenna element are all equal to 1, taking the phase centre at element 1, the electric field,

$$E = 1 + \exp(j \psi) + \exp(j 2 \psi) + \exp(j 3 \psi) + \cdots + \exp(j (n-1) \psi)$$
 (3-38)

where,

$$\psi = k \, d \cos(\Phi) \tag{3-39}$$

which is equal to the phase difference between elements

Now, the electric field can be expressed:

$$E = \frac{1 - \exp(j \, n \, \psi)}{1 - \exp(j \, \psi)} = \frac{\exp(j \, n \, \psi/2)}{\exp(j \, \psi/2)} \left(\frac{\exp(j \, n \, \psi/2) - \exp(-j \, n \, \psi/2)}{\exp(j \, \psi/2) - \exp(-j \, \psi/2)} \right) = g \, \frac{\sin(n \, \psi/2)}{\sin(\psi/2)}$$
(3-40)

If the phase centre is taken at the array centrepoint,

$$E = \frac{\sin(n\psi/2)}{\sin(\psi/2)} \tag{3-41}$$

The following graphs show the ULA antenna factor as a function of n, the number of elements with $\lambda/2$ element spacing Fig. 3-6 (left), and as a function of distance between the elements for an n=4 array Fig. 3-6 (right).

Note that $\Phi=0^{\circ}$ is the ULA end-fire orientation and $\Phi=90^{\circ}$ is the broad-side.

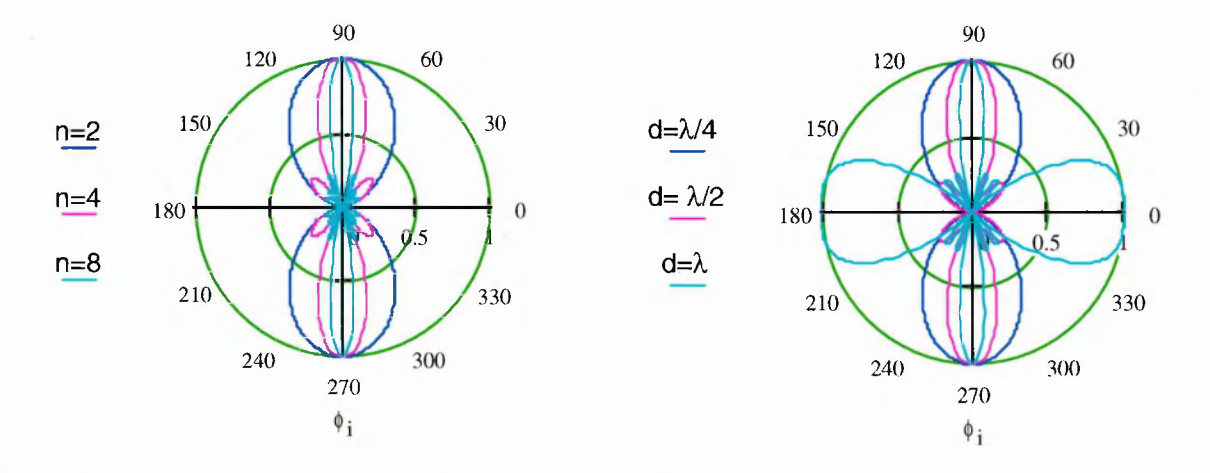


Fig. 3-6 Antenna Factor as a function of number of elements (left) and element separation (right)

Equation (3-38) can be written as the antenna array steering vector:

$$\mathbf{a}(\theta) = \begin{bmatrix} \exp(j \ k \ d \cos \theta) \\ \exp(j \ k \ 2 \ d \cos \theta) \\ \vdots \\ \exp(j \ k \ n \ d \cos \theta) \end{bmatrix}$$
(3-42)

Similarly, the weights applied to each antenna element can be written as the weight vector:

$$\mathbf{W} = \begin{bmatrix} w_1 \\ w_2 \\ \vdots \\ w_n \end{bmatrix}$$
 (3-43)

From the steering vector and the antenna weight vector, the antenna factor is found [Lib99]:

$$AF(\theta) = \mathbf{w}^{\mathsf{H}} \ \mathbf{a}(\theta) \tag{3-44}$$

Once the Antenna array pattern is found, the directivity can be found from:

$$D = \frac{4\pi}{\int\limits_{0}^{2\pi\pi} \int\limits_{0}^{\pi} AP(\theta,\phi) \sin\theta d\theta d\phi} \approx \frac{4\pi}{\sum\limits_{\phi=1}^{360} \sum\limits_{\theta=1}^{180} AP(\theta,\phi) \sin\theta}$$
(3-45)

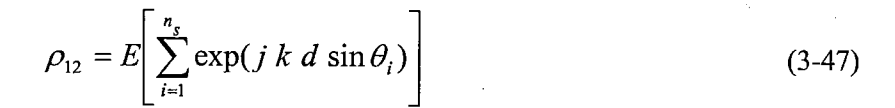
3.5.2 Correlation at antenna elements

It is important to understand and be able to predict the correlation distribution between waveforms impinging on each antenna element in a variety of environments, since the performance of diversity, multi-user detection, channel estimation and MIMO capacity for example is dependent on it.

The correlation coefficient between two waveforms at the antenna is given by [Sau99]:

$$\rho_{AB} = \frac{E[(\alpha_A - \mu_A)(\alpha_B - \mu_B)^*]}{\sigma_A \sigma_B}$$
(3-46)

where E[.] is the expectation, μ_A , μ_B are the means and σ_A , σ_B are the standard deviations of α_A and α_B . The waveforms arriving from the transmitter via each scatterer will in general have a different phase and angle of arrival. Using (3-38) and (3-46), assuming uncorrelated amplitudes, the correlation coefficient due to phase becomes the expected value of the sum of the phases associated with each scatterer:



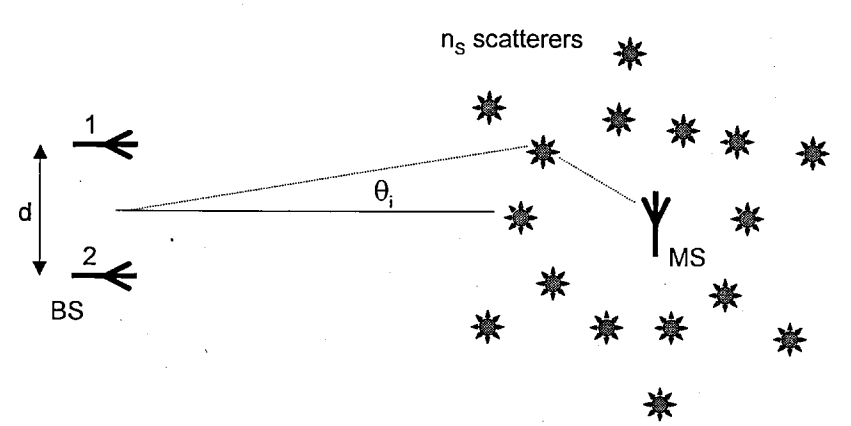


Fig. 3-7 Figure showing location of scatterers

If the probability density of the angle of arrival is known, then the expected correlation can be found from:

$$\rho_{12}(d) = \int_{\theta=0}^{2\pi} p(\theta) \exp(j k d \sin \theta) d\theta \approx \sum_{i=1}^{360} p_i \exp(j k d \sin(\theta_i))$$
 (3-48)

Correlation at the basestation (BS) antenna therefore decreases with increasing angular spread and with increasing antenna element separation. Increased angular spread also implies that scatterers around the mobile are more widely spaced increasing the distribution of time of arrival or excess delay.

To estimate the correlation at the BS antennas, Jakes [Jak74] used a single ring model:

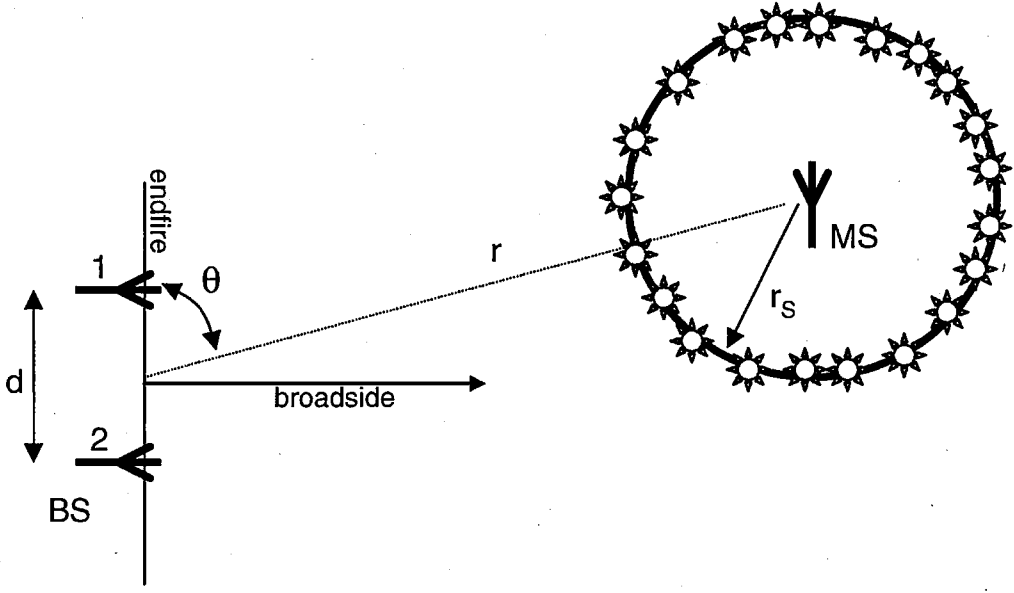


Fig. 3-8 Diagram showing single ring model

and showed:

$$\rho_{12}(d) = J_0 \left(\frac{2 \pi d}{\lambda} \frac{r_S}{r} \sin \theta \right)^2 J_0 \left(\frac{\pi d}{\lambda} \left(\frac{r_S}{r} \right)^2 . \sqrt{1 - \frac{3}{4} \cos^2 \theta} \right)^2$$
(3-49)

The function J_0 is the Bessel function of the first kind and zeroth order. Example plots for $r_S / r = 0.006$ are shown in Fig. 3-9.

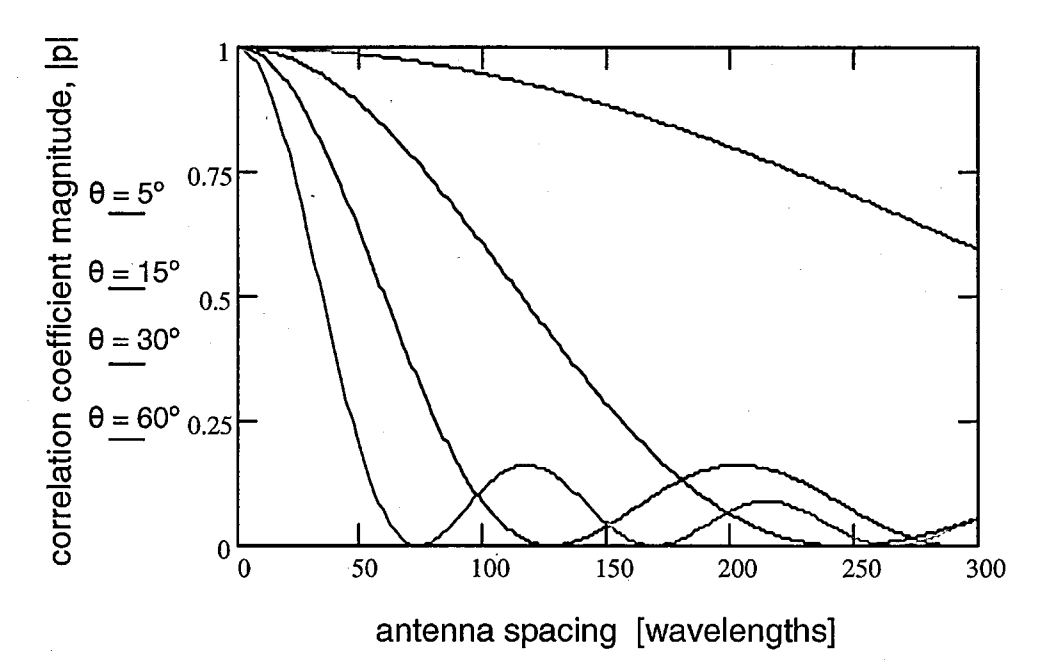


Fig. 3-9 Correlation coefficient at basestation antennas

It should be noted that this is rather pessimistic as it includes no vertical spreading [Sau99].

For mobile (MS) correlation, if we use a uniform angular distribution PDF over $[0, 2\pi]$ then the solution of (3-47) with $p(\theta) = 1/2\pi$ becomes:

$$\rho_{12}(d) = J_0\left(\frac{2\pi d}{\lambda}\right) \tag{3-50}$$

This is shown in Fig. 3-10 below:

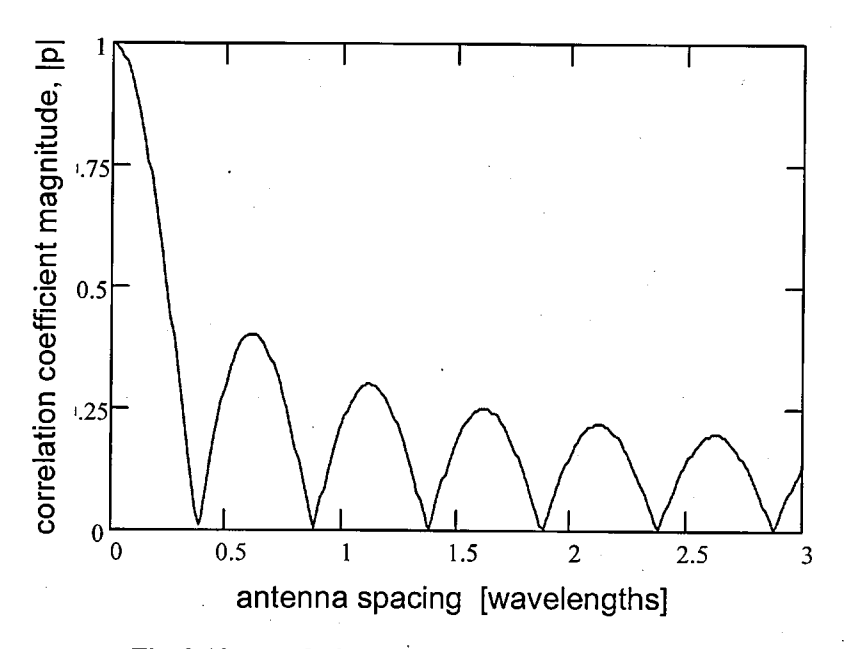


Fig. 3-10 correlation coefficient at mobile antennas

It is observed that the minimum antenna spacing is \sim 0.4 wavelengths for a zero correlation. However as the angle of arrival PDF spread is reduced below $[0,2\pi]$, antenna spacing must be increased slightly to obtain small correlation. In practice, a reduced spacing may be possible when using spatial, angular and polarization diversity combined [Bro05].

In a larger antenna array, the correlation between each element can be found from the steering vector $\mathbf{a}(\theta)$ and the angle of arrival probability density, $p(\theta)$ yielding:

$$\mathbf{R}_{XY} = \int_{\theta=0}^{2\pi} \mathbf{a}(\theta) \, \mathbf{a}(\theta)^{H} \, p(\theta) \, d\theta$$
 (3-51)

where (.) H is the complex conjugate transpose and R_{XY} is of the form:

$$\mathbf{R}_{XY} = \begin{bmatrix} \rho_{11} & \rho_{12} & \cdots & \rho_{1Y} \\ \rho_{21} & \rho_{22} & \cdots & \rho_{2Y} \\ \vdots & \vdots & \ddots & \vdots \\ \rho_{X1} & \rho_{X2} & \cdots & \rho_{XY} \end{bmatrix}$$
(3-52)

3.5.3 Angle of arrival

Whereas a mobile experiencing Rayleigh fading often has an angle of arrival described as a uniform PDF $[0,2\pi]$, at the basestation with antennas elevated above the scatterers, a narrower PDF is used. Some of the early work described this PDF as Gaussian:

$$p(\phi) = \frac{c}{\sqrt{2 \pi} \sigma} \exp\left(-\frac{\phi^2}{2 \sigma^2}\right)$$
 (3-53)

However, [Ped97] showed measurements in urban and rural environments were more accurately described by a Laplacian PDF:

$$p(\phi) = \frac{c}{\sqrt{2} \sigma} \exp\left(-\frac{\sqrt{2} |\phi|}{\sigma}\right)$$
 (3-54)

where σ is the angular spread and c is set so the total power is one.

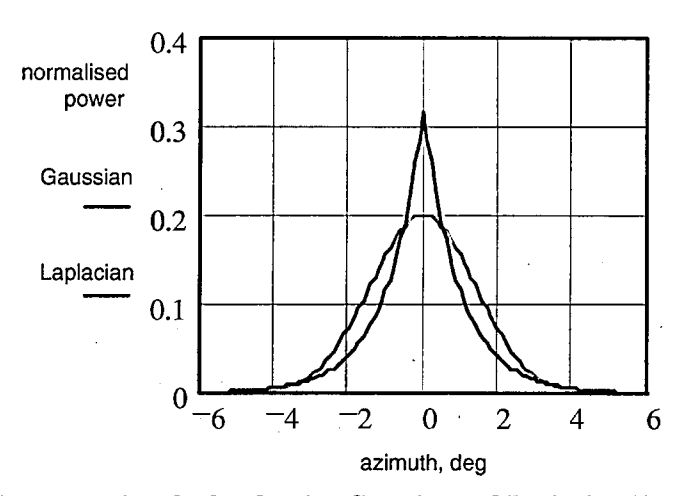


Fig. 3-11 Antenna azimuth plot showing Gaussian and Laplacian distributions

The Laplacian was shown to be a better fit to measurements and also included the peak at 0°. Zero degrees azimuth denotes the direction towards the transmitter. Typical values of σ are 1° for a rural environment [Ped97] and many tens of degrees in indoor environments. The root-mean-squared value of angular spread is calculated as shown below [Pau03]. Spatial selective fading is characterized by the coherence distance, D_C , where D_C is proportional to $(1 / S_{\theta RMS})$.

$$S_{\theta RMS} = \sqrt{\frac{1}{P_T} \sum_{i=1}^{n} P_i \ \theta_i^2 - \overline{\theta}^2}$$
 (3-55)

where
$$\overline{\theta} = \frac{1}{P_T} \sum_{i=1}^n P_i \ \theta_i \ \text{and} \ P_T = \sum_{i=1}^n P_i$$
 (3-56)

3.6 Terrestrial MIMO channel models

MIMO system design greatly benefits from the availability of an accurate channel model, as it allows system components to be optimized without recourse to time consuming and expensive field testing and refinement. Developing a good model involves capturing all those effects that affect the particular aspect of the design under test whilst remaining simple enough to use, and offering quick simulation times.

In addition to modelling SISO channel effects like path loss, shadowing, power delay profile, time of arrival, wideband small scale fading first and second order statistics, the MIMO channel model requires additional information that models the amplitude and phase of and correlation between transmission coefficients, correlation between antennas elements, angle of arrival distribution, angle of departure distribution, and their inter-dependencies. Terrestrial models can be categorized as empirical, physical-deterministic, statistical, geometric or physical-statistical:

- Empirical models are based on field measurements. A model can then be built around the measured data to capture most of the observations. These models are often only accurate in very similar environments and give little insight into the channel phenomena.
- Physical-Deterministic models are often based on ray tracing, where reflection, transmission and diffraction at every interface are traced from the transmitter to the receiver. In order to be accurate, every facet, patch and edge has to carefully described by their constitutive parameters (permitivity, permeability, conductance, loss tangent and roughness), and detailed environments need to be described (often by 3D computer aided design software like Autocad). In order to observe small scale fading, the ray-tracing algorithm requires a resolution at least one third of a wavelength, and in this case, the simulation time can be very long. However, a ray-tracing model can give some accurate results in the same location and provides insight into the channel behaviour.
- Statistical models, like empirical models, are also built around extensive measurement results. The channel is described by the statistical behaviour of each channel parameter. For example, shadowing is often described by a log-normal distribution along with its variance, or time-of-arrival of paths in an indoor environment is often described by a Poisson distribution. Statistical models are easier to simulate, and they offer reasonable accuracy in a similar environment to which the modelled phenomena was observed. However, they offer little insight into the propagation mechanisms and are dependent on the accuracy of the measurements.

- Geometric models are often cluster-scatterer models that have been positioned geometrically.
 Ray-tracing via the scatterers attempts to capture the essential MIMO channel features like correlation, angle of arrival, time of arrival and angle of departure.
- Another approach is to combine the features from a geometric model with the ease of simulation from a statistical model these are known as semi-statistical models. The 3GPP spatial channel model and FLOWS model (see below) are examples.
- Ray-tracing using a statistically correct virtual village is the basis of physical-statistical modelling, which is often used to model the LMS channel. Physical-statistical models, as described in Chapter 2, have largely been used in LMS systems as they can describe the 'on/off' nature of the channel well. However they are also gaining support in terrestrial systems where ray-tracing is used around a virtual statistically correct city.
- A correlation approach has also become popular due to its backward-compatibility and accuracy, where MIMO channel correlation matrices, based around extensive measurements are added to previously accepted SISO tapped delay line models. Antenna arrays can also be incorporated into the models. The WiMAX Forum MIMO channel model is an example.

Many channel models have been proposed for the terrestrial MIMO channel, a summary of which is given in [Sal03c]. Some of the early models include: IST METRA and I-METRA models, IST SATURN model, One-ring and Two-ring models, Distributed Scattering model, Extended Saleh-Valenzuela model, COST 259 Directional Channel model, EM Scattering model and the Virtual Channel model.

More recent MIMO channel models are the IST FLOWS model [Deb03], the 3GPP/3GPP2 spatial channel model (SCM) [3GP03] and the WiMAX Forum MIMO channel model [Wim07]. Each of these were coded in Matlab. Results from the FLOWS channel model and the 3GPP/3GPP2 spatial channel model are presented here, as they form the starting point for the land mobile satellite MIMO channel model used in the current research. More recent work for Beyond-3G systems are the IST WINNER models, which extend the performance of the 3GPP SCM, for example by using inter-tap clustering and additional taps to extend the model bandwidth validity to 100MHz, instead of the 5MHz used in the 3GPP SCM.

3.6.1 FLOWS channel model

An output from a three year EU IST FP6 project was the Wideband Double Directional Channel Model (WDDCM), which is adapted from the Modified Geometrically Based Single Bounce Elliptical (MGBSBEM) and Circular Models (MGBSBCM); this being a cluster version of the Geometrically Based Single Bounce Elliptical (GBSBEM) and Circular Models (GBSBCM).

The GBSBEM places the BS and MS at the foci of an ellipse evenly distributed with scatterers, since the BS is at low street level, and is therefore used in micro-cell scenarios. The GBSBCM places the MS in the centre of a circle evenly distributed with scatterers, since the BS is high and above rooftops, and is therefore used in macro-cell scenarios. The MGBSBEM and MGBSBCM position the scatterers in clusters as the resulting impulse response better reflects the measurements where signals arrival in groups. The WDDCM, in addition to modelling the macro-cell and micro-cell environment, adds the pico-cell scenario with the BS at the centre of a circle and the MS placed in the circle.

The WDDCM is a 2D, single-bounce, geometrically-based, semi-statistical, cluster-scatterer model that produces time of arrival (ToA), angle of arrival (AoA), angle of departure (AoD) and associated magnitude and phase of each MIMO channel. It provides a general wideband directional model framework that can be tuned to measurement campaign data. The WDDCM can be adapted to the MIMO case as shown below:

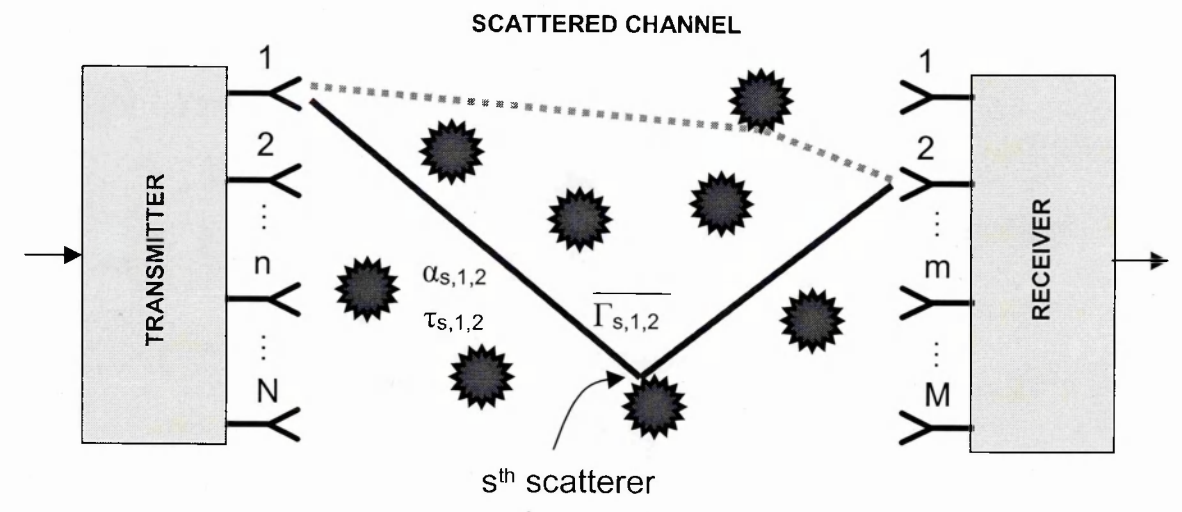


Fig. 3-12 Contribution of sth scatterer on channel response $h_{n,m}(\tau,f)$

The channel impulse response between transmit antenna n and receive antenna m at path delay τ and frequency f is given by:

$$h_{n,m}(\tau,f) = \sum_{s=1}^{S} \alpha_{s,n,m} \, \Gamma_{s,n,m} \, \exp(-j2\pi \, f \tau_{s,n,m}) \, \exp(j\phi_{s,n}) \, \exp(j\phi_{s,m}) \, \delta(t - \tau_{s,n,m})$$
(3-57)

where $\alpha_{s,n,m}$ is the attenuation from antenna n to antenna m via scatterer s. $\Gamma_{s,n,m}$ is the complex reflection coefficient between antenna n and antenna m at scatterer s. Component $\exp(-j2\pi f \tau_{s,n,m})$ adds phase shift due to the multipath delay at frequency f, $\exp(j\varphi_{s,n})$ accounts for the phase shift at antenna m from scatterer angle $\varphi_{s,n}$ and similarly, $\exp(j\varphi_{s,n})$ accounts for the phase shift at antenna m from scatterer angle $\varphi_{s,m}$ whilst $\delta(t-\tau_{s,n,m})$ is a Dirac delta at each instance of $t-\tau_{s,n,m}$.

For the circular based model, the joint PDF between ToA and AoD at the base station is [Deb03]:

$$p(\tau,\phi) = \begin{cases} \frac{(D^2 - \tau^2 c^2)(D^2 c - 2D\tau c^2 \cos\phi + \tau^2 c^3)}{4\pi R_m^2 (D\cos\phi - \tau c)^3} & \frac{(D^2 - 2\tau c.\cos\phi + \tau^2 c^2)}{\tau c - D\cos\phi} \le 2R_m \\ 0 & otherwise \end{cases}$$
(3-58)

and at the mobile unit, the joint PDF between ToA and AoA is:

$$p(\tau,\phi) = \begin{cases} \frac{(D^2 - \tau^2 c^2)(D^2 c - 2D\tau c^2 \cos\phi + \tau^2 c^3)}{4\pi R_m^2 (D\cos\phi - \tau c)^3} & \frac{(D^2 - \tau^2 c^2)}{D\cos\phi - \tau c} \le 2R_m \\ 0 & otherwise \end{cases}$$
(3-59)

For the elliptical model, the joint PDF between ToA and AoD or AoA is:

$$p(\tau,\phi) = \begin{cases} \frac{(D^2 - \tau^2 c^2)(D^2 c - 2D\tau c^2 \cos\phi + \tau^2 c^3)}{4\pi a_m b_m (D\cos\phi - \tau c)^3} & \frac{D}{c} \le \tau \le \tau_m \\ 0 & otherwise \end{cases}$$
(3-60)

where $a_{\rm m}$, the major axis: $a_{\rm m}=c\tau_{\rm m}/2$, $b_{\rm m}$, the minor axis: $b_{\rm m}=\sqrt{c^2\tau_{\rm m}^2-d^2}$, c is the speed of light, $\tau_{\rm m}$ is the maximum delay considered, D is the distance between the base station and mobile unit and $R_{\rm m}$ is the radius of the scatterer circle.

To simulate the model, we place clusters uniformly distributed over the circle in the circle model case, or over the ellipse in the elliptical model case. Each cluster contains many scatterers, which are Gaussian distributed at each cluster. The scatterers are assumed close enough together such that they contribute equal delay but different phase. The contribution from each scatterer causes the small scale fading for each of the taps, whose delay is contributed to by the cluster position. After placing the clusters and scatterers, the AoA, AoD, ToA and power levels can be found.

So far, this impulse response formula does not describe small scale fading with motion. However, it can be modelled as follows: After finding the cluster-scatterer position, recalculate the AoA, AoD, ToA and power levels for each mobile position. This will create a new set of phases from each scatterer, which will add constructively and destructively causing small scale fading. After a fixed distance of travel, a new set of cluster positions will be required as new clusters enter the circle or ellipse. Note that this is a different way of dealing with small scale fading to the 3GPP/3GPP2 spatial channel model, which has a velocity dependent phasor term that is time continuous.

3.6.2 3GPP/3GPP2 spatial channel model

A variety of MIMO channel models were proposed within the 3GPP and 3GPP2 working groups with likely candidates being the correlation based IST-METRA model and the Bell-Labs GWSSUS model [3GP03]. The Gaussian Wide Sense Stationary Uncorrelated Scattering (GWSSUS) MIMO model was adopted and each interested party added their input to fine-tune the model.

Channel model description

The model is designed to give accurate path loss predictions and representative shadowing and small scale fading MIMO data for urban macro-cell, suburban macro-cell and urban micro-cell cellular environments. Further simulation features account for polarization, far scatterer-clusters, line of sight, urban canyon and intercell interference. Correlation between delay spread, shadowing and azimuth spread is also modelled. The specification starts with link level parameters to calibrate individual simulations and ensure accuracy and then describes in a step-by-step fashion, how to set up the system level simulation. By way of example, the following section presents an overview of the system level model in a suburban macro-cell environment by way of simulation.

Power delay profile

Initially, the statistical model randomly chooses 6 paths with corresponding normalized power and delays. Four example simulated power delay profile plots are shown below. (Note that the power delay profiles are fixed during mobile station motion which is one drawback with this model.)

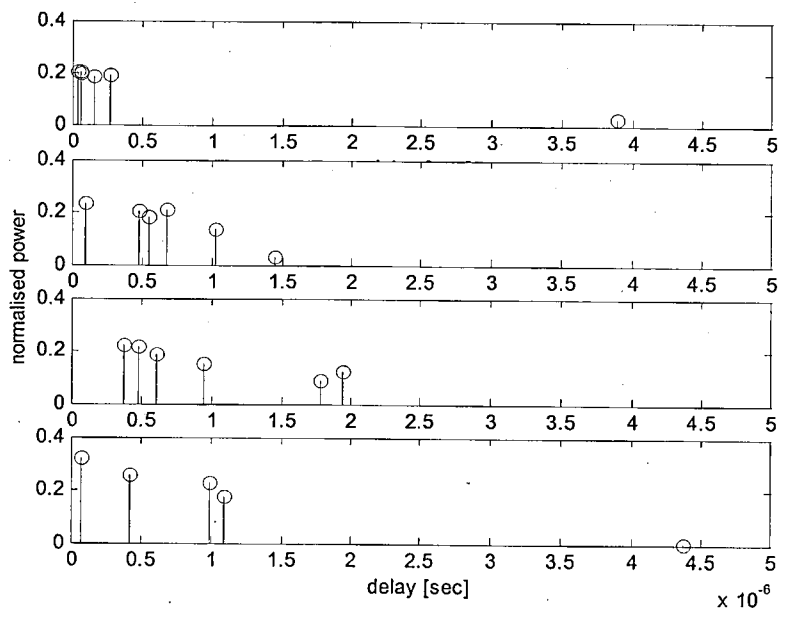


Fig. 3-13 Normalised power versus Path delay

The normalised power of the *n*th path is denoted P_n , normalized such that the total average power from all paths is 1. The delay of each path with respect to the first path time τ_1 is denoted τ_n . From

the power delay profile, the root mean squared (RMS) delay spread, frequency response and coherence bandwidth can be found. The mean delay and RMS delay spread of the power delay profile can be calculated from the following formulations:

$$\tau_{RMS} = \sqrt{\frac{1}{P_T} \sum_{i=1}^{n} P_i \ \tau_i^2 - \tau_0^2}$$
 (3-61)

where
$$\tau_0 = \frac{1}{P_T} \sum_{i=1}^n P_i \, \tau_i$$
 and $P_T = \sum_{i=1}^n P_i$ (3-62)

where τ_{RMS} is the RMS delay spread, τ_0 is the mean delay and P_i is the power at delay τ_i . The coherence bandwidth can be estimated as, $B_C \approx 1 / (2 \pi \tau_{RMS})$. However, like many delay-tap models, this model does not account for the changing power delay profile with motion.

Wideband MIMO impulse response channel matrix

Each of these paths is described by the MIMO channel matrix, $\mathbf{H}_n(t)$ which describes the channel for the n^{th} path between BS array element s=1,...,S and MS array element u=1,...,U.

$$\mathbf{H}_{n}(t) = \begin{bmatrix} h_{1,1,n} & h_{1,2,n} & \cdots & h_{1,S,n} \\ h_{2,1,n} & h_{2,2,n} & \cdots & h_{2,S,n} \\ \vdots & \vdots & \ddots & \vdots \\ h_{U,1,n} & h_{U,2,n} & \cdots & h_{U,S,n} \end{bmatrix}$$
(3-63)

Each of these matrix elements are given by:

$$h_{U,S,n}(t) = \sqrt{\frac{P_n \ \sigma_{SF}}{M}} \sum_{m=1}^{M} \left(\sqrt{G_{BS}(\theta_{n,m,AoD})} \exp(j[k \ d_S \sin(\theta_{n,m,AoD}) + \Phi n, m]) \times \sqrt{G_{MS}(\theta_{n,m,AoA})} \exp(j \ k \ d_U \sin(\theta_{n,m,AoA})) \times \exp(j \ k \|\mathbf{v}\| \cos(\theta_{n,m,AoA} - \theta_v)t) \right)$$
(3-64)

The angular parameters in (3-64) are explained as follows:

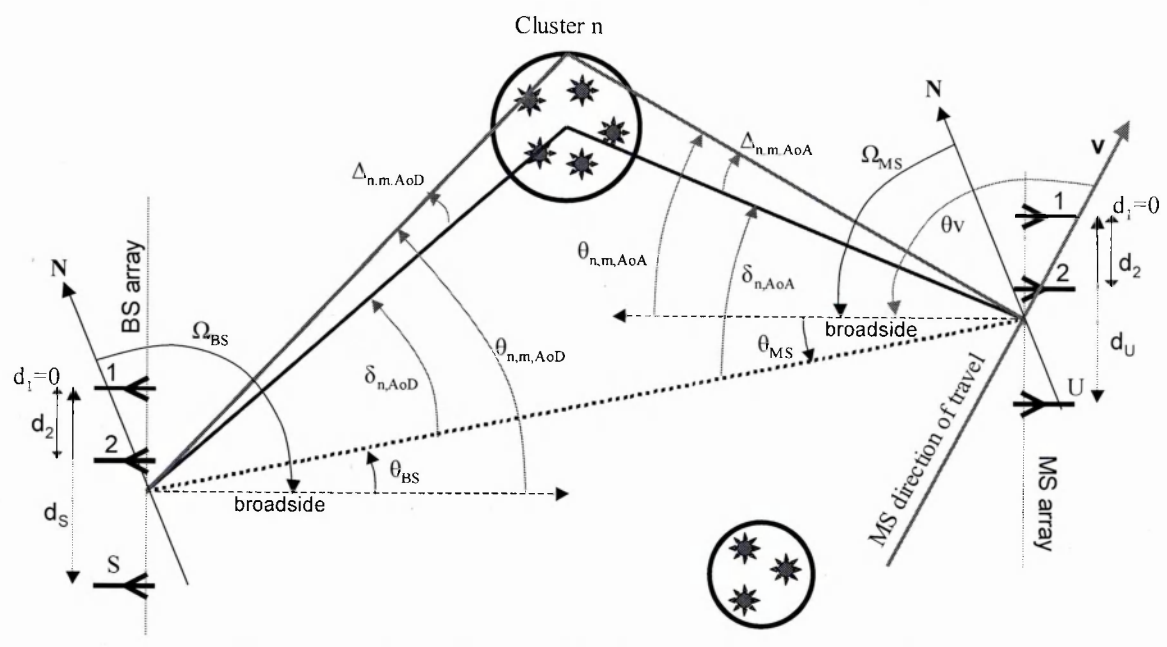


Fig. 3-14 Diagram showing nomenclature used in channel model

Shadowing (slow fading)

Parameter σ_{SF} is the lognormal shadow fading standard deviation and, based on measurements, is set to 8dB. This produces the following spread of shadow fading. A fixed random shadow fading value is applied to all subpaths, and a separate instance is applied to each path.

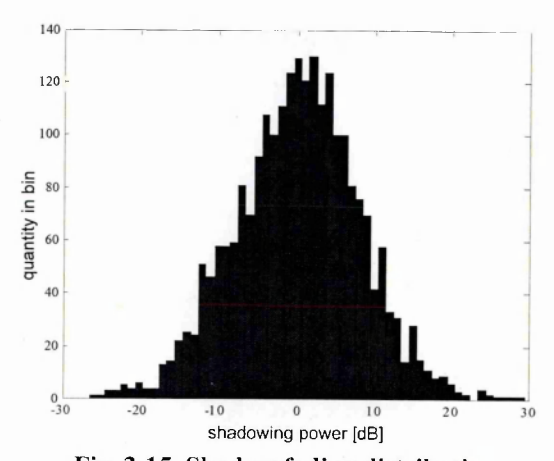


Fig. 3-15 Shadow fading distribution

M is the number of subpaths per path. In this model there are 6 paths each containing 20 subpaths.

Angle of arrival and angle of departure

 $\theta_{n,m,AoD}$ is the AoD for the m^{th} subpath of the n^{th} path

 $\theta_{n,m,AoA}$ is the AoA for the m^{th} subpath of the n^{th} path

The following plots in Fig. 3-16, show histograms of all the subpaths superimposed, at the base station (upper) and at the mobile station (lower).

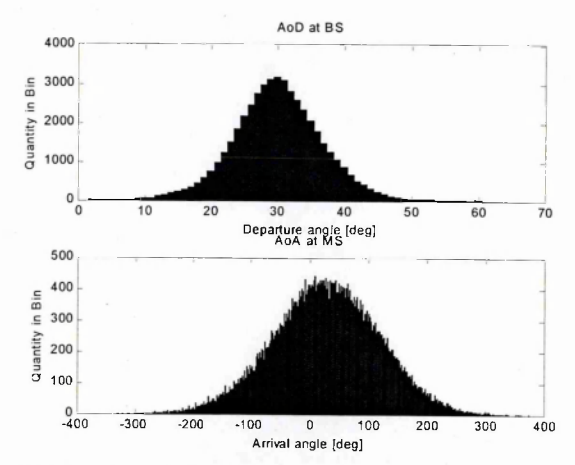


Fig. 3-16 AoD at BS and AoA at MS distribution over all m subpaths and n paths

The orientation of the antenna arrays (θ_{BS} and θ_{MS}) at the BS and at the MS are set to 30° in this simulation run.

Antenna element gain

 $G_{BS}(\theta_{n,m,AoD})$ is the BS antenna gain for each array element.

 $G_{\mathit{MS}} ig(\theta_{\mathit{n,m,AoA}} ig)$ is the MS antenna gain for each array element.

The following plots in Fig. 3-17 show the base station antenna element gain response (upper) and the mobile station antenna element gain response versus azimuth, as used in the simulation.

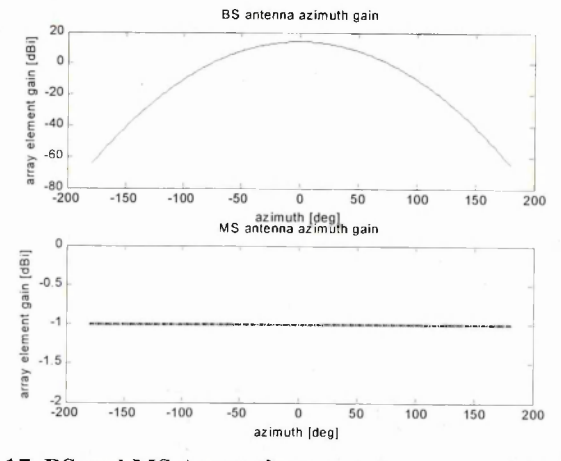


Fig. 3-17 BS and MS Array element gain versus azimuth angle

Further model parameters

 $k = 2\pi/\lambda$ = wavenumber, where λ is the carrier wavelength in metres.

f = frequency. Set to 2GHz in these simulations

 d_{S} = BS antenna distance from array element 1 to s. In this simulation, d_{S} = 10 λ

 d_U = MS antenna distance from array element 1 to U. In this simulation, d_U = 0.5 λ

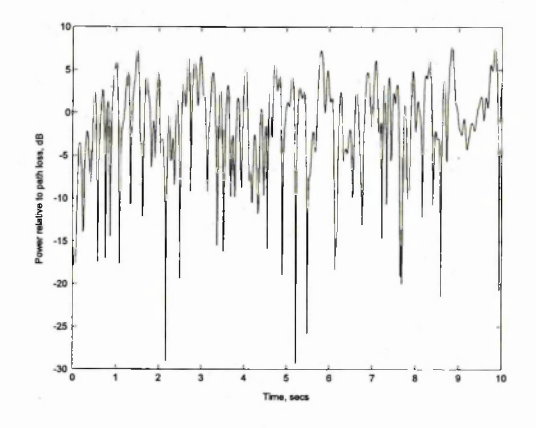
 $\|\mathbf{v}\|$ = MS velocity vector magnitude. ie mobile speed. Set to 3km/hr = 0.83 m/s

 $\Phi n, m =$ phase of the m^{th} subpath of the n^{th} path. Set to uniform random distribution over $[0,2\pi]$.

 θ_{v} = angle of MS velocity vector and set to 0° in this case.

Small scale fading

The model provides the n^{th} path channel coefficients $h_{U,S,n}(t)$ between BS antenna element u and MS antenna element s. It is a continuous function of time t. An example is shown below:



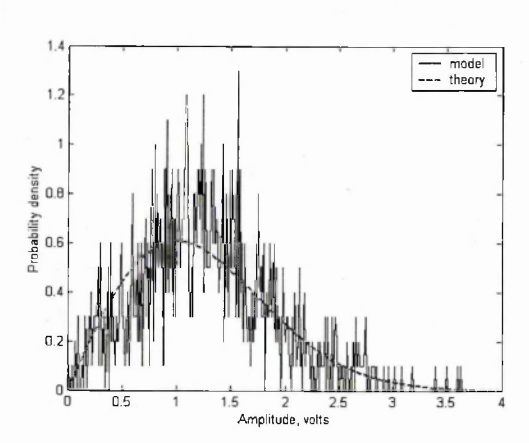


Fig. 3-18 Example small scale fading and envelope distribution for a MS at 3km/hr

In Fig. 3-18, the wideband simulated data has been converted to narrowband data by summing the phasors from each path/delay (six in this model) at each instance of time. The PDF of the data was found to accurately follow the theoretical Rayleigh distribution.

Spectrum of Signal Envelope

When the mobile is moving or the scatterers are moving, the received signal undergoes a frequency shift known as Doppler shift. The amount of shift is dependent on the spatial angles of arrival and the speed of the mobile or scatterers. In the 3GPP spatial channel model, the subpaths lie on a plane. In this 2D model, the Doppler frequency of each incoming subpath is given by:

$$v_n = \frac{\mathbf{v}}{\lambda} \cos \alpha \tag{3-65}$$

If the mobile is moving directly toward the subpath n then $\alpha=0$ and the Doppler shift will be positive and maximum. Conversely, if the mobile is moving directly away from the subpath n then $\alpha=0$ and the Doppler shift will be negative and maximum. All other subpaths have a Doppler shift in the range $\pm \nu$. If all the subpaths arrive with α uniformly distributed over $[0,2\pi]$, Clarke showed that the Doppler spectrum follows a U shape, as given by [Cla68]:

$$A(\nu) = \begin{cases} \frac{E_0}{4\pi\nu_m} \frac{1}{\sqrt{1 - (\nu/\nu_m)^2}} & |\nu| \le \nu_m \\ 0 & elsewhere \end{cases}$$
(3-66)

In practice typical Doppler spectrums vary widely from this model. The RMS Doppler spread can be found from the Doppler spectrum. If $\psi(v)$ is the average power at Doppler frequency v, then:

$$v_{RMS} = \sqrt{\frac{1}{\psi_T} \sum_{i=1}^{n} \psi_i \ v_i^2 - v_0^2}$$
 (3-67)

where
$$v_0 = \frac{1}{\psi_T} \sum_{i=1}^n \psi_i \ v_i$$
 and $\psi_T = \sum_{i=1}^n \psi_i$ (3-68)

where ν_{RMS} is the RMS Doppler spread, ν_0 is the mean Doppler. The coherence time $T_C \approx (1 / \nu_{RMS})$.

Time variant system functions

The wideband channel can be well described by a set of functions known as Bello system functions [Bel63]. Firstly, the functions are defined and then the 3GPP spatial channel model functions are presented by way of example.

Input Delay Spread Function

The wideband channel can be described by a linear time-varying filter as shown below:

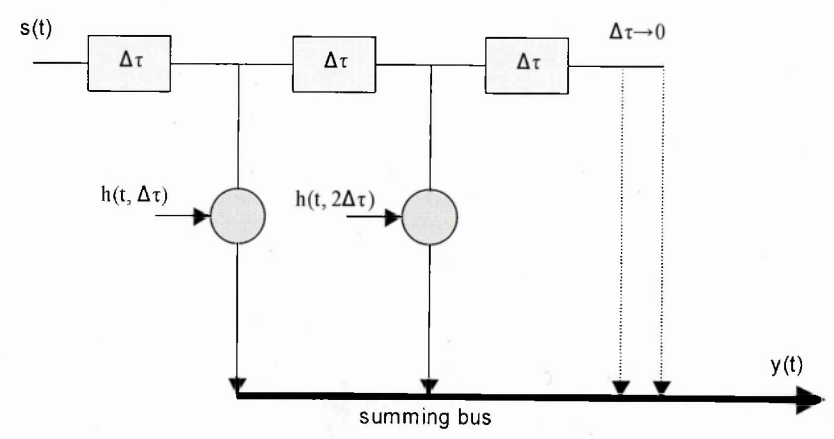


Fig. 3-19 Time domain tapped delay line model of a multipath channel

Denoting the output complex envelope by y(t) and the input complex envelope by s(t), the input delay spread function, $h(\tau;t)$ is given by:

$$y(t) = \int_{-\infty}^{\infty} s(t-\tau) h(\tau;t) d\tau = \int_{-\infty}^{\infty} s(\tau) h(t-\tau;t) d\tau$$
 (3-69)

where τ is the delay variable and t is the time variable. $h(\tau;t)$ describes the channel impulse response at time t.

Time Variant Transfer Function

The time variant transfer function describes the complex frequency response of the channel at time t. It is found be taking the Fourier transform the $h(\tau;t)$ with respect to τ . The baseband complex frequency response T(f;t) is given by:

$$T(f;t) = \int_{-\infty}^{\infty} h(\tau;t) e^{-j 2 \pi f \tau} d\tau$$
 (3-70)

Denoting the Fourier transform (complex frequency response) of the input signal s(t) by S(f;t) and the Fourier transform of the output signal y(t) by Y(f;t) the transfer function is related by:

$$Y(f;t) = T(f;t) S(f;t)$$
(3-71)

Delay-Doppler Spread Function

Taking the Fourier transform of $h(\tau;t)$ with respect to the time variable t produces the delay-Doppler spread function:

$$S(\tau;\nu) = \int_{-\infty}^{\infty} h(\tau;t) e^{-j2\pi\tau t} dt$$
 (3-72)

 $S(\tau; v)$ shows the Doppler spectrum for each delay bin, and provides information about direction of rays arriving at the vehicle for different path lengths.

Output Doppler Spread Function

Analogous to the time domain tapped delay line model, a frequency domain tapped Doppler line model can be used as shown below:

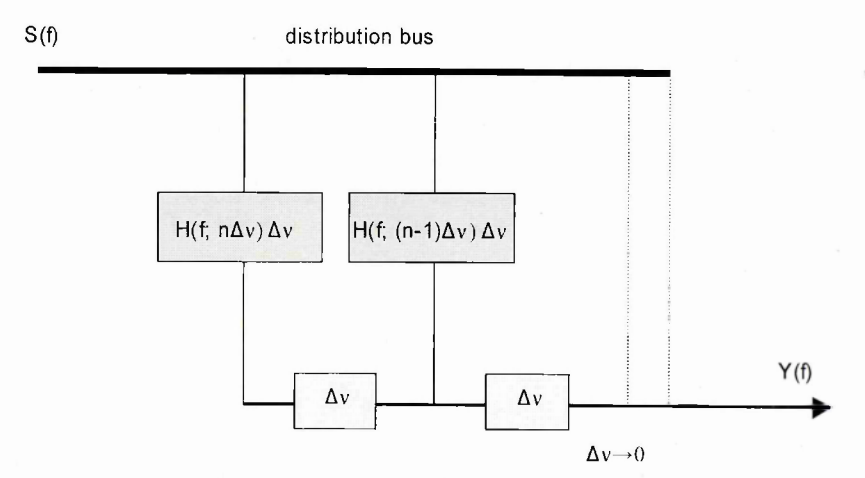


Fig. 3-20 Frequency domain tapped Doppler-shift model of a multipath channel

The output frequency spectrum Y(f) is related to the input frequency spectrum S(f) by:

$$Y(f) = \Delta \nu \sum_{m=1}^{n} S(f - m\Delta \nu) H(f - m\Delta \nu, m\Delta \nu)$$
(3-73)

where $H(f; \nu)$ is the output Doppler spread function, $H(f; n\Delta\nu).\Delta\nu$ represents a bank of filters and $\Delta\nu$ are Doppler-shifting frequency converters. $H(f; \nu)$ is found by taking a Fourier transform of the time variant transfer function T(f;t) with respect to t or by taking a Fourier transform of the delay-Doppler spread function $S(\tau; \nu)$ with respect to τ .

$$H(f;\nu) = \int_{-\infty}^{\infty} T(f;t) e^{-j 2 \pi \nu t} dt = \int_{-\infty}^{\infty} S(\tau;\nu) e^{-j 2 \pi f \tau} d\tau$$
 (3-74)

The output Doppler-spread function H(f, v) relates the output spectrum to the input spectrum at each Doppler frequency, and provides information about the transfer function for paths arriving at the vehicle coming from different directions.

The Bello system functions are related by Fourier transforms as shown in Fig. 3-21.

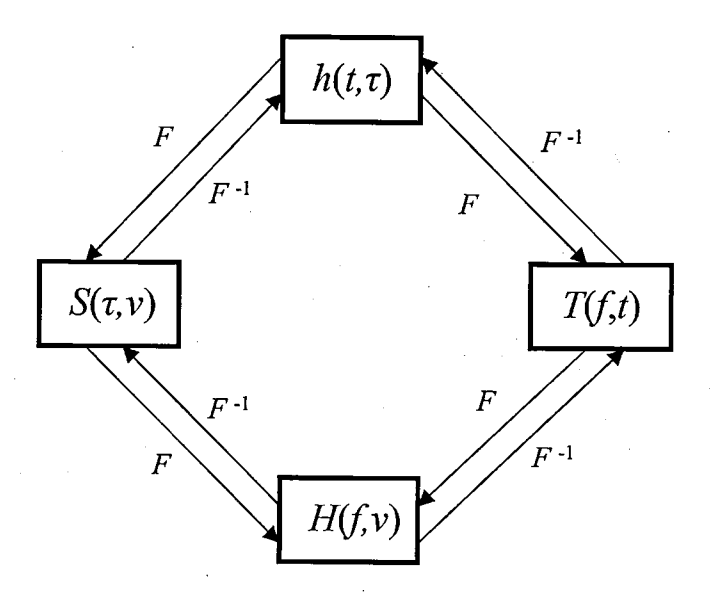


Fig. 3-21 Relationship between system functions

Bello system functions

The following plots, obtained from Matlab simulations, show example Bello system functions obtained from the 3GPP spatial channel model.

Input Delay Spread Function

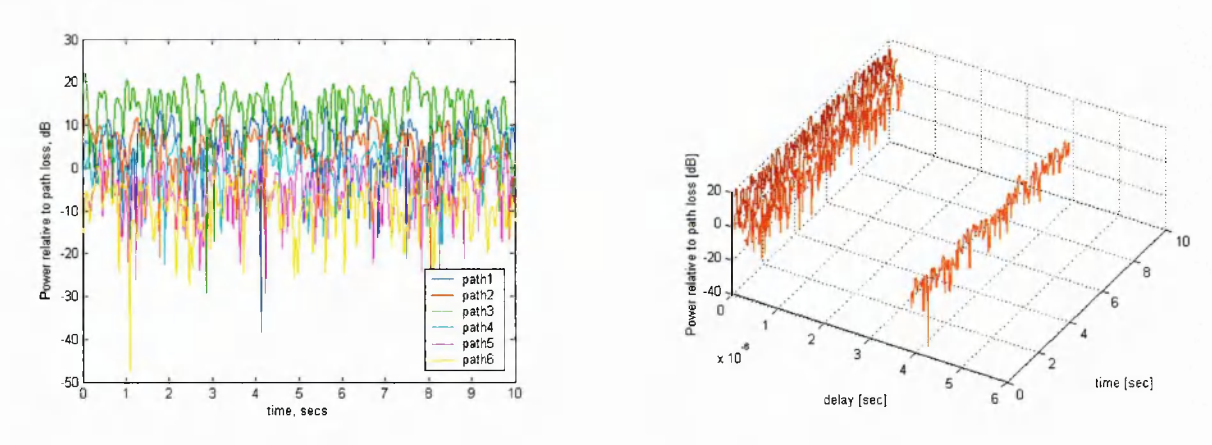


Fig. 3-22 Example of 3GPP spatial channel model Input Delay Spread Function

Time Variant Transfer Function

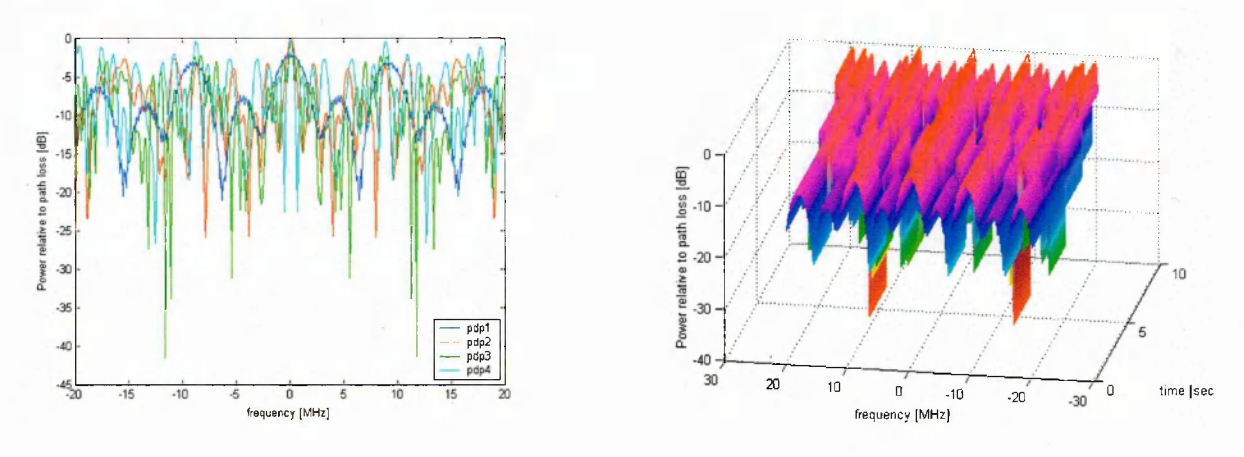
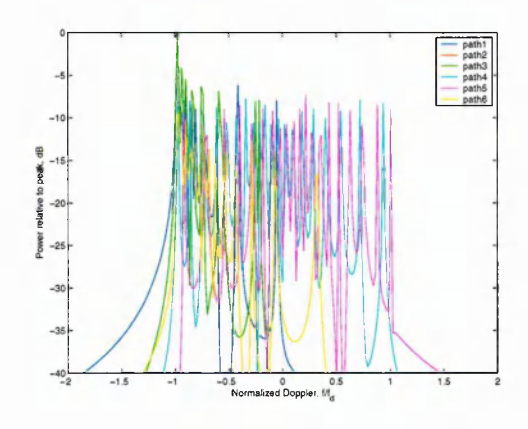


Fig. 3-23 Examples of 3GPP spatial channel model Time Variant Transfer Function

Delay-Doppler Spread Function



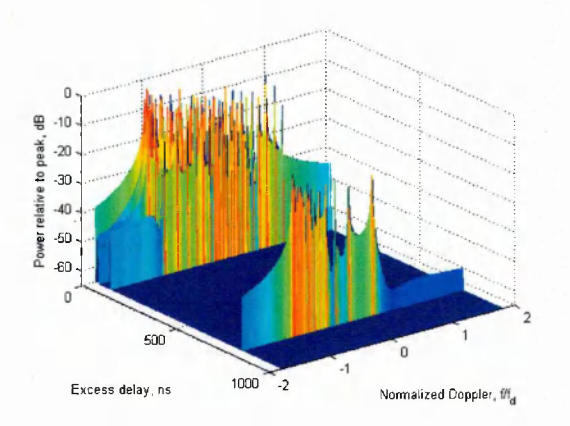


Fig. 3-24 Example of 3GPP spatial channel model Delay-Doppler Spread Function

Output Doppler Spread Function

An example of the output doppler spread function for the 3GPP spatial channel model is shown below:

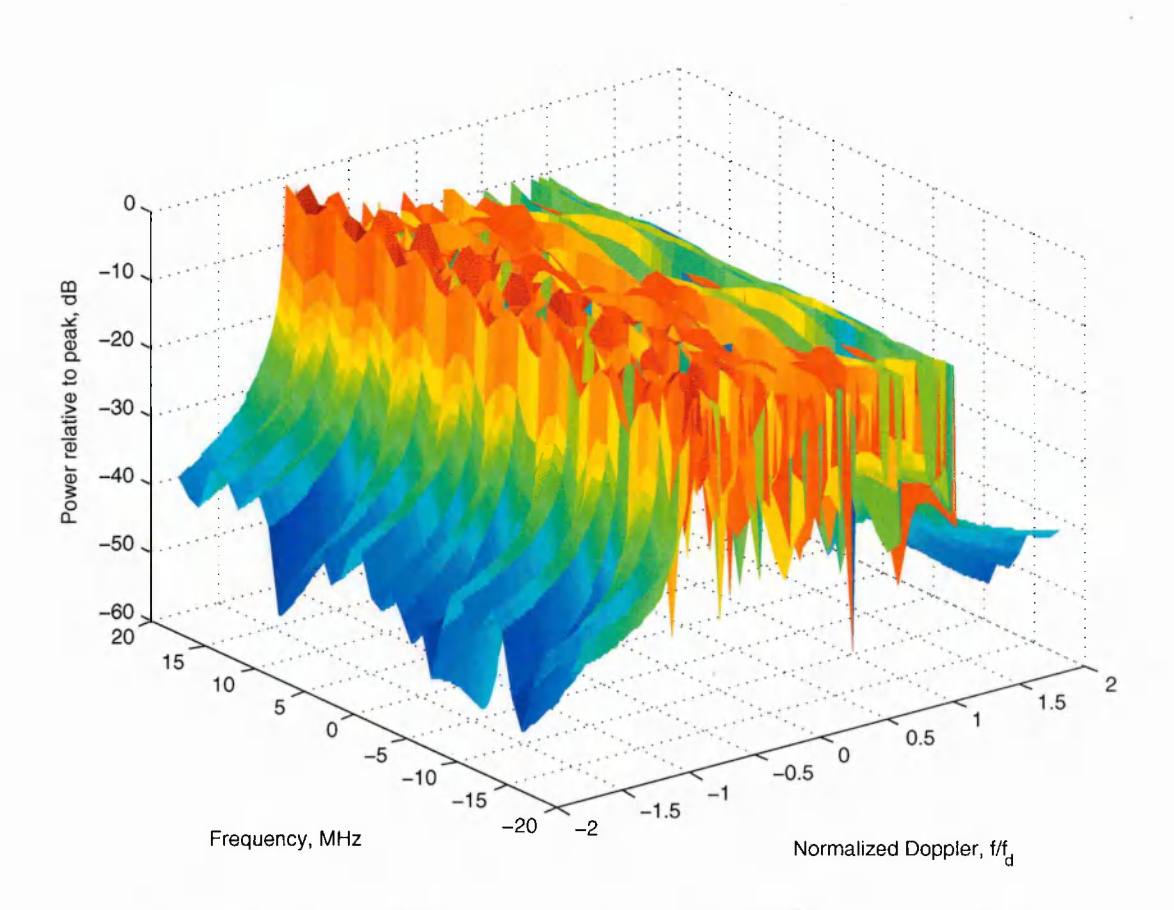


Fig. 3-25 Example of 3GPP spatial channel model Output Doppler Spread Function

Time variant correlation functions

To characterize a practical time variant linear channel requires statistical knowledge of the system functions and their correlation functions. A full explanation of these functions is given in [Bel63] and [PaD92]. Here, the auto-correlation functions are reviewed in (3-74) and their relation ship is shown in Fig. 3-26.

$$E[h(t,\tau)h^*(s,\eta)] = R_h(t,s;\tau,\eta)$$

$$E[T(f,t)T^*(m,s)] = R_T(f,m;t,s)$$

$$E[S(\tau,\upsilon)S^*(\eta,\mu)] = R_S(\tau,\eta;\nu,\mu)$$

$$E[H(f,\nu)H^*(m,\mu)] = R_H(f,m;\nu,\mu)$$
(3-75)

Where t and s are time variables, τ and η are time-delay variables, f and m are frequency variables and v and μ are Doppler frequency variables. E[.] is the ensemble average and * is the complex conjugate. In the following, DF refers to a double Fourier transform.

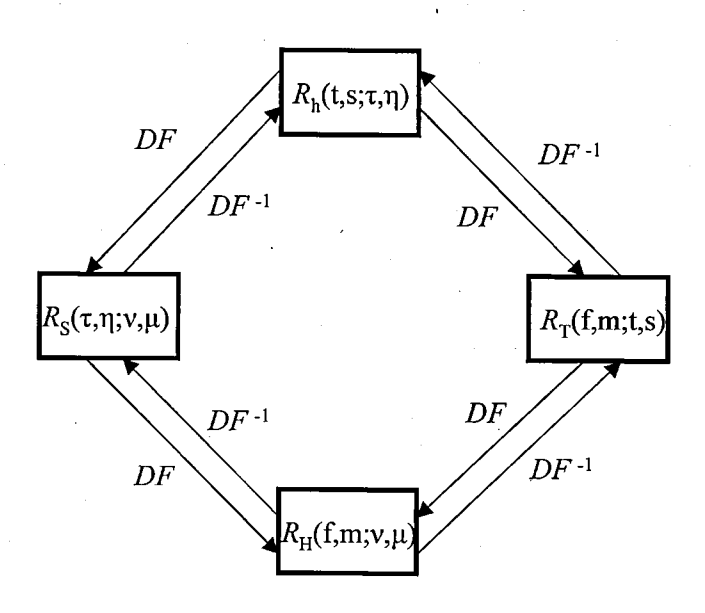


Fig. 3-26 Relationship between channel correlation functions

Wide-sense stationary channels

If we make the assumption that the correlation functions are invariant over short periods of time or over small distances, then the channel is described as wide-sense stationary (WSS). It is a useful approximation that is observed by measurement. These channels have the property that the correlation functions are invariant under a translation in time. This means that the auto-correlation functions depend on the short time interval Δt , where $\Delta t = t - s$ and not the absolute values of t and s.

The uncorrelated scattering channel

If the contributions from each scatterer with different path lengths are uncorrelated, then the channel is said to be an *uncorrelated scattering* (US) channel. In [PaD92], it is shown that for a channel composed of many scatterers each producing different delays and Doppler shifts, then the complex amplitudes from each scatterer are uncorrelated if the scatterers produce different time delays.

The WSSUS channel

Many practical channels can be described as wide sense stationary uncorrelated channels (WSSUS), meaning they exhibit wide sense stationarity in the time variable and uncorrelated scattering in the time-delay variable. Parsons [PaD92] describes the following picture of the WSSUS channel:

- In the input delay spread function, each tap in a densely tapped delay line exhibits US.
- In the input delay spread function, each tap has WSS statistics.
- In the time variant transfer function, the time variable autocorrelation is WSS.
- In the time variant transfer function, the frequency variable autocorrelation is WSS.
- In the delay Doppler spread function, US is observed in the time delay
- In the delay Doppler spread function, US is observed at each Doppler shift
- In the output Doppler spread function, the autocorrelation over frequency is WSS.
- In the output Doppler spread function, each Doppler shift exhibits US

3.7 Interim conclusions

The previous two chapters, which formed the literature review, has shown separately: (a) satellite systems and models for the SISO LMS channel, and (b) MIMO channels, capacity and antenna arrays applied to the terrestrial case. The question now becomes apparent: "What are the properties of the LMS-MIMO channel, and how much increase in capacity and diversity can be obtained from such a channel".

The rest of this thesis aims to answer these questions by theoretical and experimental means. Initially a physical-statistical LMS-MIMO channel model was developed in order to answer these questions, but the need for real channel data was soon realized. Therefore, the LMS-MIMO channel was characterized using a terrestrial platform acting as a low elevation satellite, which uncovered many of this channel's properties. Empirical-statistical channel models were also developed from the campaign data. Capacity and diversity gain from the LMS-MIMO channel are also derived.

Chapter	Four
---------	-------------

4 Physical-Statistical Model of the LMS-MIMO Channel

4.1 Multiple satellite MIMO channel model

Physical-statistical modelling [Sau99], where ray-tracing is used in a statistically accurate virtual city is perhaps the best method for LMS systems as they can predict the large scale 'on/off' nature of the channel very well, they can model the small scale effects very well, and can cover large areas applicable to satellite systems. They can also give an indication of the channel even without measurement data, although having data allows tuning of the model and validation. For these reasons, physical-statistical modelling was chosen for the LMS-MIMO model construction, prior to experimental data becoming available. In this model, a simplified ray-tracing algorithm is used that focuses on the main effects, like blockage, shadowing, rooftop diffraction and valid multipath reflections that are found in LMS systems. This simplification addresses the main channel effects and is much quicker to simulate than a full ray-tracing algorithm.

4.1.1 Model derivation

This section presents the derivation of a MIMO land mobile satellite channel model, which is a variation of similar channel models that trace rays via clusters of scatterers, [Mol03], [Mol04], [Deb03], [Corr01]. Once the scatterers are carefully positioned, the model can predict high-resolution time series data and power-spatial-delay profile data between any satellite or high altitude platform (HAP) antenna and any mobile antenna. The model can also predict the correlation between these channels. Positioning the scatterers in each environment is key to the accuracy of the model. To produce enough high-resolution data and a much reduced simulation time, the model has been coded in C++ with the data post-processed in Matlab. The parameters used in the model are representative of urban and highway environments in Munich, Germany, since published measurement data was available for comparison.

In this model, the clusters of scatterers represent buildings or trees. The cluster centre is randomly positioned above a plane representing the area at half the building or tree height as shown in Fig. 4-1.

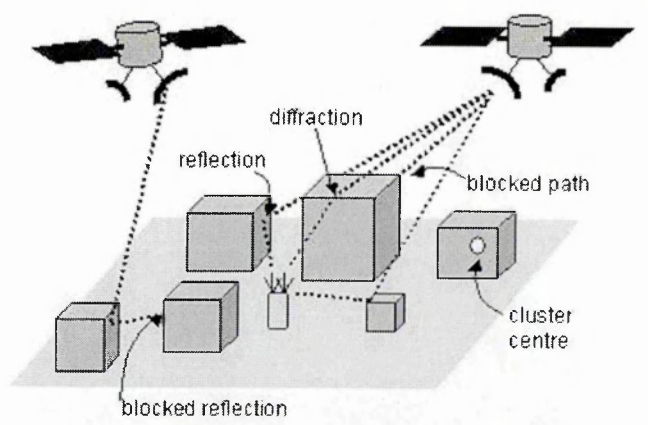


Fig. 4-1 Cluster environment around mobile

Building heights follow a log-normal statistical distribution with a mean and standard deviation derived from best-fit parameters for the city/town [Sau96]. Twenty scatterers were randomly positioned around the cluster centre with each dimension following a Laplacian distribution [Corr01], [Toe02]. Typical densities were estimated to be one building or tree in each 1000m^2 and 10000m^2 in urban and highway environments respectively. In the urban environment, clusters were defined as buildings 90% of the time, whereas in the highway environment clusters were defined as trees 90% of the time. 3D point-line distance vector algebra to be used to establish which scatterers contribute to the overall received electric field. When local clusters, representing buildings, block reflected contributions from distant clusters, the distant clusters are rejected.

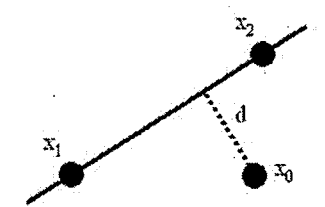


Fig. 4-2 3D Point-line geometry

For example, in Fig. 4-2, \mathbf{x}_1 represents a mobile antenna, and \mathbf{x}_0 and \mathbf{x}_2 represent cluster centres, whereas d is half the building or tree width. When the building obscures the path \mathbf{x}_1 - \mathbf{x}_2 , scatterer \mathbf{x}_2 is rejected as it is assumed that the building will totally block the signal, and when a tree obscures the path \mathbf{x}_1 - \mathbf{x}_2 , scatterer \mathbf{x}_2 remains but signal attenuation is applied.

The geometry in Fig. 4-2 is also used for the LOS path. In this case, x_1 represents the mobile antenna and x_2 represents the satellite antenna. When the path x_1 - x_2 is blocked by a building or partially blocked by a tree, diffraction loss or tree signal attenuation is applied respectively. For diffraction loss, single knife-edge rooftop diffraction has been adopted as this is the main cause of diffraction at high elevations [Lee85], [Rap96]. For tree loss, the signal reduction is calculated by finding the chord length along path x_1 - x_2 and applying 1.3dB/m, an average measured vegetation attenuation [Vog88], [Vog90], [Cav94].

In 3D space, $\mathbf{x}_0 = (x_0, y_0, z_0)$, $\mathbf{x}_1 = (x_1, y_1, z_1)$ and $\mathbf{x}_2 = (x_2, y_2, z_2)$. After some manipulation, the distance d can be found by [Wei04]:

$$d = \frac{\left| (\mathbf{x}_2 - \mathbf{x}_1) \times (\mathbf{x}_1 - \mathbf{x}_0) \right|}{\left| \mathbf{x}_2 - \mathbf{x}_1 \right|}$$
(4-1)

where | is the magnitude and x is the cross product.

Rays are traced from the satellite or HAP antennas to the mobile antennas via the valid clusters of scatterers. The reflection coefficients are made equal for every scatterer in each cluster and

are randomly assigned from a uniform magnitude distribution between 0 and 1 with uniform phase distribution between 0 and 2π . [Deb03].

As the mobile roams, the model switches between three states: a clear LOS path, a blocked LOS path and an attenuated by trees LOS path. The high-resolution time series data between each satellite or HAP antenna M and each moving mobile antenna N, $\alpha_{M,N}$ can be defined as follows:

$$\alpha_{M,N} = \begin{cases} P_{M,N} + b \sum_{i=1}^{n} T_{i} \Gamma_{i} P_{M,N,i} e^{jk d_{M,N,i}} & clear \\ D_{M,N} P_{M,N} + b \sum_{i=1}^{n} T_{i} \Gamma_{i} P_{M,N,i} e^{jk d_{M,N,i}} & blocked \\ T_{M,N} P_{M,N} + b \sum_{i=1}^{n} T_{i} \Gamma_{i} P_{M,N,i} e^{jk d_{M,N,i}} & trees \end{cases}$$
(4-2)

where $P_{M,N}$ is the LOS path loss between satellite antenna M and moving mobile antenna N, k is the wavenumber, n is the total number of valid scatterers, T_i is the tree attenuation applied to a reflected contribution from scatterer i, Γ_i is the complex reflection coefficient at scatterer i, $P_{M,N,i}$ is the path loss from satellite or HAP antenna M to moving mobile antenna N via scatterer i, $d_{M,N,i}$ is the distance between satellite or HAP antenna M and moving mobile antenna N via scatterer i, $D_{M,N}$ is the LOS diffraction loss and $T_{M,N}$ is the LOS tree loss. The term b is a clutter factor parameter derived from measurements in each environment.

The model output is high-resolution instantaneous path loss time series data, as shown in Fig. 4-3 and power-spatial-delay profile data between each mobile antenna and satellite or HAP. From these, the small scale fading statistics can be found as a function of shadowing depth, angle of arrival and arrival distribution, and wideband parameters like RMS delay spread or coherence bandwidth can be estimated in each environment.

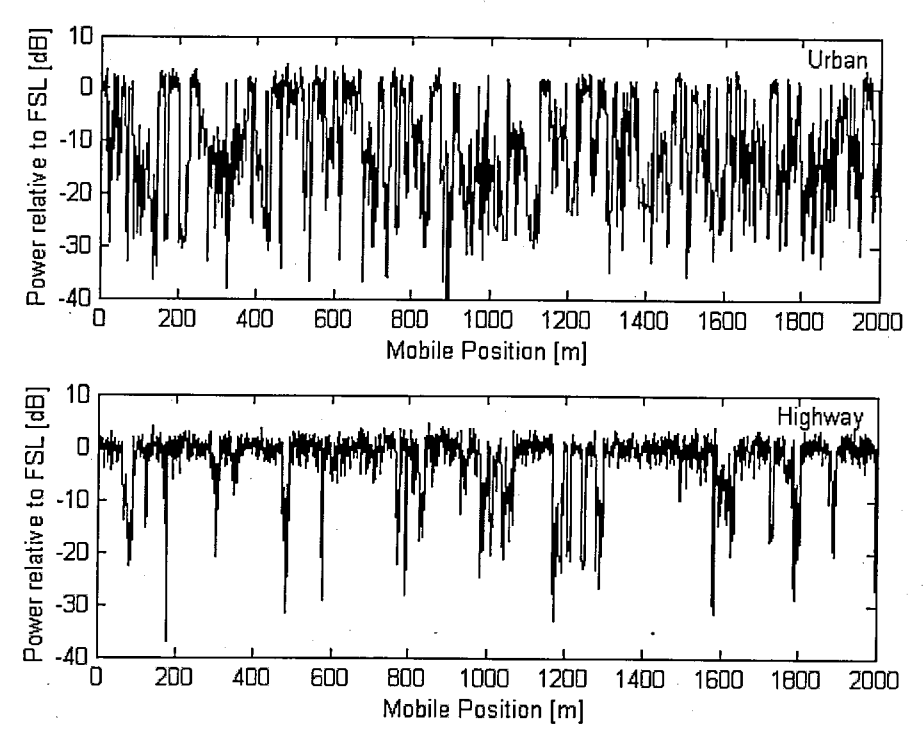


Fig. 4-3 Time series data of model

4.1.2 Model validation

The first order statistics of the high-resolution time series data were also compared with measurements performed by DLR (German Aerospace Centre) [Lut91], and this comparison is shown in Fig. 4-4.

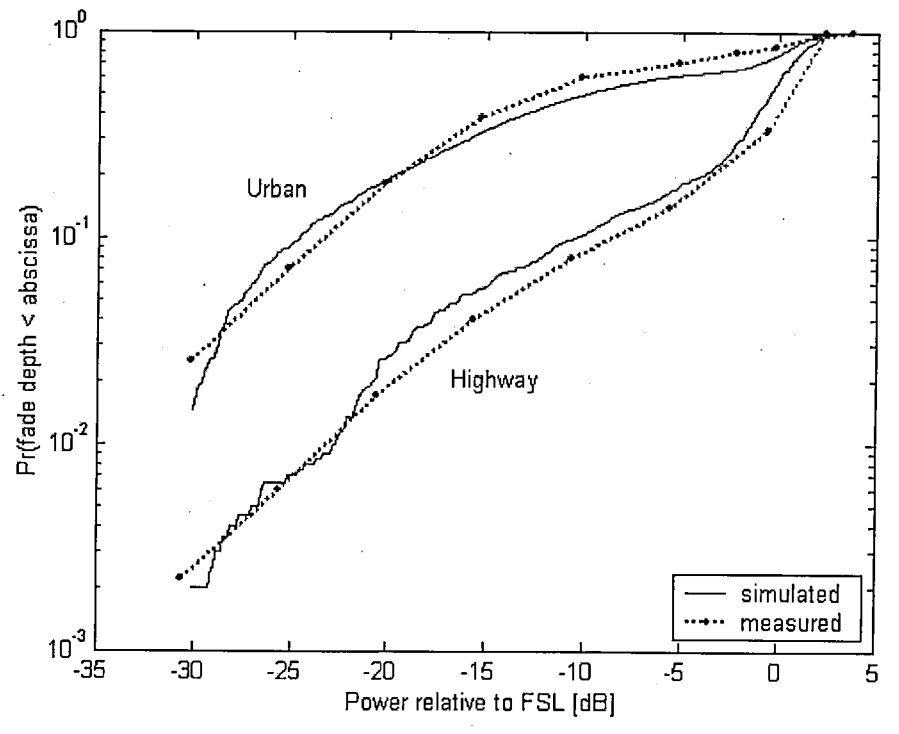


Fig. 4-4 First order statistics of model

In this previous work, the MARECS geostationary satellite at 26°W, transmitting at L-band (1.54 GHz) at an elevation of 24° was used. The urban environment was located in the narrow streets in the old city of Munich, whereas the highway environment was located away from buildings close to Munich. In the urban case, deep shadowing was observed for most of the time. However, for the highway case, only occasional shallow shadowing was observed, caused by trees and rare deep shadowing caused by bridges. The probability levels at each fade-depth and the data trends from the model are in agreement with the measurement data and therefore the model can be further used to investigate the satellite or HAP channel.

The RMS delay spread in the non-shadowed state was calculated from the model to be around 50ns for the urban case; a similar value has been suggested in [Bel00].

4.1.3 Position of satellites

Two potential means of providing service to a land-based mobile device use either (a) two satellites or (b) one HAP containing widely spaced-apart antennas.

The model has been used to investigate MIMO channel matrix decorrelation as a function of satellite separation d_S and HAP antenna separation d_H , as depicted in Fig. 4-5. The model was used to generate small scale fading channel data between two satellites or a single HAP (or multiple HAPs) and a mobile using the valid clusters of scatterers for each environment.

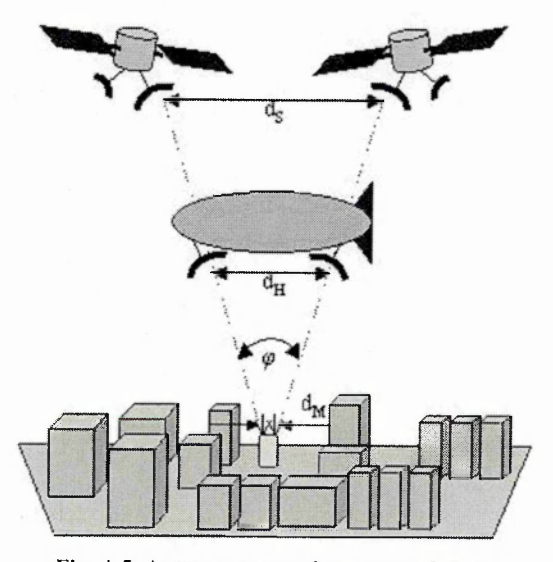


Fig. 4-5 Antenna separation nomenclature

Denoting the small scale fading from each satellite as α_A and α_B , the correlation can be defined as [Pee01]:

$$\rho_{AB} = \frac{E[(\alpha_A - \mu_A)(\alpha_B - \mu_B)^*]}{\sigma_A \sigma_B}$$
(4-3)

where E[.] is the expectation, μ_A , μ_B are the means and σ_A , σ_B are the standard deviations of the small scale fading data from satellite or HAP antennas A and B respectively. Using this approach, the correlation coefficient as a function of satellite separation was estimated, which is shown in Fig. 4-6.

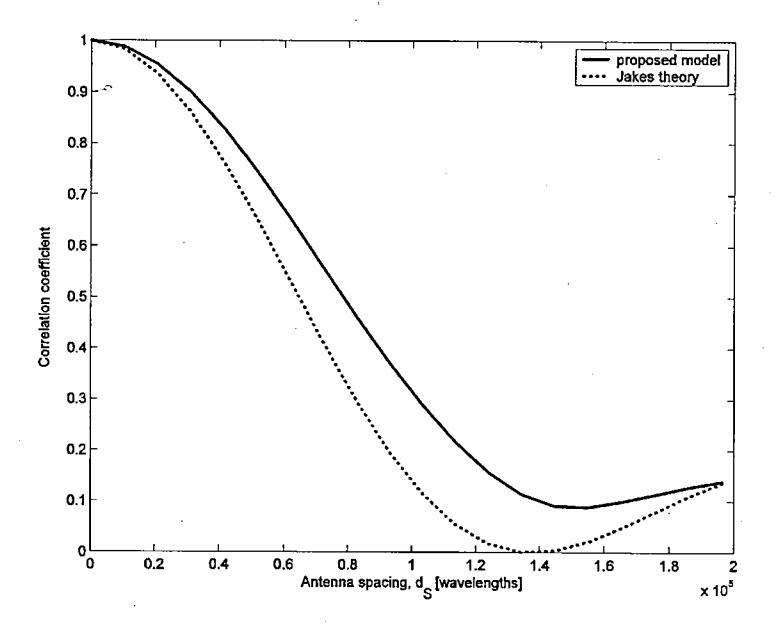


Fig. 4-6 Required antenna separation at satellite

The graph shows that in an urban environment, two geostationary satellites must have a separation of at least 1.5×10^5 wavelengths or 30km at 1.54GHz (a possible LMS L band frequency) to ensure low correlation between each channel matrix coefficient. Since suburban and highway environments have more widely spaced valid clusters, requiring a smaller satellite angular separation, the urban environment can be seen as a worst-case requirement.

As the angle φ between the satellites is only 2.9 minutes and therefore approximately parallel rays arrive at the mobile, the model has been compared with conventional base station spatial diversity 'Jakes' theory. The theory assumes a ring of scatterers around the mobile; nethertheless it provides a useful comparison case for the model. In this case, correlation as a function of antenna separation can be calculated as in [Jak74]:

$$\rho = J_0^2 \left(k d \left(\frac{r_S}{r} \right) \sin \theta \right) J_0^2 \left(\frac{k d}{2} \left(\frac{r_S}{r} \right)^2 \sqrt{1 - \frac{3}{4} \cos^2 \theta} \right)$$
 (4-4)

where k is the wavenumber, d is the antenna separation, θ is the satellite antenna array orientation angle, 90° in this case, r_S is the scattering radius and r is the average distance between the mobile and satellites. Results generated by this formula are presented in Fig. 4-6 and Fig. 4-7 and compared with the outcome of the proposed model.

Orbital slots are traditionally allocated in arcs of 2°. However, using multiple satellite clusters in each slot is becoming more common. With future precision placement, it might be possible to

position many satellites in a slot all separated by 1.5×10^5 wavelengths, forming an 'antenna array in the sky'. When used in conjunction with a multi-antenna mobile, a large uncorrelated MIMO channel matrix can be created enabling large potential gains in capacity or diversity.

For the HAP case, the model is used to find out if enough channel matrix decorrelation is possible from a single HAP at an altitude of 22km (a proposed HAP altitude in the literature), or whether two distinct HAPs are required.

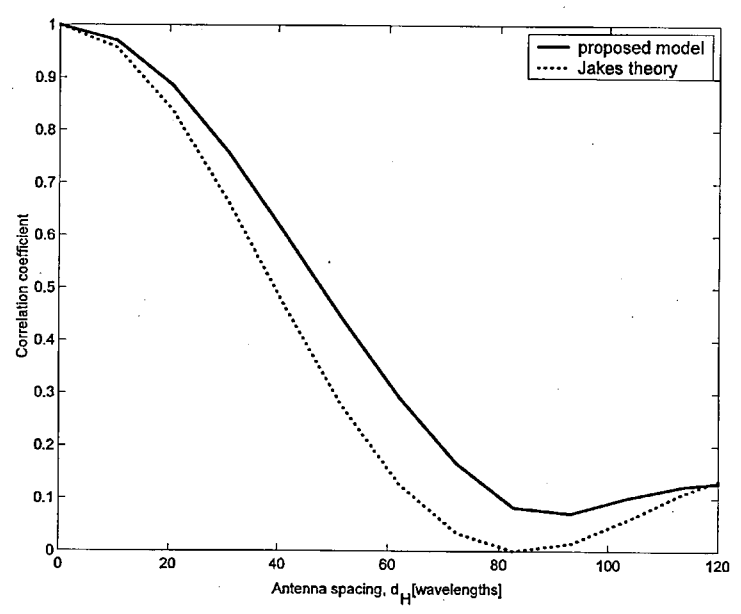


Fig. 4-7 Required antenna separation at HAP

Again, the model is compared with theory, also making the assumption that rays arriving from the HAP are approximately parallel. At 1.54GHz, the antennas require a separation of around 18 metres, which suggests that utilizing a single HAP is a viable solution.

4.2 Single satellite MIMO channel model

The following dual polarised physical-statistical LMS-MIMO channel model is an extension to the multiple-satellite LMS-MIMO model presented above. In this case, a single satellite containing right- (RHCP) and left hand circular polarisation (LHCP) antennas communicates with a mobile vehicle, also containing RHCP and LHCP antennas, although multiple-satellite dual polarized MIMO channels can also be accommodated by the model. The model, based on tracing rays via statistically positioned scatterers, can be fine-tuned around measurement campaign data.

4.2.1 Model derivation

The dual polarized physical-statistical LMS-MIMO channel model scenario is shown in Fig. 4-8.

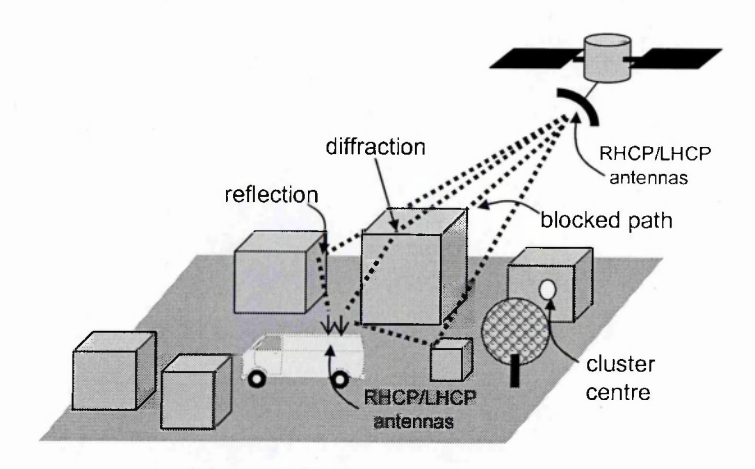


Fig. 4-8 Cluster environment around mobile vehicle

Channel model construction is described above. Additional insertion of polarization properties is achieved as follows. When the LOS path is unobstructed (clear), simple path loss is applied to the co-polar channels and cross-polar channels are discarded. When the LOS path is blocked by a building (block), rooftop diffraction is applied to both the co- and cross-polar channels; the cross-polar component is scaled below the co-polar component as observed from measured data. When the LOS path is shadowed by vegetation (tree), attenuation is applied to this path based on the distance traversed through the tree and using a typical attenuation factor of 1.3dB per metre. Similarly the cross-polar component is scaled below the co-polar component.

It is assumed in this model that the LOS paths are fully correlated between co- and cross-polar channels, and that the diffuse multipath components are fully uncorrelated between co- and cross-polar channels. This simplification is representative of many, but not all real practical channels; a full presentation of measured satellite MIMO channel correlation is provided in chapter 6.

The high-resolution time series data $\alpha_{M,N}$ between each satellite antenna M and each moving mobile antenna N, can be defined as follows:

$$\alpha_{M,N} = \begin{cases} P_{M,N} e^{jk d_{M,N}} + b \sum_{i=1}^{n} T_{i} \Gamma_{i} P_{M,N,i} e^{jk d_{M,N,i}} & clear \ co - polar \\ b \sum_{i=1}^{n} T_{i} \Gamma_{i} P_{M,N,i} e^{jk d_{M,N,i}} & clear \ cross - polar \end{cases}$$

$$D_{M,N} P_{M,N} e^{jk d_{M,N}} + b \sum_{i=1}^{n} T_{i} \Gamma_{i} P_{M,N,i} e^{jk d_{M,N,i}} & block \ co - polar \\ S_{b} D_{M,N} P_{M,N} e^{jk d_{M,N}} + b \sum_{i=1}^{n} T_{i} \Gamma_{i} P_{M,N,i} e^{jk d_{M,N,i}} & block \ cross - polar \end{cases}$$

$$T_{M,N} P_{M,N} e^{jk d_{M,N}} + b \sum_{i=1}^{n} T_{i} \Gamma_{i} P_{M,N,i} e^{jk d_{M,N,i}} & tree \ co - polar \\ S_{t} T_{M,N} P_{M,N} e^{jk d_{M,N}} + b \sum_{i=1}^{n} T_{i} \Gamma_{i} P_{M,N,i} e^{jk d_{M,N,i}} & tree \ cross - polar \end{cases}$$

$$(4-5)$$

where $P_{M,N}$ is the LOS path loss between satellite antenna M and moving mobile antenna N, k is the wavenumber, n is the total number of valid scatterers, T_i is the tree attenuation applied to a reflected contribution from scatterer i, Γ_i is the complex reflection coefficient at scatterer i, $P_{M,N,i}$ is the path loss from satellite antenna M to moving mobile antenna N via scatterer i, $d_{M,N,i}$ is the distance between satellite antenna M and moving mobile antenna N via scatterer i, $D_{M,N}$ is the LOS diffraction loss and $T_{M,N}$ is the LOS tree loss. The terms S_b and S_t account for the attenuation of the cross-polar terms for blocked and tree-shadowed conditions respectively and are derived from measured data. The term b is a clutter factor parameter also derived from measurements in each environment.

Model fitting to measured data has been carried out. It was found that with fine-tuning of the parameters in (4-5), the CDF of the modelled data can be made to closely resemble the CDF of the measured data. A presentation of these results is given in [Hor07].

4.3 Multiple satellite capacity predictions

4.3.1 Method

Satellite-MIMO capacity is demonstrated by applying narrowband uncorrelated Ricean channel data, obtained from the model in section 4.1, to the MIMO capacity equation shown below, using SNR and Rice K factor data obtained from the multiple satellite model defined above. Repeated here for clarity, when each transmitter has no knowledge of the channel, the available MIMO capacity is:

$$C = \log_2 \det \left[\mathbf{I}_m + \left(\frac{SNR}{n} \right) \mathbf{H} \mathbf{H}^H \right] \text{ bps/Hz}$$
 (4-6)

where I_m is the identity matrix of size m, m and n are the number of receive and transmit antennas respectively and \mathbf{H}^H is the complex transpose of the MIMO channel matrix, \mathbf{H} .

The time series high-resolution path loss MIMO channel matrix data was split into blocks, short enough to capture the shadowing around buildings but long enough to obtain enough samples to estimate the Rice K factor [Lee74]. Instantaneous SNR is obtained by setting the LOS SNR to 20dB and calculating the resulting SNR during a fade from the mean signal level in each block. The Rice K factor used denotes the ratio of shadowed LOS path power to the multipath components power. Each block with its associated mean SNR and Rice K factor is used to generate normalized channel matrix small scale fading data, which is entered into the capacity equation, resulting in capacity data for each block. The resultant cumulative distribution functions over all samples from each block for the urban and highway SISO and 2x2 MIMO channels are obtained.

4.3.2 Results

Since SNR can drop well below 0dB for some of the time, all curves begin at the zero capacity point. In both the SISO and MIMO cases, more time is spent at higher capacities in the highway environment since more time is spent at higher SNR levels, with the curves rising much more steeply in the highway case than the urban case. The SISO median and 10% outage capacity for the urban environment is 3.5bps/Hz and 0.1bps/Hz respectively, whereas for the 2x2 MIMO case, they are 7.6bps/Hz and 1.9bps/Hz. For the highway environment, the SISO median and 10% outage capacity is 6.5bps/Hz and 3.9bps/Hz respectively, which increases to 8.2bps/Hz and 7.2bps/Hz for the 2x2 MIMO case.

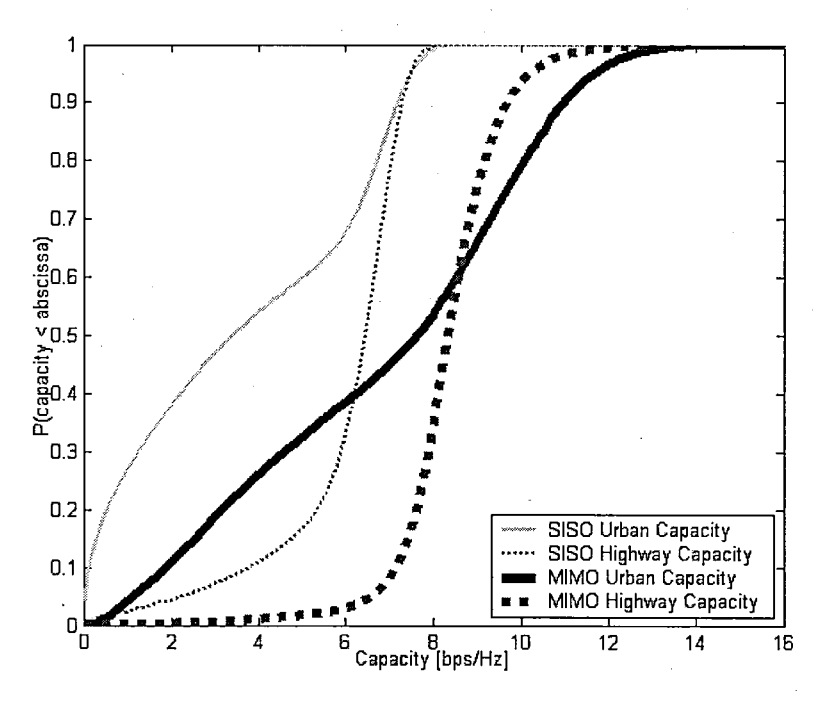


Fig. 4-9 Contrasting cumulative distribution functions of capacity for SISO and 2x2 MIMO systems in urban and highway environments with 20dB average receive SNR

4.3.3 Observations

Although these capacity curves are based on modelled data only, they provide some general trends from an expected satellite-MIMO channel. The first observation is that capacity is highly dependent on the environment surrounding the mobile. This is partially due to the amount of multipath received but mainly because of the time share of receiving strong signal to noise levels. Higher median capacity is available from the highway environment for this latter reason. However, maximum capacity is higher for the urban case as the multipath is greater in LOS channels.

It should be noted that these curves are when the satellites are positioned in a cluster and therefore the large scale fading is correlated between satellites. Positioning the satellites widely spaced apart would improve capacity as the probability of both satellites becoming shadowed would be much reduced. It should also be noted that this model is based around measurements carried out at an elevation of 24°, whereas the measurement campaign that follows in chapters 5-7, is for a lower elevation.

4.4 Multiple satellite diversity predictions

Although capacity predictions show possible capacity that can be achieved with optimum adaptive modulation and coding, they say nothing about how to achieve it. One way of improving capacity, especially at lower signal levels, is to use transmit and/or receive diversity.

Whereas a dual satellite to single antenna terminal link provides shadowing and some multipath diversity gain, a dual antenna terminal provides additional multipath diversity gain. This gain is demonstrated by simulating high resolution time series channel data for urban and highway environments, for SISO, MISO and MIMO systems, and with uncorrelated and correlated shadowing, and applying it to a bit error rate system simulator using Alamouti space-time coding [Ala98]. Bit error rate curves for each case are provided showing the benefit of 2x2 MIMO over 2x1 MISO. It is shown that 2x1 MISO diversity gain over shadowing (shadow correlation dependent) and multipath diversity gain is of order two (N=2), whereas in the 2x2 MIMO case, diversity gain over shadowing is still of order two but diversity gain over multipath is now of order four (N=4).

4.4.1 Method

Monte-Carlo simulations were performed on the channel data supplied by the model shown above by colleagues at BUTE, Hungary. An Alamouti space time block code was used with coherent QPSK modulation, a flat channel response and quasi-static fading. The Alamouti scheme can be summarized as follows. We transmit 2 symbols over the time and space domains:

$$time \ t \quad time \ t + T_S$$
 antenna 0 $s_0 - s_1 *$ (4-7) antenna 1 $s_1 s_0 *$

Where * is the complex conjugate, T_S is the symbol duration and s_0 , s_1 are the symbols to be transmitted. For a 2x1 transmit diversity system, where h_0 , h_1 are the channels between the 2 TX antennas and 1 RX antenna, the received symbols at t and $t + T_S$ are:

$$r_0 = h_0 s_0 + h_1 s_1 + n_0$$
 at time t
 $r_1 = -h_0 s_1 * + h_1 s_0 * + n_1$ at time $t + Ts$ (4-8)

Combine the signals as follows using estimated channel information at the receiver:

$$\widetilde{s}_{0} = h_{0} * r_{0} + h_{1}r_{1} * = (|h_{0}|^{2} + |h_{1}|^{2})s_{0} + h_{0} * n_{0} + h_{1}n_{1} *$$

$$\widetilde{s}_{1} = h_{1} * r_{0} - h_{0}r_{1} * = (|h_{0}|^{2} + |h_{1}|^{2})s_{1} - h_{0}n_{1} * + h_{1} * n_{0}$$

$$(4-9)$$

These combined signals for s_0 and s_1 are then sent to a maximum likelihood detector. And so diversity for each symbol now depends on the sum of each channel.

The performance from this 2x1 transmit diversity is the same as for a 1x2 maximum ratio receive diversity scheme. However if the total transmit power is equal in both cases, the transmit case is 3dB impaired.

A 2x2 transmit and receive diversity system uses similar techniques to provide 4th order diversity. The same performance as a 1x4 MRC system is obtained only 3dB impaired since the total transmit power is made constant between the single transmit case and dual transmit case.

4.4.2 Results

Results are produced from channel data generated from the physical statistical model above, for the urban and highway case. In each of the dual satellite systems, curves are given for both correlated and uncorrelated shadowing cases.

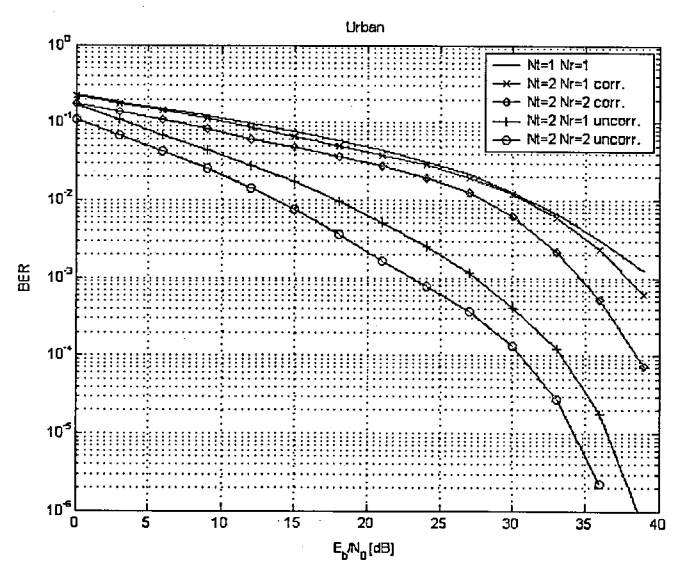


Fig. 4-10 Bit error rate curves showing the effect of large and small scale diversity improvements for the urban environment

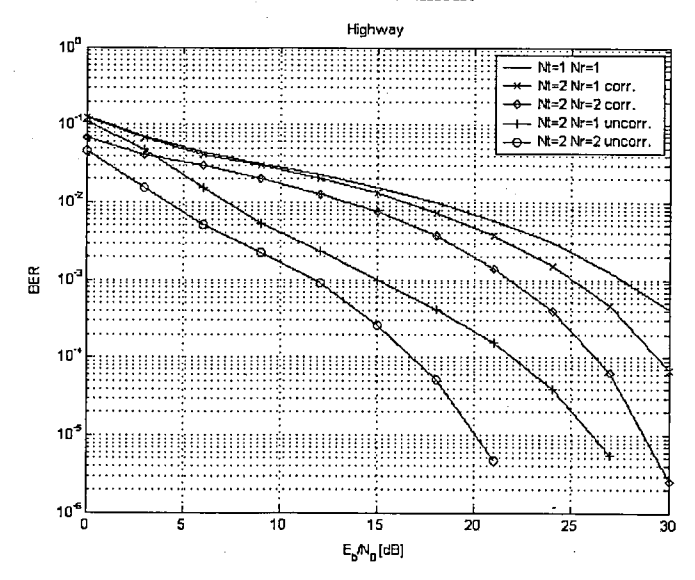


Fig. 4-11 Bit error rate curves showing the effect of large and small scale diversity improvements for the highway environment

4.4.3 Observations

These bit error rate curves were simulated from channel model data that was built around a measurement campaign with a satellite elevation of 24°. They show the gains to be made from MISO and MIMO over SISO channels in an urban and a highway environment. Two cases are presented: (a) when the shadowing between each mobile-satellite path is correlated and (b) when the mobile-satellite paths are uncorrelated.

In the case of correlated shadowing, it is only the small scale fading that is improved by diversity. However it can be observed that 3-4dB reduction in E_b/N_o for a BER of 10^{-2} (suitable for voice or streaming data) is possible with MIMO techniques with correlated shadowing.

However when the shadowing is uncorrelated a much greater improvement is possible from diversity. Around 10-15dB reduction in E_b/N_o is possible by combining signals from two satellites with uncorrelated shadowing. However an additional 3-4dB improvement is possible by using two receive antennas from two widely spatially separated satellites in a 2x2 Alamouti diversity system.

4.5 Limitations of models

These models can be fine-tuned around measurement data and produce statistically accurate results. The accuracy of the large and small scale fading first and second order statistics and power-spatial-delay profile is dependent on the reflection coefficient, size, shape and positioning of the scatterers. In this model the shape of the clusters has been defined to be spherical to simplify the simulation computational complexity. It would be better to define a set of representative building cuboids and position these in a more statistically accurate way. For example, cuboids could be positioned along either side of a road instead of randomly. Defining trees as spheres could be maintained. However, useful insight and estimations of capacity and diversity gain can be achieved with this simplified model.

Regarding small scale correlation, as has been discovered in the measurement campaign, detailed in Chapter 6, some MIMO channels are weakly correlated and some are more correlated, which changes with vehicle location. This can be explained by the co-location or non co-location of valid scatterers for each MIMO channel. For the single satellite dual polarized model, it would be better to define the polarization reflection properties statistically accurately in order to reflect the changing small scale fading MIMO channel correlation with motion. This is left for future work.

Perhaps the main limitation of this model is that it requires measurement data to fine-tune the model in addition to the validation of the model.

4.6 Interim conclusions

This chapter has detailed the methods of constructing two physical-statistical land mobile satellite MIMO channel models. The multiple satellite MIMO model has been partially validated against published measured data, although only its first order SISO statistics. The single satellite dual polarized model construction has been described and partially validated in [Hor07].

The capacity and diversity gains have been estimated from the multiple satellite channel data, and it became clear that MIMO techniques could provide a benefit to LMS systems. However, it was clear that an experiment was required to measure the dual circularly polarized and multiple satellite MIMO channel. The focus of the research thus moved onto planning and carrying out this measurement campaign.

Cha	pter	Five
-----	------	------

5 Measuring the LMS-MIMO Channel

5.1 Measurement campaign planning

5.1.1 Introduction

Extensive measurements were carried out in Guildford, U.K., a city representative of many in central and northern Europe, during the summer of 2005 (with trees in full foliage), where an artificial terrestrially based platform (acting as two satellites), each containing directional RHCP and LHCP antennas, spaced just under one wavelength apart, communicated with a mobile van. The van was fitted with two omnidirectional RHCP and two LHCP antennas spaced four wavelengths apart. The satellite elevation angles, measured using a theodolite, ranged from $7^{\circ} - 18^{\circ}$, $5^{\circ} - 10^{\circ}$, and $5^{\circ} - 15^{\circ}$, for the tree-lined road, suburban and urban environments respectively. Although many operational satellite elevations exceed these, some geostationary and low Earth orbiting mobile satellite services, are required to work at low elevations. The present experiment therefore represents these as worst case system scenarios in terms of extreme large scale fading. Small scale fading variations at higher elevations, which will also affect MIMO capacity, is work still to be investigated.

5.1.2 Equipment

An Elektrobit Propsound wideband MIMO channel sounder was configured for a carrier frequency of 2.45GHz. It transmitted a direct-sequence spread spectrum signal, produced from binary-phase-shift-keyed modulated pseudo-noise codes. The chip duration, sampled at 2 samples per chip, was 10ns and the null-to-null bandwidth was 200MHz. Each MIMO channel is obtained sequentially by using fast switching time division multiplex (TDM) techniques, where three MIMO channel matrices, are captured in each wavelength, and well within the channel coherence time. The received complex samples are written in real time to a fixed disk, where they are post-processed for the power delay profile in each MIMO channel, using a sampled sliding correlation technique. Each of the 16 MIMO channel captures produced 2048 chips of complex data in the delay domain. Synchronization of baseband processing and antenna TDM switching between the transmitting and receiving units is obtained from high stability rubidium clocks, which are synchronized before the start of the measurement campaign. A photograph of the channel sounder is given overleaf. Fig. 5-1 shows the transmitting unit and Fig. 5-2 shows the receiving unit and hard drive. Each unit is a two-man lift.



Fig. 5-1 Propsound transmitter



Fig. 5-2 Propsound receiver and disk drive

The van shown below, owned by the University, was carefully modified to enable cabling to be connected between the inside of the van (containing the channel sounder receiver) and the bespoke roof-mounted antenna rack (designed and built personally). Four antennas were mounted: 2 LHCP and 2 RHCP. The control software was installed on a laptop which was placed on the passenger seat in the cabin, allowing real-time visual feedback of the measured power delay profile.



Fig. 5-3 Measurement vehicle showing roof-mounted antenna rack

The artificial platform (acting as the satellite) is shown in Fig. 5-4. It comprised a scaffolding tower and two antenna masts. Each mast contained a LHCP and RHCP antenna mounted adjacently. The photo also shows the channel sounder transmitting unit, antenna switch box and DC supply batteries.



Fig. 5-4 Hill-mounted artificial platform showing antenna mast and sounder

Although the campaign captured a 4x4 dual polarized MIMO channel, only a 2x2 subset of these channels have been processed and analyzed in the thesis in depth. The purpose of the spatially separated antennas on the artificial platform was to estimate the capacity from a single polarized multiple satellite system scenario. Some results are presented in [Kin06c]. However, as a single satellite dual polarized system is a more viable business solution, most data processing was carried out for this case.

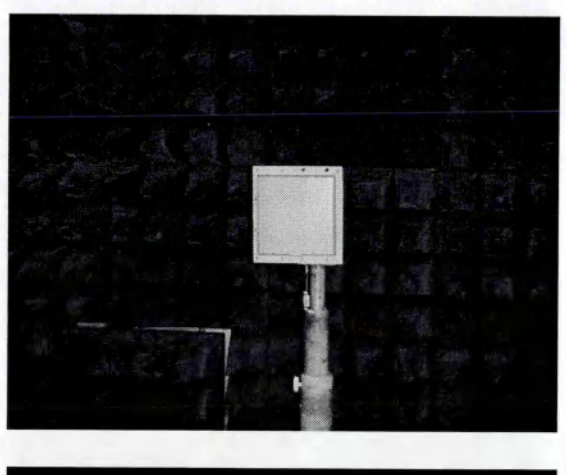
5.1.3 Antenna characterization

Each antenna was characterized in an anechoic chamber for E and H field gain and axial ratio at each angle and over the measurement frequency bandwidth. The patch antenna, used at the artificial platform had a boresight gain of 12dBi, a 3dB beamwidth of 30°, and an average axial ratio of ~1.2. The omnidirectional antenna, used at the vehicle had an azimuthal gain of 0±2dBi over 360°, a 3dB elevation beamwidth of 70° (from datasheet), and an average axial ratio of ~1.4. The axial ratios used in this experiment are representative of practical antenna performance obtainable in a real system implementation. Limitations of the campaign data when using these antennas is discussed in section 6.3.

Cross polar discrimination and axial ratio r are related by the following formulation:

$$XPD = 20\log\left(\frac{r+1}{r-1}\right), dB$$
 (5-1)

Directional antennas



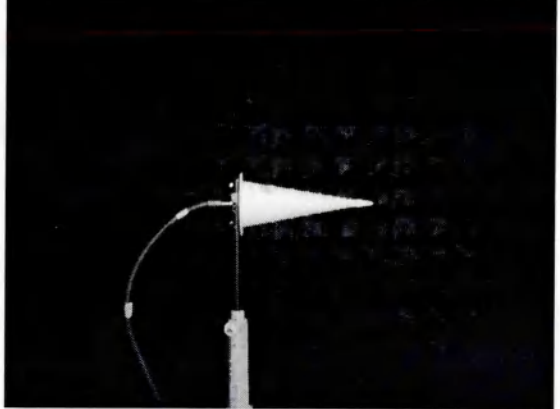




Fig. 5-5 Clockwise from top left: front view of patch antenna; antenna on turntable; reference antenna

The following example plots show the co-polarized and cross-polarized radiation patterns for a patch antenna in the anechoic chamber. The upper plot shows the elevation (vertical) patterns, and the lower plot shows the azimuth (horizontal) patterns. All antennas used in the campaign were characterized.

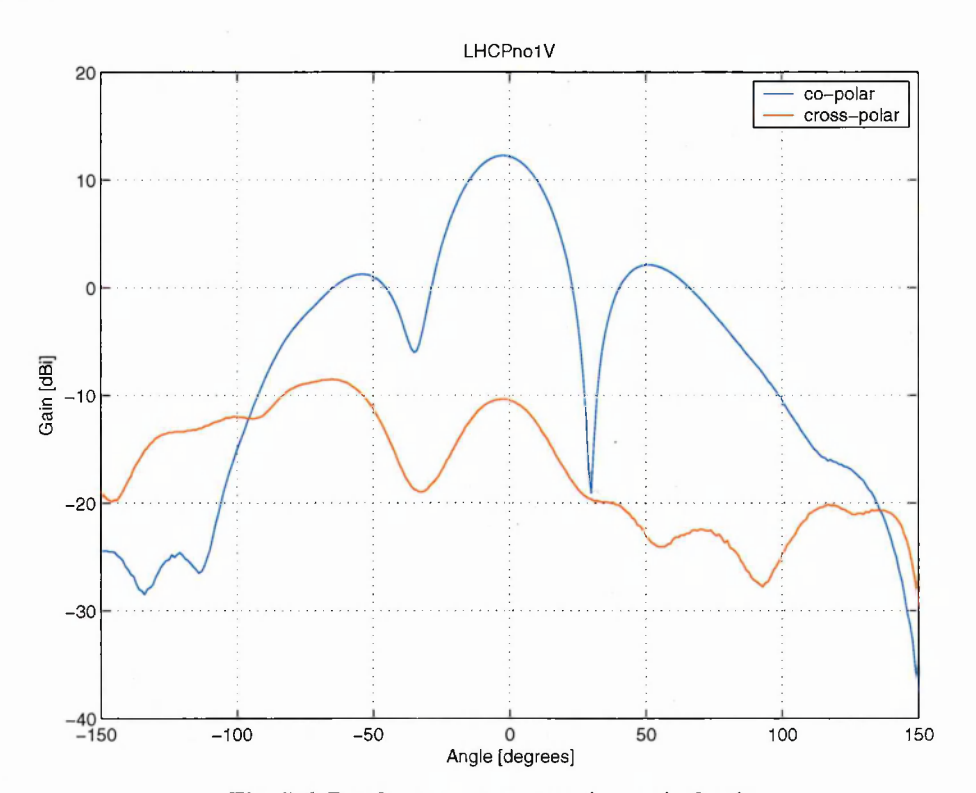


Fig. 5-6 Patch antenna pattern in vertical axis

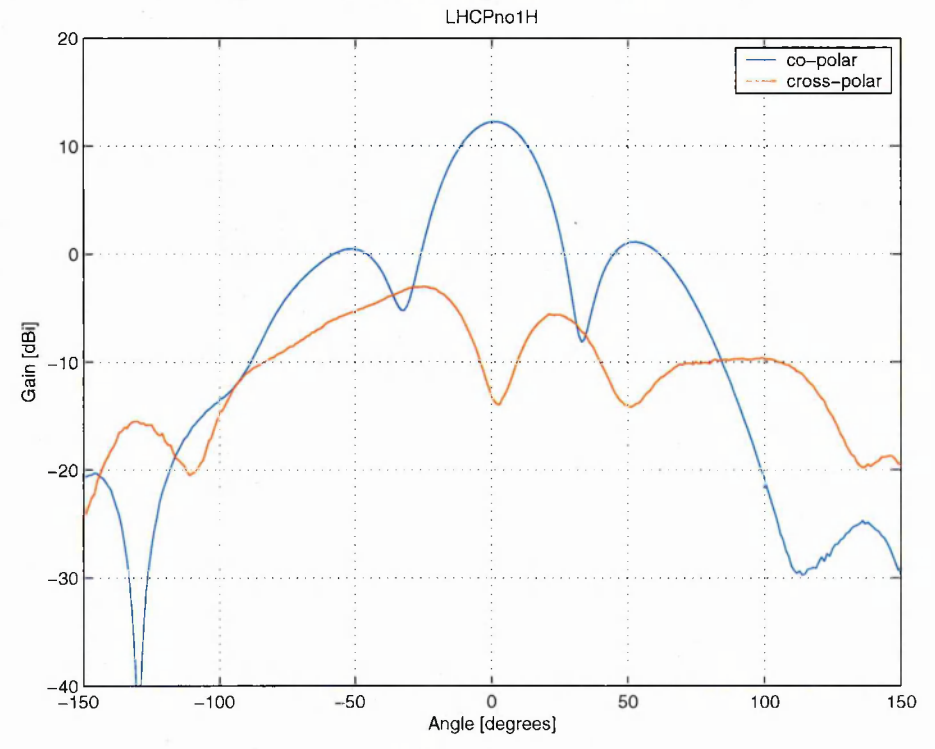


Fig. 5-7 Patch antenna in horizontal axis

Omnidirectional antennas

The following photograph shows an omnidirectional circularly polarized antenna positioned on the turntable during antenna characterization.



Fig. 5-8 Omnidirectional mobile antenna during characterization

The following example plot shows the co-polarized and cross-polarized radiation patterns for an omnidirectional antenna obtained in the anechoic chamber.

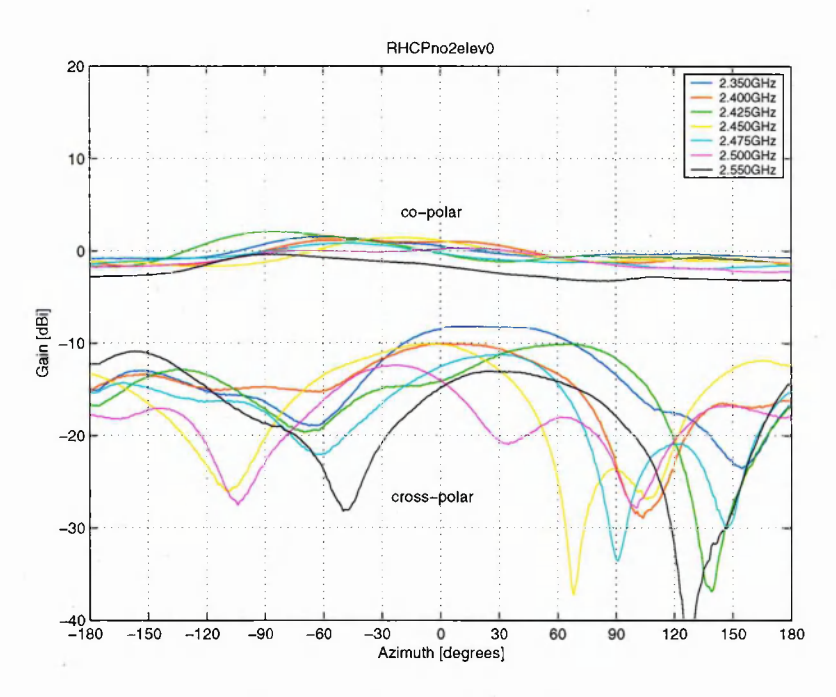


Fig. 5-9 Omnidirectional azimuth radiation pattern

Measurement of elevation for the omnidirectional antenna was difficult to achieve in the available size of anechoic chamber. It was carried out by modifying the elevation of the antenna under test; in practice only $\pm 10^{\circ}$ could be achieved. However the datasheet states the elevation beamwidth to be 70° .

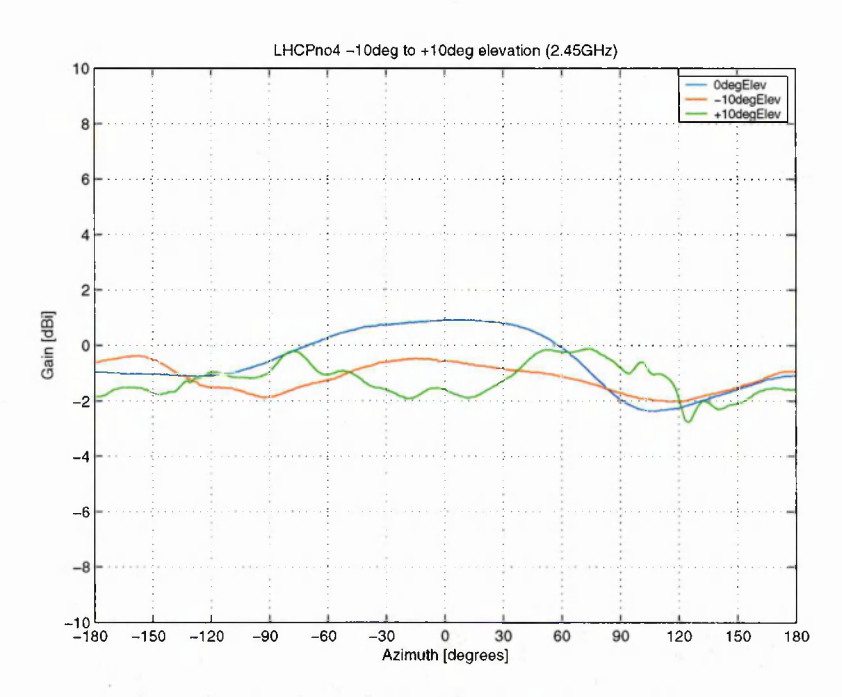


Fig. 5-10 Omnidirectional elevation radiation pattern

5.1.4 Environment

Three environments were identified: (a) a tree-lined road (a major road in the UK narrower than a motorway/highway with a single lane of traffic in each direction), characterized by a high likelihood of dense tree matter at either side of the road with occasional clearings and occasional two storey houses beyond the vegetation; (b) a suburb, characterized by densely placed two storey houses positioned either side of the road and occasional tree matter; and (c) urban, characterized by densely placed two to four storey buildings and sporadic tree matter. Vehicle speeds were 8.9m/s in the tree-lined road environment, and 5.6m/s in the suburban and urban environments. These were chosen as they are representative of typical traffic flow speeds in each environment. The locations of transmitter and each environment superimposed on a map of Guildford are shown below in Fig. 5-11.

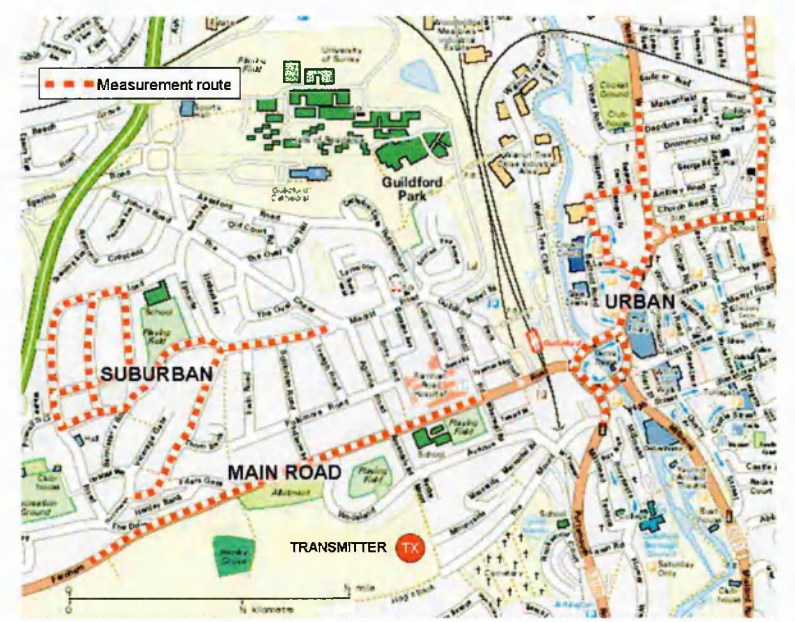


Fig. 5-11 Map of Guildford showing measurement routes in each environment

Cellular planning software and 3D map data was used to check Fresnel clearance at each mobile position. Worst case Fresnel clearance ranged between 0.7 - 4.3, 0.7 - 2.1, and 0.7 - 3.2 in the tree-lined road, suburban and urban environments respectively. A geographical cross-section, showing Fresnel clearance, satellite elevation and local satellite scatterers, is shown in Fig. 5-12. In order to reduce scattering local to the artificial platform, antennas were mounted ~6 metres above ground, at a point of increasingly steep gradient. The antenna main lobe was clear of the local terrain; however, the first sidelobe, at -12dB, faced the grass-covered hilltop verge, around 100m from the platform. Both the mobile and artificial platform antennas were mounted in such a way that no object was within their near fields.

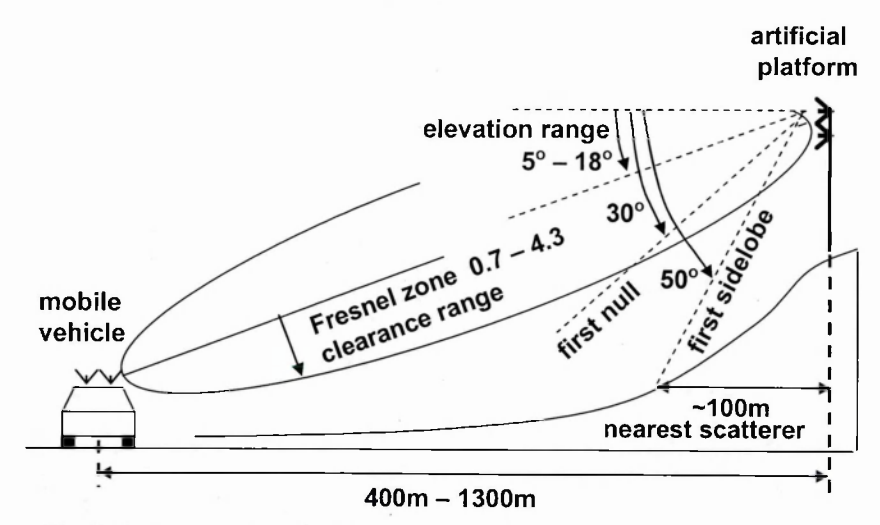


Fig. 5-12 Cross-section of environment showing elevation and Fresnel clearance

5.1.5 Link budget and calibration

The distance between the artificial platform and the mobile was less than 1.3km, in order to enable sufficient dynamic range: 52dB with respect to free space loss (FSL) was available at maximum distance. Whilst additional dynamic range would capture small scale fading in heavily shadowed areas, this was found difficult to achieve, due to regulatory constraints of radiated power, maximum practical code domain processing gain, low gain receive antennas, receiver noise figure and the wide noise bandwidth. The receiver dynamic range is now explained with reference to Fig. 5-13.

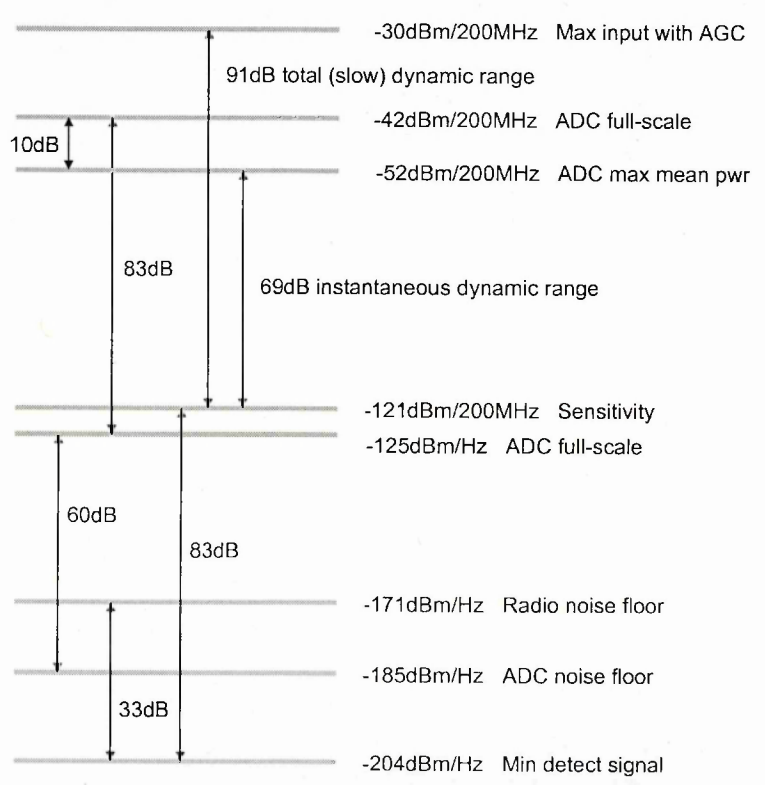


Fig. 5-13 Levels plan referred to antenna connector

Sensitivity

Sensitivity is an important parameter that defines the minimum power level that can be detected by the sounder. Lower sensitivity is fundamental to extending the measurement dynamic range. Sensitivity is expressed as follows:

```
Sensitivity [dBm] = 10\log(k \text{ T} / 10^{-3}) [dBm/Hz] + 10\log B [dB] + NF [dB] - PG [dB] where 10\log(k \text{ T} / 10^{-3}) = -174 \text{dBm/Hz} where k = Boltzmann's constant = 1.3807 \times 10^{-23} \text{ J K}^{-1}, and T = Temperature = 290K 10\log B = 83 \text{dB}, where B = Noise bandwidth = 200MHz NF = Receiver noise figure = 3.1 \text{dB} PG = m-sequence correlating Processing Gain = 10\log(2048) = 33.1 \text{dB} Therefore, sensitivity = -174 + 83 + 3.1 - 33.1 = -121 \text{dBm}
```

This is the minimum detectable signal or noise floor. In a practical measurement campaign, the mean power level should be much higher than this, to allow for signal fluctuations due to shadowing and small scale fading. The experiment should be planned so that the minimum expected signal at high excess delays, path loss, shadowing, and small scale fading fluctuations should remain just above the sensitivity level.

Dynamic range

At a range of 1500m, the FSL is 104dB (using (2-1)). With a transmit power of 23dBm, and an antenna gain of 12dBi (EIRP = 35dBm), the dynamic range at maximum distance is:

```
Maximum range dynamic range = EIRP [dBm] –FSL [dB] – Sensitivity [dBm] = 35 -104 + 121 = 52dB.
```

Therefore, at maximum distance, approximately 52dB is available for shadowing and small scale fading. As the receiver is moved closer to the transmitter, the AGC is activated, reducing the level seen by the data converters. The AGC follows the shadowing attenuation path and the data converter captures the small scale fading. The actual instantaneous dynamic range captured by the data converters depends on their effective bits. With a radio noise floor of -171dBm/Hz, and an ADC quantization noise floor of -185dBm/Hz, a 10 bit converter sampling 200MSPS would give a full-scale input referred signal of -42dBm. However for a signal with 200MHz bandwidth, assuming a signal crest factor of 10dB, a processing gain of 33.1dB and a radio noise floor of -171dBm/Hz, the instantaneous dynamic range can be estimated as follows. The maximum instantaneous signal level is

-185+60-10 = -135 dBm/Hz. The minimum instantaneous signal level is -171-33.1 = -204 dBm/Hz. Therefore the instantaneous dynamic range can be estimated to be -135 - (-204) = 69 dB

Maximum signal level

Elektrobit have stated that the receiver is overloaded when the IF reaches 7dBm. Although they have not supplied their detailed levels plan, using conventional receiver design, it can be estimated that the maximum linear point at the antenna connector (before the antenna switching unit) is -30dBm. Slow fading (AGC) dynamic range can therefore be estimated as follows. The maximum input with a 200MHz bandwidth is -30-83 = -113dBm/Hz. Therefore the total dynamic range can be estimated to be -113-(-204) = 91dB.

With an EIRP of 35dBm/200MHz and a maximum input level of -30dBm/200MHz, the minimum path loss before receiver overload is 65dB, corresponding to a minimum distance of 17m.

Signal level calibration

As the distance between the emulated satellite and vehicle varies, the path loss, antenna gain and delay changes. Since the objective is to normalize the received power to free space loss, a correction factor must be applied for each vehicle position. The channel sounder power delay profile display is merely calibrated in relative decibels. The automatic level control holds the transmit output at 23dBm. To calibrate the system, a lab-based back-back measurement was made. With 82dB loss (from cables and added attenuators) between the TX and RX switch units, the display gave -40.5dB. Therefore 0dB loss between TX – RX would give +41.5dB hypothetically. So the correction factor that needs subtracting from the power delay profile display reading is:

power offset =
$$41.5dB - L_C + G_{TX}(\phi_{TX}, \theta_{TX}) - 20\log\frac{4\pi|\mathbf{d}|}{\lambda} + G_{RX}(\phi_{RX}, \theta_{RX})$$
 (5-2)

where L_C (= 5dB) is the additional cable loss used in the campaign (2dB at the RX side and 3dB at the TX side), $G_{TX}(\phi_{TX},\theta_{TX})$ [dB] is the TX antenna gain in the direction of the LOS path, $G_{RX}(\phi_{RX},\theta_{RX})$ [dB] is the RX antenna gain in the direction of the LOS path. $|\mathbf{d}| = \sqrt{d_1^2 + d_2^2 + d_3^2}$, where d_n [metres] is the distance between the TX and RX in Cartesian dimension n. The wavelength λ at the chosen carrier frequency of 2.45GHz is 0.122m. Using this calibration factor, the displayed power level can be read relative to FSL.

The power delay profile (PDP) also requires calibration because the measured delay varies as the TX – RX distance changes. The delay is found from the following:

$$delay \ offset = \frac{|\mathbf{d}|}{3 \times 10^8} \sec s \tag{5-3}$$

It is necessary to use this method instead of detecting the LOS path and time-aligning to it, because the LOS path is not always present.

Interference

Since the channel sounder carrier frequency was centred on 2.45GHz and is of 200MHz bandwidth, it covers the whole of the ISM WLAN 802.11b/g bands. It was therefore necessary to design an algorithm that detects a rise in noise floor in each power delay profile. If the noise floor (just prior to the LOS path) rises above a threshold (given by the required impulse response dynamic range, but higher than the correlator noise floor), the PDP is discarded. Linear interpolation is then used between the adjacent PDPs to estimate the corrupted profile. In some cases, for example in the urban environment, when passing offices, many seconds of data was continuously corrupted, and in this case, the data had to be discarded and replaced by linearly interpolated estimated PDPs using the uncorrupted PDP before and after the corrupted block.

5.2 The Wideband MIMO channel sounder

5.2.1 Introduction

The wideband MIMO channel sounder, supplied by Elekrobit, is a sophisticated piece of equipment that can capture up to 32x56 MIMO channels of 200MHz null-to-null bandwidth, corresponding to a chip resolution of 10ns (or 100Mchip/s). In this experiment the supplied antennas were not used.

5.2.2 Principles of operation

System architecture

The following diagrams show the RF transmitter architecture (Fig. 5-14) and the RF receiver architecture (Fig. 5-15). The transmitter is a dual conversion with a real-IF DAC configuration. The output is maintained at a fixed level (23dBm maximum at antenna connector) using an automatic level control (ALC).

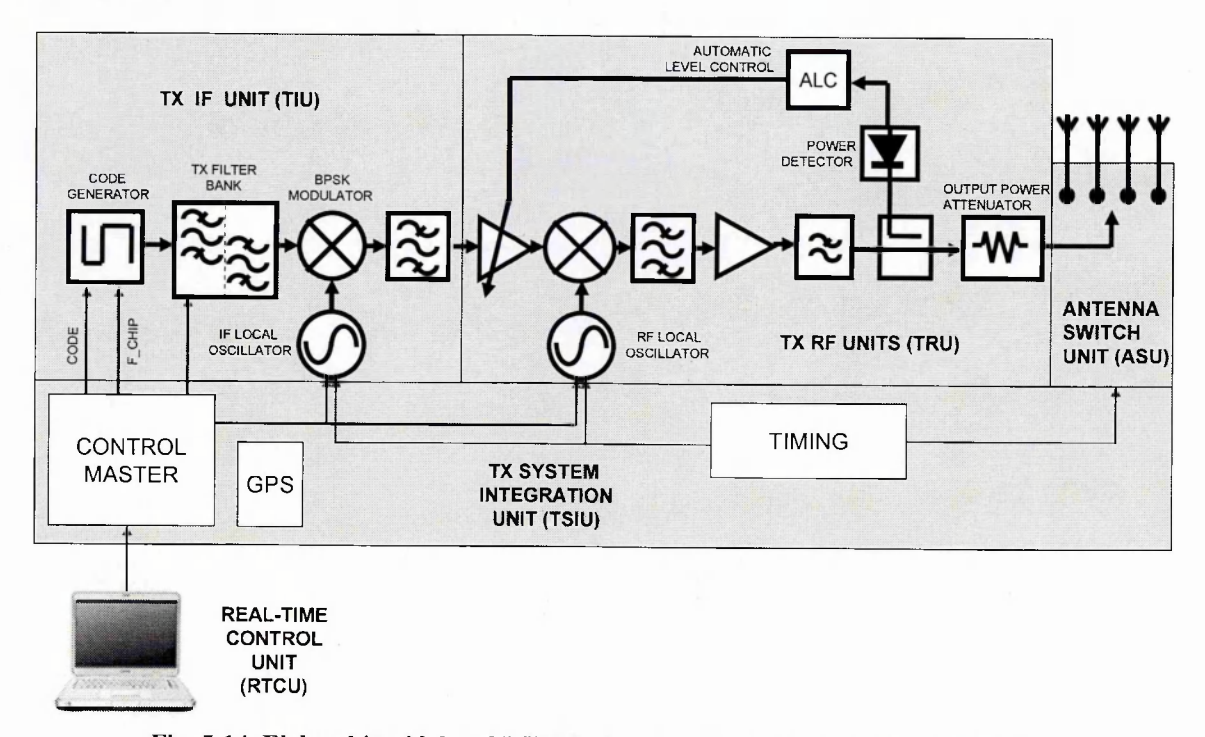


Fig. 5-14 Elektrobit wideband MIMO channel sounder transmitter architecture

The receiver is a dual conversion double superheterodyne architecture with ADC sampling at IQ baseband. Automatic gain control (AGC) is used to keep small scale fading within the ADC dynamic range. A low noise amplifier (LNA) is positioned inside the antenna switch unit enclosure to minimize receiver noise figure.

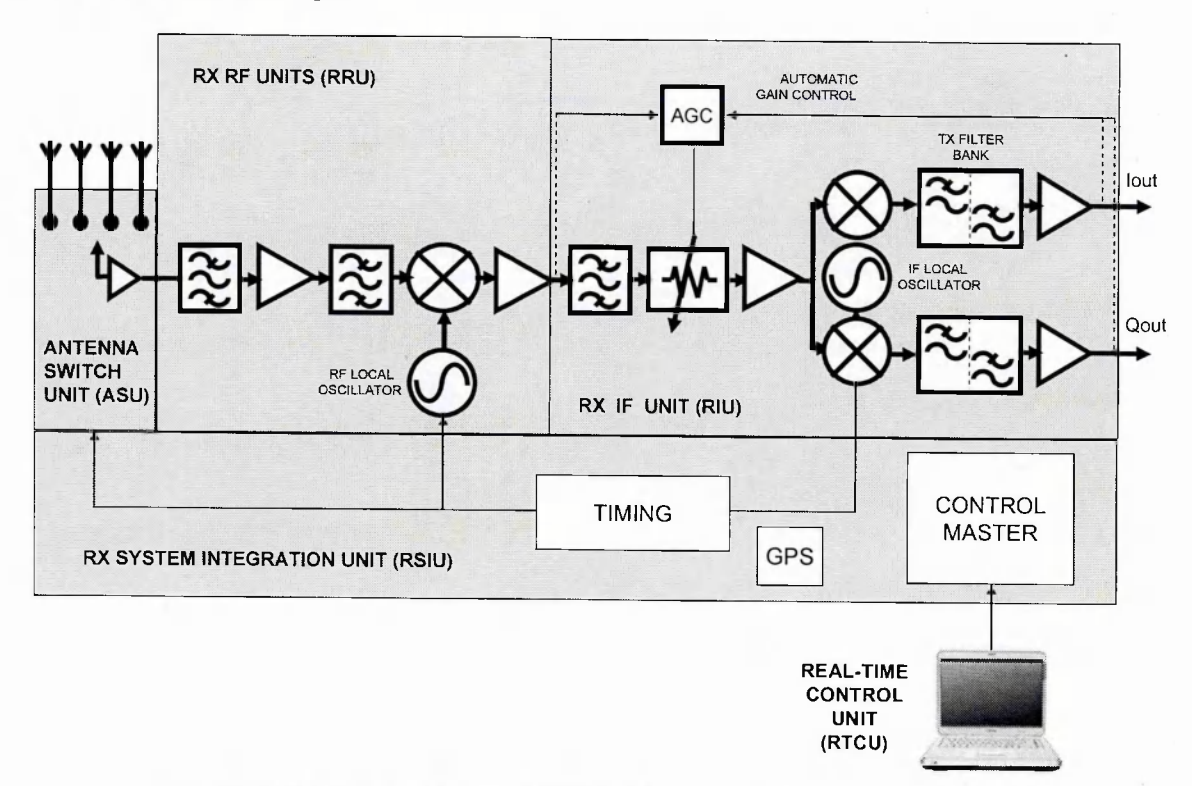


Fig. 5-15 Elektrobit wideband MIMO channel sounder receiver architecture

Receiver baseband processing uses the AGC level combined with the IQ data to produce a wide dynamic range to capture large and small scale fading. Power delay profiles for each MIMO channel are obtained by a sequential sliding correlator approach.

Synchronization and Timing

Frequency offsets between the transmitter and receiver can lead to the power delay profile exiting the display window during a measurement campaign. Even small frequency offsets can lead to phase rotation, exhibiting itself as Doppler. Receiver synchronization cannot be locked to the transmitter as the signal can be shadowed or completely blocked. In the Propsound, a rubidium frequency reference is contained within the transmitter and in the receiver. During operation, after stabilizing, a rubidium frequency reference based phase locked loop is adjusted to minimise the frequency difference between the two units. Frequency calibration is further enhanced by calibrating for minimum phase offset. The inevitable small phase offset is kept negative so that the power delay profile increments up the excess delay window, remaining on the window during the measurement campaign.

Timing, on the other hand, is concerned with matching the code and antenna switching at both the transmitter and receiver. This operation is shown in Fig. 5-16. The sounder was set for 2048 chips per code. This was chosen to capture a time window of 20.48us; although this is higher than the expected excess delay, it allows for absolute delay due to TX-RX range and the movement of power delay profile with time (due to slightly different TX and RX synchronization). Additionally, a higher chip per code setting provides increased code domain processing gain, but has the drawback of reduced MIMO matrix sampling rate (limiting the maximum speed at which the campaign can be carried out). Since there were four antennas at each end of the link, 16 codes + 4 guard codes, are transmitted in each acquisition cycle. Antenna sequencing, as shown in the diagram, switches all four RX antennas in turn for each TX antenna position. The 4x4 MIMO matrix is therefore captured in 0.4096ms. The coherence time can be estimated from $9/(16\pi f_d) = 2.5$ ms (where $f_d = v/\lambda = 8.9$ [m/s]/0.122[m] = 73Hz). Therefore the channel can be considered constant whilst a MIMO channel is captured.

The maximum Doppler frequency was 73Hz for the tree-lined road environment and 46Hz for the suburban and urban environments. In this campaign, the MIMO sampling rate was 152.7 matrices per second, which is at least twice the maximum Doppler frequency. (Sampling must be greater than twice the f_d according to Nyquist for accurate sampling.)

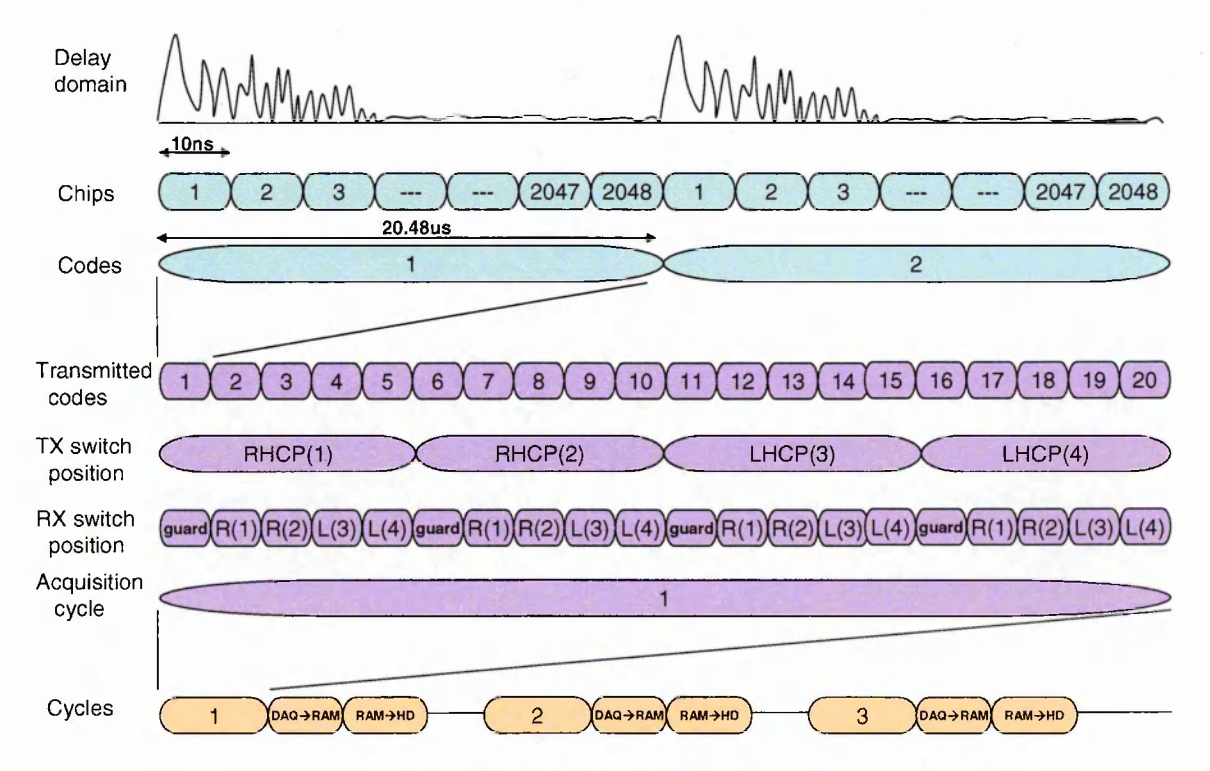


Fig. 5-16 Timing diagram

Sliding correlation post processing

Although a clean maximal length pseudo random bit stream is transmitted, the channel tends to spread the data. Multiple copies of the transmitted bit stream, or code arrive superimposed and with different weights at the receiver. Since codes with near perfect autocorrelation properties are used, a sliding window cross-correlator, can differentiate between each arriving version of the spread code in each 10ns chip bin. The cross-correlator therefore measures the amplitude and phase of code arriving in each chip bin, revealing the impulse response, here with a 10ns resolution. As mentioned, the codes are chosen to have good autocorrelation properties; an example autocorrelation function of a maximal length pseudo random bit stream is shown below:

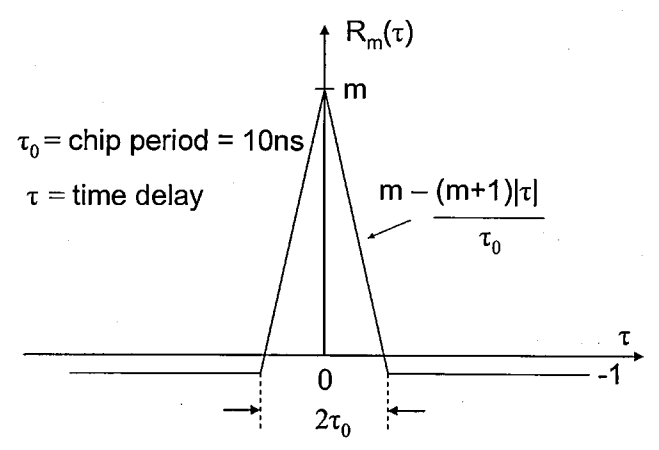


Fig. 5-17 Principles of sliding cross-correlation

5.3 Campaign procedure and data capture

Prior to the satellite-MIMO experiment being carried out, four measurement campaigns were carried out with MSc students for their projects to gain familiarization with the equipment and procedure. (Incidentally the MSc projects included campus based macrocell, microcell, indoor and outdoor-to-indoor environments.) This provided much valuable experience in operating the equipment and carrying out measurement campaigns. The MSc students returned the favour by helping with the satellite-MIMO experiments.

Well in advance of the measurement campaigns, a test and measurement licence was applied for from OFCOM. The form required details of the type of transmission, frequency, bandwidth, duty cycle and effective radiated power. A processing fee of £50 was required and the whole licence procedure took about two months to secure. From this useful insight into the U.K. regulatory and licensing regime for spectrum was gained.

The satellite-MIMO campaigns were carried out twice in each environment on two separate days. In each case the whole campaign lasted non-stop from 8am to 11pm. The morning largely

consisted of transporting and setting up the artificial platform on the 'Hog's Back'- a hilly part of Guildford, and preparing the vehicle with the antenna rack and measurement equipment. The whole of the afternoon was occupied with capturing data in each environment, and the evening was used to backup the data. Fortunately the weather was a hot sunny summer's day on both occasions.

The receiving unit writes the raw IQ data to a fast fixed disk. Around four hours of continuous data could be stored each day, which coincidentally is the time that the batteries lasted. A laptop, positioned on the passenger seat enabled visual checks that a signal was being received, at a refresh rate every few seconds. The laptop required no operation whilst the vehicle was moving.

After the measurement campaigns, the data was transferred from the fixed disk to the Microsoft Windows environment. Visual checks could be made on every power delay profile from each other the sixteen channels at each MIMO matrix sample. The data was then saved in Matlab format with one 'mat' file for each MIMO matrix power delay profile contained in a 'struct' file.

Processing the data before any analysis could be carried out was a very time consuming task taking a few weeks, as interference had to be identified and removed, and calibration of the data with respect to FSL and delay had to be carried out as explained earlier in this chapter.

Once the data had been pre-processed, around 80 Matlab files were written to analyse the data. The results of this analysis are presented in the next chapter.

Cha	pter	Six
-----	------	-----

6 Characteristics of the LMS-MIMO Channel

6.1 Narrowband LMS-MIMO characteristics

6.1.1 Initial observations

Prior to a full analysis of the channel data, an initial qualitative investigation was carried out on the narrowband data, to form some general ideas about the dual circularly polarized 2x2 MIMO channel. In each environment, the time series data was compared with the scatterers (eg. buildings and vegetation) close to the vehicle. Local and aerial photography and available information regarding the vehicle motion and location allowed the matching of the data to the environment. For example, the time series data in Fig. 6-1 shows the received signal strength along the tree-lined road, with the LOS component obstructed by trees between 0 and 5 metres, and clear between 6 and 10 metres. It can be observed that between 0 and 5 metres, the large scale components are attenuated substantially, the small scale fading contains many deep fades, and the cross-polarized component powers appear to be of similar strength to the co-polarized components. However, between 6 and 10 metres, there are strong co-polarized components, and a higher ratio exists between co-polarized and cross-polarized components.

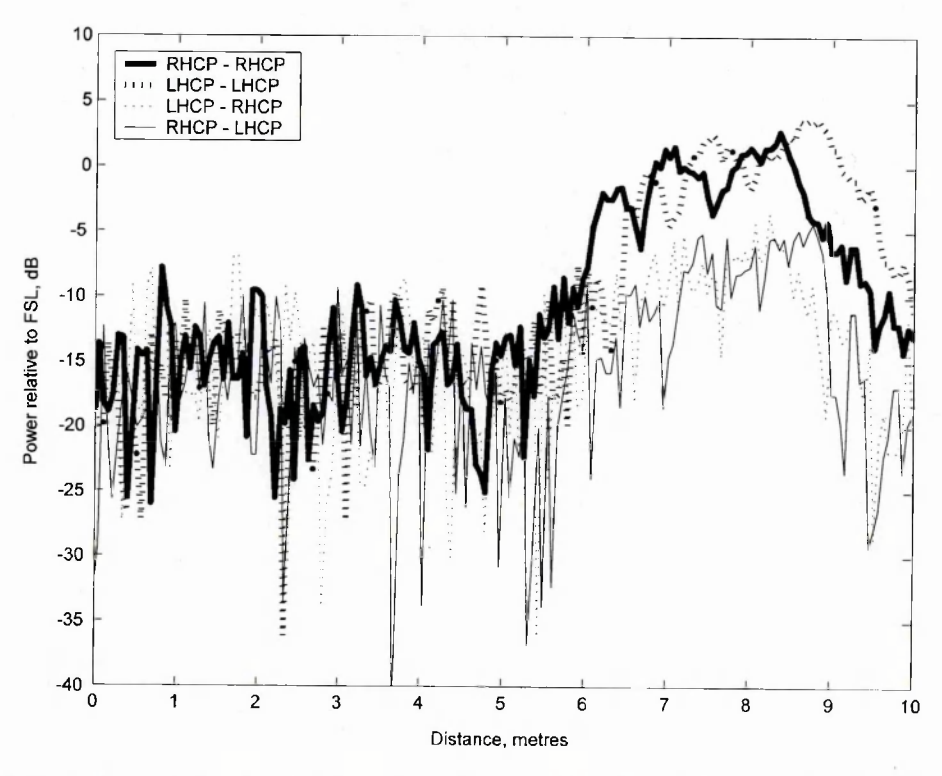


Fig. 6-1 Example narrowband received powers relative to FSL in the tree-lined road environment for dual polarization single satellite case.

For comparison a narrowband plot of the 2x2 multiple satellite case, where satellites are in the same cluster with a single polarization is shown in Fig. 6-2.

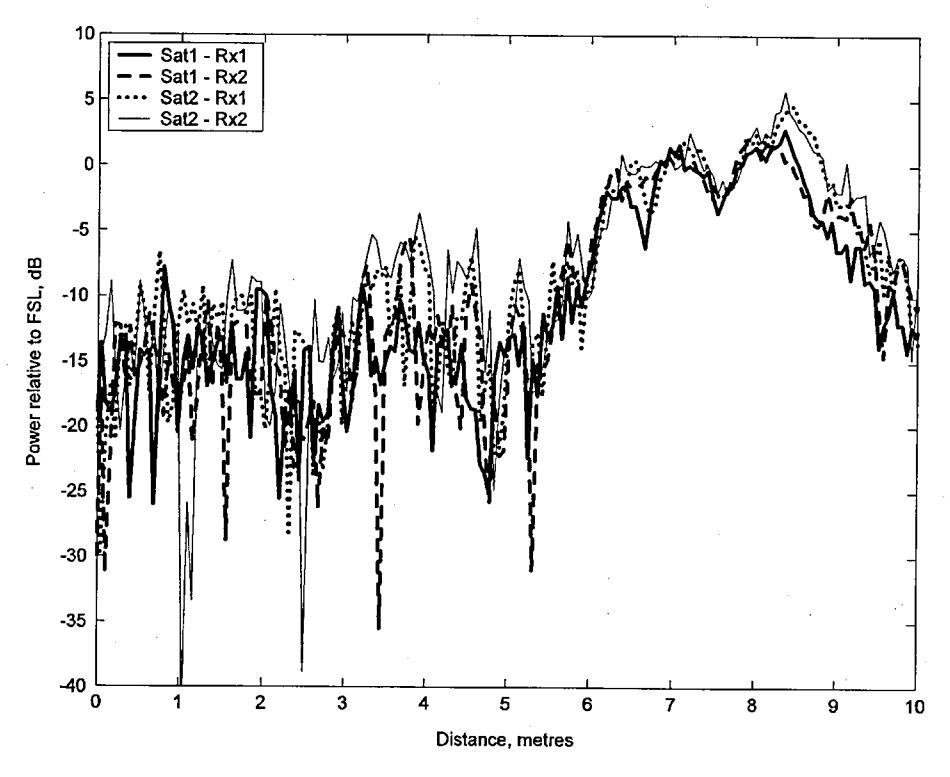


Fig. 6-2 Example narrowband received powers relative to FSL in the tree-lined road environment for dual satellite cluster case

The measurement campaign actually captured data from 2 satellites in a cluster, each with dual circular polarization, to a vehicle with 2 RHCP and 2 LHCP antennas. Analysis of this 4x4 satellite-MIMO channel data is left for future work. Since a single satellite system is a more viable business solution, the analysis was carried out in depth on the 2x2 dual polarized MIMO channel data.

6.1.2 Large scale characteristics

In this section, narrowband large scale fading properties are reported. Fading distribution, temporal variations and correlation over the MIMO channel domains are addressed.

Distribution

The time series narrowband measured data was averaged by a sliding window time technique, adhering to the Rayleigh criteria (120 data points over 40 wavelengths) [Lee74] and a probability density histogram of the large scale fading level was obtained. Initial observations showed that in the tree-lined road environment, the probability densities appeared as two adjacent and overlapping lognormally distributed segments. An example is shown in Fig. 6-3 for the co-polar channel. The suburban and urban environment exhibited probability densities that appeared as a single log-normal distribution. A model based on these observations was then tested. Each cumulative distribution segment was tested in turn for goodness-of-fit to the theoretical log-normal or two adjacent and overlapping log-normally distributed segments using the Kolmogorav – Smirnoff (K-S) test [Mas51].

In the case of adjacent and overlapping log-normal distributions, the K-S test was applied as follows. Initially the cross-over point was identified at the local minima between the two distributions and then each segment on either side of the cross-over point was tested in turn. Each segment of the experimental data was matched to the equivalent theoretical log-normal segment. Since the two distributions were overlapping, the K-S test could only be applied to the visible part of the distribution.

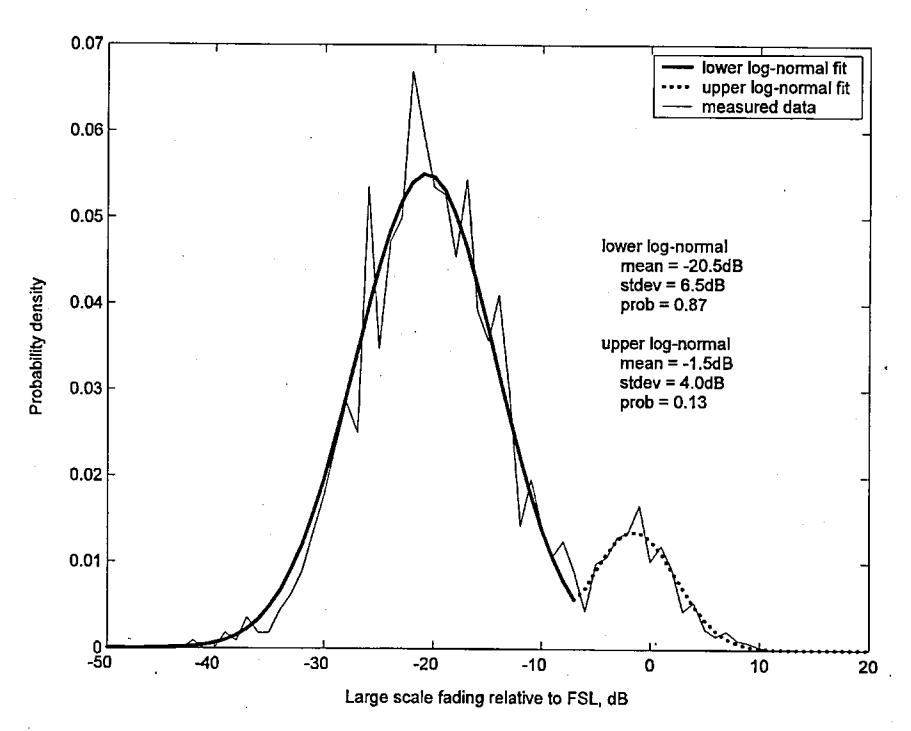


Fig. 6-3 Large scale fading co-polar distribution and model fit for tree-lined road environment

In the suburban and urban cases, the single distributions were found to be log-normal at the 1% statistical significance level. For the two overlapping distributions, they were also both found to be log-normal at the 1% statistical significance level for the visible part of the distribution. The probability density function of the two overlapping log-normal distribution model can be formulated as follows:

$$p(s) = \begin{cases} \frac{P_u}{\sqrt{2\pi} \sigma_u} exp \left[-\frac{1}{2} \left(\frac{s - \mu_u}{\sigma_u} \right)^2 \right] / \left[1 - \frac{1}{2} \left[1 + erf \left(\frac{x - \mu_u}{\sigma_u \sqrt{2}} \right) \right] \right] &, \quad s > x \\ \frac{P_l}{\sqrt{2\pi} \sigma_l} exp \left[-\frac{1}{2} \left(\frac{s - \mu_l}{\sigma_l} \right)^2 \right] / \frac{1}{2} \left[1 + erf \left(\frac{x - \mu_l}{\sigma_l \sqrt{2}} \right) \right] &, \quad s \le x \end{cases}$$

$$(6-1)$$

where s is the large scale fading level (dB), x is the cross-over point (dB), σ_u and σ_l are the standard deviations (dB) for the upper and lower log-normal components respectively. The means (dB) for the upper and lower log-normal components are μ_u and μ_l respectively. The probability of

the large scale signal level residing in the upper log-normal component is given by P_u . The probability of the large scale signal level residing in the lower log-normal component or at the cross-over point is given by P_t . The term erf is the error function defined as:

$$erf(\beta) = \frac{2}{\sqrt{\pi}} \int_{0}^{\beta} \exp(-t^2) dt$$
 (6-2)

Table 1 shows the statistics for the log-normal or dual log-normal model in each environment.	Table	I shows the statist	ics for the log-norm	al or dual log-norma	l model in each e	nvironment.
---	-------	---------------------	----------------------	----------------------	-------------------	-------------

	Lower lo	g-normal	Upper log	g-normal		
	mean	stdev	mean	stdev		
Road, co-polar	-20.5dB	6.5dB	-1.5dB	4.0dB		
Road, x-polar	-21.5dB	6.0dB	-4.5dB	3.0dB		
Suburb, co-polar	-25.0dB	9.5dB	modelled by sin	gle log-normal		
Suburb, x-polar	-28.0dB	7.0dB	modelled by sin			
Urban, co-polar	-23.5dB	6.5dB		modelled by single log-normal		
Urban, x-polar	-23.0dB	6.5dB	modelled by single log-normal			

Table 1 Large scale fading log-normal model parameters

Temporal variations

To describe the temporal variations, the large scale autocorrelation functions were obtained for co- and cross-polarized channels in each environment and the coherence distance at the 1/e point was found. The normalized autocorrelation function, repeated here for clarity can be defined [Pee01] as:

$$\rho(\tau) = \frac{E(\alpha(t)\alpha^*(t+\tau))}{E(|\alpha(t)|^2)}$$
(6-3)

where E[.] is the expectation, $\alpha(t)$ is the complex fading signal and τ is the delay separation. The shadowing autocorrelation function was found to follow accurately a decaying exponential as suggested in [Mar90], [Gud91]. The exponential autocorrelation decay model was matched to the measured data autocorrelation empirically. The 1/e autocorrelation distance was found for co-/cross-polarized channels to be 23/29m, 120/128m and 128/129m in the tree-lined road, suburban and urban environments respectively. An example of shadowing autocorrelation decay curve for the urban environment is shown in Fig. 6-4.

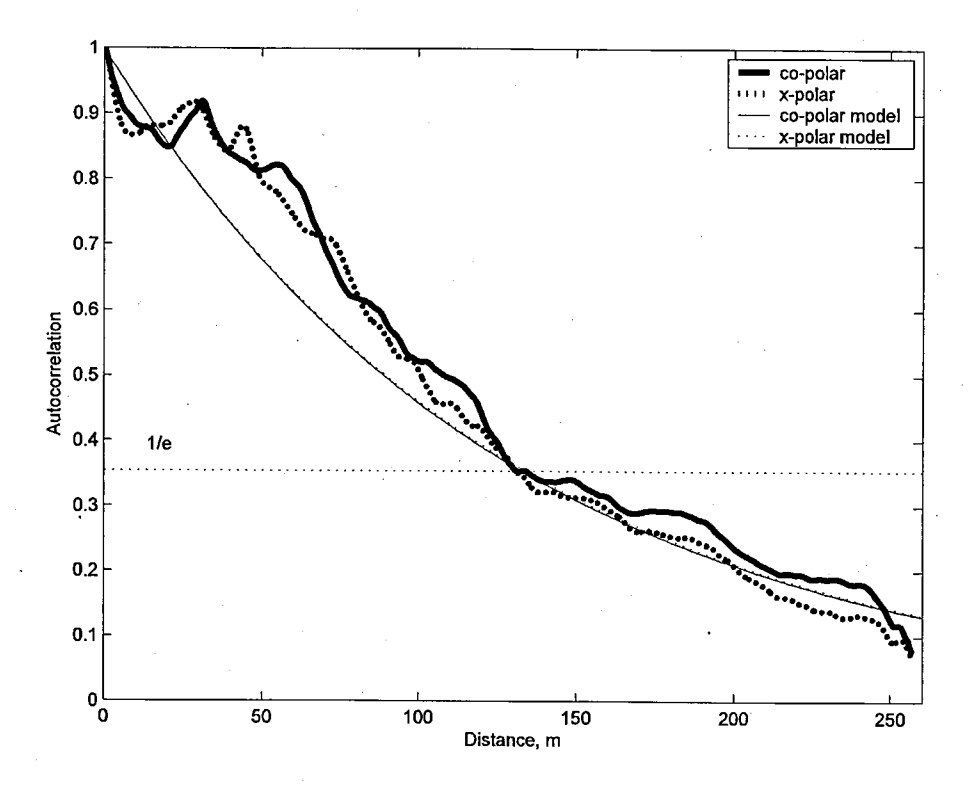


Fig. 6-4 Large scale fading autocorrelation model fit to measured data for urban environment

MIMO channel correlation

In the combined spatial/polarization domain, the large-scale fading correlation coefficient between MIMO channels was found, in each environment. The analysis revealed a strong correlation coefficient between each pair of large scale fading MIMO channels. This correlation coefficient of the narrowband data, is shown in Table 2 for each environment. In this table, 'R/L' for example refers to a transmitting RHCP antenna (artificial platform) to a LHCP receiving antenna (vehicle).

			Main				Subu				Urt	oan	
		R/R	L/L	R/L	L/R	R/R	L/L	R/L	L/R	R/R	L/L	R/L	L/R
Large	R/R	1.00				1.00				1.00	_		
Scale	L/L	0.86	1.00			0.76	1.00			0.86	1.00		
Fading	R/L	0.85	0.91	1.00		0.76	0.83	1.00		0.86	0.89	1.00	
	L/R	0.90	0.87	88.0	1.00	0.83	0.75	0.78	1.00	0.92	0.85	0.93	1.00

Table 2 Average large scale correlation coefficients between MIMO channels

It can be seen therefore that there is a strong correlation between MIMO channel large scale fading, which is as expected as both antennas were co-located at one satellite and similarly co-located at one vehicle.

6.1.3 Small scale characteristics

In this section, the small scale fading properties are reported from the narrowband data. Fading distribution, with its conditioning on large scale fading, temporal variations, and correlation over the MIMO channel domain are addressed.

Distribution

The narrowband large scale fading was split into temporal windows of 180 samples over around 60 wavelengths. The average power in each window was subtracted from the measured data revealing the small scale fading. The cumulative distribution of the experimental small scale fading in each temporal window was tested against the theoretical Ricean cumulative distribution. The probability density of the Ricean distribution can be formulated [Cor94] as:

$$p_{R}(r) = 2r(K+1) \exp\left[-r^{2}(K+1) - K\right] I_{0}\left(2 r \sqrt{K(K+1)}\right) \qquad (r \ge 0)$$
 (6-4)

where K is the Rice factor defined as the ratio of direct path power to diffuse multipath power. The function I_0 is the modified Bessel function of the first kind and zeroth order. Every time window for co- and cross-polarized channels in each environment was checked against the theoretical Ricean distribution. The Kolmogorav – Smirnoff test [Mas51] was used to check the validity of the Ricean fit and it was found that every window was Ricean distributed at the 1% statistical significance level. By optimizing the theoretical distribution to the measured distribution also revealed the Rice K factor that best described the data in each window.

Rice K conditioning on large scale fading

A scattergram was obtained of Rice K factor versus shadowing level, and their correlation coefficients were found. Moderate correlations were found for the tree-lined road and suburban environments only; only a weak correlation was found for the urban environment. Correlation coefficients for co-/cross-polarized channels were 0.42/0.44 for the tree-lined road, and 0.58/0.61 for the suburban environment.

Since a moderate correlation was found for the tree-lined road and suburban cases, a polynomial fitting was carried out. A scattergram for the tree-lined road case and suburban case along with polynomial fitting for each polarization is shown in Fig. 6-5 and Fig. 6-6. The urban case is also shown for interest in Fig. 6-7.

In the urban environment the lack of polynomial to describe the Rice K factor dependency on large scale fading is as expected, as the received signal is predominantly made from local multiple reflections and is therefore much harder to model in a generic fashion.

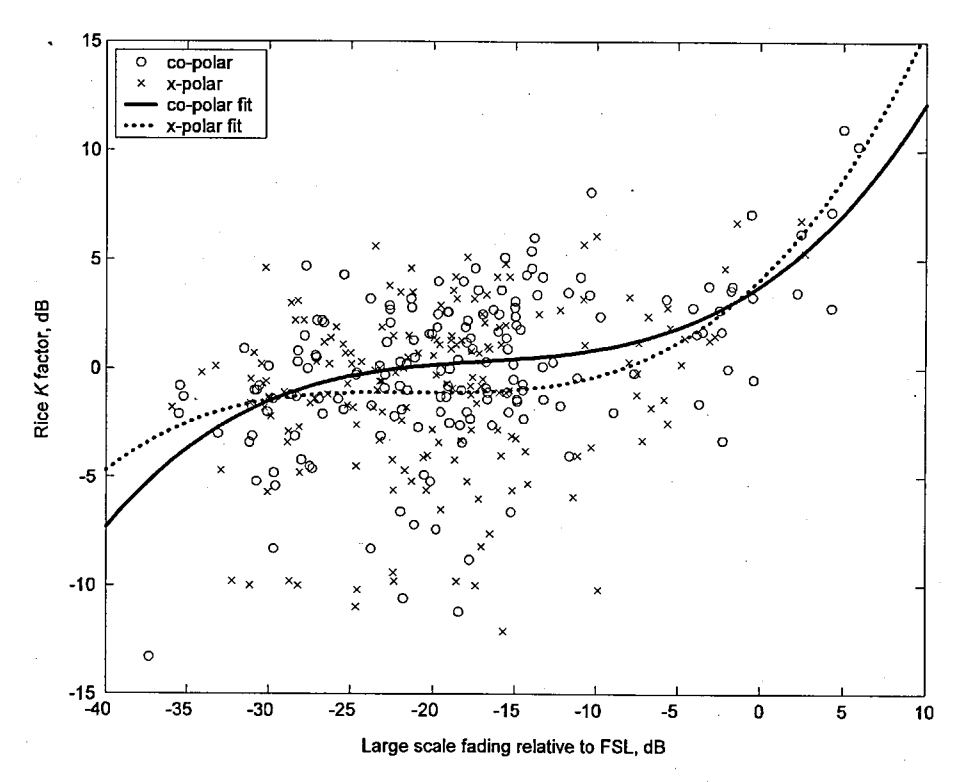


Fig. 6-5 Rice K factor conditioning on large scale fading level for road environment

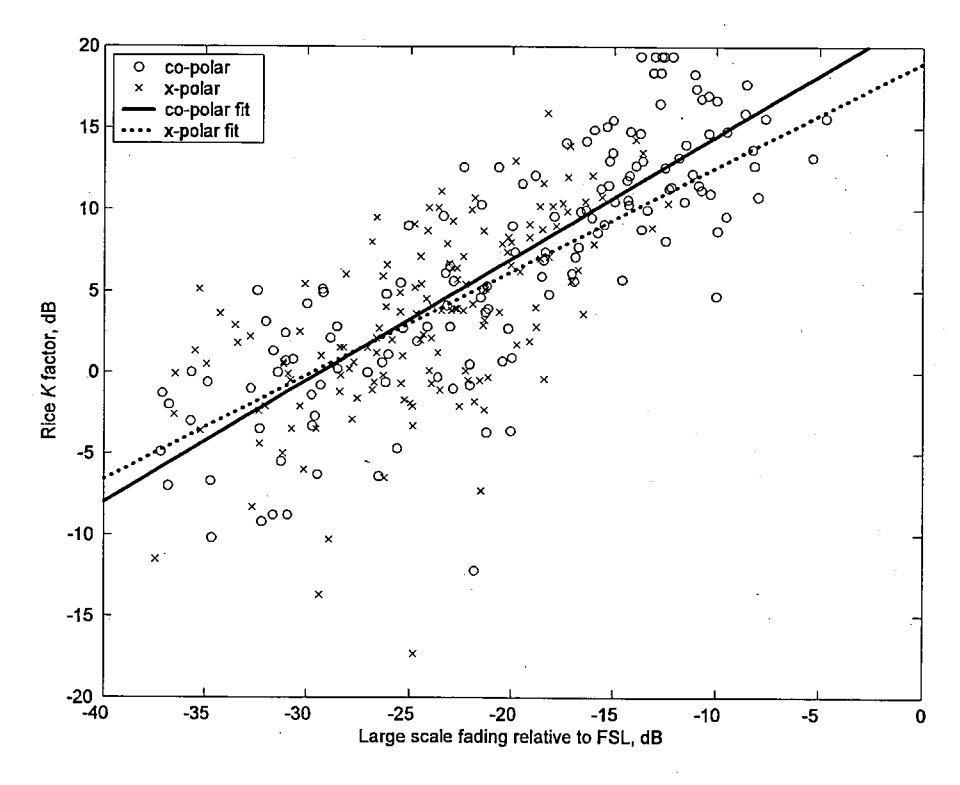


Fig. 6-6 Rice K factor conditioning on large scale fading level for suburban environment

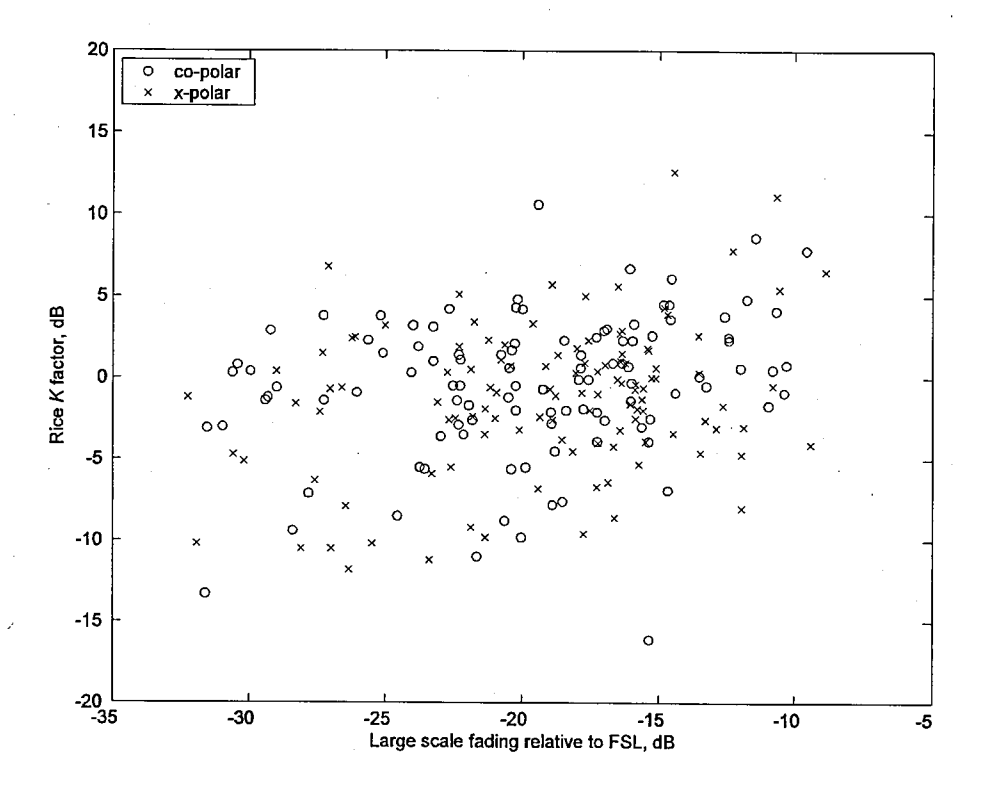


Fig. 6-7 Rice K factor conditioning on large scale fading level for urban environment Polynomial fitting interpolation was carried out using the following formula:

$$K_{dB}(S_{dB}) = \mu_0 + \mu_1 S_{dB} + \mu_2 S_{dB}^2 + \mu_3 S_{dB}^3$$
 (6-5)

Coefficients for co- and cross-polarized channels for road and suburban environments are given in Table 3. The root-mean-squared errors (RMSE) were obtained between the measured data and fitted curves for linear, quadratic and cubic polynomials. The cubic polynomial incurred the minimum RMSE and closely resembled the high K factors found at lower levels of shadowing for the tree-lined road case. The linear fitting incurred minimum RMSE and closely resembled the K factor trends for the suburban case. Using higher order polynomials did not suggest a benefit in RMSE. The RMSE in co-/cross-polarized channels was 4.1/5.1 and 5.1/5.3 in the tree-lined road and suburban environments respectively. The polynomial can be used in the modelling process.

		μ_{o}	μ_1	μ_{2}	μ_3	Valid range
Road	Co-polar	3.8	0.51	0.027	0.0005	-45 <s₀s<0< th=""></s₀s<0<>
	X-polar	4.1	0.74	0.035	0.0006	-45 <s₀s<0< th=""></s₀s<0<>
Suburb	Co-polar	22	0.75	0	0	-40 <s<sub>18<-5</s<sub>
	X-polar	19	0.64	0	0	-40 <s<sub>d8<-5</s<sub>
Urban	Co-polar		We	eak correla	tion only	
	X-polar		We	eak correla	tion only	

Table 3 Rice K factor polynomial parameters for narrowband data

Rice K factor analysis

Each time window of measurement data was analysed for Rice K factor, by fitting the measured data cumulative distribution to the theoretical distribution. The K factor cumulative distributions in each environment are given in Fig. 6-8 (road), Fig. 6-9 (suburban) and Fig. 6-10 (urban). The mean, median and standard deviation of the K factor is also given in Table 4 (road), Table 5 (suburban) and Table 6 (urban).

In the tree-lined road and urban cases, the cumulative distributions of both the co- and cross-polarized K factors follow a similar curve. However, in the suburban case, the spread of K factors is greater for the co-polarized channels.

The range of K factors is around -15dB to +15dB for all channels in all environments. A K factor of +15dB has a high constant part, whereas K factors of under 0dB are approaching a Rayleigh distribution, where the LOS part is blocked, revealing mostly a random multipath part.

Tree-lined road Environment

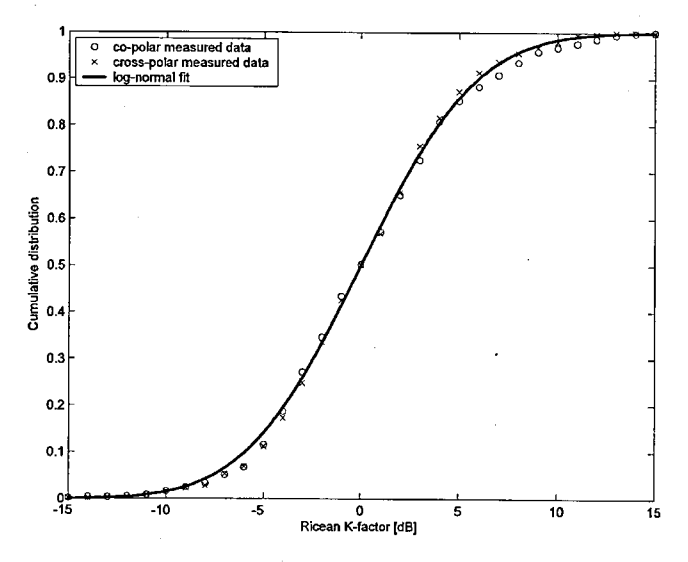


Fig. 6-8 Cumulative distribution of Rice K factor in road environment (normalized to median)

component	mean	median	sigma
co-polar	2.9dB	-0.1dB	4.9dB
cross-polar	1.5dB	-0.9dB	4.5dB

Table 4 Rice K factor statistics in road environment

Suburban Environment

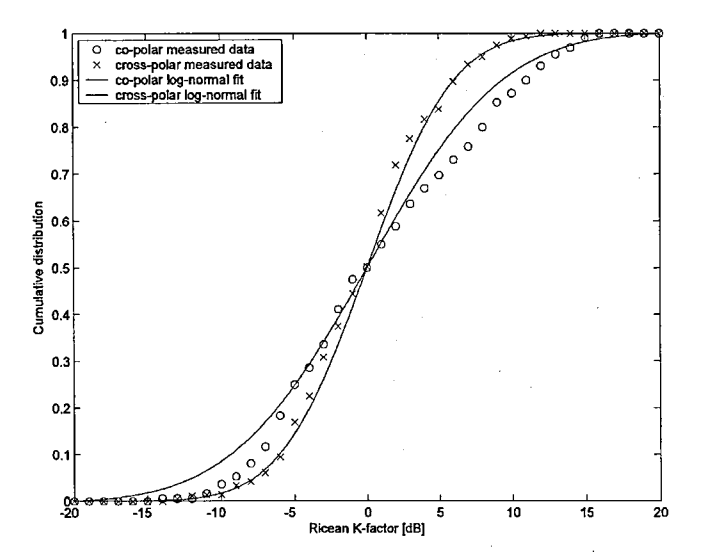


Fig. 6-9 Cumulative distribution of Rice K factor in suburban environment (normalized to median)

component	mean	median	sigma
co-polar	4.2dB	3.4dB	7.4dB
cross-polar	1.2dB	1.5dB	4.7dB

Table 5 Rice K factor statistics in suburban environment

Urban Environment

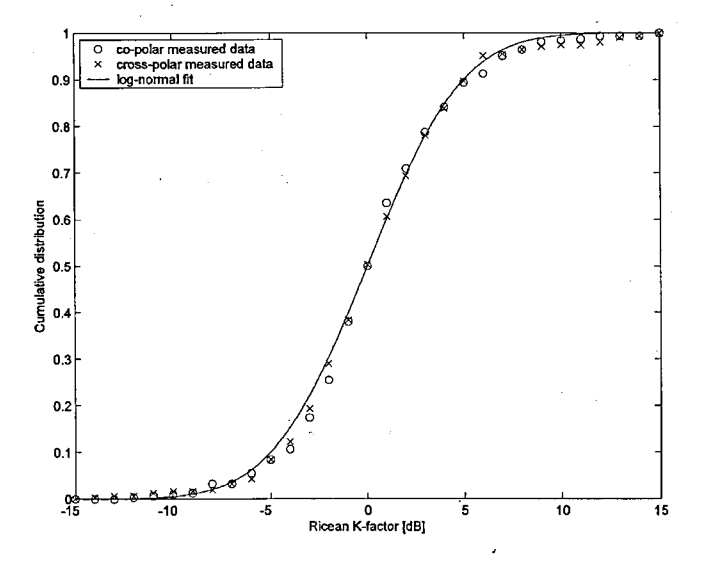


Fig. 6-10 Cumulative distribution of Rice K factor in urban environment (normalized to median)

		*	
component	mean	median	sigma
co-polar	-1.2dB	-1.5dB	4.1dB
cross-polar	-1.3dB	-1.5dB	4.3dB

Table 6 Rice K factor statistics in urban environment

Temporal variations

The small scale data was split into temporal windows. The normalized autocorrelation was found in each window. The mean $1/\sqrt{2}$ correlation point was found for co-/cross-polarized channels to be 0.55/0.50, 0.50/0.60 and 0.45/0.40 for the tree-lined road, suburban and urban environments respectively. The estimated coherence time can be found by de-normalizing to the maximum Doppler frequency: $T_C = \tau / f_d = \tau / (v/\lambda) = 0.55 / (8.94/0.122) = 0.0075s$. So the tree-lined co-polar channel can be assumed undistorted by the effects of Doppler spread for 7.5ms.

Another representation of the temporal variations is the Doppler spectrum. An example of the Doppler spectrum for a tree-lined road case is shown in Fig. 6-11.

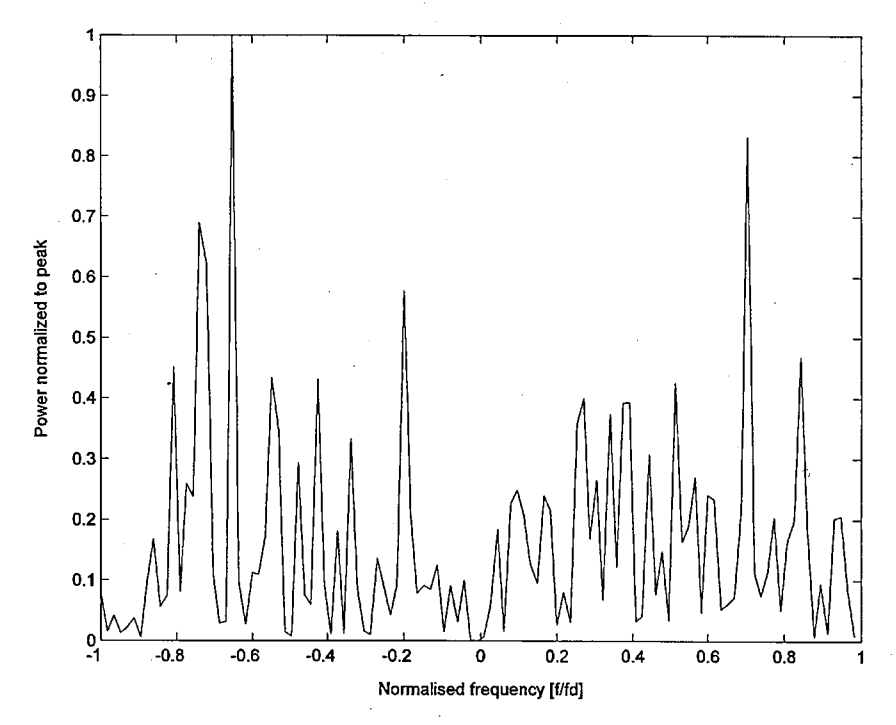


Fig. 6-11 Tree-lined road small scale fading multipath Doppler spectrum

It is interesting to compare Fig. 6-11 with the classical U-shape Doppler spectrum in (3-66) as proposed by Clarke. It can be observed that not all small scale fading channels are U-shaped; however some stronger Doppler components can be observed at higher Doppler frequencies, which is in accordance with the classical Clarke Doppler spectrum.

MIMO channel correlation

Small scale tap correlations between MIMO channels are of primary importance for capacity analysis with regards to MIMO spatial multiplexing as shown in Chapter 3. The small scale fading was obtained by subtracting the large scale fading from the data, and then the correlation coefficient was obtained for blocks of channel data of length 40 wavelengths. The correlation coefficient between two signals, α_A and α_B is defined as [Pee01], repeated here for clarity:

$$\rho_{AB} = \frac{E[(\alpha_A - \mu_A)(\alpha_B - \mu_B)^*]}{\sigma_A \sigma_B}$$
(6-6)

where E[.] is the expectation, μ_A , μ_B are the means and σ_A , σ_B are the standard deviations of α_A and α_B . Table 7 shows the average correlation coefficient in the MIMO matrix for road, suburban and urban environments respectively, from the narrowband channel. The correlation is a function of the vehicle position in each environment. Cross-correlation cumulative distributions of the four MIMO channels not emanating from the same mobile antenna showed that the 10/90% distribution points of correlation coefficients were -0.35 and +0.2 for the tree-lined road, -0.35 and +0.2 for suburban, and -0.3 and +0.3 for the urban environments. However, the cross-correlations between channels emanating from the same mobile antenna, showed increased correlations for some channels. In this case, the 10/90% distribution points of correlation coefficients were -0.15 and +0.55 for tree-lined road, -0.3 and +0.3 for suburban, and -0.2 and +0.35 for urban environments. These distributions are shown in Fig. 6-12 (road), Fig. 6-13 (suburban) and Fig. 6-14 (urban).

The temporal variation of MIMO channel correlation coefficient requires further exploration, and requires an examination of the scattering process. Due to the constructive/destructive vector addition small scale fading process, it is evident that identically located scatterers will cause highly correlated fading, and separately located scatterers will provide weakly correlated fading. An example of an identically located scatterer is one which reflects a RHCP incident wave into both RHCP and LHCP component waves, towards the satellite. An example of separately located scatterers is where one scatterer reflects the incident RHCP wave predominantly into a LHCP wave, and another reflects it primarily into a RHCP wave, which is dependent on the angle of incidence.

			Main	Road			Subu	ırban			Urk	oan	1
		R/R	L/L	R/L	L/R	R/R	L/L	R/L	L/R	R/R	L/L	R/L	L/R
Small	R/R	1.00				1.00				1.00			
Scale	Ŀ/L	0.03	1.00			0.01	1.00			0.05	1.00		
Fading	R/L	0.02	0.12	1.00		0.09	0.10	1.00		0.01	0.07	1.00	
	ĽR	0.09	0.01	0.01	1.00	0.05	0.06	0.06	1.00	0.21	0.02	0.04	1.00

Table 7 Average small scale correlation coefficients between MIMO channels

In this table, 'R/L' for example refers to a transmitting RHCP antenna (artificial platform) to a LHCP receiving antenna (vehicle).

Tree-lined road environment

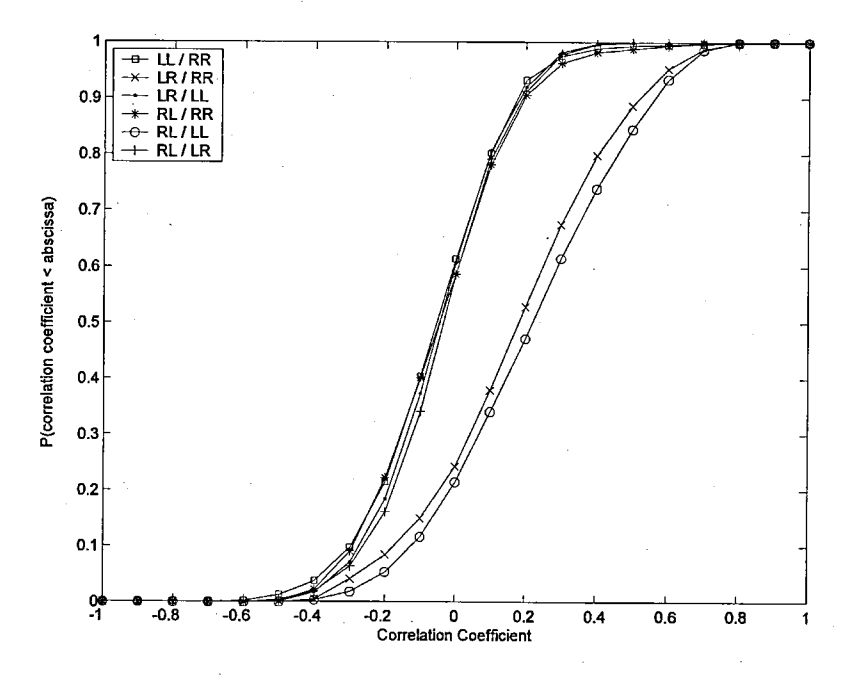


Fig. 6-12 Cumulative distributions of MIMO channel correlation coefficients in tree-lined road environment

Suburban environment

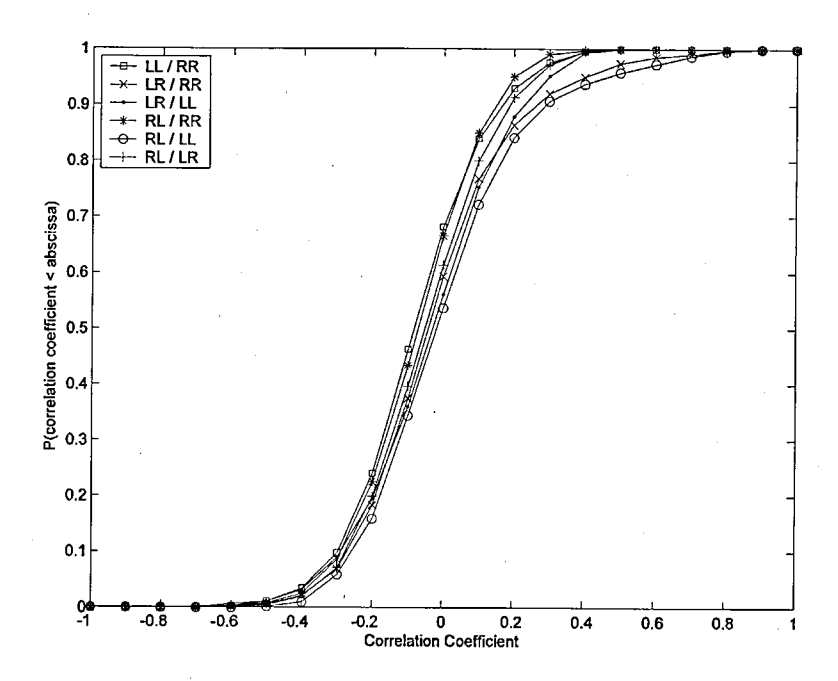


Fig. 6-13 Cumulative distributions of MIMO channel correlation coefficients in suburban environment

Urban Environment

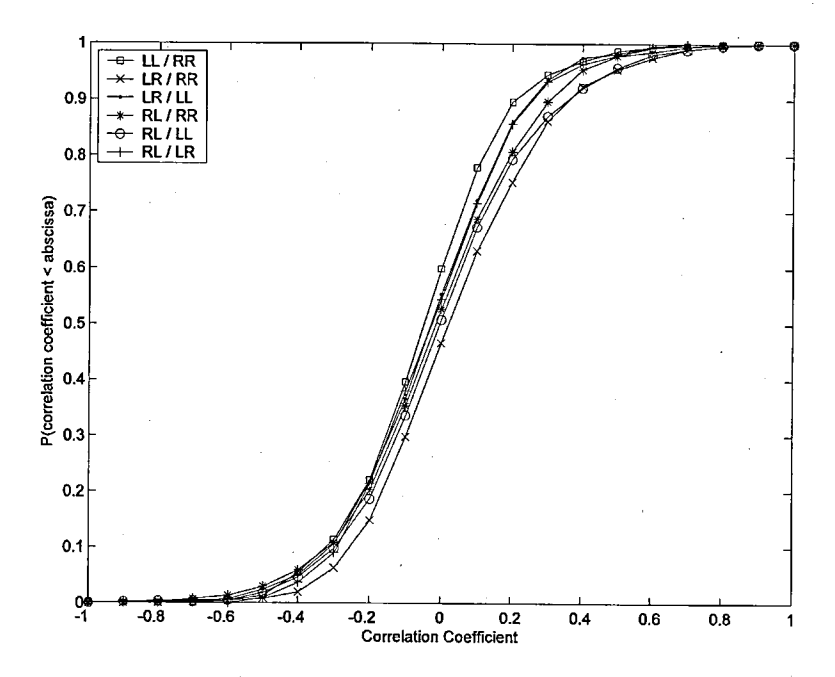


Fig. 6-14 Cumulative distributions of MIMO channel correlation coefficients in urban environment

In these figures, the terminology LR/RL for example refers to the correlation between the LHCP(TX)-RHCP(RX) channel and the RHCP(TX)-LHCP(RX) channel.

6.1.4 Combined large and small scale characteristics

Some analysis is best performed on the measured data direct, as this includes both the large scale and small scale fading components combined. This section presents details of the distribution, cross-polar discrimination, and second order statistics of the narrowband measured data.

Distribution

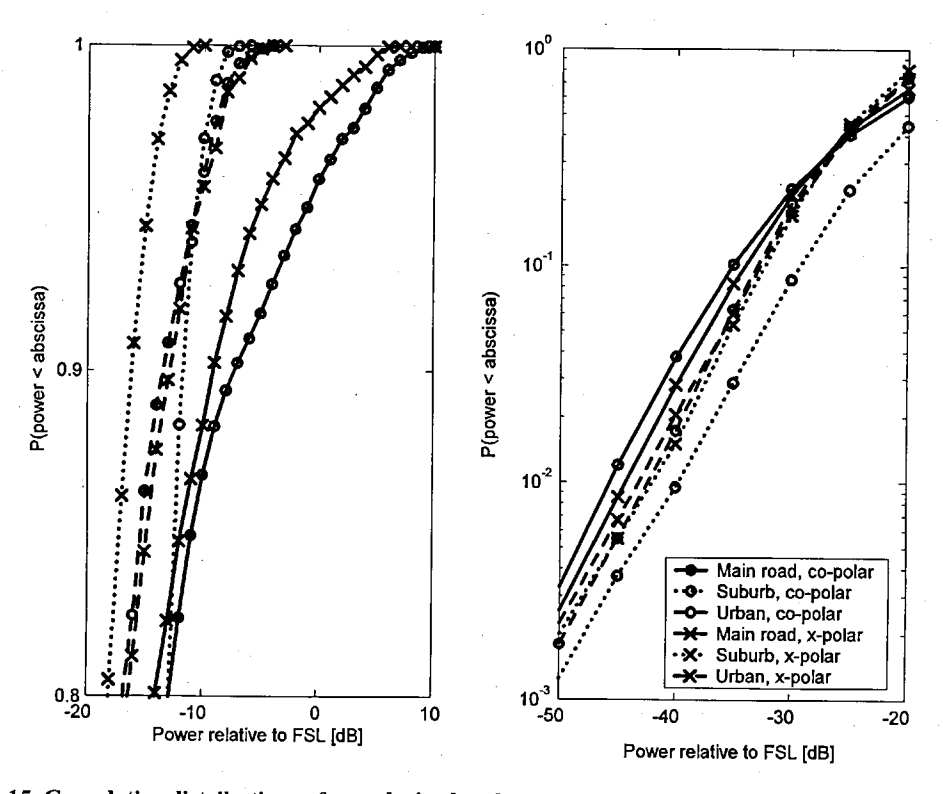


Fig. 6-15 Cumulative distributions of co-polarized and cross-polarized components in each environment

The cumulative distribution of co-polarized and cross-polarized components in each environment is shown in Fig. 6-15. The sub-plot on the left shows the top tail of the distribution at high received power levels, whereas the sub-plot on the right shows the distribution at low power levels. It can be observed that some tree-lined road channels are higher than free space loss, and that all the channels in the suburban and urban environments are less than free space loss. In the tree-lined road case, both co- and cross-polarized channels are of similar strengths except around free space loss, where co-polarized channels are higher power. For the suburban environment, co-polarized channels are always a few decibels higher than the cross-polarized channels for all signal strengths. Co- and cross-polarized channels are of similar strengths for all power levels, in the urban case.

Cross polar discrimination and cross polar isolation

Cross polar discrimination (XPD) is a measure of how much of a signal in a given polarization is scattered into the opposite polarization by the medium alone. Cross polar isolation (XPI) shows how much two signals of opposite polarizations transmitted simultaneously will interfere with each other at the receiver.

They can be expressed in terms of the time averaged electric field E terms:

$$XPD = 10\log\frac{\overline{E_{ac}^2}}{\overline{E_{ax}^2}} \qquad XPI = 10\log\frac{\overline{E_{ac}^2}}{\overline{E_{bx}^2}}$$
(6-7)

where the E terms are defined in Fig. 6-16.

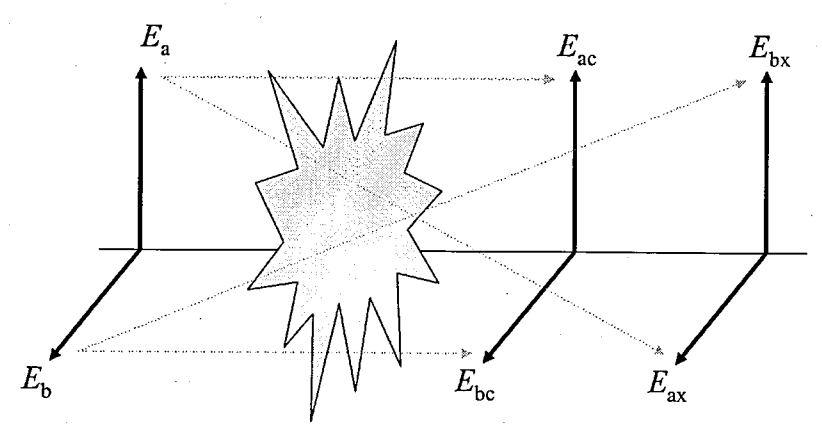


Fig. 6-16 Definitions of XPD and XPI

The dual polarized 2x2 MIMO channel was split into blocks of 40 wavelengths. Each block was tested for XPD and XPI. The cumulative distributions of XPD and XPI are shown in Fig. 6-17 (road), Fig. 6-18 (suburban) and Fig. 6-19 (urban). The distributions are centred on their median values. Table 8 (road), Table 9 (suburban) and Table 10 (urban) show the mean, median and standard deviations of the data.

Tree-lined road environment

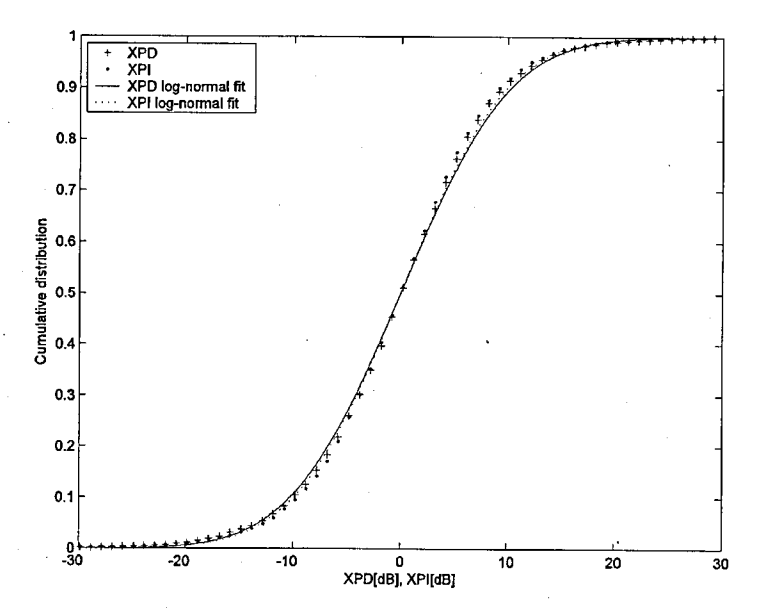


Fig. 6-17 Cumulative distributions of XPD and XPI for road environment (normalized to median)

component	mean	median	sigma
XPD	0.74dB	0.83dB	8.0dB
XPI	0.70dB	0.80dB	7.8dB

Table 8 XPD and XPI statistics for road environment

Suburban environment

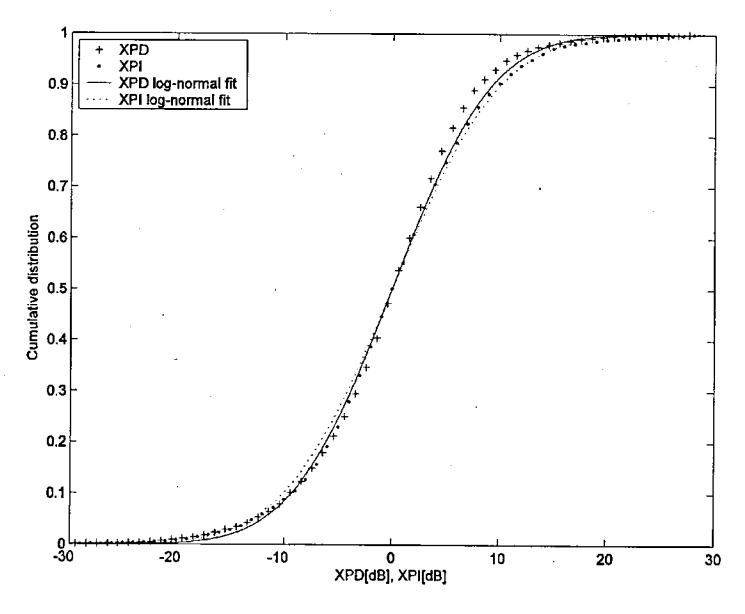


Fig. 6-18 Cumulative distributions of XPD and XPI for suburban environment (normalized to median)

component	mean	median	sigma
XPD	2.2dB	2.4dB	7.3dB
XPI	2.2dB	2.0dB	7.9dB

Table 9 XPD and XPI statistics for suburban environment

Urban environment

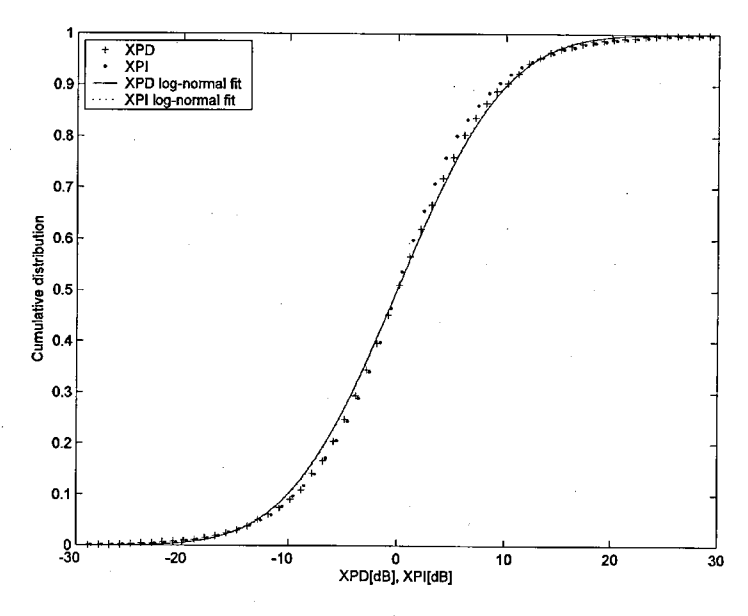


Fig. 6-19 Cumulative distributions of XPD and XPI for urban environment (normalized to median)

component	mean	median	sigma
XPD	-0.1dB	-0.2dB	7.9dB
XPI	-0.4dB	-0.4dB	7.8dB

Table 10 XPD and XPI statistics for urban environment

These findings suggest only around 10% of channels have a cross-polar discrimination greater than +10dB. A high cross-polar discrimination channel lends itself well to independent dual polarization coding with interference cancellation. The channel would benefit from polarization time coding in the remaining 90% of channels. Establishing the optimum channel coding for each channel would be a useful area of future work.

Second order statistics

Theoretical derivations of LCR and AFD for a Rayleigh channel were given in chapter 2. In general the LCR, N_R , the number of crossings per second, for a wide sense stationary random process is given as:

$$N_R(R) = \int_0^\infty \dot{r} p(R, \dot{r}) d\dot{r} \tag{6-8}$$

where the dot indicates the time derivative and $p(R, \dot{r})$ is the joint probability density function of \dot{r} and r at r = R. The AFD is the average length of a fade below a specified level R, and is given by:

$$L_R(R) = \frac{\Pr[r \le R]}{N_R(R)} \tag{6-9}$$

where $\Pr[r \le R]$ is the cumulative distribution function (CDF) probability at r = R, and $N_R(R)$ is the LCR. The following section presents the normalized LCR and AFD of the measurement campaign data for co- and cross-polarized channels in each environment.

Level crossing rate

The following graphs present the level crossing rate which was extracted from the measured narrowband data. In each case, the data is normalized to the maximum Doppler frequency, $f_{\rm m}$. As described earlier in this chapter, this was (8.941/0.122) = 73Hz for the tree-lined road case and (5.6/0.122) = 46Hz for the suburban and urban environments.

Tree-lined road environment

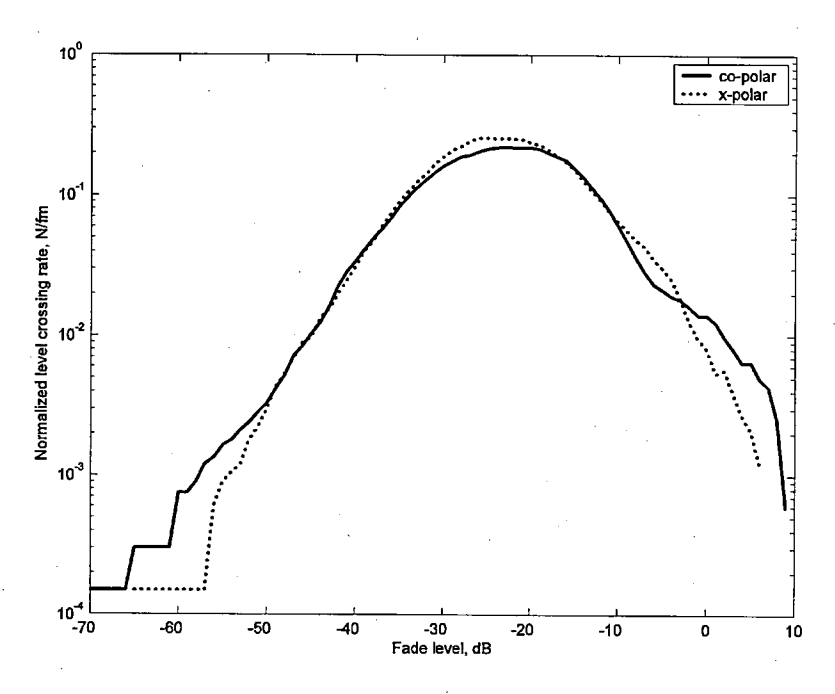


Fig. 6-20 Normalized level crossing rate in tree-lined road environment

Suburban environment

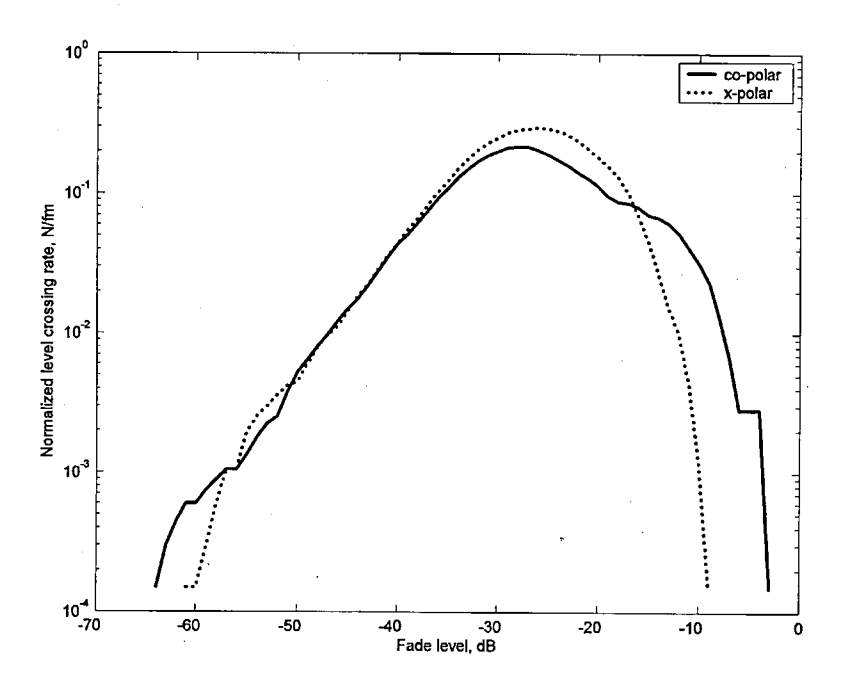


Fig. 6-21 Normalized level crossing rate in suburban environment

Urban environment

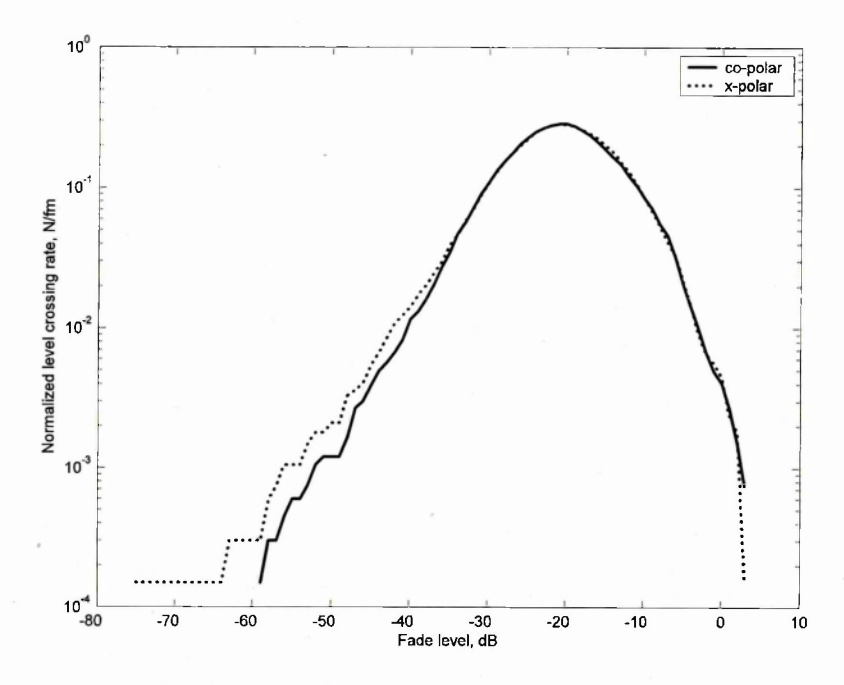


Fig. 6-22 Normalized level crossing rate in urban environment

Observations

Level crossing rates are shown in Fig. 6-20 (road), Fig. 6-21 (suburban) and Fig. 6-22 (urban). The maximum Doppler frequency, $f_{\rm m}$ in the measurement campaign was 73Hz, 46Hz and 46Hz in the tree-lined road, suburban and urban environments respectively. The maximum level crossing rate of co- and cross-polarized channels is shown in Table 11

	1.00		100	N1/6	<u> </u>	0 . /		
	LCR ma	aximum	LCR,	N/tm	Crossings/sec			
57.5	co-polar x-polar		co-polar	x-polar	co-polar	x-polar		
road	-22dB	-24dB	0.22	0.23	16.1	16.8		
suburb	-28dB	-26dB	0.22	0.30	10.1	13.8		
urban	-21dB	-21dB	0.30	0.30	13.8	13.8		

Table 11 Maximum level crossing rate

At the other extreme of level crossing rate, it is also of interest to quantify the LCR at the maximum signal level, and this is shown in Table 12

	Maximum level		LCR, N/fm		Crossings/min	
4.5	co-polar	x-polar	co-polar	x-polar	co-polar	x-polar
road	9dB	6dB	0.00060	0.00120	2.63	5.26
suburb	-3dB	-9dB	0.00013	0.00013	0.36	0.36
urban	3dB	3dB	0.00070	0.00013	1.93	0.36

Table 12 Level crossing rate at maximum signal level

It is also worth noting that these normalized LCR curves are comparable with those presented by [Loo85], except the present campaign had far greater dynamic range.

Average fade duration

Tree-lined road environment

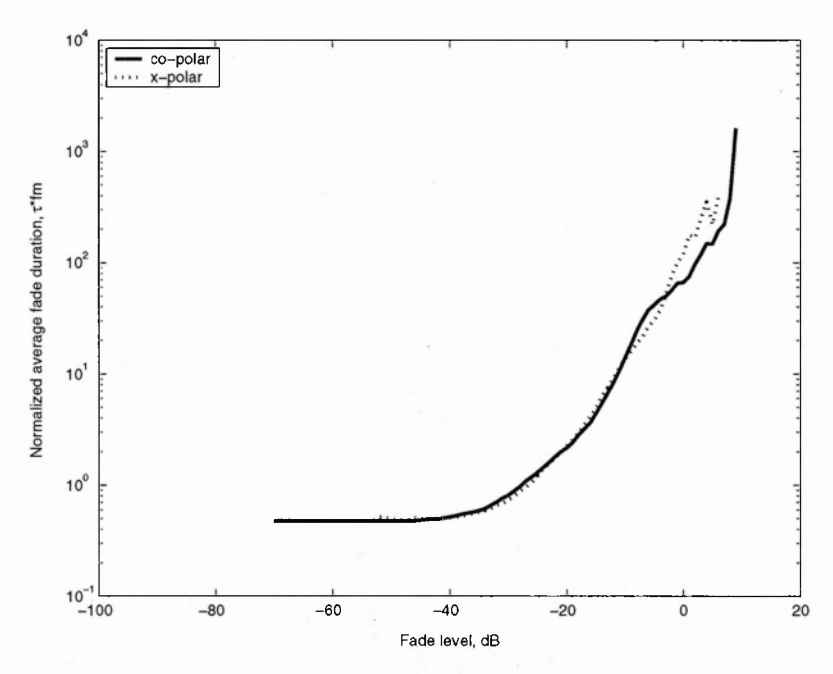


Fig. 6-23 Normalized average fade duration in tree-lined road environment

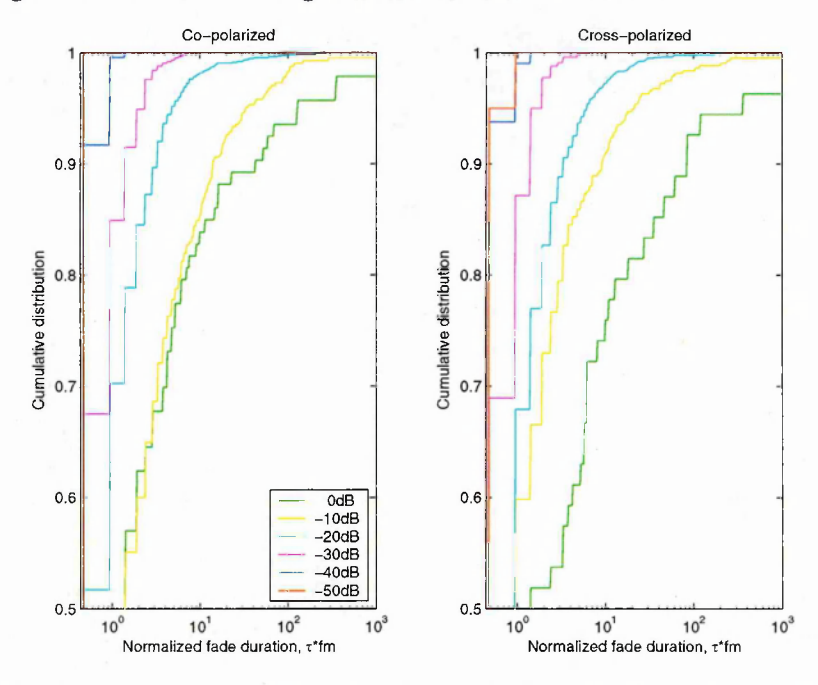


Fig. 6-24 Normalized fade duration cumulative distributions in tree-lined road environment

Suburban environment

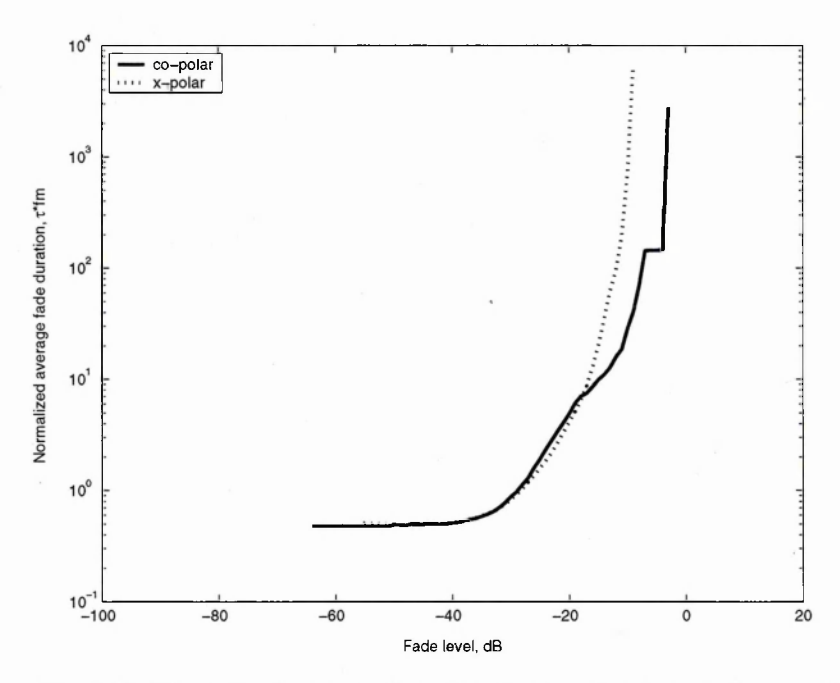


Fig. 6-25 Normalized average fade duration in suburban environment

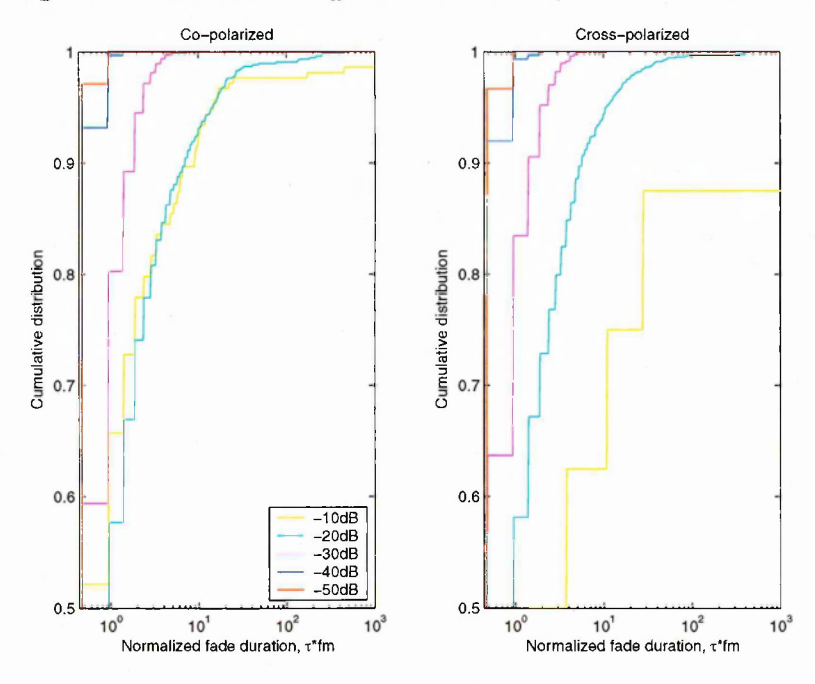


Fig. 6-26 Normalized fade duration cumulative distributions in suburban environment

Urban environment

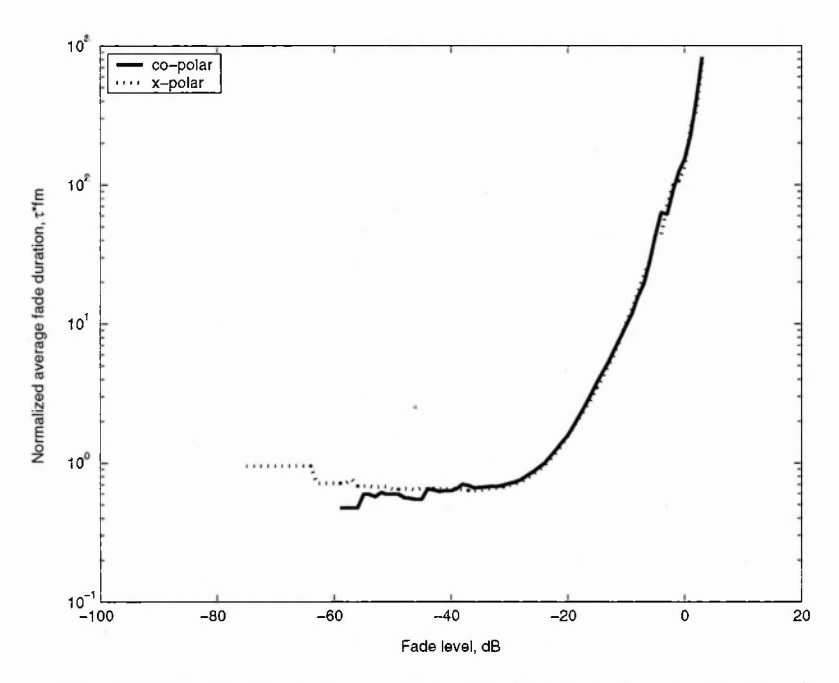


Fig. 6-27 Normalized average fade duration in urban environment

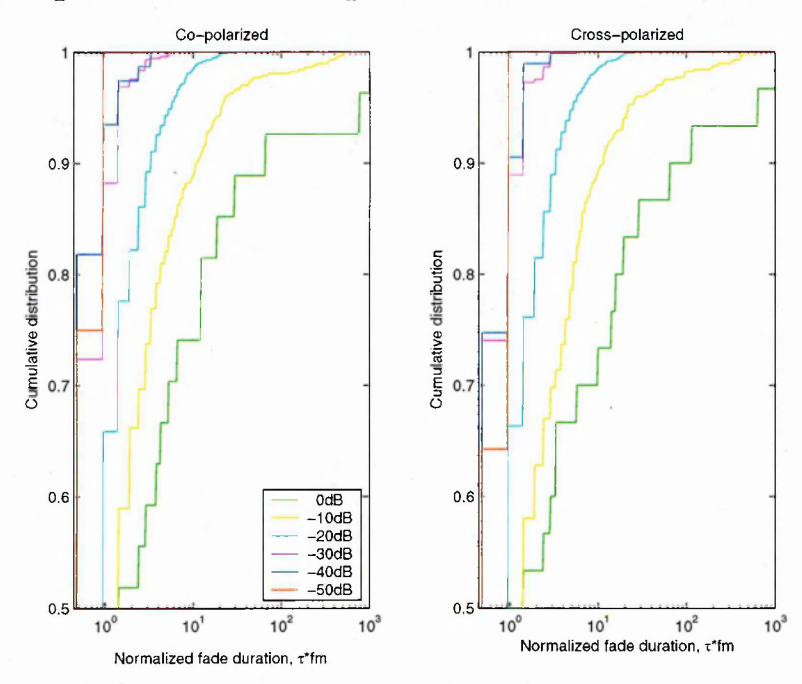


Fig. 6-28 Normalized fade duration cumulative distributions in urban environment

Observations

Normalized average fade durations are shown in Fig. 6-23 (road), Fig. 6-25 (suburban) and Fig. 6-27 (urban). Normalized fade duration cumulative distributions are shown in Fig. 6-24 (road), Fig. 6-26 (suburban) and Fig. 6-28 (urban). The maximum Doppler frequency, fm in the measurement campaign was 73Hz, 46Hz and 46Hz in the tree-lined road, suburban and urban environments respectively.

•	AFD maximum		AFD, $\tau * fm$		AFD, τ [secs]	
	co-polar	x-polar	co-polar	x-polar	co-polar	x-polar
road	9dB	6dB	2000	400	27	5.5
suburb	-3dB	-9dB	3000	6000	65	130
urban	3dB	3dB	800	800	17	17

Table 13 Maximum average fade duration

	AFD at -20dB		AFD, τ * fm		AFD, τ [ms]	
,	co-polar	x-polar	co-polar	x-polar	co-polar	x-polar
road	-20dB	-20dB	2	2	27	27
suburb	-20dB	-20dB	5	4	109	87
urban	-20dB	-20dB	1.3	1.3	28	28

Table 14 Average fade duration at -20dB level

Table 13 shows the maximum average fade duration in normalized and un-normalized form using the actual Doppler frequencies in the measurement campaign (for interest). This gives the system designer the ability to estimate the length of a maximum fade, which is useful when designing fade mitigation techniques.

Table 14 shows the average fade duration at -20dB, which is a possible level towards the lower end of the link budget range. It informs the system designer about the likely fade durations at small levels of link budget margin.

6.2 Wideband LMS-MIMO characteristics

6.2.1 Large scale characteristics

In this section, wideband large scale fading properties are reported. Fading distribution, temporal variations and correlation over the delay and MIMO channel domains are addressed.

Distribution

The following wideband analysis follows a similar approach to that used for the narrowband data and the approach is repeated here for clarity. The time series wideband measured data was averaged by a sliding window time technique in each delay bin, adhering to the Rayleigh criteria (120 data points over 40 wavelengths) [Lee74]. A probability density histogram of the large scale fading level was obtained in each delay bin. Initial observations showed that in general, earlier delay bins and always the first delay bin exhibited probability densities appearing as two adjacent and overlapping log-normally distributed segments, an example of which is shown in Fig. 6-29. This is intuitive as the earlier delay bins will have a higher proportion of LOS components in addition to the NLOS components.

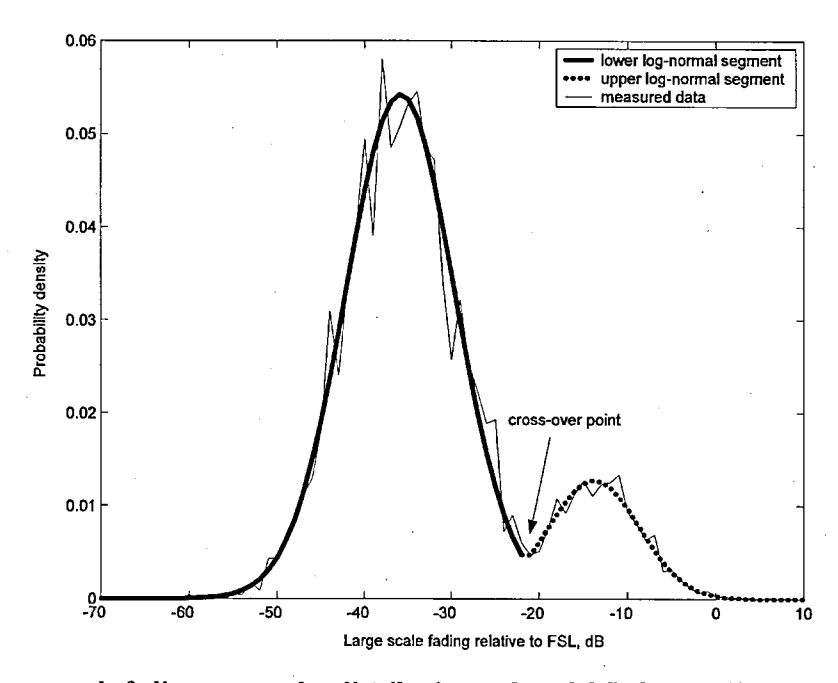


Fig. 6-29 Large scale fading cross-polar distribution and model fit for tree-lined road environment

Whereas, later delay bins exhibited probability densities that appeared as a single log-normal distribution. A model based on these observations was then tested. Each cumulative distribution segment was tested in turn for goodness-of-fit to the theoretical log-normal or two adjacent and overlapping log-normally distributed segments using the Kolmogorav – Smirnoff test [Mas51]. In the

case of adjacent and overlapping log-normal distributions, the K-S test was applied as follows. Initially the cross-over point was identified at the local minima between the two distributions and then each segment on either side of the cross-over point was tested in turn. Each segment of the experimental data was matched to the equivalent theoretical log-normal segment. Since the two distributions were overlapping, the K-S test could only be applied to the visible part of the distribution.

In all cases, the single distributions were found to be log-normal at the 1% statistical significance level. For the two overlapping distributions, they were also both found to be log-normal at the 1% statistical significance level for the visible part of the distribution. The probability density function of the two overlapping log-normal distribution model can be formulated as follows (repeated here for clarity):

$$p(s) = \begin{cases} \frac{P_u}{\sqrt{2\pi} \sigma_u} exp \left[-\frac{1}{2} \left(\frac{s - \mu_u}{\sigma_u} \right)^2 \right] / \left[1 - \frac{1}{2} \left[1 + erf \left(\frac{x - \mu_u}{\sigma_u \sqrt{2}} \right) \right] \right] &, \quad s > x \\ \frac{P_l}{\sqrt{2\pi} \sigma_l} exp \left[-\frac{1}{2} \left(\frac{s - \mu_l}{\sigma_l} \right)^2 \right] / \frac{1}{2} \left[1 + erf \left(\frac{x - \mu_l}{\sigma_l \sqrt{2}} \right) \right] &, \quad s \le x \end{cases}$$

$$(6-10)$$

where s is the large scale fading level (dB), x is the cross-over point (dB), σ_u and σ_l are the standard deviations (dB) for the upper and lower log-normal components respectively. The means (dB) for the upper and lower log-normal components are μ_u and μ_l respectively. The probability of the large scale signal level residing in the upper log-normal component is given by P_u . The probability of the large scale signal level residing in the lower log-normal component or at the cross-over point is given by P_l . The term erf is the error function.

The results are shown in Fig. 6-30 (tree-lined road), Fig. 6-31 (suburban) and Fig. 6-32 (urban). Each figure shows the mean and plus-and-minus one standard deviation of the co- and cross-polarized log-normal distributions in each 10ns delay bin. The same presentation is used for the dual log-normal case, which also shows the cross-over points between the two log-normal distributions by the dashed line. Beneath the lower of each dual log-normal delay bin is stated the probability of samples residing in the lower log-normal segment for co-/cross-polarized channels.

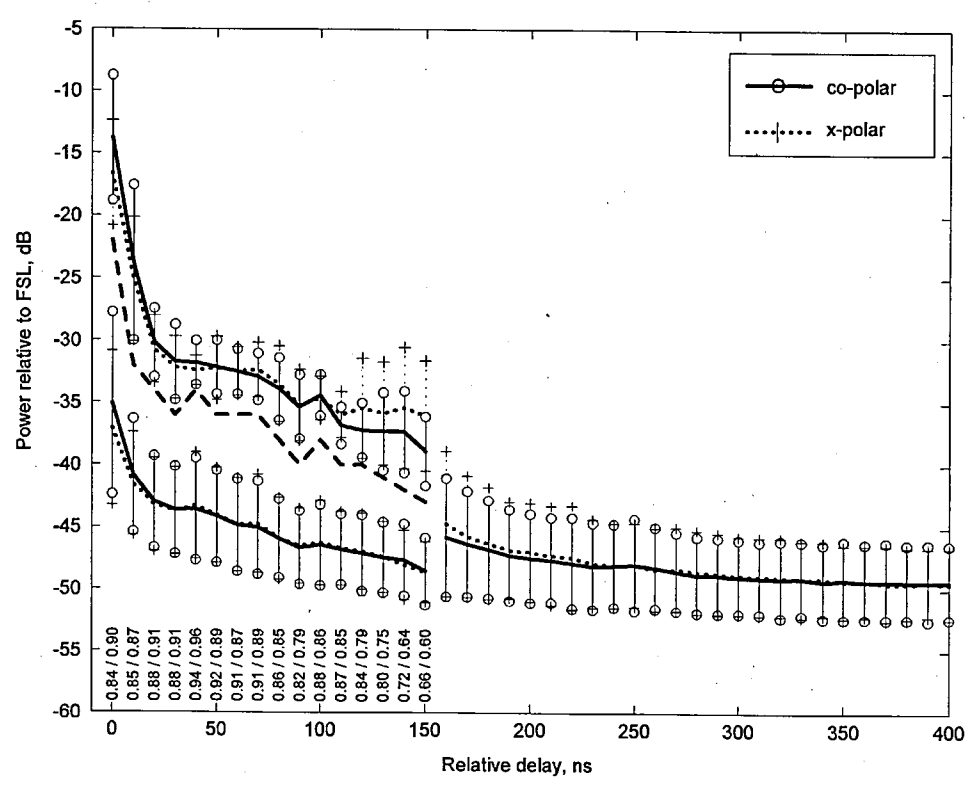


Fig. 6-30 Mean power versus excess delay profile and standard deviation for large scale fading in tree-lined road environment

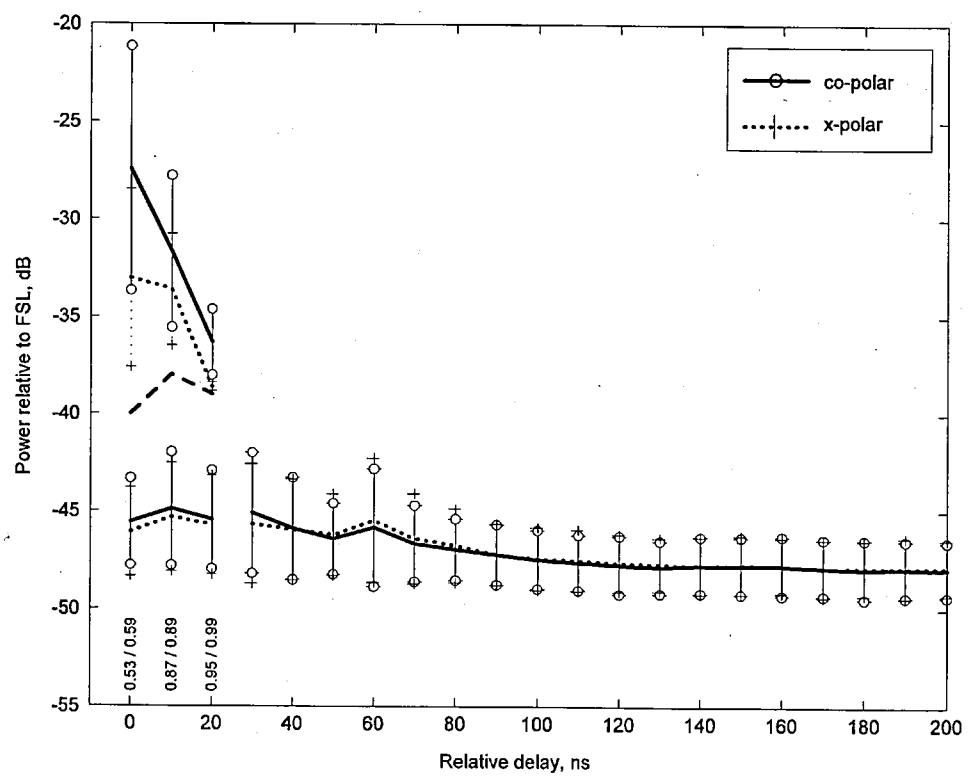


Fig. 6-31 Mean power versus excess delay profile and standard deviation for large scale fading in suburban environment

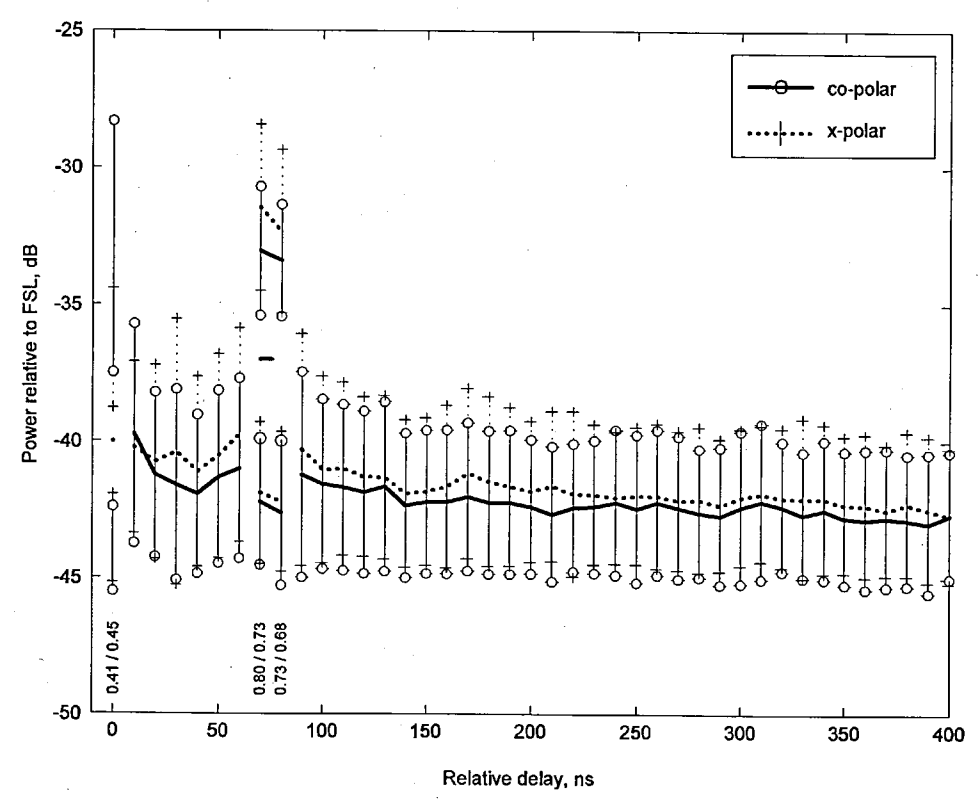


Fig. 6-32 Mean power versus excess delay profile and standard deviation for large scale fading in urban environment Temporal variations

To describe the temporal variations, the large scale autocorrelation functions were obtained for every delay bin for co- and cross-polarized channels in each environment and the coherence distance at the 1/e point was found. The normalized autocorrelation function, repeated here for clarity can be defined [Pee01] as:

$$\rho(\tau) = \frac{E(\alpha(t)\alpha^{*}(t+\tau))}{E(|\alpha(t)|^{2})}$$
(6-11)

where E[.] is the expectation, $\alpha(t)$ is the complex fading signal and τ is the delay separation. The shadowing autocorrelation function was found to follow accurately a decaying exponential as suggested in [Mar90], [Gud91].

The coherence distance for the first delay bin for co-/cross-polarized channels was 29/31m for tree-lined road, 132/160m for suburban and 204/291m for the urban environment. This was found to increase with excess delay. For example for the tree-lined road case, the coherence distance for co-/cross-polarized channels was 56/75m at 50ns excess delay, 92/104m at 100ns excess delay and 198/240m at 200ns excess delay.

Delay domain correlation

The correlation coefficient between two signals, $\alpha_A(t)$ and $\alpha_B(t)$ is defined as [Pee01] (repeated here for clarity):

$$\rho_{AB} = \frac{E[(\alpha_A(t) - \mu_A)(\alpha_B(t) - \mu_B)^*]}{\sigma_A \sigma_B}$$
(6-12)

where E[.] is the expectation, μ_A , μ_B are the means and σ_A , σ_B are the standard deviations of $\alpha_A(t)$ and $\alpha_B(t)$. Large scale fading correlation coefficients were obtained between each pair of bins in the delay domain.

In Fig. 6-33, the average correlation coefficient plus and minus one standard deviation between all pairs with the same delay separation is shown for co- and cross-polarized components in each environment. As expected, increased delay separations have a lower correlation coefficient, since this implies a longer and different shadowing path.

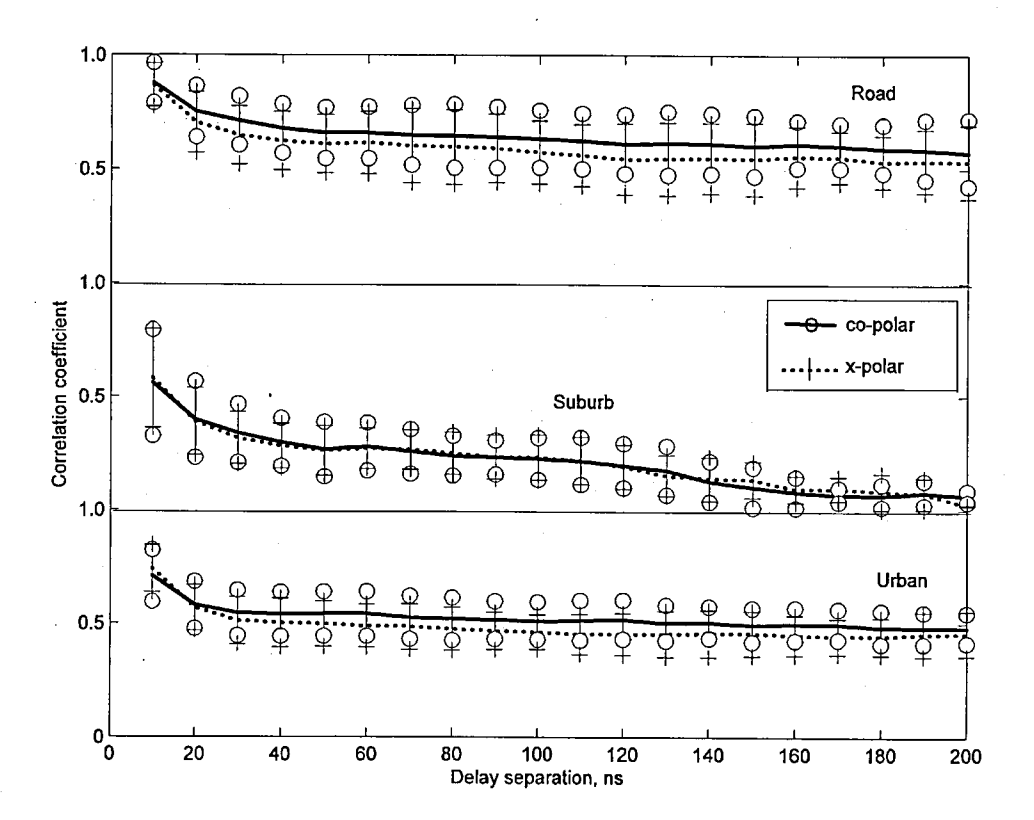


Fig. 6-33 Large scale fading correlation versus delay separation

MIMO channel correlation

The large scale fading correlation coefficient was also found between MIMO channels as a function of excess delay, and is shown in Fig. 6-34 for the tree-lined road, suburban and urban environments. In the figure, the terminology LR/RL for example refers to the correlation between the LHCP(TX)-RHCP(RX) channel and the RHCP(TX)-LHCP(RX) channel.

A strong correlation was found between MIMO channels for lower excess delays implying that the channels follow a similar shadowing path. However, in general, higher excess delays exhibited lower correlation between MIMO channels, implying that the channels follow an increasingly different shadowing path.

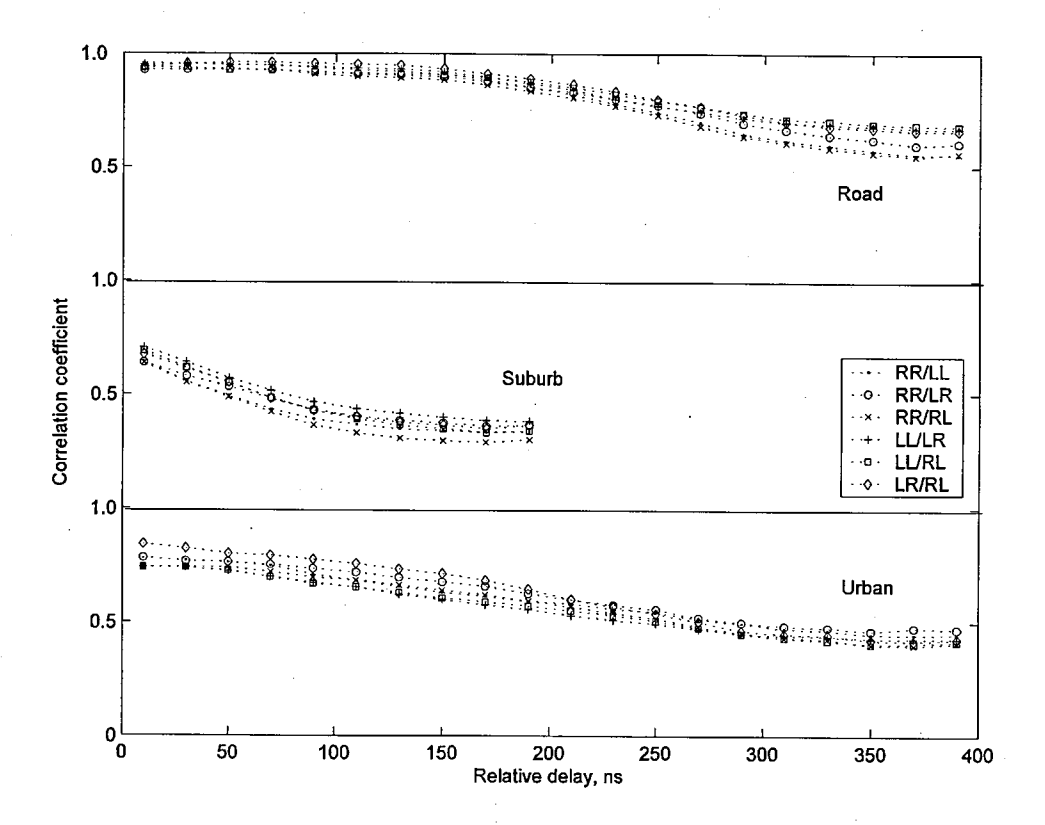


Fig. 6-34 Large scale MIMO channel correlation coefficient over delay domain

6.2.2 Small scale characteristics

In this section, the wideband small scale fading properties are reported. Fading distribution, with its conditioning on large scale fading, power delay profile, temporal variations, and correlation over the delay and MIMO channel domain are addressed.

Distribution

The large scale fading was split into temporal windows of 180 samples over 60 wavelengths. The average power in each window was subtracted from the measured data revealing the small scale fading. The cumulative distribution of the experimental small scale fading in each temporal window and each 10ns delay bin was tested against the theoretical Ricean cumulative distribution. The probability density of the Ricean distribution can be formulated [Cor94] as (repeated here for clarity):

$$p_{R}(r) = 2r(K+1) \exp\left[-r^{2}(K+1) - K\right] I_{0}\left(2 r \sqrt{K(K+1)}\right) \qquad (r \ge 0)$$
 (6-13)

where K is the Rice factor defined as the ratio of direct path power to diffuse multipath power. The function I_0 is the modified Bessel function of the first kind and zeroth order. Every time window in each delay bin for co- and cross-polarized channels in each environment was checked against the theoretical Ricean distribution. The Kolmogorav – Smirnoff test was used to check the validity of the Ricean fit and it was found that every bin was Ricean distributed at the 1% statistical significance level. By optimizing the theoretical distribution to the measured distribution also revealed the Rice K factor that best described the data in each window and delay bin.

A scattergram was obtained of Rice K factor versus shadowing level for each delay bin, and the correlation coefficients were found. Moderate correlations were found in the first delay bin for the tree-lined road and suburban environments only; no significant correlation was found in the first delay bin for the urban environment. In all environments, no significant correlation was found in any delay bin from 10ns and above. Direct path correlation coefficients for co-/cross-polarized channels were 0.66/0.72 for the tree-lined road, and 0.38/0.42 for the suburban environment.

Since a moderate correlation was found for the tree-lined road and suburban cases, a polynomial fitting was carried out. A scattergram of the direct path for the tree-lined road and suburban cases along with polynomial fitting for each polarization is shown in Fig. 6-35 and Fig. 6-36.

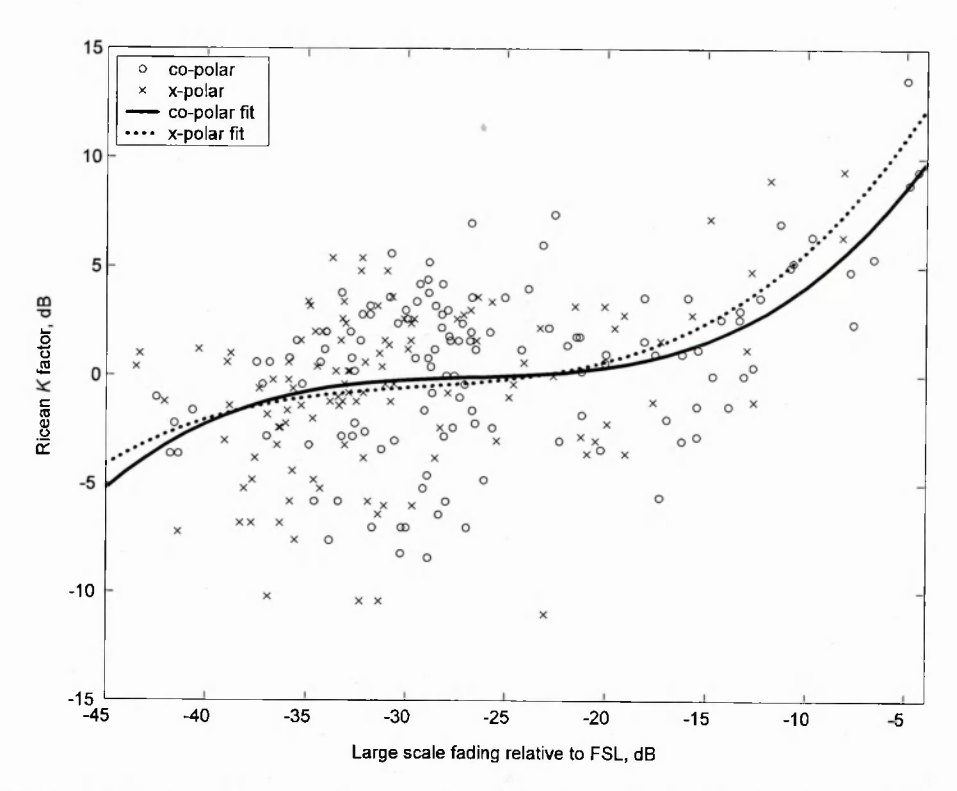


Fig. 6-35 Rice K factor conditioning on large scale fading for direct path in tree-lined road environment

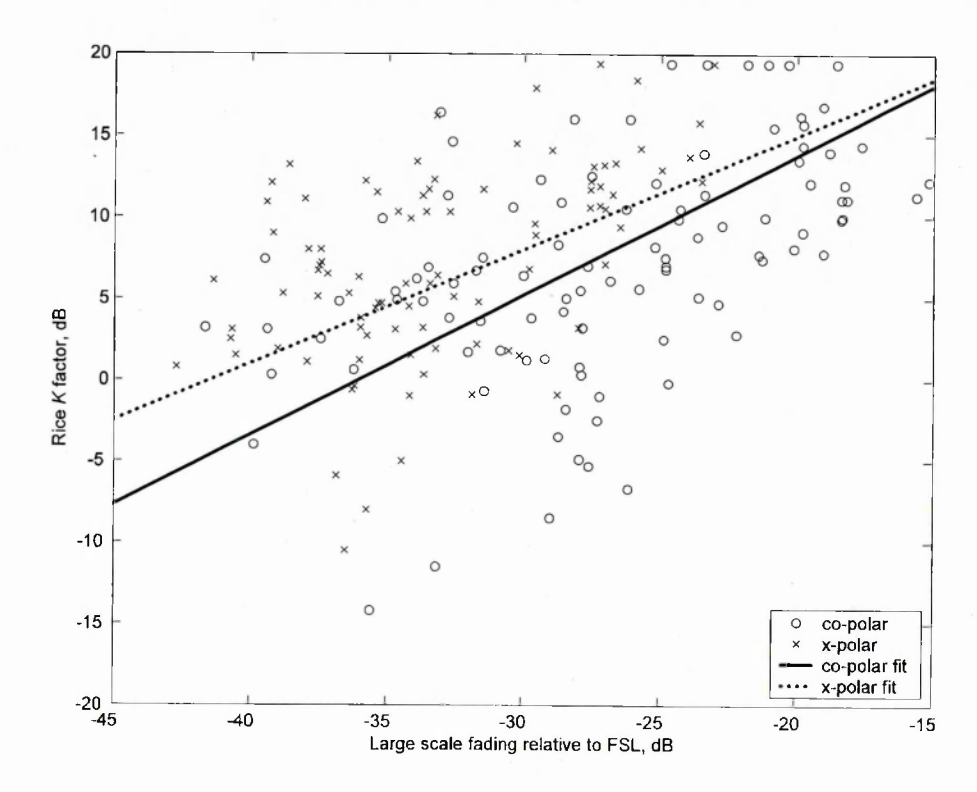


Fig. 6-36 Rice K factor conditioning on large scale fading for direct path in suburban environment

Polynomial fitting interpolation was carried out using the following formula:

$$K_{dB}(S_{dB}) = \mu_0 + \mu_1 S_{dB} + \mu_2 S_{dB}^2 + \mu_3 S_{dB}^3$$
 (6-14)

Coefficients for co- and cross-polarized channels for road and suburban environments are given in Table 15. The root-mean-squared errors (RMSE) were obtained between the measured data and fitted curves for linear, quadratic and cubic polynomials. The cubic polynomial incurred the minimum RMSE and closely resembled the high K factors found at lower levels of shadowing for the tree-lined road case. The linear fitting incurred minimal RMSE and closely resembled the K factor trends for the suburban case. Using higher order polynomials did not suggest a benefit in RMSE. The RMSE in co-/cross-polarized channels was 3.6/3.6 and 5.2/4.5 in the tree-lined road and suburban environments respectively. The polynomial can be used in the modelling process.

		μ_{o}	μ_1	μ_2	μ_3	Valid range
Road	Co-polar	15.7	1.7	0.062	0.0008	-45 <s<sub>dB<0</s<sub>
	X-polar	18.7	1.83	0.06	0.0007	-45 <s<sub>dB<0</s<sub>
Suburb	Co-polar	31	0.86	0	0	-40 <s<sub>dB<-15</s<sub>
	X-polar	29	0.7	0	0	-40 <s<sub>dB<-15</s<sub>
Urban	Co-polar	Weak correlation only Weak correlation only				
	X-polar					

Table 15 Rice K factor polynomial parameters

The Rice K factor was also analysed in the delay domain. The distribution remained Ricean in each 10ns delay bin, with varying K factor in each temporal window. Insufficient temporal data inhibited accurate calculation of the K factor distribution in each delay bin, although the narrowband channel K factor was shown by the authors in [Kin06b] to be log-normally distributed. The mean of the mean K factor for channels between 10ns and 200ns in all environments was found to be -1.0dB, and the mean of the standard deviation was 3.3dB, which can be used during a modelling procedure.

With these values it is therefore now possible to model the Rice K factor in many key environments, namely tree-lined road, suburban and urban. In the urban environment the lack of polynomial to describe the Rice K factor dependency on large scale fading is as expected, as the received signal is predominantly made from local multiple reflections and is therefore much harder to model in a generic fashion.

Temporal variations

The small scale autocorrelation functions were found from each temporal window (representing 10m of distance) in each delay bin, for co- and cross-polarized channels in each environment. Cumulative distributions of coherence time (at the $1/\sqrt{2}$ correlation point) were then obtained in each delay bin. It was found that coherence time reduced with increasing delay, i.e. the small scale fading is more rapid at higher excess delays. For example, the median normalized coherence time (τf_d , where f_d is the maximum Doppler frequency), for co-polarized tree-lined road channels, was 0.86 at 0ns, decreasing to 0.44 at 10ns, 0.28 at 20ns and 0.18 at 30ns. Higher excess delays had similar coherence times to the 30ns delay point. Cross-polarized channels also had similar median coherence times and decay versus excess delay curves.

The same effect can be represented by the Doppler spectrum. The small scale Doppler spectrum was found for each temporal window in each delay bin for co- and cross-polarized channels in each environment. An example plot of four delay bins (0ns, 50ns, 100ns and 150ns) for the tree-lined road case is shown in Fig. 6-37. Each subplot shows the normalized Doppler spectrum variation in the temporal domain. Power is presented relative to the peak level in the 0ns delay bin. It can be observed for the direct path (0ns delay bin) that the vehicle is moving towards the artificial platform at the start and moving away from the platform at the end of the run. Since the vehicle was traversing along a straight road, this shows a limitation in the measurements, which is discussed in section 6-3. The Doppler spectrum at higher relative delays showed that the direction of arrival of rays were more random in nature.

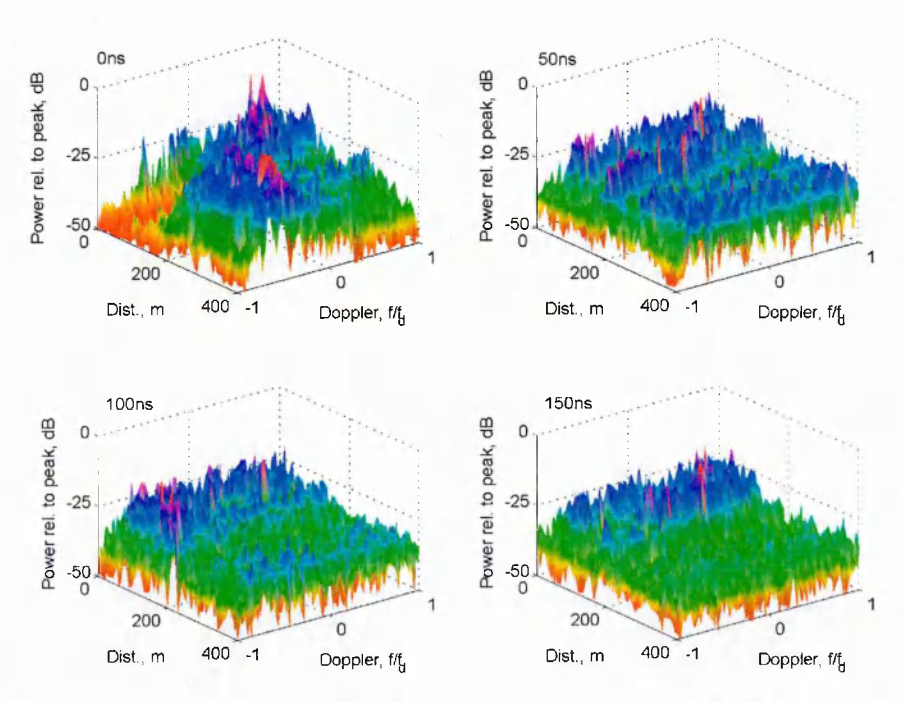


Fig. 6-37 Example Doppler spectrums in temporal domain in tree-lined road environment

Delay domain correlation

The often used hypothesis of uncorrelated scattering can also be applied to the bins in the delay domain. This is intuitive as rays arriving in each 10ns delay bin will have independent phase angles and any constructive/destructive vector addition will be uncorrelated. The average correlation coefficient for different delay separations, for co- and cross-polarized components in each environment is shown in Fig. 6-38, which suggests a weak correlation in all the small scale fading separations, except the adjacent delay bins which are loosely correlated. This result suggests uncorrelated small scale fading simulators in each delay bin may be utilized in a channel simulator implementation.

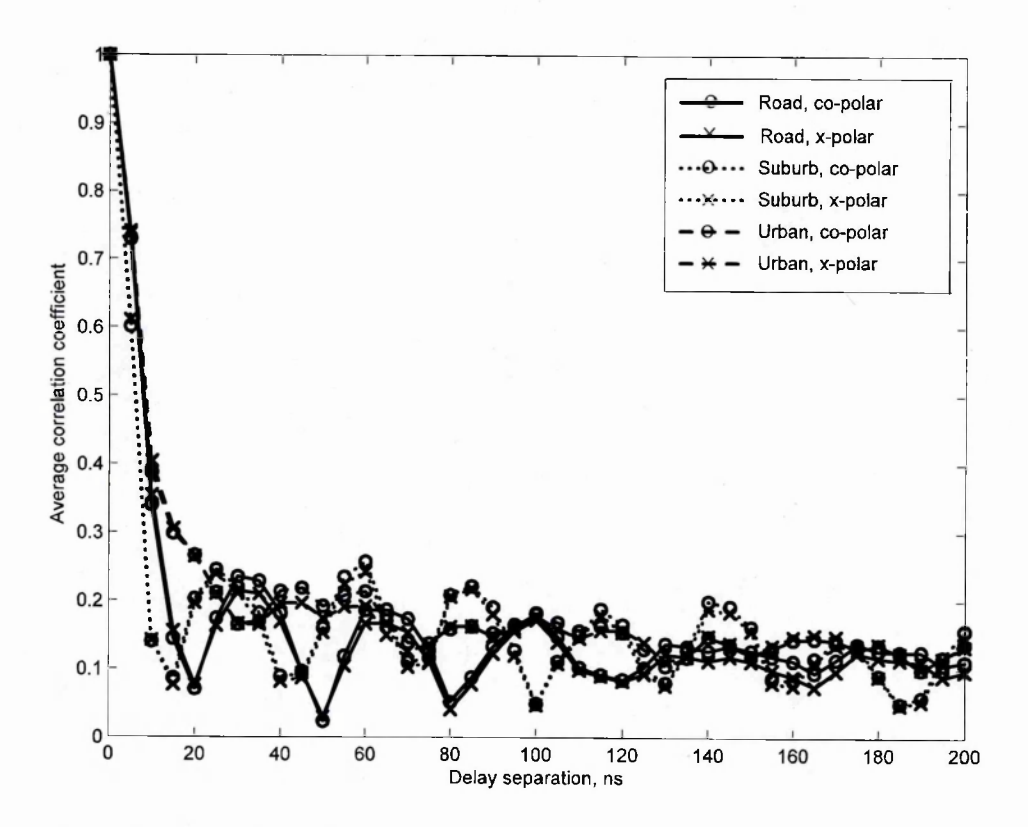


Fig. 6-38 Small scale fading average correlation coefficient over delay separation

MIMO channel correlation

Small scale correlation between MIMO channels is of primary importance for capacity analysis in MIMO systems as shown in Chapter 3. An investigation of the correlation between MIMO channels in a LMS dual polarization system and across the delay domain was also carried out. The small scale data was split into temporal windows of 10m and delay bins of 10ns. Cumulative distributions of correlation coefficients between all four channels were obtained in each window and delay bin, showing how the MIMO channel correlation coefficient varied through vehicle motion at different excess delays.

As explained earlier, repeated here for clarity, it was found that cumulative distribution correlation coefficients were allied to two distinct categories: those channels emanating from the same vehicle antenna and those not emanating from the same vehicle antenna. The results from a different vehicle antenna were in general less correlated, possibly due to the multiplicative de-correlation effect from polarization and spatial separation [Vau03].

For example, in the tree-lined road, for the 0ns delay bin, the 10/50/90% distribution points were -0.12/0.11/0.45 for different vehicle antennas increasing to 0.02/0.47/0.72 for the same vehicle antenna. Furthermore, MIMO channel correlation reduced with increasing delays. For the 50ns delay bin, the 10/50/90% distribution points were -0.1/0.03/0.22 from different vehicle antennas increasing to -0.6/0.18/0.4 for the same vehicle antenna, and -0.12/0.03/0.17 and -0.2/0.15/0.3 for the 100ns delay bin respectively.

The 10/50/90% cumulative distribution points are presented below at each delay bin, for channels emanating from the same vehicle antenna and different vehicle antenna, marked on the graphs below as 'Same' and 'Diff' respectively. These are shown in Fig. 6-39 (road), Fig. 6-40 (suburb) and Fig. 6-41 (urban).

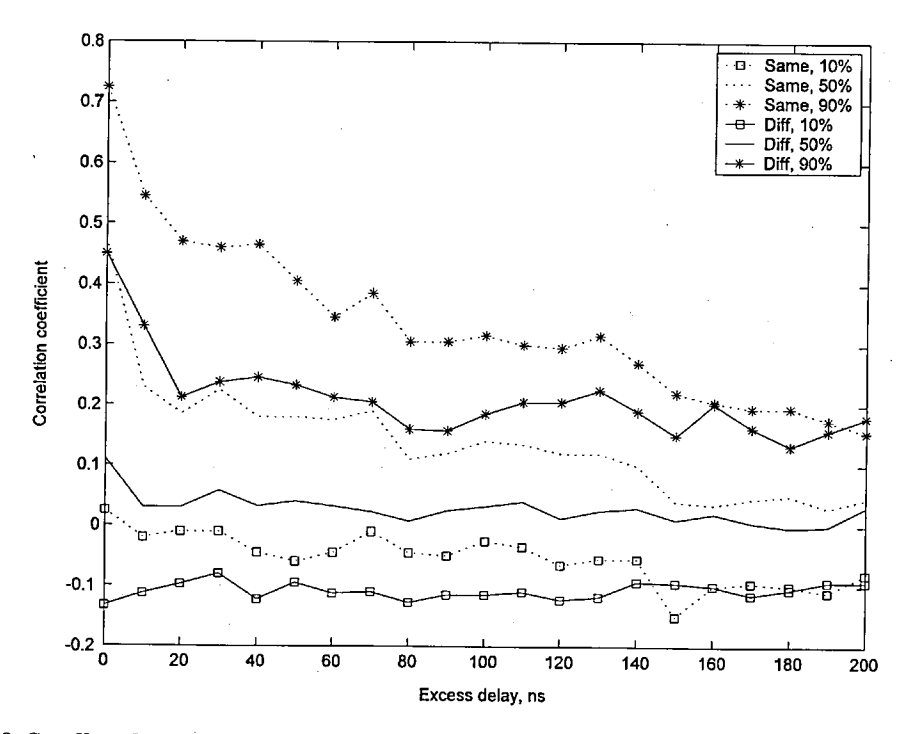


Fig. 6-39 Small scale correlation coefficient 10/50/90% distribution points versus excess delay for channels emanating from the same and different vehicle antennas in the tree-lined road environment

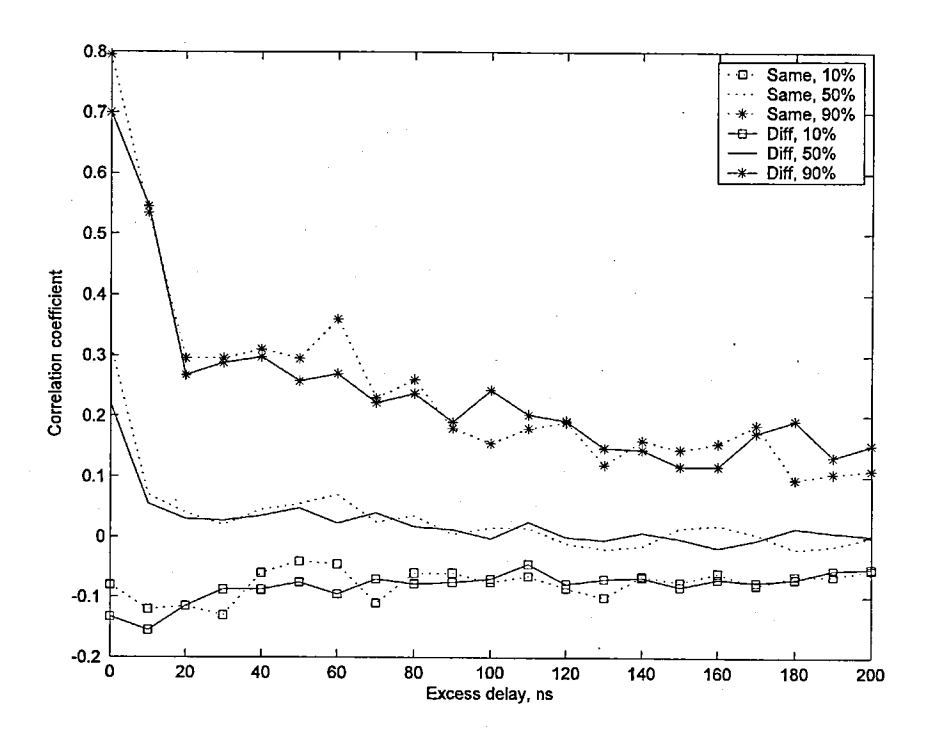


Fig. 6-40 Small scale correlation coefficient 10/50/90% distribution points versus excess delay for channels emanating from the same and different vehicle antennas in the suburban environment

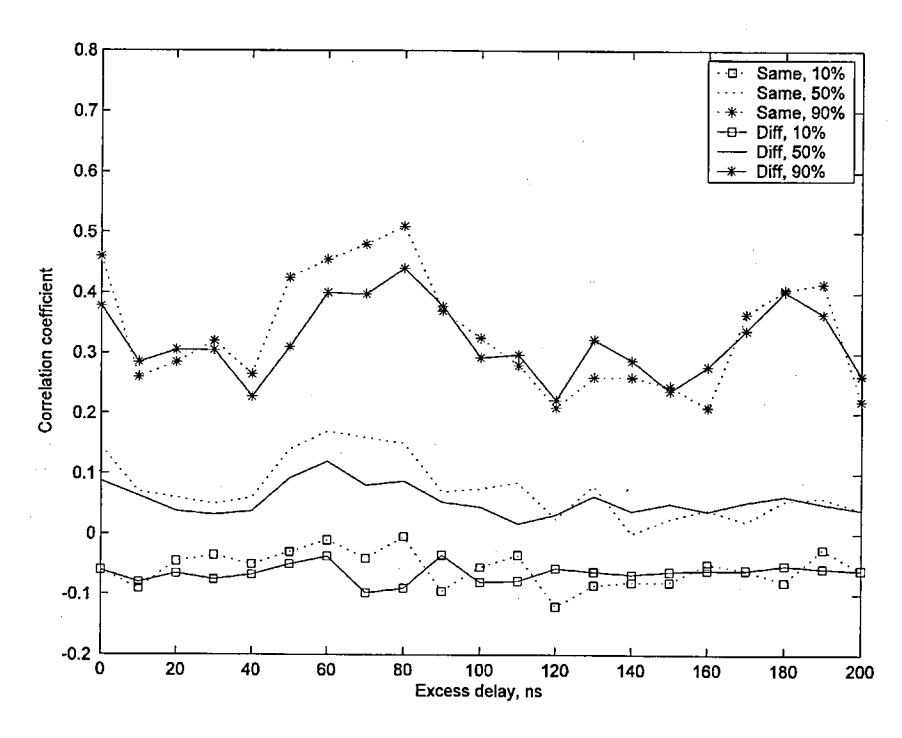


Fig. 6-41 Small scale correlation coefficient 10/50/90% distribution points versus excess delay for channels emanating from the same and different vehicle antennas in the urban environment

6.2.3 Combined large and small scale characteristics

Power delay profile

As stated in Chapter 3, the power delay profile provides the system engineer with the impulse response of the channel and its frequency response (a Fourier transform pair). This knowledge is useful as it is possible to estimate for example the maximum symbol rate without the signal being degraded beyond acceptable limits by intersymbol interference. The root mean squared (RMS) delay spread is often used in these calculations.

The mean delay and RMS delay spread of the impulse response can be calculated from the following formulations (repeated here for clarity):

$$\tau_{RMS} = \sqrt{\frac{1}{P_T} \sum_{i=1}^{n} P_i \ \tau_i^2 - \tau_o^2}$$
 (6-15)

where
$$\tau_0 = \frac{1}{P_T} \sum_{i=1}^n P_i \ \tau_i$$
 and $P_T = \sum_{i=1}^n P_i$ (6-16)

where τ_{RMS} is the RMS delay spread, τ_0 is the mean delay and P_i is the power at delay τ_i . The power delay profile in each sample was analyzed for RMS delay spread and the cumulative distributions obtained. It was found that at the 1% point the co-/cross-polarized RMS delay spreads were 5ns/6ns, 3ns/7ns, and 5ns/6ns for the tree-lined road, suburban and urban environments respectively. At the 99% point the co-/cross-polarized RMS delay spreads were 126ns/125ns, 167ns/169ns, and 167ns/168ns for the tree-lined road, suburban and urban environments respectively. The median RMS delay spreads for the co-/cross-polarized power delay profiles were 54ns/58ns, 29ns/44ns, and 63ns/58ns for the tree-lined road, suburban and urban environments respectively.

The average power delay profile for the tree-lined road, suburban and urban environments are shown in Fig. 6-42, Fig. 6-44 and Fig. 6-46 respectively. The RMS delay spread cumulative distributions for the tree-lined road, suburban and urban environments are shown in Fig. 6-43, Fig. 6-45 and Fig. 6-47 respectively.

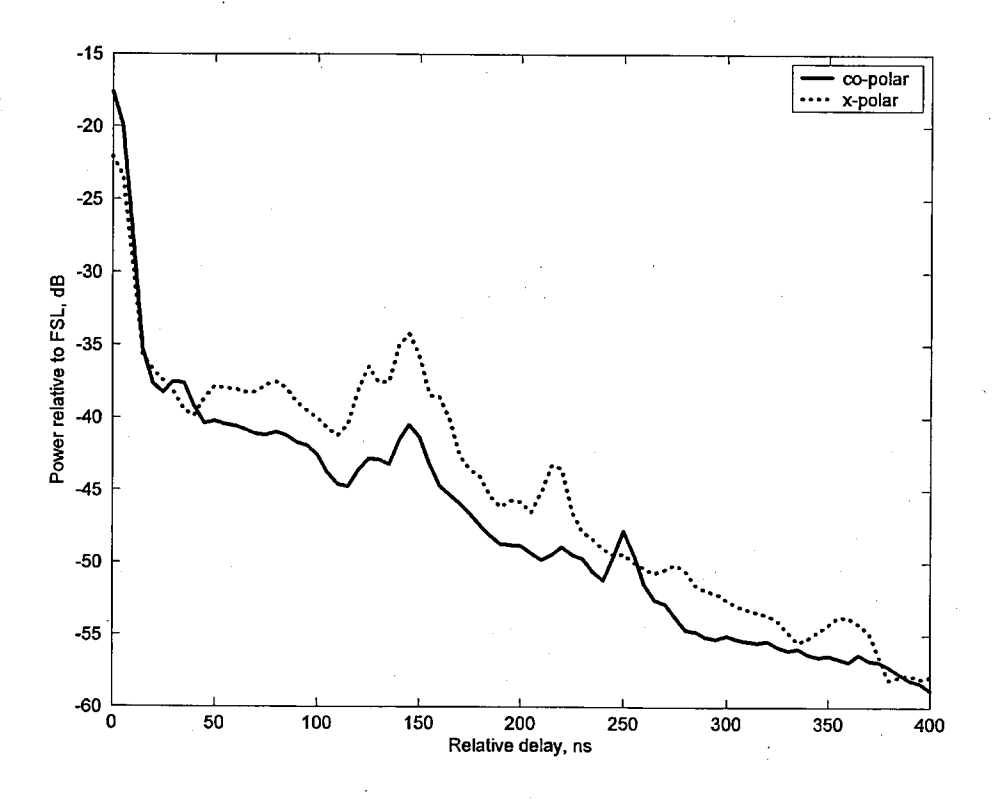


Fig. 6-42 Average power delay profile in road environment

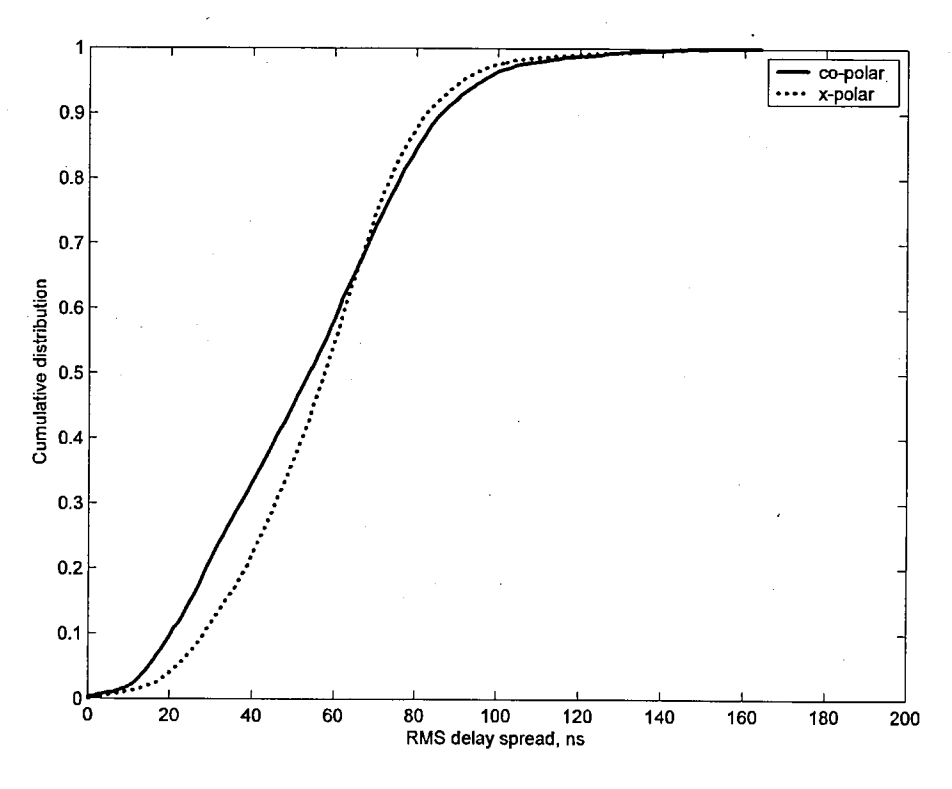


Fig. 6-43 Cumulative distribution of RMS delay spread in road environment

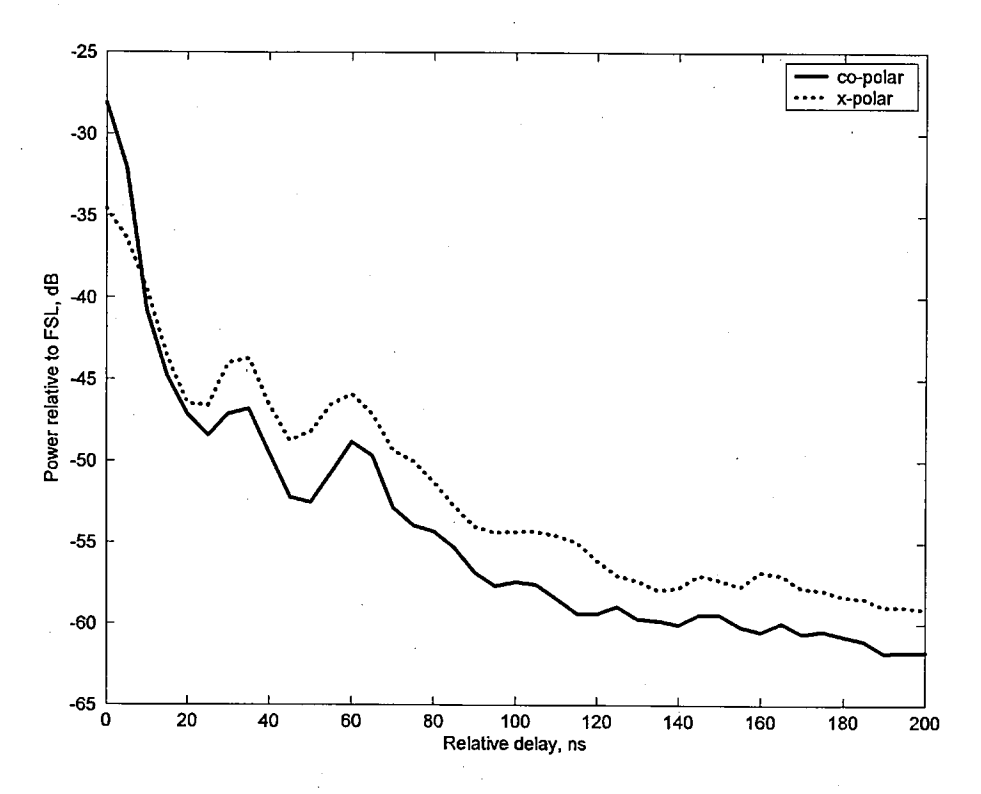


Fig. 6-44 Average power delay profile in suburban environment

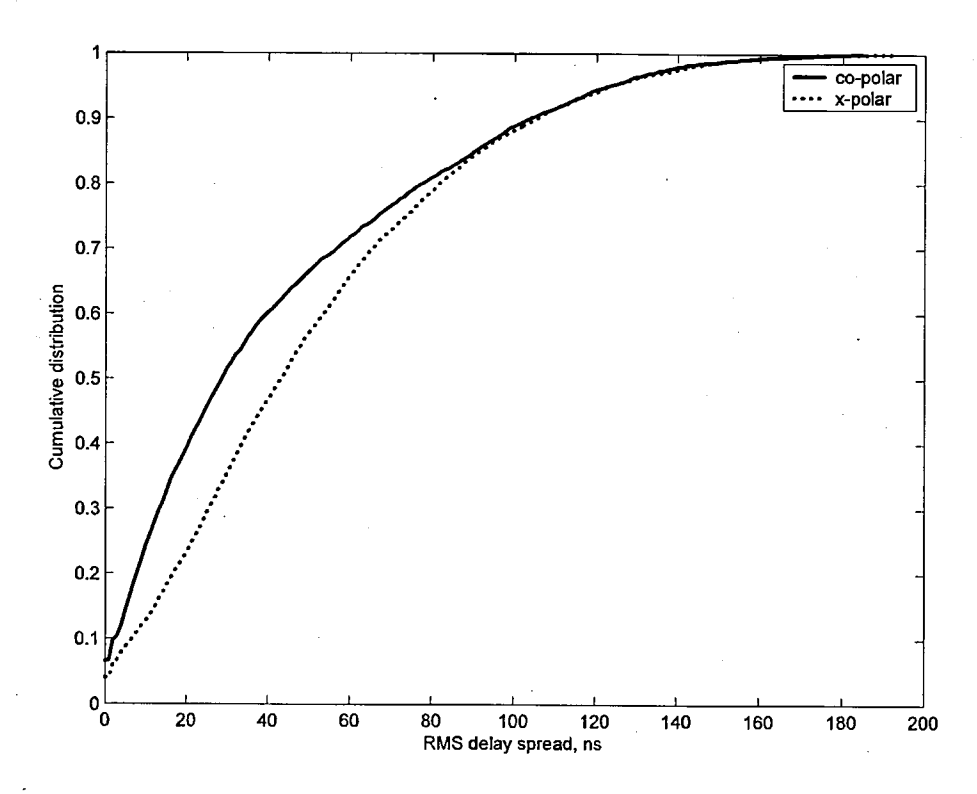


Fig. 6-45 Cumulative distribution of RMS delay spread in suburban environment

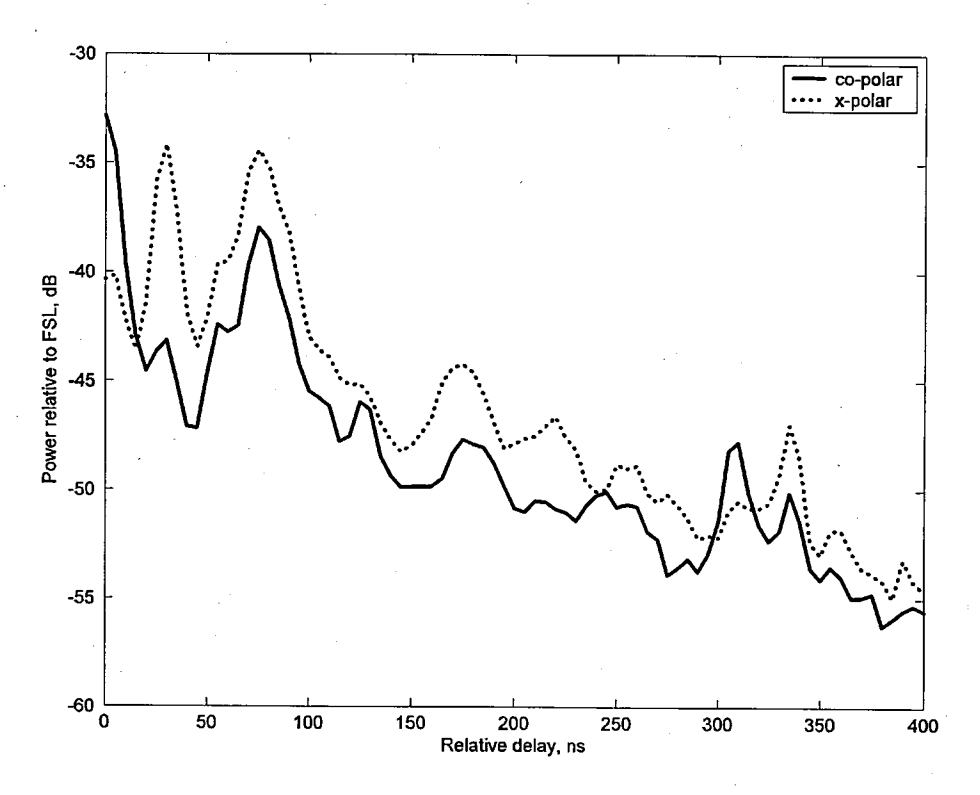


Fig. 6-46 Average power delay profile in urban environment

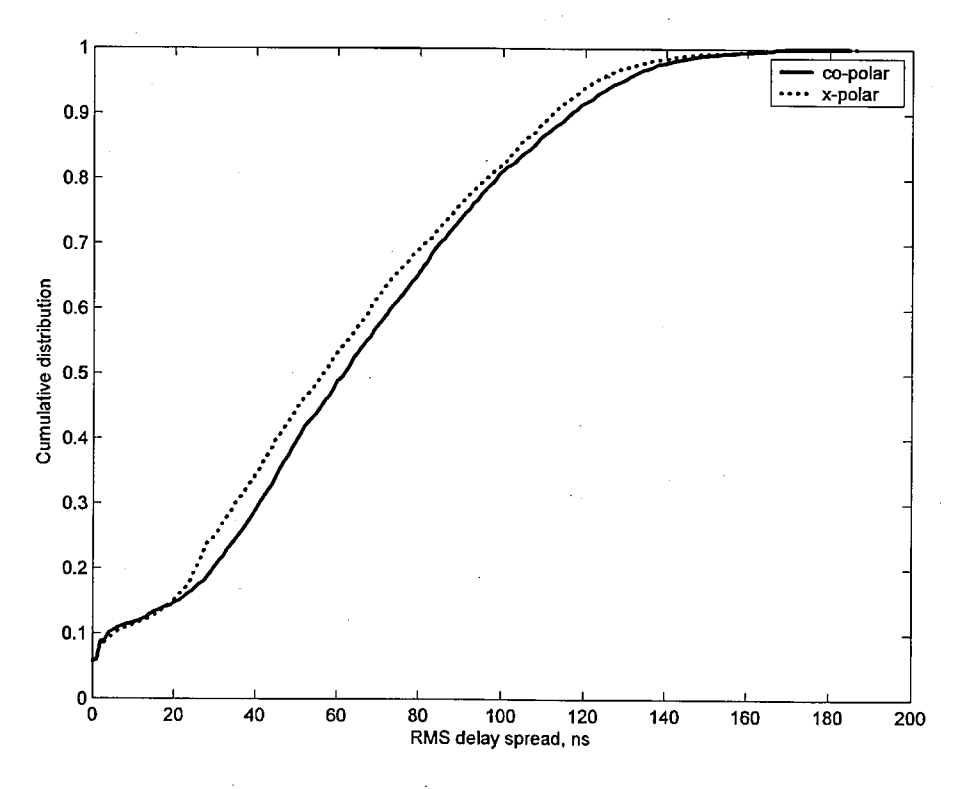


Fig. 6-47 Cumulative distribution of RMS delay spread in urban environment

Bello system functions

Bello functions were described in chapter 3. Here they are presented from the campaign data.

Input delay-spread function

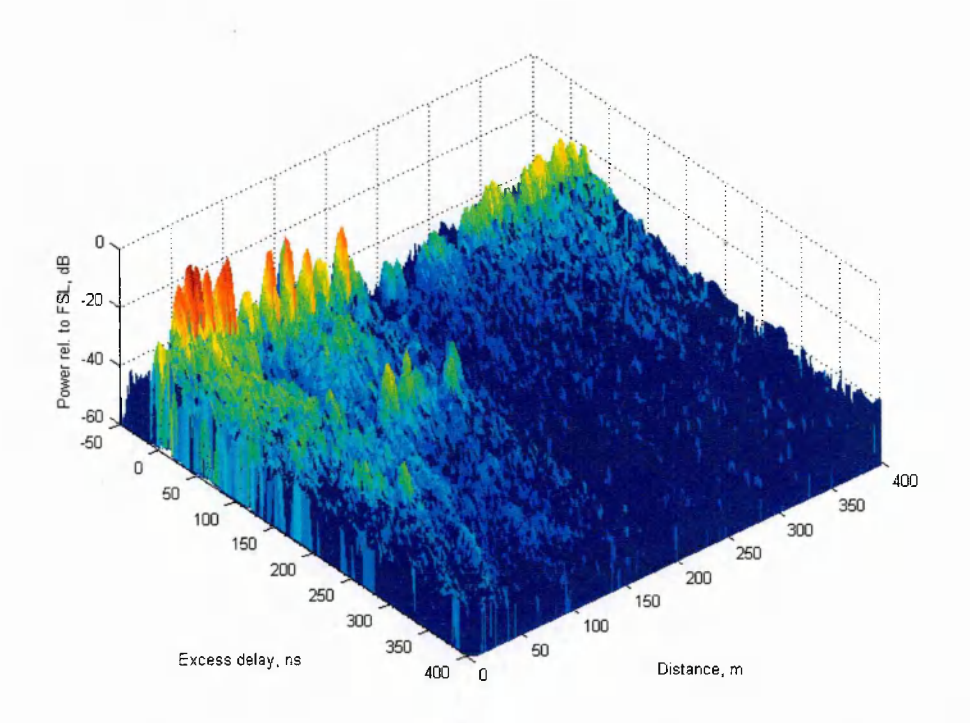


Fig. 6-48 Input delay-spread function of co-polarized channel in tree-lined road environment

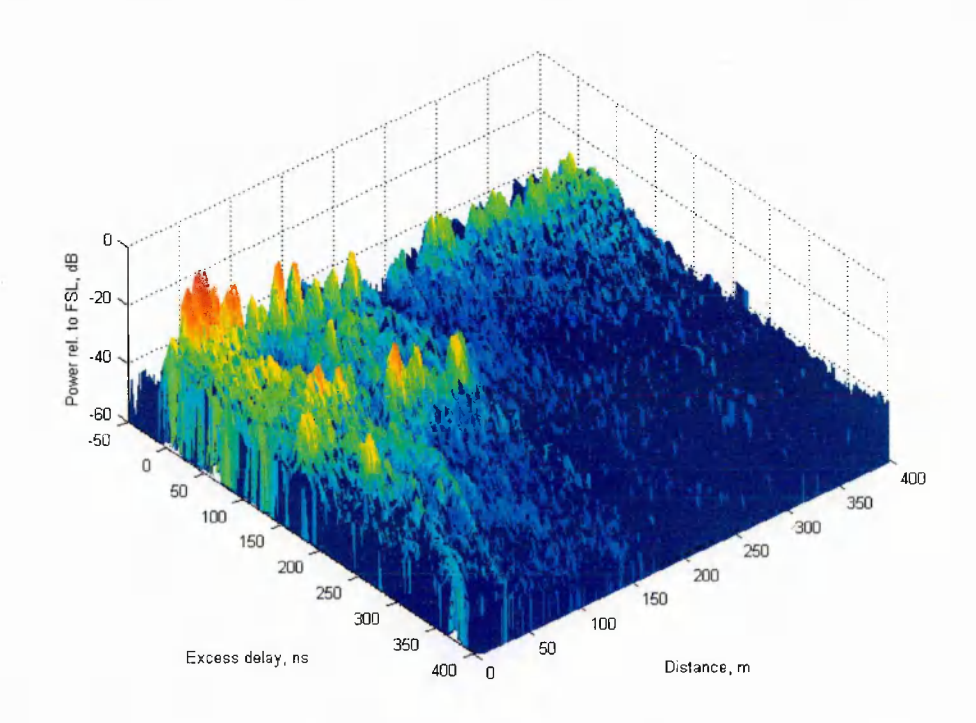


Fig. 6-49 Input delay-spread function of cross-polarized channel in tree-lined road environment

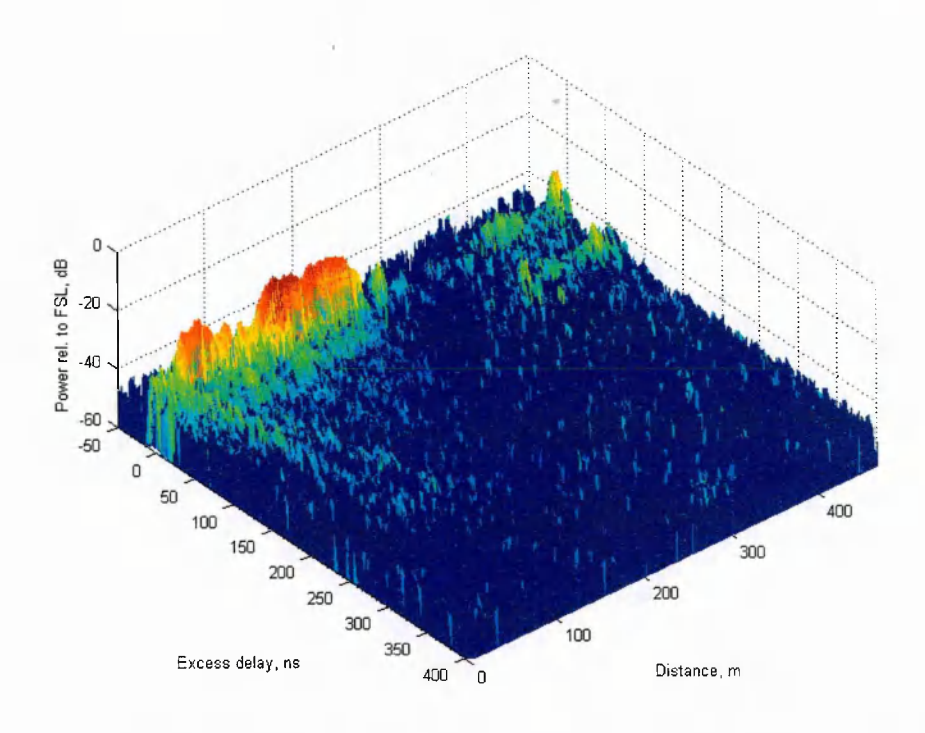


Fig. 6-50 Input delay-spread function of co-polarized channel in suburban environment

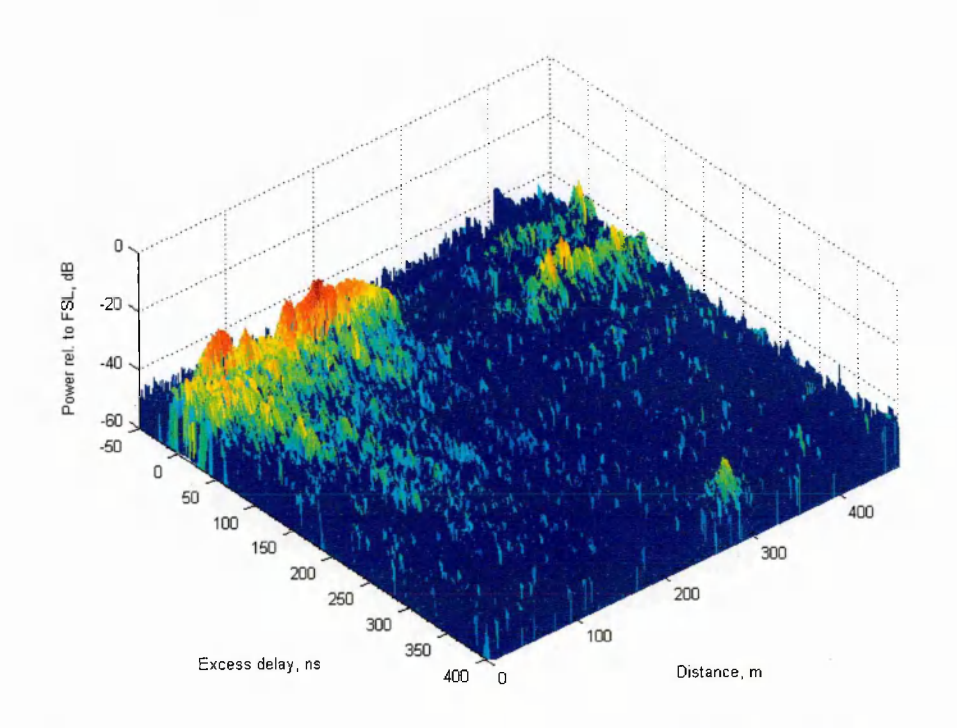


Fig. 6-51 Input delay-spread function of cross-polarized channel in suburban environment

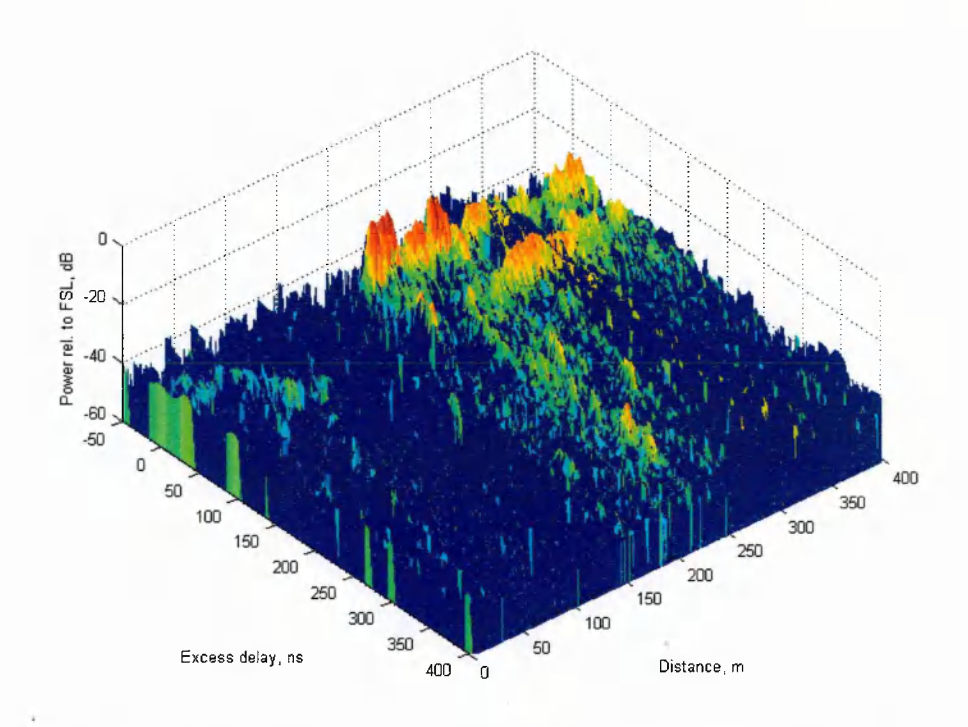


Fig. 6-52 Input delay-spread function of co-polarized channel in urban environment

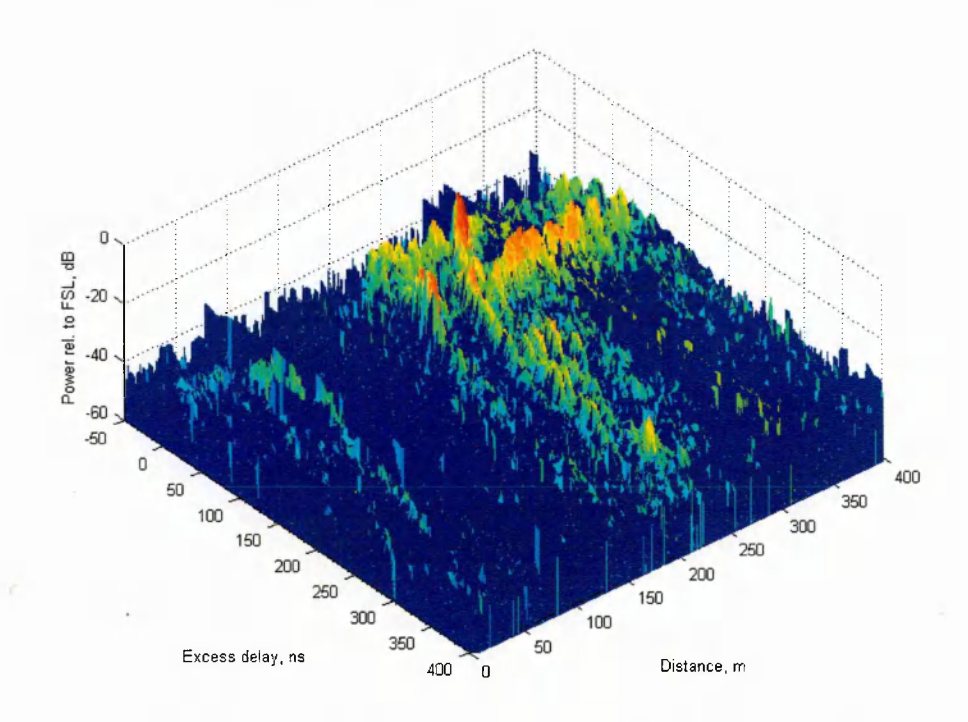


Fig. 6-53 Input delay-spread function of cross-polarized channel in urban environment

Observations

The graphs show the input delay-spread function of co-polarized and cross-polarized channels for the tree-lined road, suburban and urban environments.

It can be observed for the tree-lined road case that at earlier excess delays, the data experiences rapid fluctuations in level – showing an 'on/off' channel response, whereas at higher excess delays the data fluctuates less. This is intuitive as the earlier delay components are more associated with the LOS or near-LOS paths, which follow a single direct path and so are more prone to rapid 'on/off' fading. At later delays, the received signal is contributed by many paths from different directions so the likelihood of 'on/off' fading is less. At around 150ns delay, 'on/off' fading is also present, which could occur due to a single specular reflection path. The tree-lined road data also shows a change between the first 200m of the data and the second 200m. This is likely to be attributable to the fact that the distance between TX-RX was higher for the second 200m as the vehicle moved further away from the transmitter. In this case the artificial platform elevation was lower and therefore and path through vegetation was considerably higher creating higher tree-path losses.

For the suburban case, the earlier delays also follow 'on/off' channel conditions but the distance in each state is longer due to the fact that the obstructions were buildings or rows or house located closely together. The powers, at higher excess delays are much less than the tree-lined road case. Perhaps the main cause of specular reflection is from buildings the other side of the road. Taking a value of 20m for this additional path length, suggests specular reflections would occur at an excess delay of (d/c) = 20/3e8 = 66ns, which is indeed the case observed from the data.

The graphs in the urban case show that the data is heavily attenuated for the first 200m and of higher powers during the second 200m. This was because the first 200m was carried out in the centre of town where the environment consisted of many four storey buildings, whereas the second 200m of data was obtained as the vehicle was moving away from the town centre. In this second part, the environment was densely covered with two storey buildings and much clutter, which accounts for high signal power overall, and higher signal powers at higher excess delays.

Delay Doppler-spread functions

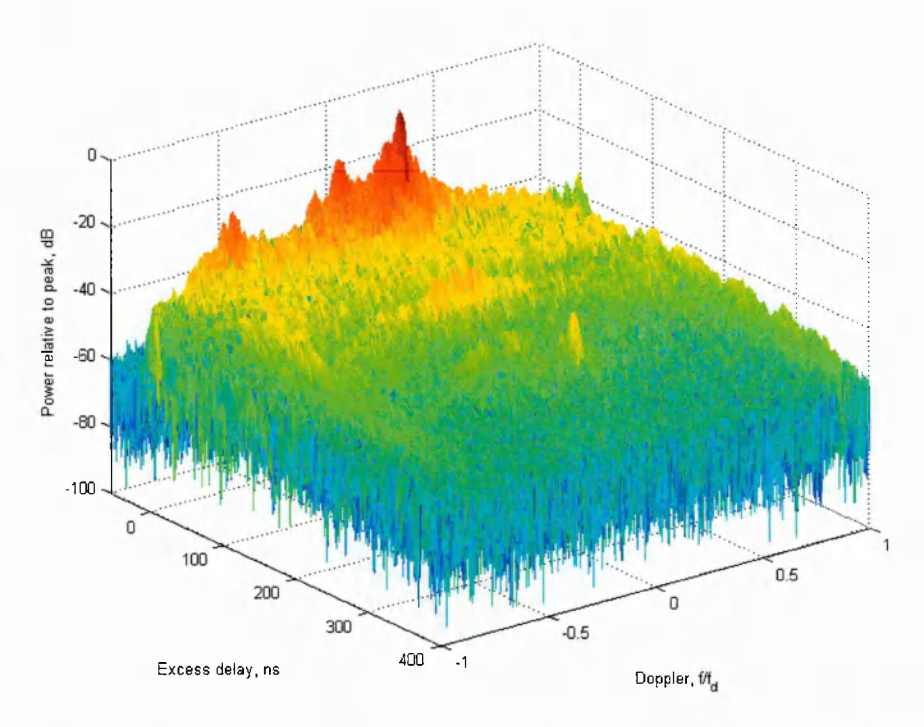


Fig. 6-54 Delay Doppler-spread function of co-polarized channel in tree-lined road environment

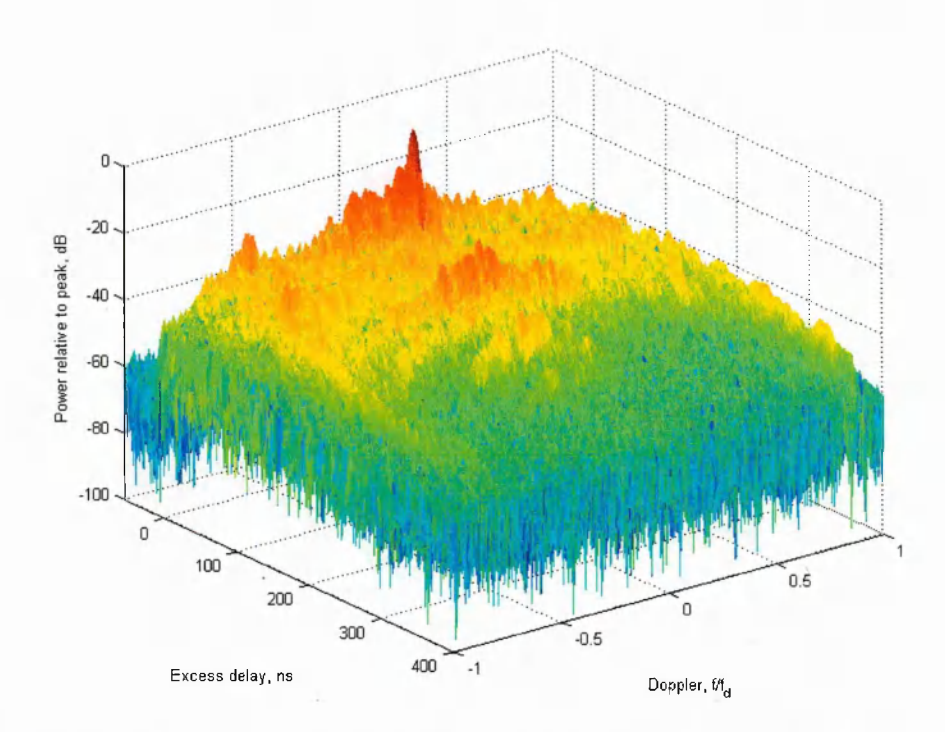


Fig. 6-55 Delay Doppler-spread function of cross-polarized channel in tree-lined road environment.

The power axes in both the co- and cross-polarized graphs are relative to the co-polarized peak.

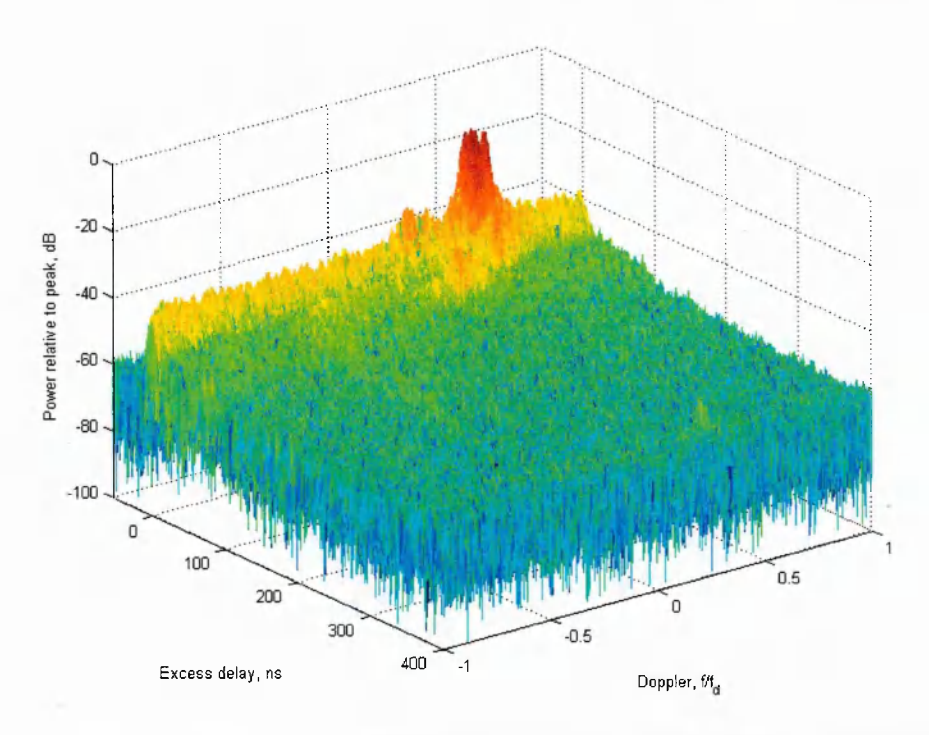


Fig. 6-56 Delay Doppler-spread function of co-polarized channel in suburban environment

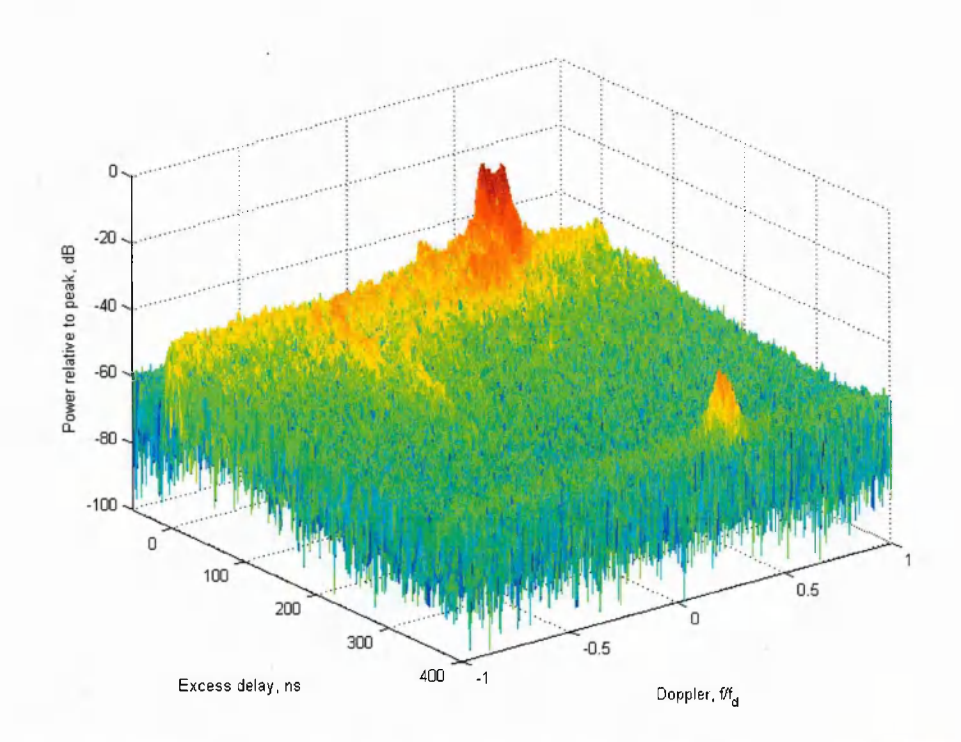


Fig. 6-57 Delay Doppler-spread function of cross-polarized channel in suburban environment

The power axes in both the co- and cross-polarized graphs are relative to the co-polarized peak.

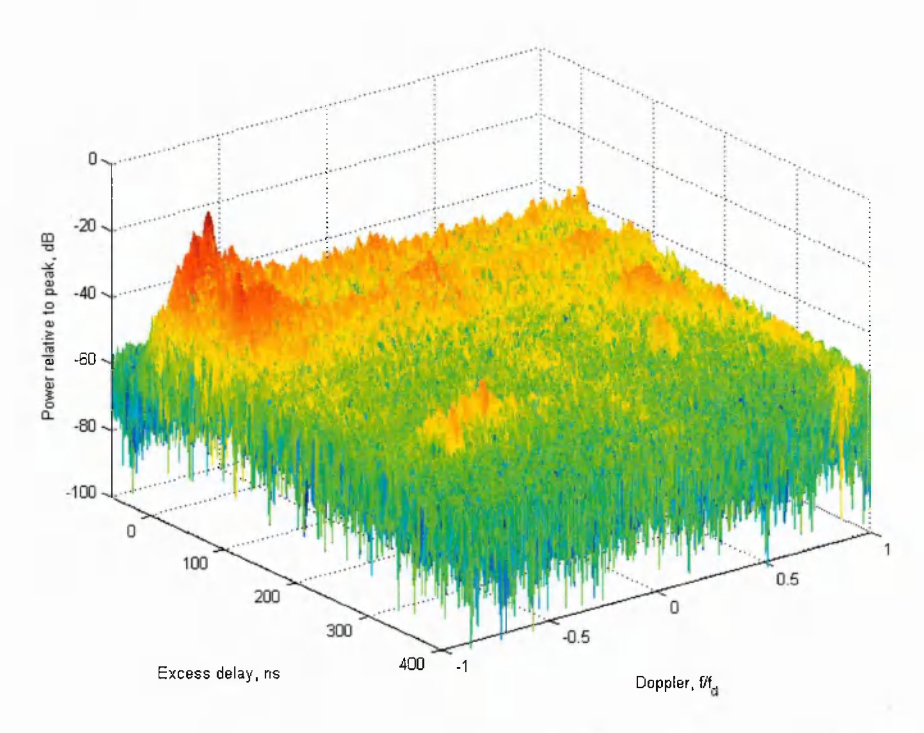


Fig. 6-58 Delay Doppler-spread function of co-polarized channel in urban environment

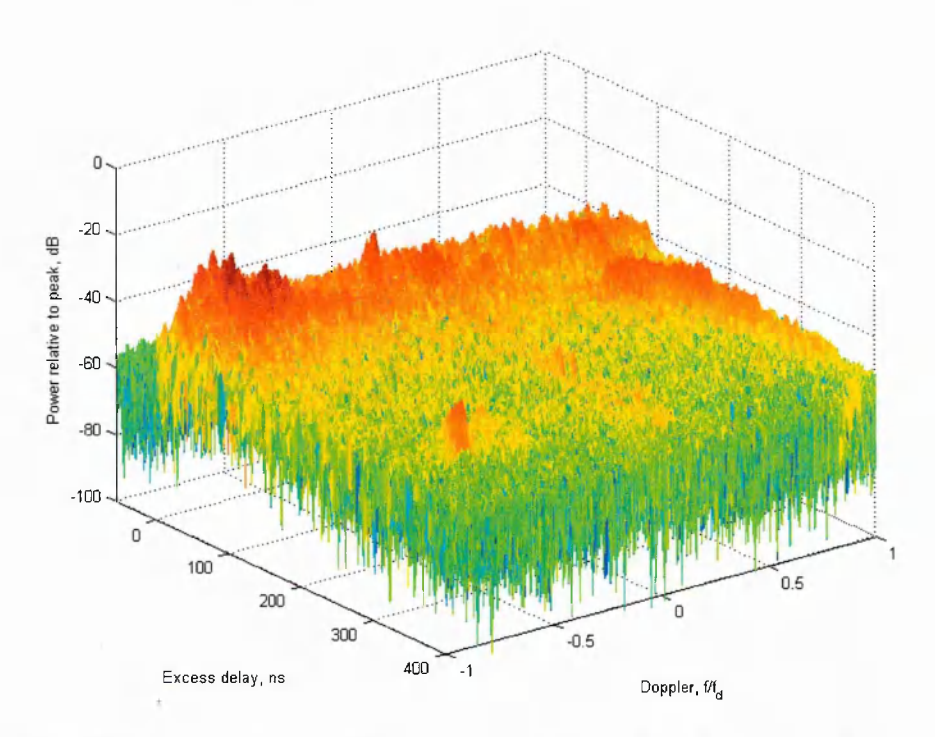


Fig. 6-59 Delay Doppler-spread function of cross-polarized channel in urban environment

The power axes in both the co- and cross-polarized graphs are relative to the co-polarized peak.

Observations

These graphs show the co-polarized and cross-polarized delay Doppler-spread functions for the tree-lined road, suburban and urban environments. The Doppler-spread function was calculated on 400m of channel data, and so averages of the Doppler spread through distance. An example of how the small scale Doppler spectrum changes with distance was shown in Fig. 6-37.

In the tree-lined road case, there is a strong confined Doppler component at small excess delays, which suggests a direct path at slightly positive Doppler frequencies and therefore during the motion towards the artificial platform. There are some components at negative Doppler frequencies which depict the LOS path when the vehicle is moving away from the transmitter. For the cross-polarized channel, there are some stronger Doppler components around 120ns representing specular reflections from buildings beyond the vegetation.

For the suburban case, there is a strong Doppler component for the direct paths spread around +23Hz. The direction of arrival can be estimated from $f_d = (v/\lambda) \cos \alpha$. So for 23Hz Doppler, the contributing rays arrive at the vehicle at $\pm 60^{\circ}$ with respect to the direction of motion. Apart from this dominant component there are other lower level components at low excess delays arriving at the vehicle from all directions during the vehicle motion.

The urban delay Doppler spread function also agrees with the measurement data. During the second part of the urban experiment, the vehicle was moving away from the transmitter and the environment was more open. This fact is found in the Doppler spectrum, which shows a strong negative Doppler at around -40Hz, corresponding to the arrival of rays from behind the direction of forward motion, which was indeed the case. There are also many additional Doppler components arriving at the vehicle from all directions which correspond to the large amount of clutter in the urban environment.

Time-variant transfer function

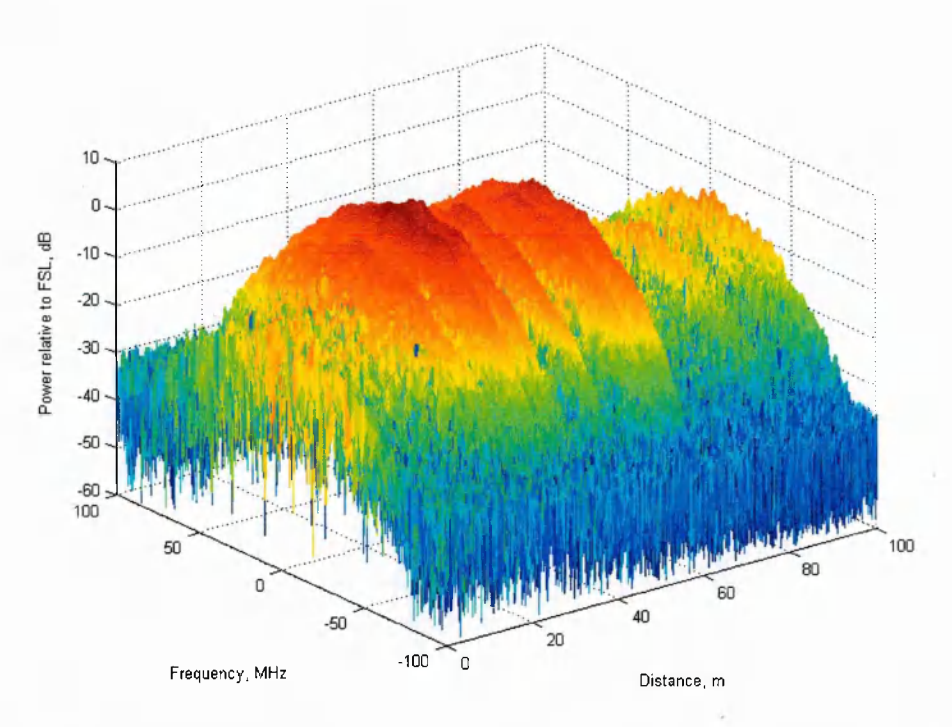


Fig. 6-60 Time-variant transfer function of co-polarized channel in tree-lined road environment

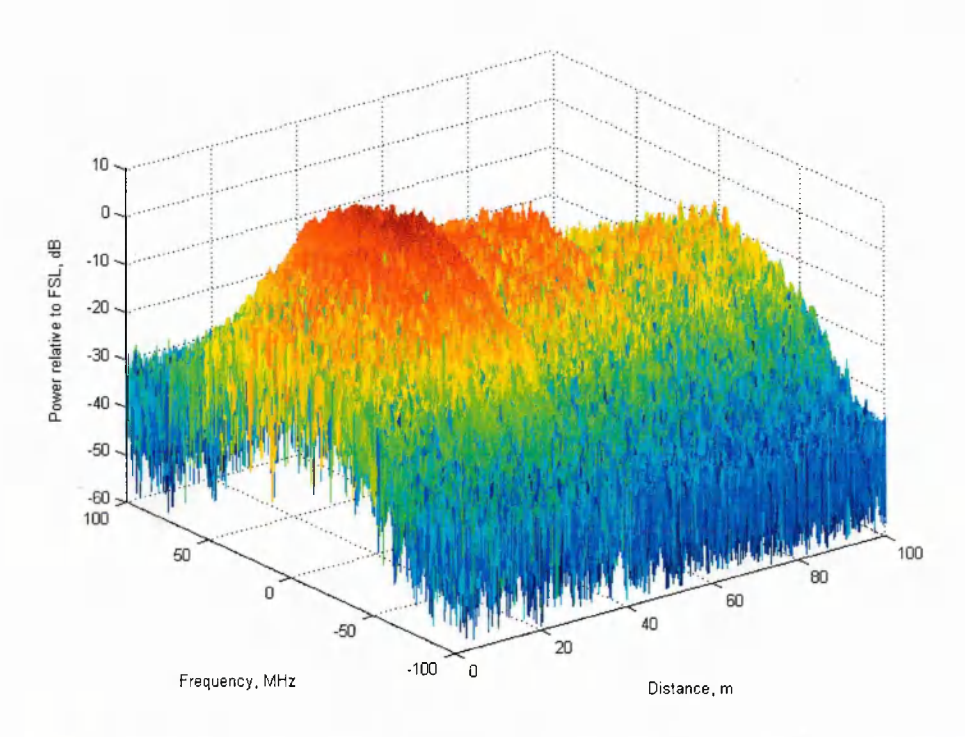


Fig. 6-61 Time-variant transfer function of cross-polarized channel in tree-lined road environment

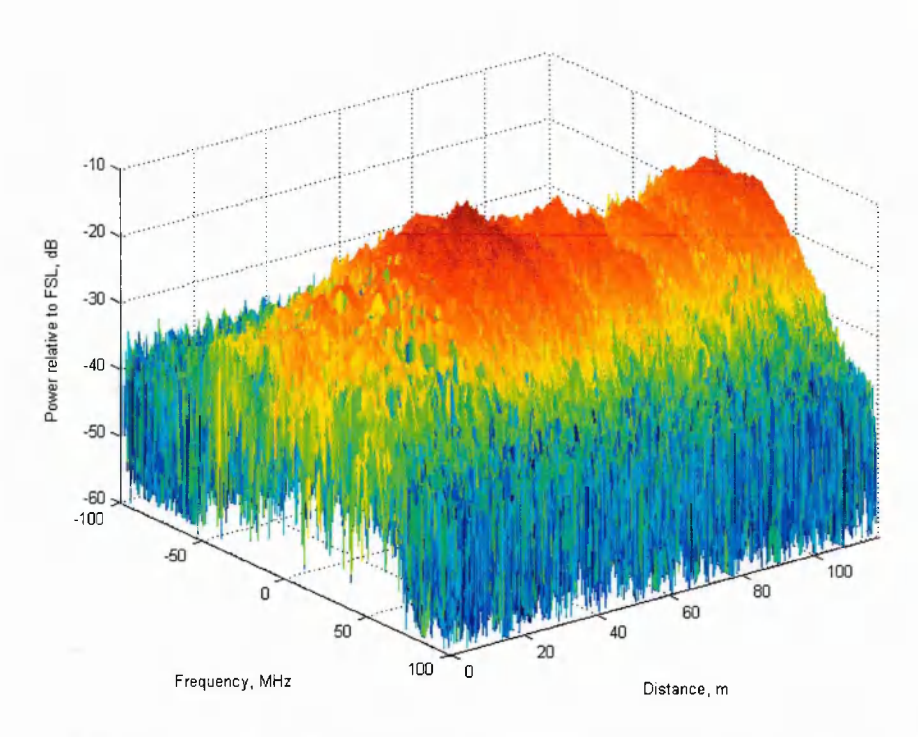


Fig. 6-62 Time-variant transfer function of co-polarized channel in suburban environment

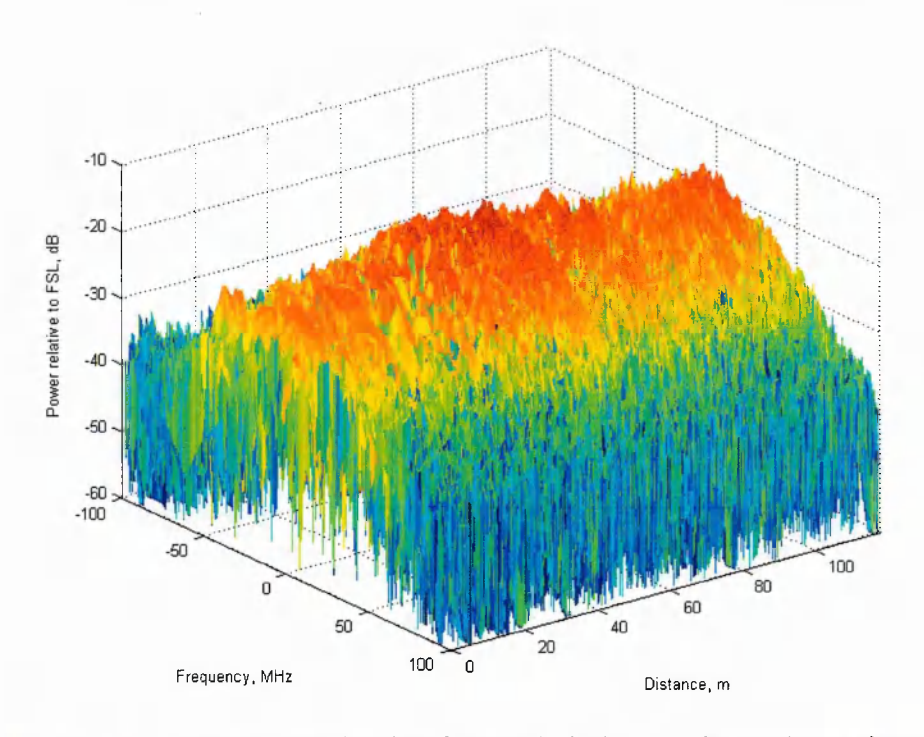


Fig. 6-63 Time-variant transfer function of cross-polarized channel in suburban environment

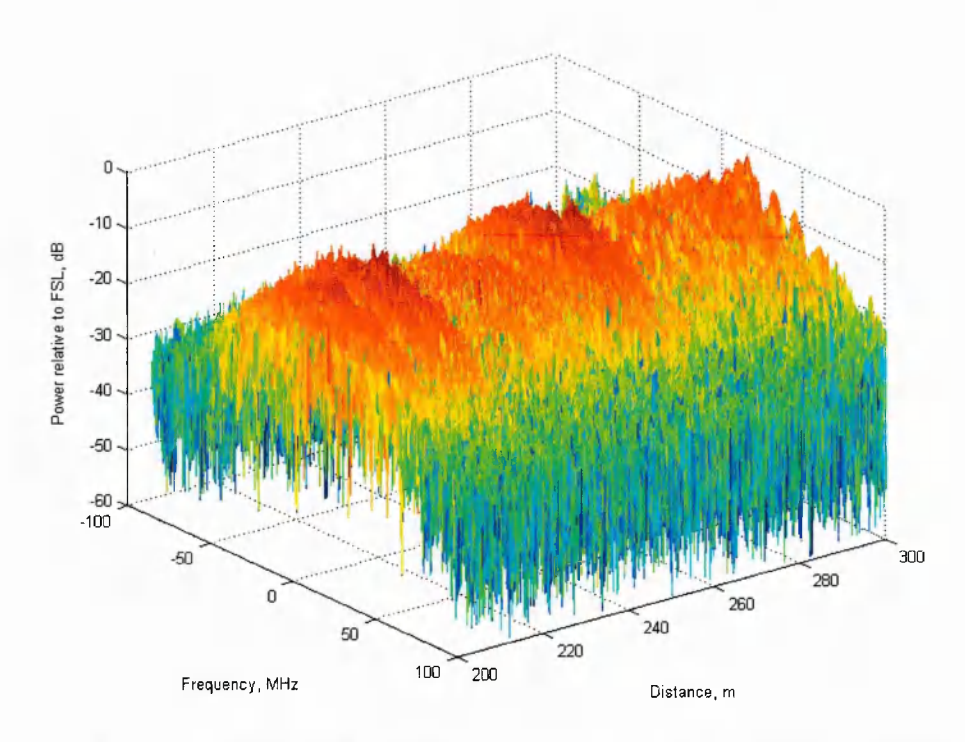


Fig. 6-64 Time-variant transfer function of co-polarized channel in urban environment

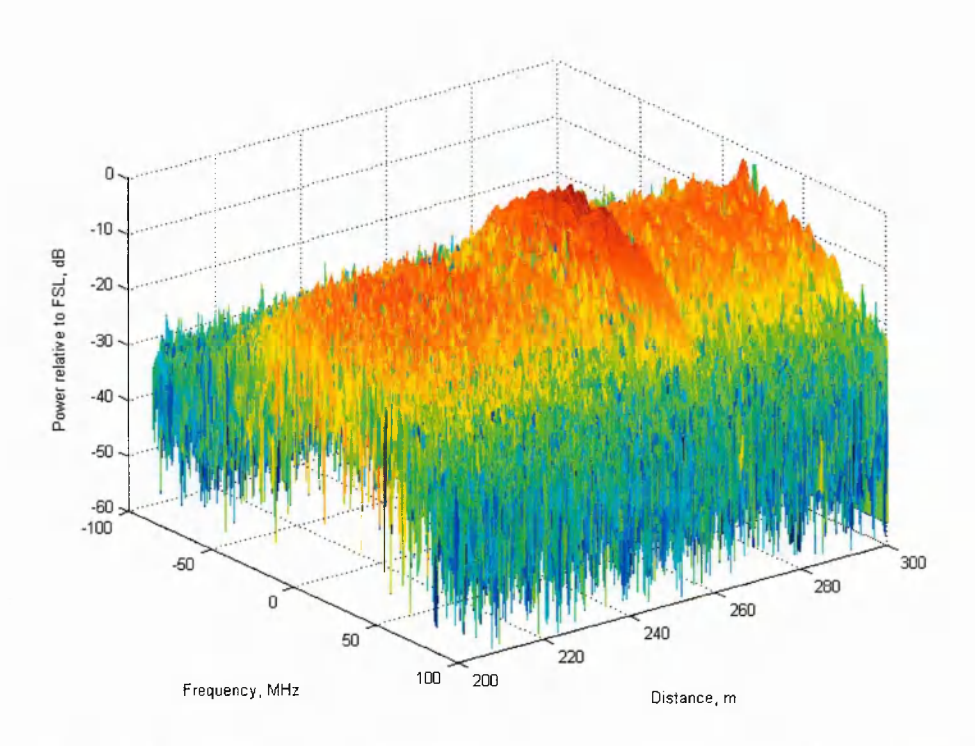


Fig. 6-65 Time-variant transfer function of cross-polarized channel in urban environment

Observations

These graphs present the co-polarized and cross-polarized transfer function as a function of distance for the tree-lined road, suburban and urban environments.

The first point to note is that the spectrum covers the range $F_C \pm 100 MHz$. This is due to the fact BPSK modulation was utilized in the sounder operating at 100Mchips/s. This is in effect the spectrum of the modulation scheme used. However, the data can be used to model a wideband channel over modulation bandwidths of 100MHz or less more accurately.

The next point to note is that the transfer function attenuation follows the same power delay profile power through distance. However, whereas the input delay-spread function informs about the changing power delay profile through vehicle location, the transfer function informs about the frequency response and coherence bandwidth through vehicle location.

An example of the transfer function for three co-polarized channels in the tree-lined road case is shown in Fig. 6-66.

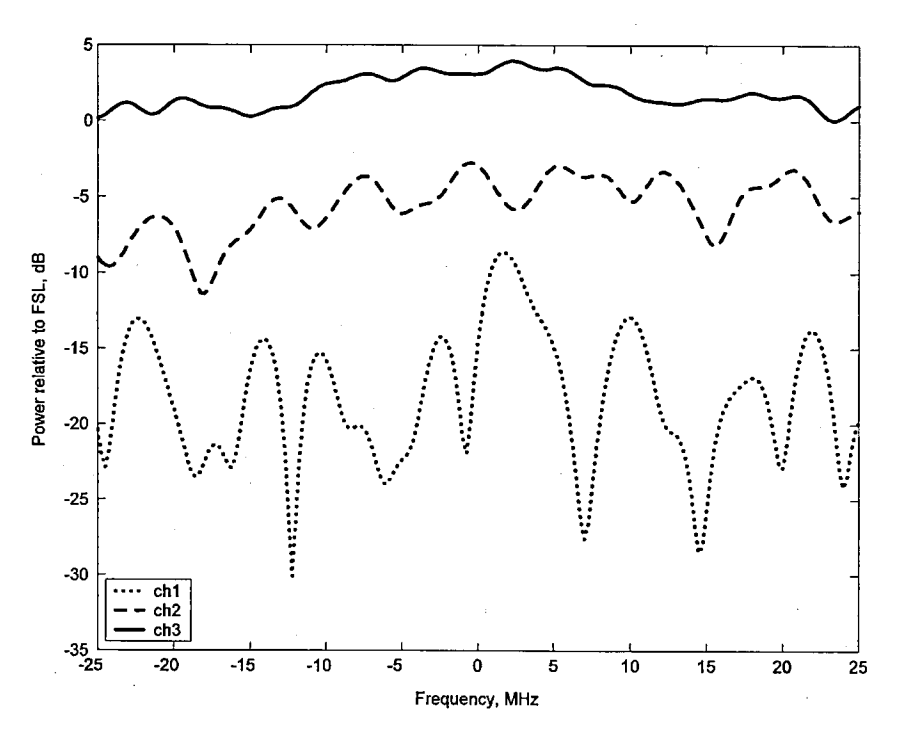


Fig. 6-66 Example frequency response of co-polarized tree-lined road channel

Channel 1 shows an attenuated case where multiple rays with different excess delays are creating high frequency selective fading. Channel 2 is a less attenuated channel with fewer frequency fluctuations. Channel 3 becomes more frequency flat and has gain slightly above FSL. This could be due to more than one ray arriving at similar excess delay, which could be caused by some channel waveguide effect. The coherence bandwidth was found to vary over $1-40 \mathrm{MHz}$.

Output Doppler-spread function

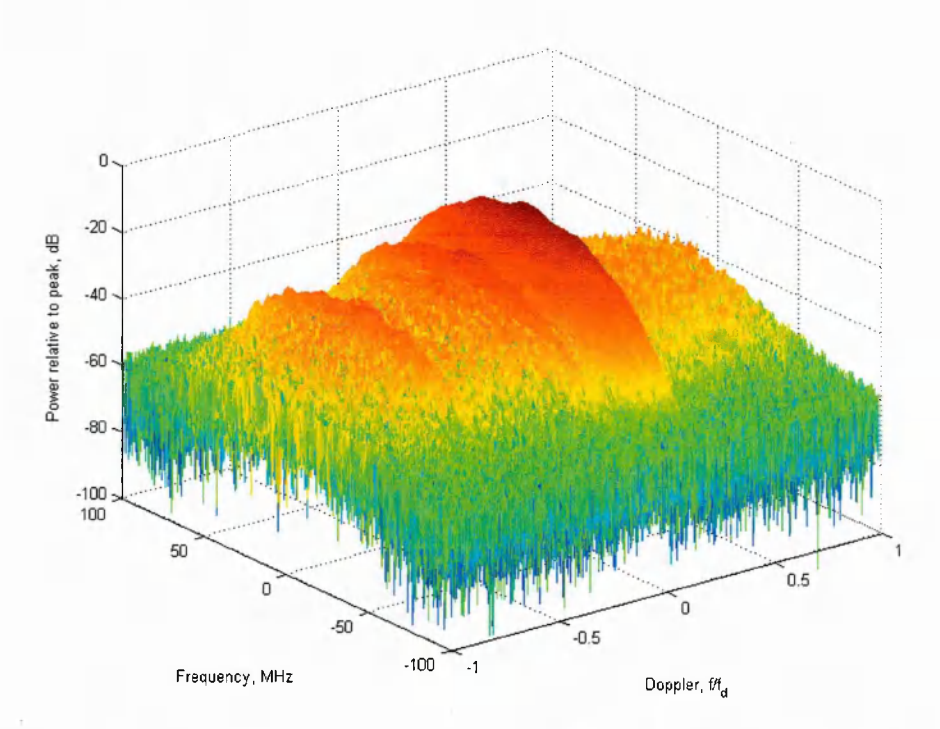


Fig. 6-67 Output Doppler-spread function of co-polarized channel in tree-lined road environment

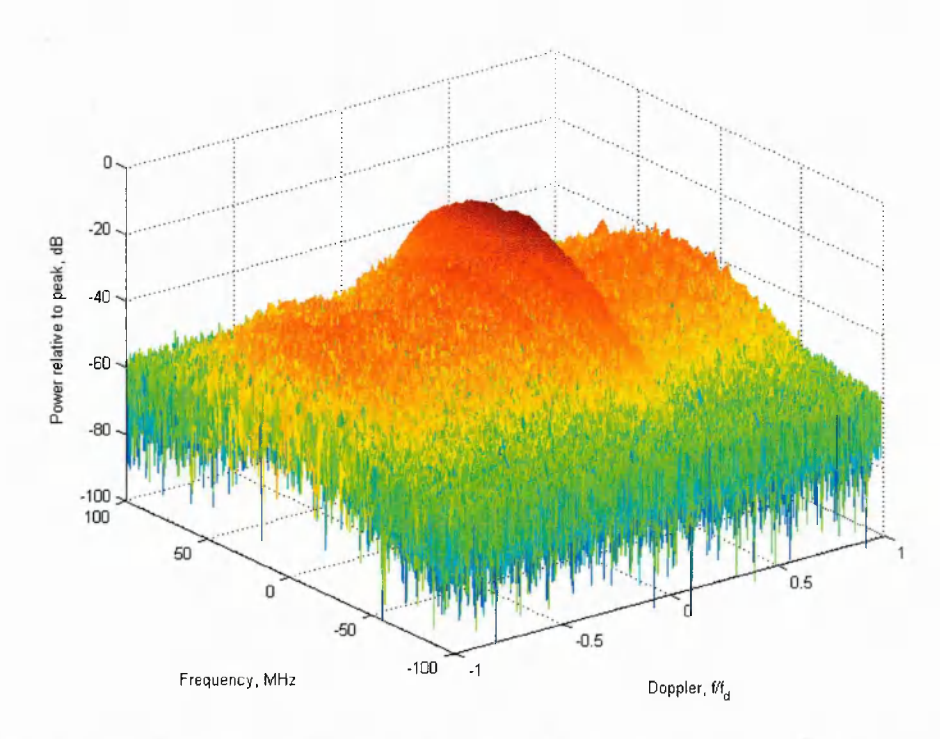


Fig. 6-68 Output Doppler-spread function of cross-polarized channel in tree-lined road environment.

The power axes in both the co- and cross-polarized graphs are relative to the co-polarized peak.

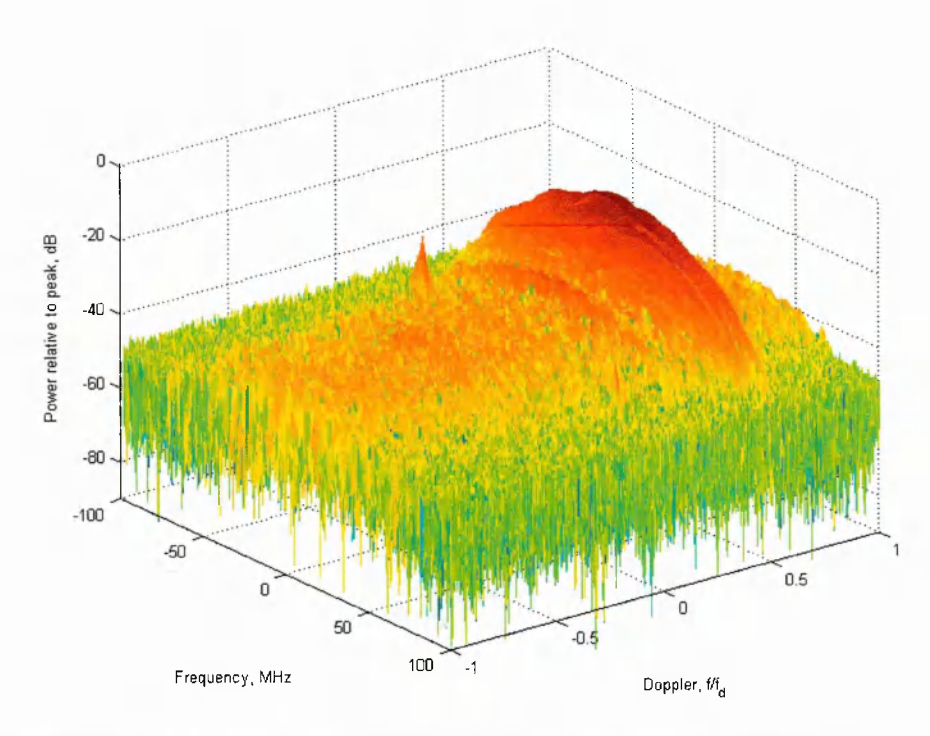


Fig. 6-69 Output Doppler-spread function of co-polarized channel in suburban environment

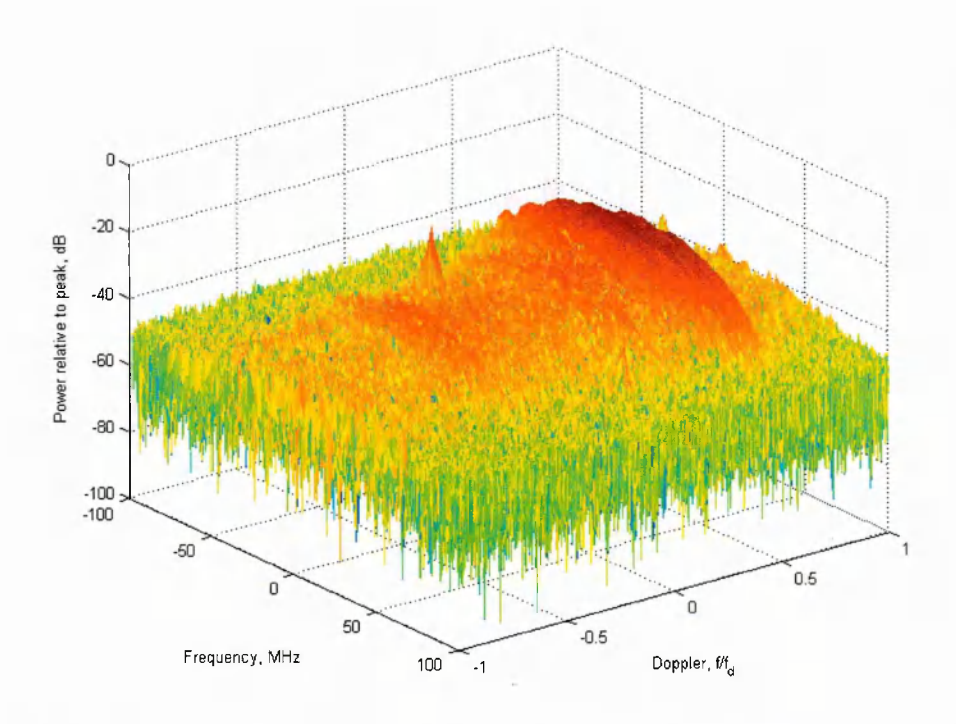


Fig. 6-70 Output Doppler-spread function of cross-polarized channel in suburban environment

The power axes in both the co- and cross-polarized graphs are relative to the co-polarized peak.

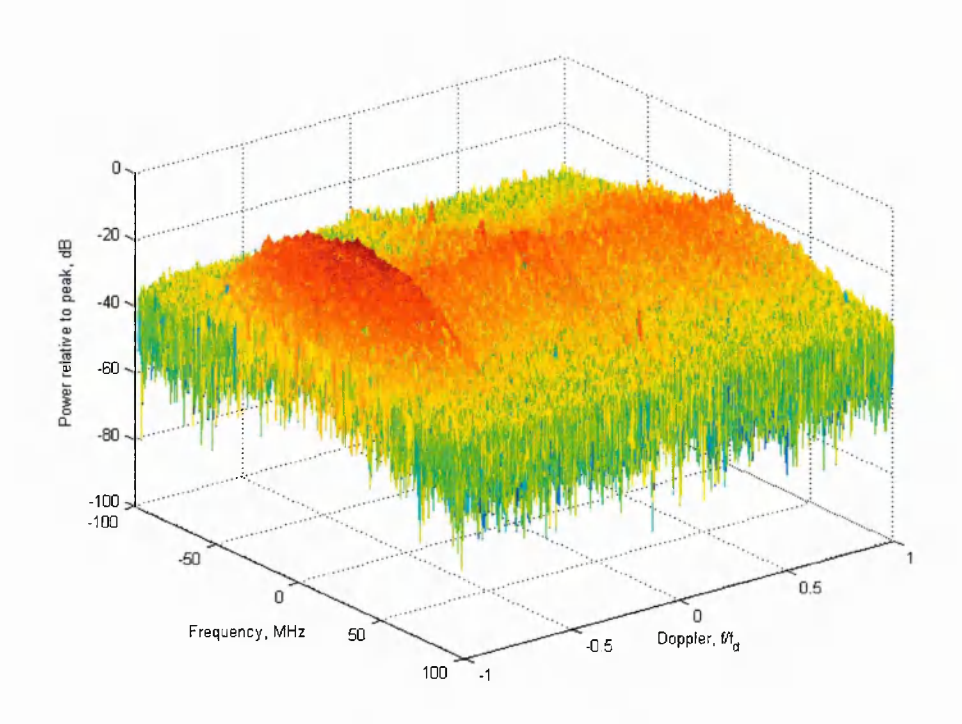


Fig. 6-71 Output Doppler-spread function of co-polarized channel in urban environment

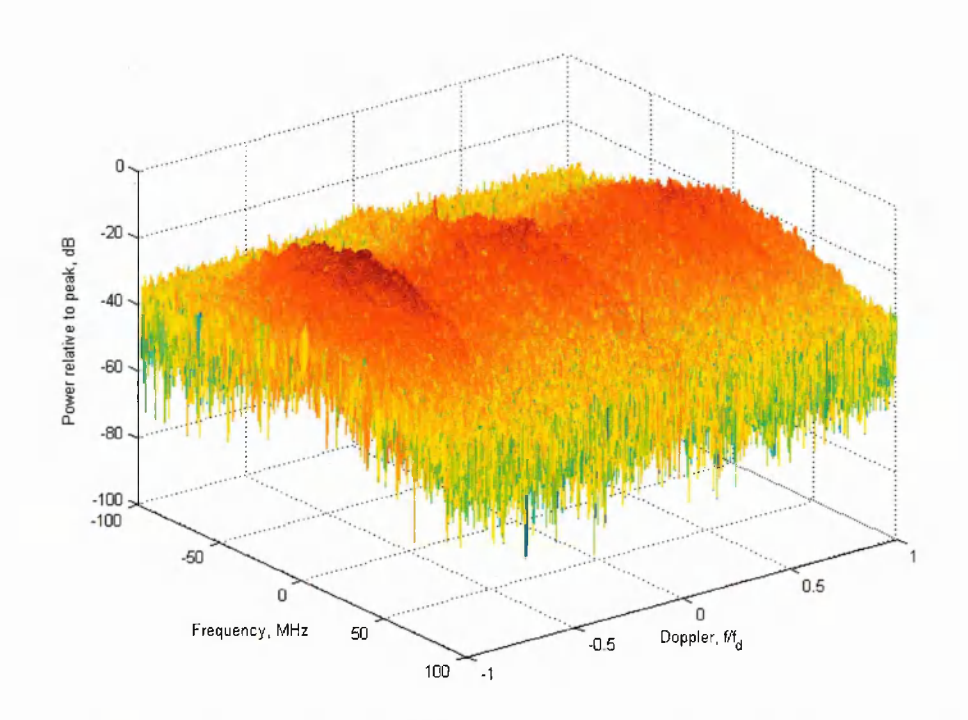


Fig. 6-72 Output Doppler-spread function of cross-polarized channel in urban environment

The power axes in both the co- and cross-polarized graphs are relative to the co-polarized peak.

Observations

These graphs present the co-polarized and cross-polarized transfer function as a function of Doppler frequency for the tree-lined road, suburban and urban environments.

It can be observed that the dominating Doppler frequencies are the same as the dominant Doppler frequencies in the delay Doppler-spread functions. However in this function the transfer functions are given at these Doppler frequencies.

These functions provide information about the frequency response obtained from rays coming from certain angular directions, which can be estimated from the Doppler spectrum.

6.3 Measurement data limitations

Since this campaign emulated the LMS channel, it is important to make an assessment of potential sources of error between the data set and LMS channels using a real satellite and perfect antennas.

Firstly, the data included in this campaign was obtained under low elevation conditions. It is therefore useful for the further development of a model that could test the performance of, for example, polarization time coding signal processing under similar conditions. Note that at least 70% of the first Fresnel zone was unblocked by terrain during all measurement runs.

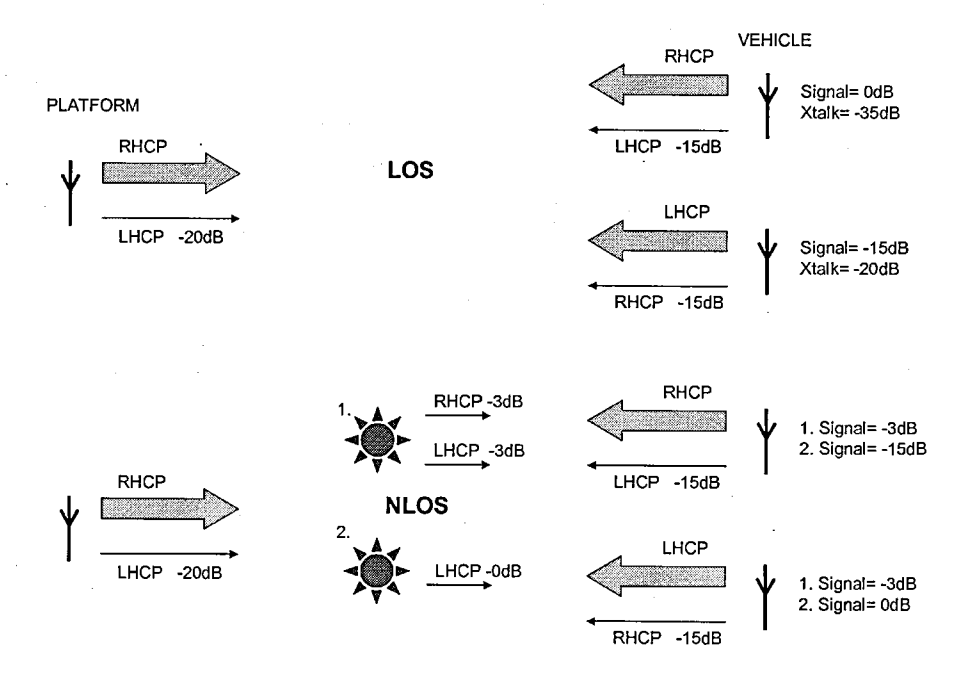


Fig. 6-73 Channel dynamic range validity

Another limitation is the dynamic range validity of the channel data. Since the satellite antennas had a mean cross polar discrimination of 20dB and the mobile antennas had a mean cross polar discrimination of 15dB, the channel data represents the channel alone for the top 15dB signal

level range only. The signal level fading beyond 15dB represents a combination of the channel and antenna system. However, in a practical system, 15dB mobile antenna cross polar discrimination is a typical cost-effective requirement on a vehicle. Data analysis and results are therefore valid for the design of a practical system. A schematic of the scenario is shown Fig. 6-73, which shows the effect in a LOS and NLOS situation assuming zero path loss. 20dB XPD TX, 15dB XPD RX and 0dBi antennas are used for explanation purposes. When in LOS, the co-polar received signal is 0dB and the cross-polar signal is -15dB. When in NLOS, example 1 shows that system XPD is -3dB at LHCP and RHCP RX antennas and XPD is primarily due to the channel. In example 2, the scatterer is an ideal reflection and the cross-polar signal is 0dB, and the co-polar signal is -15dB due to the antenna XPD.

Any terrestrially based mobile-satellite measurement campaign, may be affected by the close proximity of scatterers to the artificial platform, which would not be present in the real satellite case, as discussed in section 5.1.4. Due to the soil reflection coefficient loss [Lan96] in addition to the antenna first sidelobe loss, and rough scattering effect, these scatterers are considered negligible.

Additionally, due to the geometry of the rays at short mobile-satellite distances, characteristics at higher excess delays may not fully represent the characteristics that would be obtained from real LMS channels. At large distances, as in a real satellite system, rays tend to arrive at each scatterer parallel to each other. In contrast, at relatively shorter distances, angles of incidence will be different at each scatterer compared to the real satellite case. An estimation of a scatterer reflection coefficient amplitude error due to incident angle error was obtained by modelling using a spherical scatterer perpendicular to the mobile-platform path forming a right-angled triangle, such that the mobile-scatterer-satellite path incident angle was 45°. At the minimum mobile-platform distance, the mobile-scatterer-platform incident angle ranged from 45°, at zero excess delay, to 38° at 400ns excess delay. Typical building reflection coefficients [Lan96] suggest a reflected power error over this incident angle change, of around 3dB. In the case where scatterers are modelled as cuboids, the location of significant reflecting scatterers may differ between the real satellite and the artificial platform case. However, with cuboids rotated randomly, channel error is expected to be statistically low.

Observations of the small scale Doppler spectrum temporal variations were consistent with the artificial measurement scenario. For example, in the tree-lined road case, the vehicle motion was along a straight road oriented oblique to the direct path. Since the artificial platform was stationary, the Doppler spectrum for the direct path changed from positive to negative frequencies during the measurement run, and therefore was not consistent with a real satellite scenario, where the rays would be parallel at each vehicle position, producing more static direct path Doppler frequency components.

6.4 Capacity predictions

In this section, the benefit in terms of available capacity from the 2x2 MIMO matrix measurement data is presented. The whole measurement dataset was used in these calculations.

6.4.1 Method

A realistic fade margin of 10dB was added to the narrowband normalized channel data to combat channel fluctuations [EvJ98]. A practical representative mobile satellite reference FSL SNR of 15dB was chosen, since a typical required SNR for QPSK with channel coding is 5dB. This normalizing procedure produced an average received SNR^(k) value for each channel matrix at sample (k).

The channel matrices were then normalized, such that $\mathbf{H}^{(k)} = A^k \hat{\mathbf{H}}^{(k)}$, where $\hat{\mathbf{H}}^{(k)}$ and $\mathbf{H}^{(k)}$ represent the observed and normalized matrices respectively at sample (k), to unity power transfer [Wal03]:

$$\frac{1}{4} \sum_{m=1}^{2} \sum_{n=1}^{2} \left| A^{k} \hat{H}_{mn}^{(k)} \right|^{2} = 1, \text{ and therefore } A^{k} = \left(\frac{1}{4} \sum_{m=1}^{2} \sum_{n=1}^{2} \left| \hat{H}_{mn}^{(k)} \right|^{2} \right)^{-(1/2)}$$
(6-17)

At each sample point (k), SNR^(k) and the normalized channel matrix $\mathbf{H}^{(k)}$ was used to find the capacity. When the transmitter has no knowledge of the channel, the available MIMO capacity can be obtained from [Fos96]:

$$C^{(k)} = \log_2 \det \left[\mathbf{I}_2 + \left(\frac{SNR^{(k)}}{2} \right) \mathbf{H}^{(k)} \mathbf{H}^{(k)H} \right]$$
 bits/cycle (6-18)

where I_2 is the 2x2 identity matrix, and $\mathbf{H}^{(k)^H}$ is the complex transpose of the MIMO channel matrix, $\mathbf{H}^{(k)}$ at sample (k). The resultant capacity complementary cumulative distribution functions of SISO and 2x2 MIMO channels are obtained for tree-lined road, suburban and urban environments.

6.4.2 Results

Obtained results suggest a doubling of median capacity in a dual polarized 2x2 satellite MIMO system compared with a single polarized SISO system. Capacity complementary cumulative distribution functions curves of SISO and 2x2 MIMO channels, as shown in Fig. 6-74, suggest that 50% of channels are greater than 0.39, 0.80, 0.27 bits/cycle for SISO, and 0.96, 1.35, 0.67 bits/cycle for MIMO in the tree-lined road, suburban and urban environments respectively. Significant improvements to outage capacity are also suggested by the data, with a 10% outage capacity of 0.02,

0.09, 0.03 bits/cycle for SISO, and 0.14, 0.37, 0.26 bits/cycle for MIMO in the tree-lined road, suburban and urban environments respectively. Capacity units are given in standard units of bits per cycle, which is identical to bits per second per Hz.

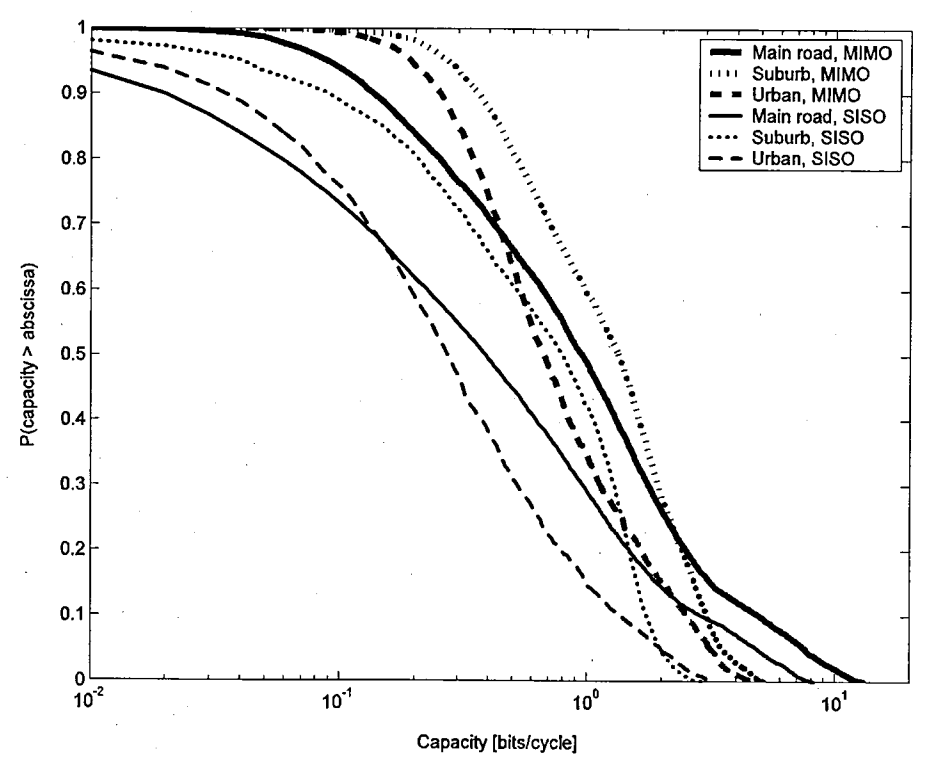


Fig. 6-74 Contrasting complementary cumulative distribution functions of capacity for SISO and 2x2 dual polarization MIMO systems in the tree-lined road, suburban and urban environments with 15dB FSL SNR

6.4.3 Observations

It was shown in [McN00], that at higher SNR levels, the capacity gain from MIMO channel effects is reduced, yet at lower SNR, the channel is more scattered and MIMO capacity gain is increased. This is also the case observed in this present campaign data. At higher signal to noise ratios, an approximate doubling in capacity is available due to the two polarizations. However, at lower signal to noise ratios, the channel around the vehicle is more scattered and spatial multiplexing can be use to obtain far greater ratio increases in channel capacity, although capacity is still lower due to reduced SNR.

Although capacity predictions show possible capacity that can be achieved with optimum adaptive modulation and coding, they say nothing about how to achieve it. In a LMS system, adaptive modulation and coding is difficult to achieve effectively because of the significant delay. It is therefore more appropriate to find the optimum fixed modulation and coding strategy. One way of improving capacity, especially at lower signal levels, is to use transmit and/or receive diversity.

6.5 Diversity predictions

In this section, the improvement to bit error rate (BER) is shown for QPSK modulation. The BER curves from the uncoded SISO channel are compared with maximum ratio receive combining, transmit diversity polarization time 2x1 coding, and transmit and receive diversity polarization 2x2 coding.

6.5.1 Method

The bit error rate of a coherent QPSK modulated system is given by:

$$P(e) = \frac{1}{2} \operatorname{erfc} \sqrt{\frac{E_b}{N_o}}$$
 (6-19)

where P(e) is the probability of error or BER, erfc is the complementary error function, E_b is the energy per bit and N_o is the noise power spectral density.

For a SISO channel the above equation can be combined with the channel response to provide the instantaneous BER at each E_b/N_0 and channel condition:

$$P(e) = \frac{1}{2} erfc \sqrt{\frac{E_b}{N_0} |h|^2}$$
 (6-20)

where h is the channel relative to FSL.

For the case of maximum ratio receive combining, the SNR from each channel is effectively added. In this case the BER expression becomes:

$$P(e) = \frac{1}{2} \operatorname{erfc} \sqrt{\frac{E_b}{N_0} \left(|h_1|^2 + |h_2|^2 \right)}$$
 (6-21)

where h_1 and h_2 correspond to two channels from one satellite antenna to dual polarized mobile station receive antennas.

The case on 2x1 polarization time coded transmit diversity also produces a summing of SNR; however in this case the transmit power from each antenna is halved so that the total transmit power identical. In this case the formulation becomes:

$$P(e) = \frac{1}{2} \operatorname{erfc} \sqrt{\frac{E_b}{N_o}} \frac{\left| |h_1|^2 + |h_2|^2 \right|}{2}$$
 (6-22)

Polarization time coding with 2 transmit antennas and 2 receive antennas provides fourth order diversity gain. Again we find the SNR from each channel is added and the transmitter power is halved. In this case we find the following formulation:

$$P(e) = \frac{1}{2} \operatorname{erfc} \sqrt{\frac{E_b}{N_0} \frac{|h_1|^2 + |h_2|^2 + |h_3|^2 + |h_4|^2}{2}}$$
 (6-23)

The results using the narrowband channel data in the above formulas are now presented for the tree-lined road, suburban and urban cases.

It should be noted that additional diversity can be obtained by using the frequency diversity properties of modulation schemes such as OFDM-MIMO. In this case, higher order modulation can be applied to sub-carriers with high transfer function power. An investigation of LMS-OFDM-MIMO is left for future work.

6.5.2 Results

Tree-lined road

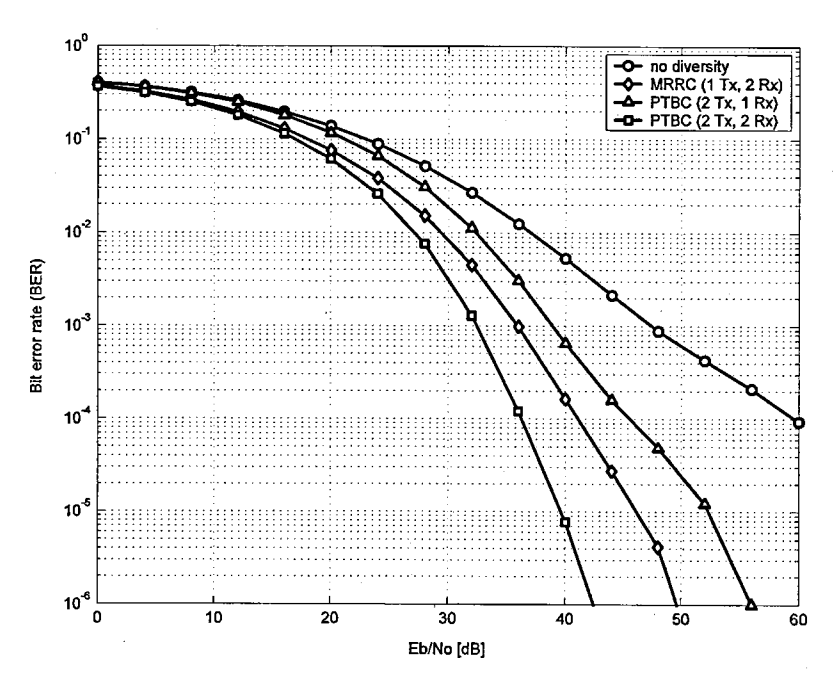


Fig. 6-75 Bit error rate curves for road environment

Suburban

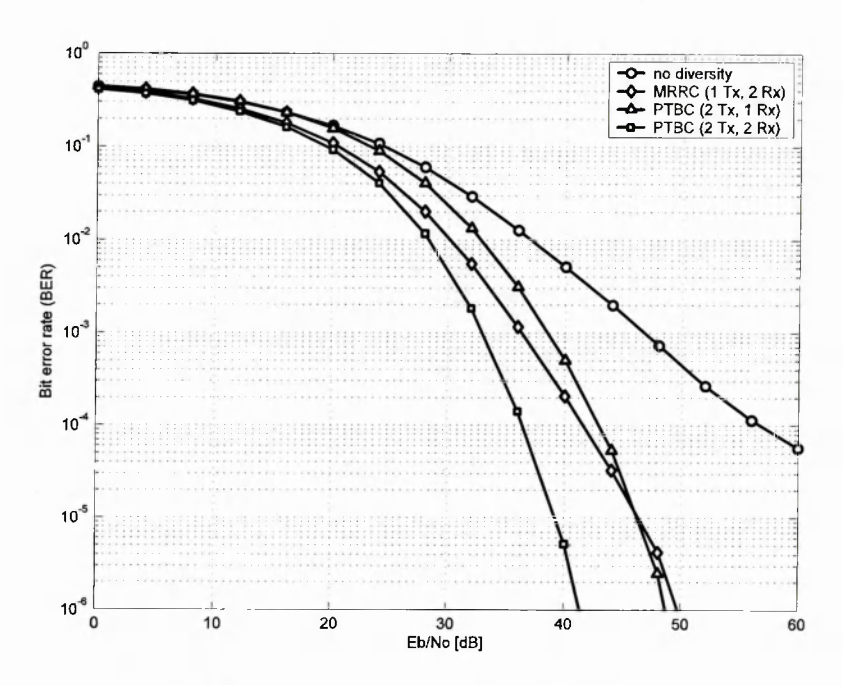


Fig. 6-76 Bit error rate curves for suburban environment

Urban

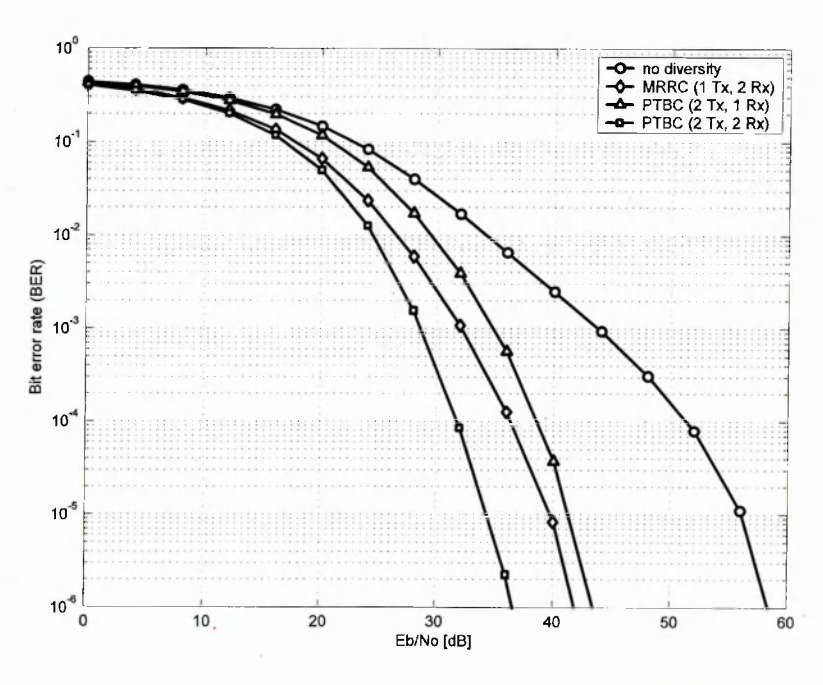


Fig. 6-77 Bit error rate curves for urban environment

6.5.3 Observations

The results present coherent QPSK bit error rate curves, derived from the 2x2 dual circularly polarized measured data, in the tree-lined road, suburban and urban environments. Bit error rate for the SISO case, labelled 'no diversity', obtained from the RHCP-RHCP channel, is given for reference. This is compared to three forms of diversity: (a) maximum ratio receive combining, (b) transmit diversity, and (c) transmit and receive diversity combined.

The first observation is a high link margin is required at low elevations. It was previously observed that shadowing occupied a high channel time-share, and LOS conditions were quite rare in these environments at low satellite elevations. For example, in an AWGN channel, an E_b/N_o of 5dB is enough for a BER of 10^{-2} . However in these harsh shadowed channels, around 37dB is required, requiring a link fade margin of around 32dB. This fade margin is a combined large scale and small scale fade margin.

Since in this case shadowing is highly correlated as the antennas are co-located at each end of the link, diversity gain in this case is mostly small scale diversity gain. Further large scale diversity gain can be achieved from widely separated satellites. Nevertheless, a substantial diversity gain over small scale fading is very worthwhile.

From the results, it can be observed that around 7dB improvement can be achieved using maximum ratio receive diversity. This means 7dB can be subtracted from the required link budget fade margin in LMS systems. This result is important as it may be more easily obtained from current orbiting satellites. At higher satellite elevations, where the time-share of LOS channels is much greater, it is expected that small scale diversity gain to be reduced as the effects of multipath fading would be less (ie. the Rice K factor is higher for LOS channels).

For satellites with dual circularly polarized antennas along with polarization time coding, approximately 4dB improvement in link budget is available from transmit diversity, with the total satellite transmit power equal in single antenna and dual antenna cases.

Combining two transmit antennas with two receive diversity can offer a four-fold diversity gain increase. In this case 10dB can be removed from the link budget fade margin at a BER of 10⁻².

The gains available from diversity are worthwhile for low elevation satellite systems. For example LMS systems using a single GEO satellite could benefit from 2x2 MIMO diversity coding. Whereas HEO systems are less likely to benefit as much from 2x2 MIMO diversity coding as they would experience a high likelihood of LOS channels.

Diversity coding is merely one option for a LMS-MIMO system. Optimization of the modulation and coding strategy is a useful area for future research.

Chapter Seve	n			
	•			
	•			
7 Empirical-St	tatistical Mod	lel of the L	MS-MIMO	Channel
·				
			·	
				•
•				·
			,	
	•			

7.1 Introduction

This chapter provides a step-by-step construction guide for a narrowband and a wideband statistical channel model based around the measurement campaign statistics that were presented in chapter 6.

It is expected that the target audience has a good grasp of channel modelling and are familiar with basic modelling techniques like generating Ricean fading. For these parts of the model, the details are omitted and a reference to a key paper on the subject is given.

The approach provides a framework to build a 2x2 dual polarized LMS-MIMO channel model based around measured statistical parameters. However the generated model will represent the same low elevation conditions as the measurement campaign. The procedure is generic to most LMS-MIMO system scenarios though, and can be used with them once statistical parameters become available from future measurement campaigns.

Both models use a Markov chain approach to account for the 'on/off' nature of the observed data. In the narrowband model, single or dual log-normal fading is applied across each Markov state and is correlated over the MIMO domains. In the wideband case, log-normal fading is further applied and correlated over the delay domains. Ricean fading is added to the large scale amplitude in such a way that the Rice K factor is dependent on the large scale fading level. Ricean samples are generated using a sum-of-sinusoids approach. This small scale fading is correlated over the MIMO domain but uncorrelated over the delay domain.

The model output has been validated against the measurement data, and can be made statistically accurate in terms of first order, second order and their correlation statistics.

7.2 Narrowband model

In cases where the signal bandwidth is less than the channel coherence bandwidth, a narrowband model will often suffice, and is easier to implement and uses less computing resources. The following step-by-step procedure shows how to generate statistically accurate data based around the data obtained in the measurement campaign.

Step1 - Generate large scale fading simulators:

Firstly, log-normal fading (normal in dB) is generated using a Gaussian random number generator with zero mean and unity standard deviation. One sample is generated for each frame length of the Markov chain, 1 metre in this case. Separate log-normal data is generated for each of the four channels in each Markov state.

These data samples represent memoryless data streams; it is therefore necessary to filter the samples in order to achieve the correct temporal fading. This is achieved using a first order recursive linear time-invariant digital filter, as detailed in [Gud91], [Man90], with the following difference equation:

$$y_n = x_n + ay_{n-1} (7-1)$$

Where $a = \exp(-vT/r_c)$. The parameters v, T and r_c are the speed (m/s), sampling time (s) and coherence distance (m) respectively. The samples are then scaled by $\sigma_L(1-a^2)+m_L$, where σ_L is the shadowing standard deviation and m_L is the shadowing mean. The mean and the standard deviation to be used are obtained from the measurement data.

Cross correlation is then applied between each large scale fading channel using their correlation properties. Correlation is applied to the data as follows:

$$vec(\mathbf{Y}) = \mathbf{C}^{(1/2)}.vec(\mathbf{Y}) \tag{7-2}$$

where C is the correlation matrix; for the tree-lined road case:

$$\mathbf{C} = \begin{bmatrix} 1 & 0.86 & 0.85 & 0.90 \\ 0.86 & 1 & 0.91 & 0.87 \\ 0.85 & 0.91 & 1 & 0.88 \\ 0.90 & 0.87 & 0.88 & 1 \end{bmatrix}$$
 (7-3)

Since the large scale probability density is defined by a dual log-normal, we define two large scale time series vectors, for each state. This produces 8 time series correlated vectors with correct

large scale autocorrelation properties: 4 vectors for each MIMO channel, for each Markov state, L_1 and L_2 .

Step2 - Define Markov chain for dual log-normal and generate random walk:

Markov chains are characterized by their state frame length, transition matrix \mathbf{P} and state vector \mathbf{W} . The 4x4 transition \mathbf{P} matrices and 4-state \mathbf{W} vectors were derived from the narrowband data, and are shown in Table 16 (road), Table 17 (suburban) and Table 18 (urban). A minimum state frame of 1 metre was found adequate to capture the rapid changes in level by observation. For each element in matrix \mathbf{P} , P_{ij} represents the probability of changing from state-i to state-j, where each state S_i represents the state of both [co-polar; cross-polar] states: $S_i = [Sc_1; Sx_1]$, $S_2 = [Sc_1; Sx_2]$, $S_3 = [Sc_2; Sx_1]$, $S_4 = [Sc_2; Sx_2]$. P_{ij} is calculated from:

$$P_{ij} = N_{ij} / N_i \tag{7-4}$$

where N_{ij} is the number of transitions from state-*i* to state-*j* and N_i is the number of state frames corresponding to state-*i*. The state probability matrix **W** is found from:

$$W_i = N_i / N_t \tag{7-5}$$

where W_i is probability corresponding to state-i, N_i is the number of frames in state-i and N_i is the total number of frames.

Р			W	
0.6822	0.1579	0.0561	0.1037	0.0764
0.2887	0.2474	0.0447	0.4192	0.0416
0.1682	0.0966	0.1745	0.5607	0.0229
0.0098	0.0199	0.015	0.9554	0.8591

Table 16 Markov state and transition matrices for tree-lined road environment

	F	D		W
1.0000	0.0000	0.0000	0.0000	0.0000
0.0000	0.6487	0.0000	0.3513	0.0221
0.0000	0.0000	1.0000	0.0000	0.0000
0.0000	0.0079	0.0000	0.9921	0.9779

Table 17 Markov state and transition matrices for suburban environment

	F			W
0.0294	0.0588	0.2059	0.7059	0.0024
0.0052	0.1937	0.0838	0.7173	0.0136
0.0521	0.0625	0.1875	0.6979	0.0206
0.0013	0.0099	0.0156	0.9732	0.9634

Table 18 Markov state and transition matrices for urban environment

Using the Metropolis-Hastings algorithm [Chib95] – a Markov chain Monte Carlo method, create a random walk through the states for co- and cross-polar channels. For a current state X_t generate the next state X_{t+1} based on the probability entries α_{ij} in the transition matrix P[i,j], as follows:

(i) Given $X_t = i$, generate a state from the *i*th row of P[i,j] namely sample from P[i,:].

Let the simulated value be j. (This is the candidate value.)

(ii) Generate $U \sim \text{Uniform}(0,1)$. If $U \le \alpha_{ij}$, then set $X_{t+1} = j$, else set $X_{t+1} = i$.

New states are generated every 1 metre, upon which the state and transition matrices were derived.

Step3: - Associate Markov states with log-normal fading generators

For each of the 4 MIMO channels (2 co-polar and 2 cross-polar), 2 channels were generated for each state. The next step is to associate each of these channels with the appropriate Markov state. This results in 4 channels for each MIMO channel with preserved first and second order statistics and correctly correlated.

Step4 - Resample:

Re-sample the data with at least 3 samples per wavelength, from the 1 sample per metre obtained above.

Step5 - Generate Ricean samples:

Now generate unit mean Ricean random samples with K as an input parameter. Define K using the polynomial approach, which conditions it on the large scale fading level. Ricean sample generation can be achieved with Rice's sum of sinusoids method [Pat98]. This method lends itself well to simulating Ricean data with correct probability density, autocorrelation, level crossing rate and average fade duration. Use the autocorrelation derived from the measurement data. This results in the correlated Ricean random sample matrix \mathbf{R} .

$$\mathbf{R} = \begin{bmatrix} r_{RR} & r_{LR} \\ r_{RL} & r_{LL} \end{bmatrix} \tag{7-6}$$

Step6 - Create for each MIMO channel:

Using the small scale MIMO channel correlation measurement data, the modelling can be simplified by using the average correlation coefficient value.

$$vec(\mathbf{R}) = \mathbf{D}^{(1/2)}.vec(\mathbf{R}) \tag{7-7}$$

where **D** is the small scale correlation matrix; for the tree-lined road case:

$$\mathbf{D} = \begin{bmatrix} 1 & 0.03 & 0.02 & 0.09 \\ 0.03 & 1 & 0.12 & 0.01 \\ 0.02 & 0.12 & 1 & 0.01 \\ 0.09 & 0.01 & 0.01 & 1 \end{bmatrix}$$
 (7-8)

As a further refinement, cross-correlations could be varying through time and environment. The second order statistics of the MIMO channel cross-correlation will be reported in future work.

Step7: Combine large and small scale fading

Combine the large scale and small scale fading time series data for each MIMO channel. This can be achieved by simply adding (dB) the signals in each MIMO channel at each time sample.

The model has been constructed in Matlab. The narrowband channel time series data, cumulative distributions, level crossing rate and average fade durations have been validated and are shown in Fig. 7-1, Fig. 7-2 and Fig. 7-3. The correlations over the MIMO domain have also been validated.

The model outline presented here is merely a guide. Additional features can be added as more measurement data becomes available, for example at different satellite elevations using real satellites. The model can be made as accurate as required, based on the measurement data. The simulation generated 10km of statistically accurate wideband LMS-MIMO channel data in under five minutes.

7.3 Narrowband model output

An example of the model output from the tree-lined road environment is shown in Fig. 7-1, where co- and cross-polar channels are presented.

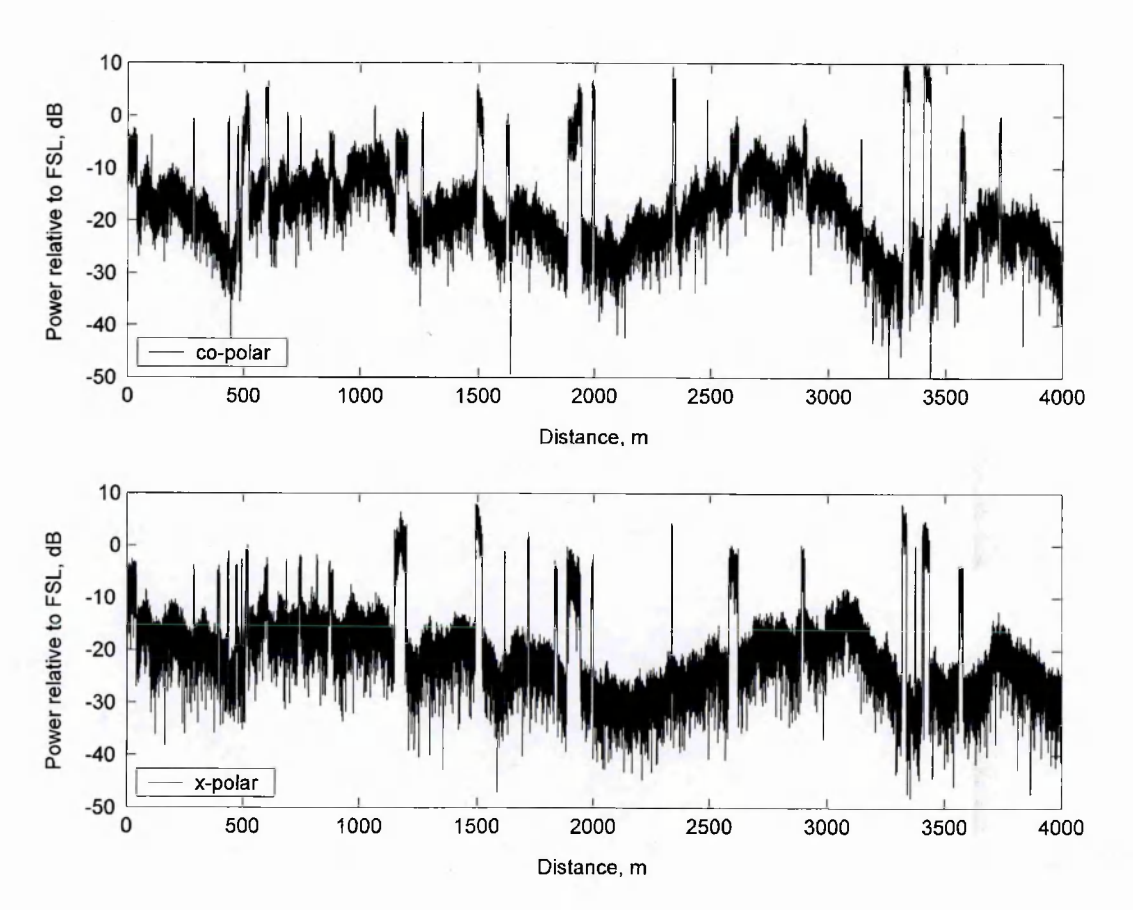


Fig. 7-1 Example of simulated co- and cross-polar channels

Note the rapid change in signal level between LOS and NLOS conditions as the Markov chain switches. This is an inaccuracy in the simulator which is discussed in section 7.4.

A cumulative distribution of this time series data signal is shown in Fig. 7-2, which shows a close match in distribution and trend.

A validation of the second order statistics is presented in Fig. 7-3, which shows a comparison of level crossing rate and average fade duration between the measured narrowband data and the modelled narrowband data.

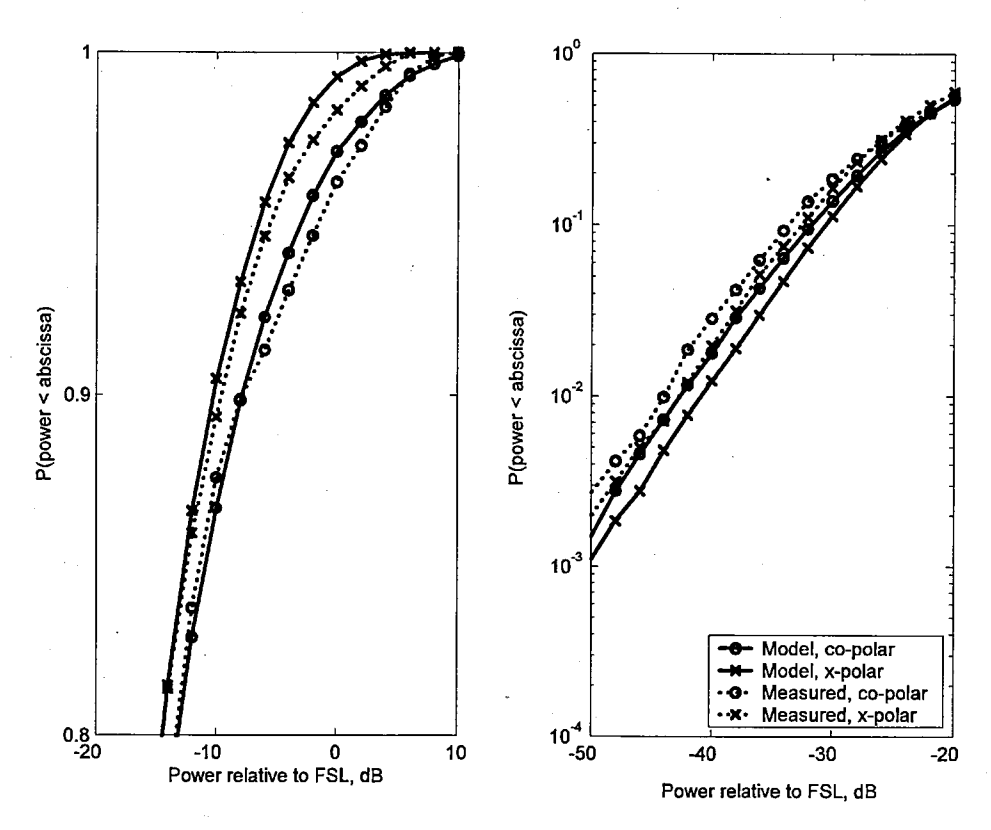


Fig. 7-2 Tree-lined road cumulative distribution comparison between modelled and measured data

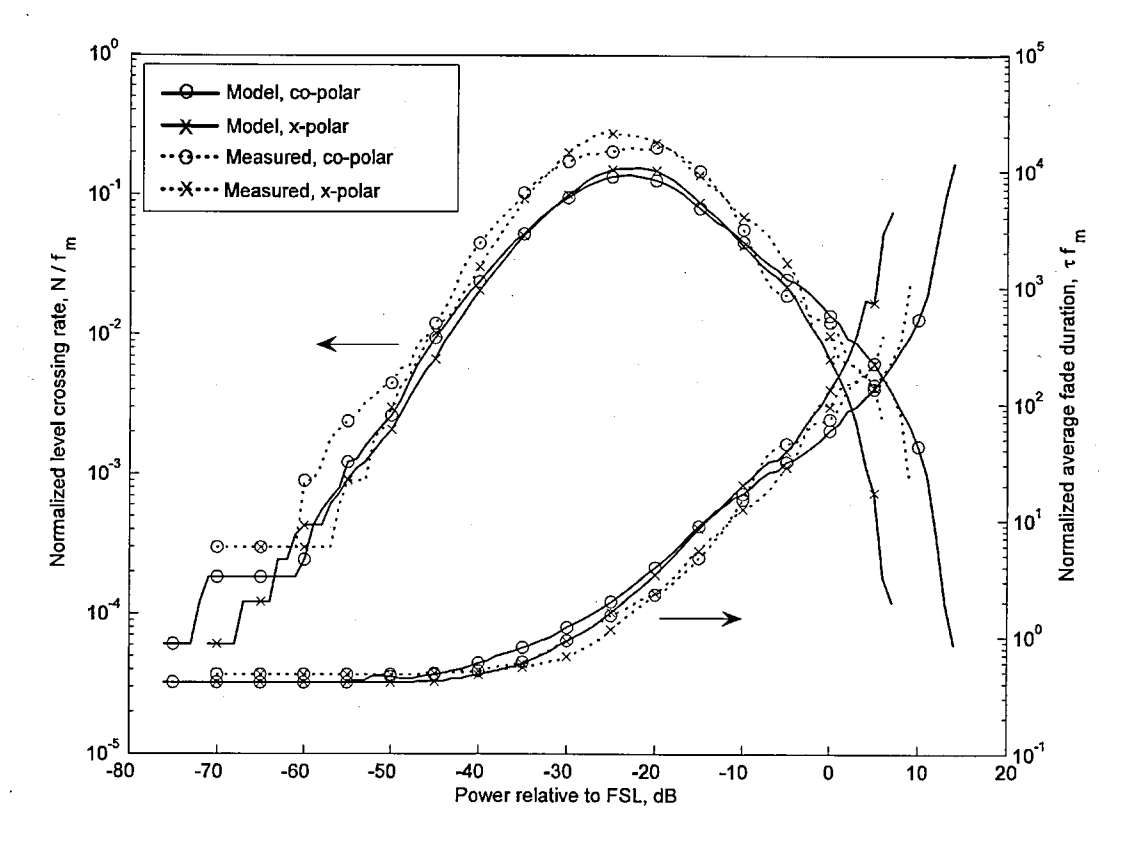


Fig. 7-3 Level crossing rate and average fade duration model validation

7.4 Limitations of narrowband model

This model provides narrowband channel generation with well preserved first order statistics, second order statistics and MIMO channel cross-correlation. Since the parameters used to generate the data are based around a specific measurement campaign, the generated data can only be used for similar conditions. In particular the satellite was emulated by a low elevation artificial platform which has some limitations, as discussed in section 6.3. In addition the antennas had their own imperfections and were placed at specific separations, which are also discussed. Additionally all measurements were carried out at S band frequencies, so the model may not be as accurate at other frequencies.

Another limitation is that a Markov chain was used to switch between LOS and NLOS conditions. This generated transitions that were much more rapid than that observed in the measured data. In practice, due to diffraction around building edges, the transition between LOS and NLOS occurs over around 1-10m as observed from the data. This can be simulated by low pass filtering the large scale fading data [Per01].

In this model a fixed correlation coefficient was used to describe the MIMO channel correlation. However in practice the correlation coefficient varies within each environment as well as between each environment. This can be incorporated during the model fine-tuning procedure.

7.5 Wideband model

A guide to constructing a wideband MIMO channel model based around the measurement data shall now be described. Reference will be made to the channel model depicted in Fig. 7-4.

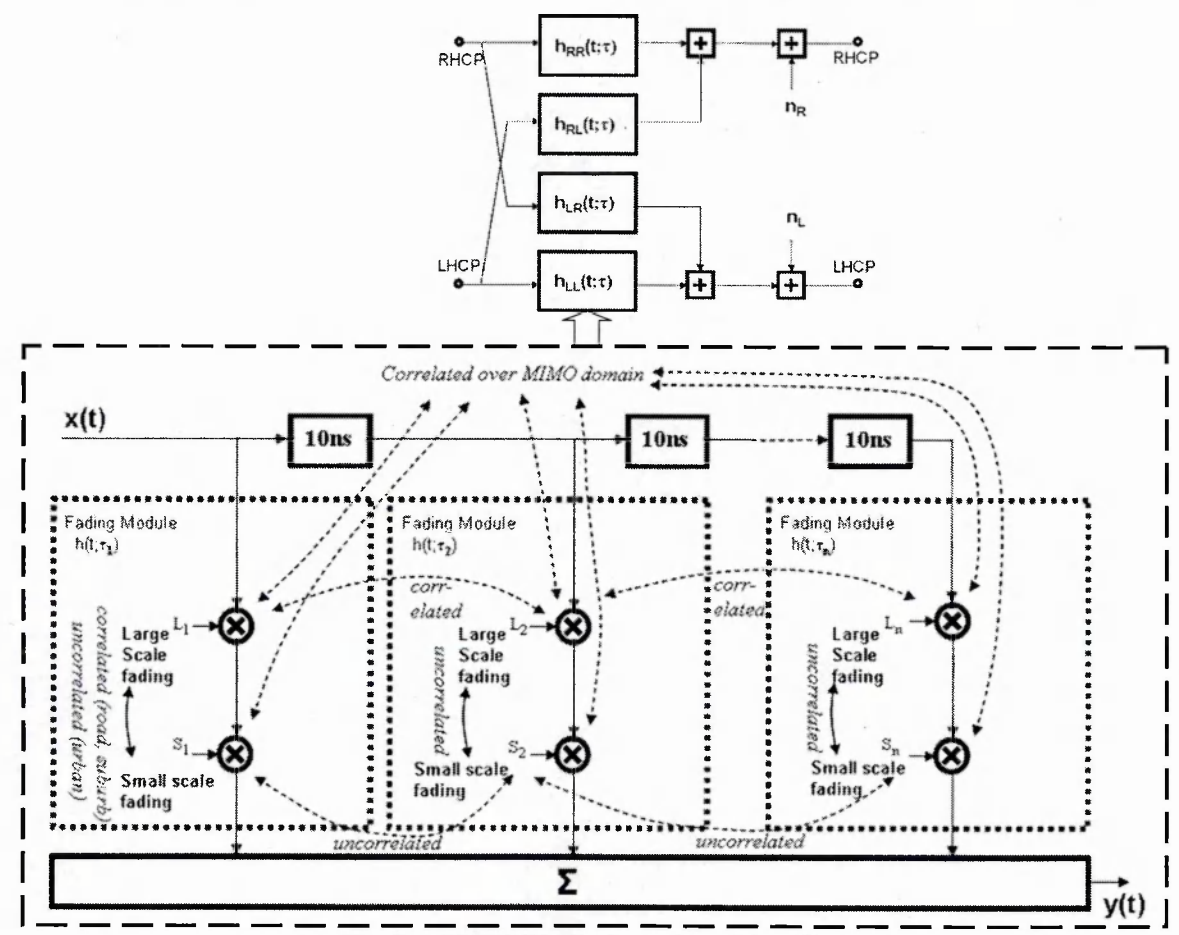


Fig. 7-4 LMS-MIMO channel model outline

The lowpass complex 2x2 LMS-MIMO channel matrix can be expressed as:

$$Y_{R,L} = \begin{bmatrix} h(t;\tau)_{RR} & h(t;\tau)_{RL} \\ h(t;\tau)_{LR} & h(t;\tau)_{LL} \end{bmatrix} X_{R,L} + N_{R,L}$$
 (7-9)

where $Y_{R,L}$ is the received vector, $X_{R,L}$ is the transmitted vector and $N_{R,L}$ is the noise vector. Subscripts R and L denote the RHCP and LHCP antennas at each end of the link. The lowpass complex impulse response of each multipath channel can be expressed [PaD92], [Pro95] as:

$$h(t;\tau) = \sum_{i} A_{i}(t) \,\delta(\tau - \tau_{i}(t)) \exp(j\phi_{i}(\tau)) \tag{7-10}$$

where A_i is the amplitude of the i^{th} resolvable path, τ_i is its propagation delay of each tap, ϕ_i its phase and $\delta(.)$ is the Dirac delta function. As a result of satellite and vehicle motion, each of these

parameters is a randomly time-varying function. The phases of each path ϕ_i are universally assumed a priori [Bel63], [Tur72] to be mutually independent random variables uniformly distributed over the range $[0, 2\pi]$. To maintain delay and frequency domain resolution, it was decided to include all taps, spaced at 10ns, in the simulation up to the maximum resolvable delay. This was 400ns for the tree-line road and urban environments and 200ns for the suburban environment. The remainder of the model is to define A_i for each MIMO channel and each delay tap. A step-by-step outline guide of the approach follows with particular attention paid to the areas not defined for the narrowband model:

Step1 - Generate log-normal fading for each tap:

Log-normal samples with correct autocorrelation and MIMO cross-correlation properties are generated using the same method as the narrowband case. However in this case, single or dual log-normal samples are generated for each tap, using the measurement data parameters. In the wideband case, the large scale fading is also correlated across the delay domain

Step2 - Generate Markov chain:

To simplify the model, we use the narrowband Markov transition and state matrices for all taps in the wideband case. In this case, all taps will be in state 1 or in state 2 simultaneously. This simplification resembles but is not identical to observations in the real data. For more accuracy a separate Markov chain would be required for each tap and then the transitions would require to be correlated across the delay domain. This was found too computer intensive to implement and requires further investigation: each of the 40 taps would require a 4x4 transition matrix and a 40x40 Markov correlation matrix would be required for each MIMO channel.

Step3 – Associate Markov states with log-normal fading generators:

Each state in the Markov chain for co- and cross-polar channels was associated with the set of log-normal fading generators obtained from Step 1:

$$L_{1} = \begin{bmatrix} l_{1}(i;\tau)_{RR} & l_{1}(i;\tau)_{RL} \\ l_{1}(i;\tau)_{LR} & l_{1}(i;\tau)_{LL} \end{bmatrix}, \quad for \ State1$$

$$L_{2} = \begin{bmatrix} l_{2}(i;\tau)_{RR} & l_{2}(i;\tau)_{RL} \\ l_{2}(i;\tau)_{LR} & l_{2}(i;\tau)_{LL} \end{bmatrix}, \quad for \ State2$$
(7-11)

where l is the log-normal sample at time index i, and τ refers to the delay index. Note a separate matrix of MIMO channels is generated for each Markov state.

Step4 - Resample:

Each of the large scale fading samples at each delay tap was re-sampled as outlined for the narrowband model.

Step5: - Generate Ricean samples:

Ricean samples were generated as performed in the narrowband case. The first tap of the delay line model was correlated with the large scale fading level using the polynomial fit. The remaining taps had a K value that was independent of large scale fading level as derived from the measurement data. The value of K for these remaining taps were given a log-normally distributed K value with the correct mean and standard deviation. Each small scale fading generator was uncorrelated between taps, due to the uncorrelated scattering effect, as shown from the data.

For each delay tap, the small scale MIMO matrix samples were found to be partially correlated. To simplify the model, the median value was used; however the model can be improved by adding the variation of MIMO channel correlation and their temporal variations.

Step6 - Combine large and small scale fading generators:

The large scale fading generators and small scale fading generators are now combined and the outputs of each tap summed to form an impulse response time series generator.

7.6 Wideband model output

The model has again been constructed in Matlab. The wideband performance of the model has been tested against the measured data by comparing the Bello system functions [Bel63] using quantitative and qualitative means. The wideband model impulse response has been converted to a narrowband channel and the signal level cumulative distributions, level crossing rate and average fade durations have been validated. The correlations over the delay and MIMO domains have also been validated.

The model outline presented here is merely a guide. Additional features can be added as more measurement data becomes available, for example at different satellite elevations using real satellites. The model can be made as accurate as required, based on the measurement data. The simulation generated 200m of statistically accurate wideband LMS-MIMO channel data in under five minutes.

An example input delay-spread function plot for the co-polar tree-lined road channel is shown in Fig. 7-5.

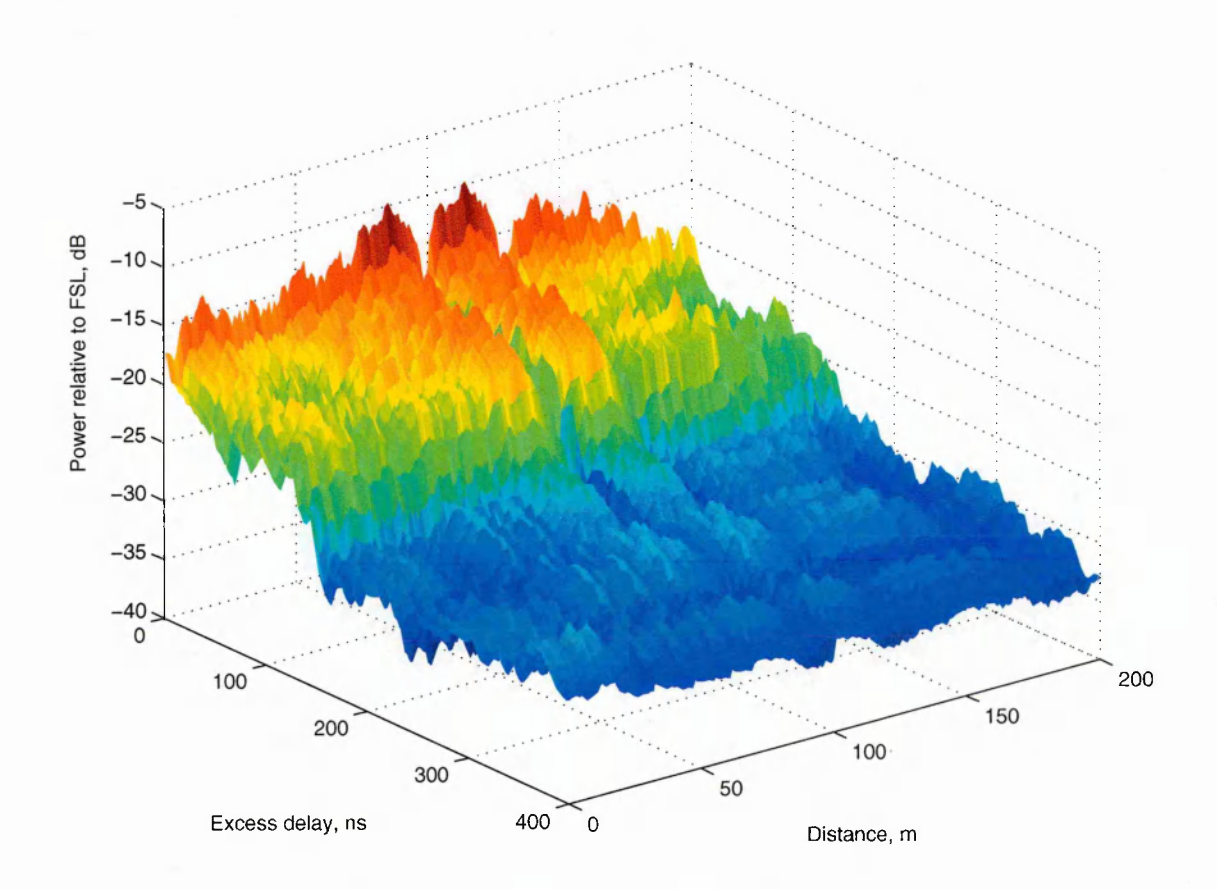


Fig. 7-5 Example input delay-spread function

7.7 Limitations of wideband model

This model provides wideband channel generation with well preserved first order statistics, second order statistics and MIMO channel cross-correlation. As for the narrowband case, since the parameters used to generate the data are based around a specific measurement campaign, the generated data can only be used for similar conditions. In particular the satellite was emulated by an low elevation artificial platform which has some limitations, as discussed in section 6.3. In addition the antennas had their own imperfections and were placed at specific separations. Additionally all measurements were carried out at S band frequencies, so the model may not be as accurate at other frequencies.

As in the narrowband case, another limitation is that a Markov chain was used to switch between LOS and NLOS conditions. This generated transitions that were much more rapid than that observed in the measured data.

Additionally, this wideband model makes the simplification that Markov transitions occur for all delay bins simultaneously. This simplification greatly eases the modelling procedure, but may not be true for all cases in the measured data. To improve the model Markov state and transition matrices would be separately generated for each delay bin and a much more complex method of switching between states in a correlated fashion would be required. This is left for future work.

In this model a fixed correlation coefficient was used to describe the MIMO channel correlation. However in practice the correlation coefficient varies within each environment as well as between each environment. This can be incorporated during the model fine-tuning procedure.

7.8 Using the models

These models can reproduce statistically accurate large scale and small scale fading for the dual polarized LMS-MIMO channel. First and second order statistics as well as MIMO and delay domain correlations are addressed. The parameters are derived from a low elevation scenario but can be adjusted for other satellite elevations as measurement data becomes available.

A good example for using the model is to optimize modulation and coding strategies in a satellite OFDM-MIMO system. Alternatively, the large scale and small scale properties of the model can be separated to address various PHY and cross-layer MAC layer design requirements.

A presentation of the models, along with their validation, is future work to be published.

Cha	pter	Eig	ht
-----	------	-----	----

8 Conclusions and Further Investigation

8.1 Introduction

The aim of this research thesis was to quantify the benefit (if any) of using multiple-input multiple-output (MIMO) technology for land mobile satellite (LMS) systems. Since it is the channel which principally dictates any benefit, the primary focus of the research work was to discover the nature of the land mobile satellite MIMO radio propagation channel, and develop accurate channel models that can be used by the research community.

At the beginning of this research, no channel model or measurement data was in existence for the LMS-MIMO channel to the author's knowledge. However throughout the course of the research, other research establishments have begun similar research. For example Budapest University of Technology and Economics are carrying out theoretical studies on LMS-MIMO capacity and LMS-MIMO now appears in the European Space Agency's vision and strategic research agenda [ESA07].

8.2 Review of literature survey

The methodology used for the literature survey and the identification of the PhD research topic can best be described with the aid of the following diagram (repeated from Chapter 1 for clarity):

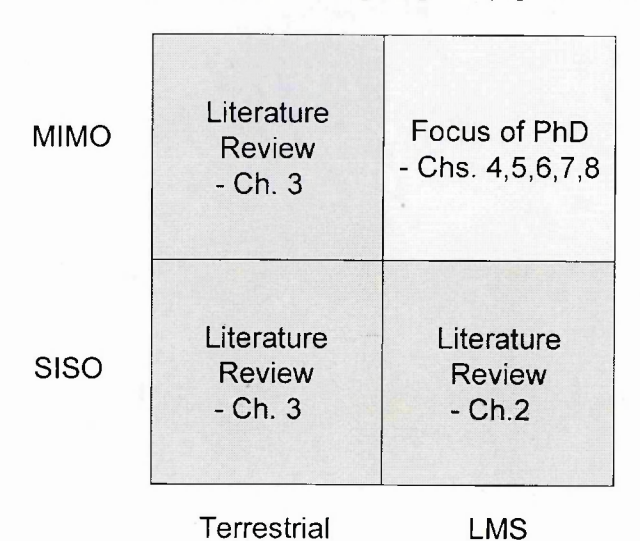


Fig. 8-1 Methodology

The survey began (lower-right box in Fig. 8-1) looking at some of the technical difficulties in a viable mobile satellite system business, highlighting the problems of poor QoS (due to harsh propagation channel and latency) and limited spectral efficiency. Many of the key existing LMS-SISO models were then reviewed, with perhaps the physical-statistical optimum for further development into a LMS-MIMO channel model.

Capacity was then studied (upper-left box in Fig. 8-1) with the aim of identifying its effect from the MIMO channel. It was found that the instantaneous SNR and MIMO channel matrix play key roles in LMS-MIMO capacity. Terrestrial channel models were then studied (upper-left and lower-left

box in Fig. 8-1) as these were much more advanced than LMS-MIMO models, and much could be learnt from them. Models that traced rays via clusters of scatterers formed a useful input to the LMS-MIMO physical-statistical model development. Additionally an overview of antenna arrays (upper-left box in Fig. 8-1) as used in MIMO systems and methods of ensuring weak correlation between signals impinging on each array element were also reviewed.

8.3 Review of physical-statistical channel model

A physical-statistical LMS-MIMO channel model was derived, which can simulate multiple satellite and/or dual polarization channels under different environments and satellite elevations. The model was used to estimate performance gains from the MIMO channel compared with a SISO channel. Improvements in capacity and diversity were investigated from a dual satellite with a single polarization.

The model was partially validated using published experimental data. However, only the SISO subset of the channel could be validated, as no LMS-MIMO channel data or literature was available.

The main findings from the physical-statistical LMS-MIMO channel model data analysis were: (a) methods of creating uncorrelated channels by spatial and polarization separation, and (b) the fact that a doubling of capacity could be achieved from the dual satellite or dual polarization LMS-MIMO channel.

8.4 Review of experimental findings

The highlights of the LMS-MIMO dual circularly polarized measurement campaign analysis is a strong understanding of the behaviour of this channel. Under LOS conditions, the multipath effects are reduced and a 2x2 dual circularly polarized channel is observed with a high degree of isolation between each polarization. However, as the LOS path becomes obstructed, the multipath effects are much more pronounced relative to the LOS component, and the small scale fading Rice *K* factor reduces towards a Rayleigh channel. Under fully NLOS conditions the 2x2 LMS-MIMO channel comprises four Rayleigh fading weakly correlated channels.

From the capacity analysis on the data, it was revealed that a doubling in capacity between the SISO and 2x2 MIMO cases is available at high signal to noise ratios, due to separable dual polarizations. At lower signal to noise ratios, a much greater capacity ratio increase is available due to the four fold diversity increase in a more Rayleigh like fading channel.

A study on the diversity gain from the 2x2 MIMO channel data was also carried out. At a bit error rate of 10^{-2} (worst case limit for voice or streaming data), around 10dB reduction in E_b/N_o was possible for 2x2 polarization time coding. Transmit diversity (2x1 channel) provided a 4dB

improvement in E_b/N_o , whilst 7dB improvement in E_b/N_o was available from 1x2 maximum ratio receive diversity.

8.5 Review of resultant empirical-statistical channel model

A second LMS-MIMO channel modelling approach was an empirical-statistical model, which was formed from the measurement campaign data.

The model uses Markov chains for the very slow fading effects, log-normal distributions for the large scale fading and conditioned Ricean distributions for the small scale fading. A narrowband and a wideband model were presented.

The model, which will be expanded for a future publication, can be used by the global research community to gain a good understanding of the dual polarized LMS-MIMO channel.

8.6 Implications of the research

The primary implication from this thesis is that increased throughput (around a doubling at higher SNR and over a ten-fold increase at lower SNR values) is available from mobile satellite communication systems using multiple antenna techniques. This is achieved with identical spectrum utilization in the satellite downlink. However for a dual antenna satellite system, a non-regenerative satellite would require two Earth station uplink channels.

The same 2x2 channel can be coded to improve QoS by providing a fourfold diversity gain, thus reducing the probability of a small scale deep fade. Furthermore, two widely spaced satellites each with dual circular polarization can be used to provide diversity over large and small scale fading.

One important point about taking advantage of high capacity ratio increases in the LMS-MIMO channel is that increased link margin should be provided from the link budget, so that a link can still be established in a partially or highly shadowed region, where the channel is predominantly Rayleigh and better for MIMO capacity increase. Future satellites may offer this increased radiated power, and then many advantages of terrestrial communications will also be available for mobile satellite communications, instead of the 'on/off' channel nature that currently exists.

It is envisaged that LMS-MIMO systems will form a key part in future mobile satellite communication systems, and LMS-MIMO research is now gaining much interest from global research centres.

8.7 Further investigation

8.7.1 Further processing of measurement campaign data

The measurement campaign carried out in this thesis captured a 4x4 channel with two dual polarized satellites in a cluster communicating with a vehicle with 2 RHCP and 2 LHCP antennas. Since the data is already available it would be sensible to process this 4x4 channel further and calculate the capacity and diversity gain from such a system.

8.7.2 Combined LMS and repeater MIMO channel modelling

Many current LMS-SISO systems use terrestrial gapfillers to overcome adverse channel conditions. In this way the benefits of satellite communications are retained and repeaters are used to improve coverage in a few hard-to-reach areas.

One possibility in LMS-MIMO systems is to transmit dual polarizations from the satellite and use a gapfiller that re-transmits both polarizations into shadowed areas. This creates a channel that combines rays arriving from the satellite with signals from the repeater.

The benefit (if any) of the LMS-MIMO channel with repeaters is a new line of research that could be investigated, in the case of co-channel repeater spectrum usage.

8.7.3 LMS-MIMO channel modelling with shadowing diversity

In this thesis both antennas were attached to a single satellite or forming a satellite cluster. In these channels, diversity was gained over small scale fading but little gain was obtained over large scale fading. This line of future research would include a study of the MIMO channel from satellites that are widely spaced apart. MIMO channel coding for distributed systems is also another field of research that is in its infancy when applied to multiple satellites. Investigations using two Inmarsat satellites could be used for example.

8.7.4 Effect of satellite elevation on the LMS-MIMO channel

One of the primary parameters in measuring the LMS-MIMO channel is the satellite elevation. It is well known that high elevations lend themselves to a lower probability of blocked channels, but the effect on the MIMO channel has not been characterized before (to our knowledge).

It could be expected that high elevation channels would be less blocked and be represented as Ricean with a higher K factor. In this case, it is more likely that a doubling in capacity from isolated dual polarizations is attained, with a greater time-share.

A further experiment to characterize the 2x2 MIMO dual circularly polarized channel as a function of a range of elevations and environment using a helicopter as an artificial satellite platform communicating with a mobile vehicle is a useful area of future research.

8.7.5 Characterizing the HAP-MIMO channel

As was touched upon in the chapter on the physical-statistical satellite-MIMO channel model, MIMO techniques may be possible by using spatial diversity and polarization diversity from a single HAP. Whether the size of a single HAP can support spatial diversity requires further research. Again, this could be emulated by use of a helicopter containing spatially separated dual polarized antennas. It may be possible to install 4 spatially separated dual polarized antennas underneath the helicopter. Access to a real HAP would be even more ideal. However at high elevations, it can be expected that gains from spatially separated antennas will be small. However, dual polarizations can be expected to work well.

Combining satellites and HAPs to form a LMS-HAP-MIMO channel is another area of research that could be investigated for future system scenarios.

9 Bibliography

- [Abd01] Abdi, A, Lau, W.C., Alouini, M-S. and Kaveh, M.: "A New Simple Model for Land Mobile Satellite Channels: First- and Second-Order Statistics", *IEEE Transactions on Wireless Communications*, vol.2, no.3, May 2003, pp.519-528
- [Ala98] Alamouti, S.M.: "A Simple Transmit Diversity Technique for Wireless

 Communications", *IEEE Journal on Selected Areas in Communications*, vol.16, no.8,

 Oct.1998, pp.1451-1458
- [And00a] Andersen, J.B.: "Antenna Arrays in Mobile Communications: Gain, Diversity, and Channel Capacity", *IEEE Antennas and Propagation Magazine*, vol.42, no.2, Apr. 2000, pp.12-16
- [And00b] Andersen, J.B.: "Array Gain and Capacity for Known Random Channels with Multiple Element Arrays at Both Ends", *IEEE Journal on Selected Areas in Communications*, vol.18, no.11, Nov.2000, pp.2172-2178
- [And02] Andersen, J.B.: "A Propagation Overview", *IEEE Symposium on Wireless Personal Multimedia Communications*, vol.1, 2002, pp.1-6
- [Aul79] Aulin, T.A.: "Modfied model for the fading signal at a mobile radio channel", *IEEE Transactions*, 1979.W-28, (3), pp.182-203
- [Bab98] Babalis, P.G., and Cafsalis, C.N.: "A new model for the characterization of the combined shadowing and multipath effects in satellite systems." *ICT* '98, Jun.1998, IV, (4), pp.25-28
- [Bal97] Balanis, C.A.: Antenna Theory Analysis and Design. J.Wiley & Sons, 1997
- [Bea89] Beach, M.A., Swales, S.C., Bateman, A., Edwards, D.J. and McGeehan, J.P.: "A diversity combining antenna array for land mobile satellite communications", *IEEE VTC* 1989, pp.749-756
- [Bea01] Beach, M.A., McNamara, D.P., Fletcher, P.N. and Karlsson, P.: "MIMO A Solution for Advanced Wireless Access", 11th International Conference on Antennas and Propagation, Apr.2001, pp.231-235
- [Bel63] Bello, P.A.: "Characterization of randomly time-variant linear channels", *IEEE Transactions on. Communications*, vol.11. Jun.1963, pp.360-390.
- [Bel00] Belloul, B., Saunders, S. R., Parks, M. A. N., and Evans, B. G.: "Measurement and modelling of wideband propagation at Land S-bands applicable to the LMS channel",

- IEE Proc. Microwaves, Antennas and Propagation, vol.147, no.2, Apr.2000, pp.116121
- [Blo03] Blostein, S.D. and Leib, H.: "Multiple Antenna Systems: Their Role and Impact in Future Wireless Access", *IEEE Communications Magazine*, July 2003, pp.94-101
- [Bra74] Brandenburg, L.H. and Wyner, A.D.: "Capacity of the Gaussian Channel With Memory: The Multivariate Case", *The Bell System Technical Journal*, vol.53, no.5, May-June 74, pp.745-778
- [Bro05] Brown, T.W.C., Saunders, S.R. and Evans, B.G.: "Analysis of mobile terminal diversity antennas", *IEE Proceedings on Microwaves, Antennas and Propagation*, vol.152, no.1, Feb.2005, pp.1-6
- [Bur02] Burr, A.G.: "Evaluation of capacity of indoor wireless MIMO channel using ray tracing", *International Zurich Seminar on Broadband Communications*, Feb.19-21, ETH Zurich, Switzerland, 2002.
- [Bur03] Burr, A.G.: "Capacity Bounds and Estimates for a Finite Scatterers MIMO Wireless Channel", *IEEE Journal on Selected Areas in Communications*, vol.21, no.5, June 2003, pp.812-818
- [Bra02] Bråten, L.E. and Tjelta, T.: "Semi-Markov Multistate Modeling of the Land Mobile Propagation Channel for Geostationary Satellites", *IEEE Transactions on Antennas and Propagation*, vol.50, no.12, Dec.2002, pp.1795-1802
- [Cav94] Cavdar, I. H., Dincer H. and Erdogdu, K.: "Propagation measurements at L-band for land mobile satellite link design", Proc. 7th Mediterranean Electrotechnical Conference, Apr. 1994, pp.1162-1165
- [Chi01] Chiurtu, N., Rimoldi, B. and Teletar, E.: "On the Capacity of Multi-Antenna Gaussian Channels", *IEEE Symposium on Information Theory*, 2001, pp.53
- [Chib95] Chib, S. and Greenberg, E.: "Understanding the Metropolis-Hastings Algorithm", *The American Statistician*, vol.49, no.4, Nov.1995, pp.327-335
- [Chiz00] Chizhik, D., Farrokhi, F.R., Ling, J. and Lozano, A.: "Effect of Antenna Separation on the Capacity of BLAST in Correlated Channels", *IEEE Communications Letters*, vol.4, no.11, Nov.2000, pp.337-339
- [Chiz02] Chizhik, D., Foschini, G.J., Gans M.J. and Valenzuela, R.A.: "Keyholes, Correlations, and Capacities of Multielement Transmit and Receive Antennas", *IEEE Transactions on Wireless Communications*, vol.1, no.2, Apr. 2002, pp.361-368

- [Chiz03] Chizhik, D., Ling, J., Wolniansky, P., Valenzuela, R., Costa, N. and Huber, K.:

 "Multiple Input Multiple Output Measurements and Modeling in Manhattan", *IEEE Journal on Selected Areas in Communications*, vol.21, no.3, 2003, pp.321-331

 [Chu03] Chung, J., Hwang, C.-S., Kim, K. and Kim, Y.K.: "A Random Beamforming
- [Chu03] Chung, J., Hwang, C.-S., Kim, K. and Kim, Y.K.: "A Random Beamforming Technique in MIMO Systems Exploiting Multiuser Diversity", *IEEE Journal on Selected Areas in Communications*, vol.21, no.5, June 2003, pp.848-855
- [Cla68] Clarke, R.H.: "A Statistical Theory of Mobile-Radio Reception", *The Bell System Technical Journal*, vol.47, July-Aug.1968, pp.957-1000
- [Cor94] Corazza, G.E., and Vatalaro, F.: "A statistical model for land mobile satellite channels and its application to nongeostationary orbit systems", *IEEE Transactions on Vehicular Technology*, vol.43, no.3, Aug. 1994, pp.738-742.
- [Corr 01] Correia, L.M.: Wireless Flexible Personalised Communications Cost 259: European Co-operation in Mobile Radio Research, Wiley 2001, pp.148 – 200
- [Cox 73] Cox, D.C.: "910MHz Urban Mobile Radio Propagation: Multipath Characteristics in New York City", IEEE Transactions on Communications, vol. 21, no.11, Nov.1973, pp.1188-1194
- [Dav02] Davarian, F., "Sirius Satellite Radio: Radio entertainment in the sky", *Aerospace Conference Proceedings*, vol.3, 2002, pp.1031-1035
- [Deb03] Debbah, M., Gil, J., Venes, J., Cardoso, F., Marques, G. and Correia, L. M.: *IST-FLOWS project report D13: Final report on channel models*, 2003
- [Dri99] Driessen, P.F. and Foschini, G.J.: "On the Capacity Formula for Multiple Input-Multiple Output Wireless Channels: A Geometric Interpretation", *IEEE Transactions on Communications*, vol. 47, no. 2, Feb.1999, pp.173-176
- [Dur99] Durgin, G.D. and Rappaport, T.S.: "Effects of Multipath Angular Spread on the Spatial Cross-correlation of Received Voltage Envelopes", *IEEE VTC*, 1999, pp.996-1000
- [Dot01] Dottling, M., Jahn, A., Didascalou, D. and Wiesbeck, W.: "Two- and three-dimensional ray tracing applied to the land mobile satellite (LMS) propagation channel", *IEEE Antennas and Propagation Magazine*, vol.43, no.6, Dec.2001, pp.27-37.
- [Dur03] Durgin, G.D.: Space-Time Wireless Channels, ch.3, 1st ed., Prentice Hall, 2003

[Egg93] Eggers, P.C.F., Toftgård, J. and Oprea, A.M.: "Antenna Systems for Base Station Diversity in Urban Small and Micro Cells", IEEE Journal on Selected Areas in Communications, vol.11, no.7, Sep.1993, pp.1046-1057 [Egg95] Eggers, P.C.F.: "Angular Dispersive Mobile Radio Environments sensed by highly Directive Base Station Antennas", IEEE PIMRC, 1995, pp.522-526 [Erc02] Erceg, V., Soma, P., Baum, D.S. and Paulraj, A.J.: "Capacity obtained from multipleinput multiple-output channel measurements in fixed wireless environments at 2.5 GHz", IEEE International Conference on Communications, vol.1, 2002, pp.396-400 [Erc03] Erceg, V. et al.: "Channel Models", IEEE P802.11 standard (working document). Nov.2003 [Erc04] Erceg, V., Soma, P. Baum, D.S. and Catreux, S.: "Multiple-Input Multiple-Output Fixed Wireless Radio Channel Measurements and Modeling Using Dual-Polarized Antennas at 2.5GHz", IEEE Transactions on Wireless Communications, vol.3, no.6, Nov.2004, pp.2288-2298 [Erc06] Erceg, V. Sampath, H. and Catreux-Erceg, S.: "Dual-Polarization Versus Single-Polarization MIMO Channel Measurement Results and Modeling", IEEE Transactions on Wireless Communications, vol.5, no.1, Jan.2006, pp.28-33 [Ert98] Ertel, R.B., Cardieri, P., Sowerby, K.W., Rappaport, T.S. and Reed, J.H.: Overview of spatial channel models for antenna array communication systems, IEEE Personal Communications, Feb.1998, pp.10-22 Evans, B. (ed.) Satellite Communication Systems, 3rd Edition. IEE, 1999 [EvB99] [EvJ97] Evans, J.V.: "Satellite systems for personal communications", IEEE Antennas and Propagation Magazine, vol.39, no.3, 1997, pp.7-20 [EvJ98] Evans, J.V.: "Satellite systems for personal communications", Proceedings of the IEEE, vol.86, no.7, 1998, pp.1325-1341 [Fos96] Foschini, G.J.: "Layered space-time architecture for wireless communication in a fading environment when using multi-element antennas", Bell Labs. Tech. Journal, vol. 1, no.2, Autumn 1996, pp 41-59 [Fos98] Foschini, G.J. and Gans, M.J. On Limits of Wireless Communications in a Fading Environment when Using Multiple Antennas, Wireless Personal Communications,

Kluwer 1998, pp.311-335

- [Gan02] Gans, M.J., Amitay, N., Yeh, Y.S., Xu, H., Damen, T.C., Valenzuela, R.A. Sizer, T., Storz, R., Taylor, D., MacDonald, W.M., Tran, C. and Adamiecki, A.: "Outdoor BLAST Measurement System at 2.44GHz: Calibration and Initial Results", *IEEE Journal on Selected Areas in Communications*, vol.20, no.3, Apr.2002, pp.570-583
- [Ges00] Gesbert, D., Bölcskei, H., Gore, D. and Paulraj, A.: "MIMO Wireless Channels: Capacity and Performance Prediction", *IEEE Globecom*, San Francisco, CA, vol.2, Nov.2000, pp.1083-1088
- [Ges02] Gesbert, D., Bölcskei, H., Gore, D.A. and Paulraj, A.J.: "Outdoor MIMO Wireless Channels: Models and Performance Prediction", *IEEE Transactions on Communications*, vol.50, no.12, Dec.2002, pp.1926-1934
- [Ges03] Gesbert, D., Shafi, M., Shiu, S., Smith, P. and Naguib, A.: "From theory to practice: an overview of MIMO space time coded wireless systems", *IEEE Journal on Selected Areas in Communications*, vol.21, no.3, Apr.2003, pp.281-302
- [Gki02] Gkizeli, M.: "Service Availability and QoS of Mobile Satellite Systems", *Ph.D Thesis*, University of Surrey, July 2002.
- [Gre99] Greenstein, L.J., Michelson, D.G., and Erceg, V.: "Moment-method estimation of the Ricean K-factor", *IEEE Communications Letters*, vol.3, no.6, June 1999, pp.175-176.
- [Gol89] Goldhirsh, J. and Vogel, W.: "Mobile Satellite System Fade Statistics for Shadowing and Multipath from Roadside Trees at UHF and L-band", *IEEE Transactions on Antennas and Propagation*, vol.37, no.4 Apr.1989, pp.489-498
- [Gol93] Goldhirsh, J., and Vogel, W.J.: "Earth-satellite tree attenuation at 20 GHz: foliage effects" *IEE Electronics Letters*, Sep.1993, 29, (18), pp.1640-1641
- [Gud91] M. Gudmundson, "Correlation model for shadow fading in mobile radio systems", *IEE Electronic Letters*, vol.27, no.23, 1991, pp.2145-2146.
- [Has91] Hase, Y., Goldhirsh, J. and Vogel, W.J.: "Fade-durations derived from land mobile satellitaneasurements in Australia", *IEEE Transactions on Communications*, May 1991,39, (5), pp.664-668
- [Has05] Hashim, M.H. and Stavrou, S.: "Wind influence on radio waves propagating through vegetation at 1.8GHz", *IEEE Antennas and Wireless Propagation Letters*, vol.4, 2005, pp.143-146.
- [Hor07] Horvath, P., Karagiannidis, G.K., King, P.R., Stavrou, S., Frigyes, I.: "Investigations in satellite MIMO channel modeling: accent on polarization", *EURASIP Journal on*

- Wireless Communications and Networking special issue on Satellite Communications, in Press.
- [Hwa97] Hwang, S.H., Kim, IC-J.: "A channel model for nongeostationary orbiting satellite systems". *Proc. IEEE Vehicular Technology Conf.*, 1997, pp.41-45
- [ITU-R618-8] International Telecommunication Union/ Radiocommunication Sector (ITU-R.): "Propagation data and prediction methods required for the design of Earth-space telecommunication systems", 2003.
- [ITU-R P531-8] International Telecommunication Union/ Radiocommunication Sector (ITU-R.): "Ionospheric propagation data and prediction methods required for the design of satellite services and systems", 2005.
- [ITU-R P681-6] International Telecommunication Union/Radiocommunication Sector (ITU-R.): "Propagation data required for the design of Earth-space land mobile telecommunication systems", 2003.
- [Jah96] Jahn, A., Bischl, H., and Heiss, G.: "Channel characterisation for spread spectrum satellite communications", *IEEE 4th International Symposium on Spread Spectrum Techniques and Applications Proceedings*, vol.3, 22-25, Sep.1996 pp.1221 1226.
- [Jah01] Jahn, A.: "Propagation considerations and fading countermeasures for mobile multimedia services", *International Journal of Satellite Communications*, 19, 2001, pp.223-250
- [Jak74] Jakes, W.C.: Microwave Mobile Communications, Wiley, 1974.
- [Kan96] Kanatas, G., and Konsantinou, P.: "Narrow-band characterization of the land mobile satellite channel: a comparison of the empirical models." *Eur. Trans. Telecommun*, July-Aug.1996, 7, (41), pp.315-321
- [Kar99] Karaliopoulos, M. S. and Pavlidou, F.-N.: "Modelling the land mobile satellite channel: a review", *Electronics & Communication Engineering Journal*, Oct.1999, pp.235-248.
- [Kas06] Kasparis C., King P.R., Evans B.G.: "Doppler Spectrum of the Multipath Fading Channel in Mobile Satellite Systems With Directional Terminal Antennas", Ka and Broadband Communications Conference, Sep.2006.
- [Ker02] Kermoal, J.P.: "Measurement, Modelling and Performance Evaluation of the MIMO Radio Channel", Ph.D. thesis, Centra for PersonKommunikation – Aalborg University, Denmark, 2002

- [Kha01] Khalighi, M.A., Brossier, J.-M., Jourdain, G. and Raoof, K. "On capacity of Ricean MIMO channels", *IEEE PIMRC*, 2001, pp.150-154
- [Kin05] King, P.R., Evans, B., and Stavrou, S.: "Physical-statistical model for the land mobile-satellite channel applied to satellite/HAP-MIMO", 11th European Wireless

 Conference, Vol. 1, Apr.2005, pp.199-204.
- [Kin05b] King, P.R., Horváth, P., Pérez-Fontán, F., Frigyes, I., and Stavrou, S.: "Satellite channel impairement mitigation by diversity techniques", *IST Mobile Summit*, Dresden, June 2005.
- [Kin05c] King, P. R. and Stavrou, S.: "Land mobile-satellite MIMO capacity predictions", *IEE Electronics Letters*, vol.41, no.13, 2005, pp.749-750.
- [Kin06] King, P.R., Stavrou, S.: "Capacity improvement for a land mobile single satellite MIMO system", IEEE Antennas and Wireless Propagation Letters, vol.5, 2006, pp.98-100
- [Kin06b] King, P.R., Stavrou, S.: "Tree obscured mobile satellite channel characteristics and mitigation", *IST Mobile Summit*, Myconos, June 2006
- [Kin06c] King, P.R., Stavrou, S.: "Characteristics of the land mobile satellite MIMO channel", *VTC Montreal*, Sep.2006, pp.1-4
- [Kin07] King, P.R. and Stavrou, S.: "Low elevation wideband land mobile satellite MIMO channel characteristics", *IEEE Transactions on Wireless Communications*, in Press
- [Kra87] Kraus, J. D.: *Electromagnetics*, McGraw-Hill, 3rd ed., Ch. 12, 1987.
- [Lan96] Landron, O, Feuerstein, M.J. and Rappaport, T.S.: "A comparison of theoretical and empirical reflection coefficients for typical exterior wall surfaces in a mobile radio environment", IEEE Transactions on Antennas and Propagation, vol.44, no.3, 1996, pp.341-351
- [Lee74] Lee, W.C.Y and Yeh, Y.S.: "On the Estimation of the Second-Order Statistics of Log Normal Fading in Mobile Radio Environment", *IEEE Transactions on Communications*, vol.22, June 1974, pp.869-873.
- [Lee85] Lee, W.C.Y.: Mobile Communications Engineering, McGraw Hill, 1985.
- [Lib99] Liberti, Jr. J.C. and Rappaport, T.S.: Smart Antennas for Wireless Communications,
 Prentice Hall 1999
- [Loo85] Loo, C.: "A statistical model for a land mobile satellite link", *IEEE Transactions on Vehicular Technology*, vol. vt-34, no.3, Aug.1985, pp.122-127.

- [Loo97] Loo, C. and Butterworth, J.S.: "Land Mobile Satellite Channel Measurements and Modeling", Proceedings of the IEEE, vol.86, no.7, Jul 1998, pp.1442-1463 [Loy00] Loyka, S. and Mosig, J.R.: "Channel capacity of n-antenna BLAST architecture", IEE Electronics Letters, vol.36, no.7, Mar.2000, pp.660-661 [Loy01a] Loyka, S.: "Channel capacity of MIMO architecture using the exponential correlation matrix", IEEE Communication Letters, vol. 5, no.9 2001, pp 369-371. [Loy01b] Loyka, S. and Kouki, A.: "Correlation and MIMO communication architecture (Invited), 8th International Symposium on Microwave and Optical Technology, Montreal, Canada, June 19-23, 2001. [Loy02] Loyka, S. and Kouki, A.: "On MIMO channel capacity, correlations, and keyholes: analysis of degenerate channels", IEEE Communications Letters, vol.50, no.12, 2002, pp.1886-1888. [Lut91] Lutz, E., Cygan, D., Dippold, M., Dolainsky, F. and Papke, W.: "The land mobile satellite communication channel – recording, statistics, and channel model", IEEE Transactions on Vehicular Technology, vol.40, no.2, May 1991, pp.375-386 [Lut96] Lutz, E.: "A Markov Model for Correlated Land Mobile Satellite Channels", International Journal of Satellite Communications, Vol.14, 1996, pp.333-339. [Lut98] Lutz, E.: "Issues in satellite personal communication systems", Wireless Networks vol.4, 1998, pp.109-124 [Lut00] Lutz, E., Werner, M. and Jahn, A.: Satellite Systems for personal and broadband communications, Springer. 2000 [Mac97] Macario, R.: Cellular Radio – principles and design, 2nd edition. Macmillan. 1997 M. J. Marsan, G. C. Hess and S. S. Gilbert, "Shadowing variability in an urban land [Man90] mobile environment at 900MHz", IEE Electronic Letters, vol.26, no.10, 1990, pp.646-648. [Mar00] Maral, G., Bousquet, M.: Satellite Communication Systems, 3rd edition. Wiley 2000 [Mar01a] Martin, C.C., Winters, J.H. and Sollenberger, N.R.: "Multiple-Input Multiple-Output (MIMO) Radio Channel Measurements", IEEE Symposium on Antennas and Propagation, 2001, pp.418-421
- [Mar01b] Martin, C.C., Winters, J.H. and Sollenberger, N.R.: "MIMO Radio Channel Measurements: Performance Comparison of Antenna Configurations", *IEEE VTC*, 2001, pp.1225-1229

[Mas51] Massey, J.F.: "The Kolmogorov-Smirnov test for goodness-of-fit", Journal of the American Statistical Association, 1951, pp.46-70. [McN00] McNamara, D.P., Beach, M.A., Karlsson, P. and Fletcher, P.N.: "Initial Characterisation of Multiple-Input Multiple-Output (MIMO) Channels for Space-Time Communications", IEEE VTC, 2000, pp.1193-1197 [Mol02] Molisch, A.F., Steinbauer, M., Toeltsch, M., Bonek, E. and Thomä, R.S.: "Capacity of MIMO Systems Based on Measured Wireless Channels", IEEE Journal on Selected Areas in Communications, Vol. 20, No.3, Apr.2002, pp.561-569 [Mol03] Molisch, A.F.: "A Generic Model for MIMO Wireless Propagation Channels in Macro- and Microcells", MERL technical report TR2003-042, May 2003. [Mol04] Molisch, A.F.: "A Generic Model for MIMO Wireless Propagation Channels in Macro- and Microcells", MERL technical report TR2004-013, Mar 2004. [Oes99] Oestges, C. and Vanhoenacker-Janvier, D.: "Physical-statistical prediction of performance for land mobile satellite communication systems", IEE Proceedings on Microwaves Antennas and Propagation, vol.146, issue 5, Oct.1999, pp.362-368 [Oes99b] Oestges, C., Saunders, S.R. and Vanhoenacker-Janvier, D.: "Physical statistical modelling of the land mobile satellite channel based on ray tracing", IEE Proceedings Microwave Antennas and Propagation, vol.146, no.1, Feb.1999, pp.45-49 [Pal01] Palomar, D.P., Fonollosa, J.R. and Lagunas, M.A.: "Capacity results of spatially frequency-selective MIMO channels in UMTS", IEEE VTC, 2001, pp.553-557 [Par96] Parks, M.A.N.: "Wideband Propagation Channel Characterisation Applicable to Mobile Satellite Systems at L and S Bands", Ph.D Thesis, University of Surrey, Oct 1996. [PaJ91] Parsons, J. I. and Turkmani, A M. D.: "Characterization of mobile radio signals: model description", IEE Proc.-I, Dec.1991,138, (6), pp.549-556 [PaD92] Parsons, D.: The Mobile Radio Propagation Channel. Pentech Press, London, 1992. [Pat98] Patzold, M., Killat, U., Laue, F., and U, Y.: "On the statistical properties of deterministic simulation models for mobile fading channels" IEEE Transactions on

Paulraj, A.J., Gesbert, D. and Papidias, C.: Smart antennas for mobile

communications, Encyclopedia for Electrical Engineering, John Wiley, 2000

Vehicular Technology, vol.47, no.1, Feb 1998, pp.254-269

[Pau00]

- [Pau03] Paulraj, A., Nabar, R. and Gore, D.: Introduction to Space-Time Wireless

 Communications. Cambridge University Press, 2003
- [Pau04] Paulraj, A.J., Gore, D.A., Nabar, R.U. and Bölcskei, H.: "An Overview of MIMO Communications A Key to Gigabit Wireless", *Proceedings of the IEEE*, vol.92, no.2, Feb.2004, pp.198-218
- [Ped97] Pedersen, K.I., Mogensen, P.E. and Fleury, B.H.: "Power azimuth spectrum in outdoor environments", *IEE Electronics Letters*, vol.33, no.18, Aug.1997, pp.1583-1584
- [Ped00] Pedersen, K.I., Andersen, J.B., Kermoal, J.P. and Mogensen, P.: "A Stochastic Multiple-Input-Multiple-Output Radio Channel Model for Evaluation of Space-Time Coding Algorithms", *IEEE VTC*, 2000, pp.893-897
- [Pov02] Povey, G.J.R. and Levey, D.: "Multiple Input Multiple Output (MIMO) Radio Channel Models", 3G Mobile Communication Technologies, IEE, 8-10 May 2002, pp.414-417
- [Pee01] Peebles, Jr, P.Z.: *Probability, Random Variables and Random Signal Principles*, McGraw-Hill, 4rd ed., Ch. 5, 2001.
- [Per97] Pérez-Fontán, F., Castro, M.A.V., Kunisch, J., Pamp, J., Zollinger, E., Buonomo, S., Baptista, P., and Arbesser, B.: "A versatile framework for a narrow- and wide-band statistical propagation model for the LMS channel", *IEEE Transactions on Broadcasting*, vol.43, no.4, Dec.1997, pp.431-458.
- [Per97b] Pérez-Fontán, F., Gonzalez, J. P., Ferreiro, M. J. S., Castro, M. A V., Buonomo, S., and Baptista J. P.: 'Complex envelope threestate Markov model based simulator for the narrow-band LMS channel', *International Journal on Satellite Communications*, 15, 1997, pp.1-15
- [Per98] Pérez-Fontán, F., Vazquez-Castro, M.A., Buonomo, S., Poiares-Baptista, J.P., and Arbesser-Rastburg, B.: "S-Band LMS propagation channel behaviour for different environments, degrees of shadowing and elevation angles", *IEEE Transactions on Broadcasting*, vol.44, no.1, Mar.1998, pp.40-76.
- [Per01] Pérez-Fontán, F., Vazquez-Castro, M.A., Cabado, C.E., Garcia, J.P. and Kubista, E.: "Statistical modelling of the LMS channel", *IEEE Transactions on Vehicular Technology*, vol.50, no.6, Nov.2001, pp.1549-1567.
- [Pro95] Proakis, J.G., Digital Communications, 3rd edition, McGraw Hill, 1995
- [Rap96] Rappaport, T. S.: Wireless Communications, Prentice Hall, 1996.

[Ric48] Rice, S.O.: "Mathematical analysis of a sine wave plus random noise", Bell System Technical Journal, 27 (1), pp.109-157, 1948 [Ric58] Rice, S.O.: "Distribution of the duration of fades in radio transmission: Gaussian noise model", Bell System Technical Journal 37 (3), 1958, pp.581-635 [Sal87] Saleh, A.A.M. and Valenzuela, R.A.: "A Statistical Model for Indoor Multipath Propagation", IEEE Journal on Selected Areas in Communications, vol. SAC-5, no.2, Feb.1987, pp.128-137 [Sal03a] Salous, S.: "Multiple Input Multiple Output Systems: Capacity and Channel Measurements", Dept. of Electrical Engineering and Electronics, UMIST [Sal03b] Salous, S.: "The Provision of an Initial Study of Multiple In Multiple Out Technology." Section 1: Executive Summary. Contract: AY4252 (510010100), Dept. of Electrical Engineering and Electronics, UMIST [Sal03c] Salous, S.: "The Provision of an Initial Study of Multiple In Multiple Out Technology." Section 2: Literature Search. Contract: AY4252 (510010100), Dept. of Electrical Engineering and Electronics, UMIST [Sar03] Sarkar, T.K., Ji, Z., Kim, K., Medouri, A. and Salazar-Palma, M.: "A Survey of Various Propagation Models for Mobile Communications", IEEE Antennas and Propagation Magazine, vol.45, no.3, June 2003, pp.51-82 [Sat06] SatNEx project partners: Influence of the propagation channel on satellite communications - channel dynamics effects on mobile, fixed and optical multimedia applications, EU IST FP6 SatNEx project: Satellite Communications Network of Excellence [Sau96] Saunders, S.R., and Evans, B.G.: "Physical model of shadowing probability for land mobile satellite propagation", IEE Electronics Letters, Aug. 1996, 32, (1), pp. 1548-1549 [Sau99] Saunders, S.R.: Antennas and Propagation for Wireless Communication Systems., J.Wiley & Sons, 1999 [Sau01] Saunders, S.R., Tzaras, C. and Evans, B.G.: "Physical-statistical methods for determining state transition probabilities in mobile-satellite channel models", International Journal of Satellite Communications, 19, 2001, pp.207-222 [Sch00] Schumacher, L., Pedersen, K.I., Kermoal, J.P. and Mogensen, P.: "A Link-Level MIMO Radio Channel Simulator for Evaluation of Combined Transmit/Receive

Diversity Concepts within the METRA project", Center for PersonKommunikation, Aalborg University, Denmark, 2000 [Sch01] Schumacher, L., Pedersen, K.I. and Mogensen, P.E.: "From Antenna Spacings to Theoretical Capacities - Guidelines for Simulating MIMO Systems", IEEE PIMRC, 2001, pp.587-592 [Sha06] Shafi, M., Zhang, M., Moustakas, A.L., Smith, P.J., Molisch, A.F., Tufvesson, F. and Simon, S.H.: "Polarized MIMO Channels in 3-D: Models, Measurements and Mutual Information", IEEE Journal on Selected Areas in Communications, vol.24, no.3, Mar. 2006, pp.514-527 [She01] Sheriff, R.E. and Hu, Y.F.: Mobile Satellite Communication Networks, Wiley 2001 [Shi00] Shui, D.-S., Foscini, G.J., Gans, M.J. and Kahn, J.M.: "Fading Correlation and its effect on the Capacity of Multielement Antenna Systems", IEEE Transactions on Communications, vol.48, no.3, Mar.2000, pp.502-513 [Skl97a] Sklar, B.: "Rayleigh Fading Channels in Mobile Digital Communication Systems. Part1: Characterization", IEEE Communications Magazine, vol.35, issue 7, July 1997, pp.90-100 [Sk197b] Sklar, B.: "Rayleigh Fading Channels in Mobile Digital Communication Systems. Part2: Mitigation", IEEE Communications Magazine, vol.35, issue 7, July 1997, pp.102-109 [Skl01] Sklar, B.: Digital Communications – Fundamentals and Applications, 2nd Edition. Prentice Hall. 2001. [Spe00] Spencer, Q.H., Jeffs, B.D., Jensen, M.A. and Swindlehurst, A.L.: "Modeling the Statistical Time and Angle of Arrival Characteristics of an Indoor Multipath Channel", IEEE Journal on Selected Areas in Communications, vol.18, no.3, Mar. 2000, pp.347-360 [Sun05] Sun, Z.: Satellite Networking, Wiley 2005 [Suz77] Suzuki, H.: "A Statistical Model for Urban Radio Propagation", IEEE Transactions on Communications, vol.25, no.7, Jul.1977, pp.673-680

[Taa97]

Taaghol, P. and Tafazolli, R.: "Correlation model for shadow fading in land mobile

satellite systems", IEE Electronics Letters, vol.33, no.15, Jul.1997, pp.1287-1289

- [Tar03] Taricco, G. and Biglieri, E.: "MIMO transmission for mobile satellite communication systems: a review", 8th International Workshop on Signal Processing for Space Communications, Sep.2003 [Tel95] Teletar, İ.E.: "Capacity of Multi-antenna Gaussian Channels", European Transactions on Telecommunications, vol.10, no.6, 1995, pp.585-595 [3GP03] Third Generation Partnership Project -Technical Specification Group Radio Access Network: Spatial channel model for Multiple Input Multiple Output (MIMO) simulations (Release 6). 3GPP TR 25.996 v6.1.0 (2003-09). Thomä, R.S., Hampicke, D., Richter, A. and Sommerkorn, G.: "MIMO Vector [Tho01] Channel Sounder Measurement for Smart Antenna System Evaluation", European Transactions on Telecommunications, ETT, vol.12, no.5, Sep/Oct 2001, pp.427-438 [Toe02] Toeltsch, M., Laurila, J., Kalliola, K., Molisch, A.F., Vainikainen, P. and Bonek, E.: "Statistical Characterization of Urban Spatial Radio Channels", IEEE Journal on Selected Areas in Communications, vol.20, no.3, Apr.2002, pp.539-549 [Tur72] Turin, G.L., Clapp, F.D., Johnson, T.L., Fine, S.B. and Lavry, D.: "A Statistical Model of Urban Multipath Propagation", IEEE Transactions on Vehicular Technology, vol. VT-21, no.1, Feb.1972, pp.1-9 [Tur01] Turin, W., Jana, R., Martin, C. and Winters, J.: "Modeling Wireless Channel Fading", IEEE VTC, Oct.2001, pp.1740-1744 [Tza98] Tzaras, C., Evans, B.G. and Saunders, S.R.: "Physical-statistical analysis of land mobile-satellite channel", IEE Electronics Letters, vol.34, no.13, Jun.1998, pp.1355-1357 [Vas00] Vasseur, H.: "Degradation of availability performance in dual-polarized satellite communications systems", IEEE Transactions on Communications, vol.48, no.3, 2000, pp. 465-472 [Vat95] Vatalaro, F.: "Generalised Rice-lognormal channel for wireless communications", IEE Electronic Letters, vol.31, issue 22, Oct.1995, pp.1899-1900 [Vau03] Vaughan, R. and Andersen, J.B.: Channels, Propagation and Antennas for Mobile Communications, The IEE, 2003
- propagation at UHF and L-band", *IEEE Transactions on Antennas and Propagation*, vol.36, no.5, May 1988, pp.707-719

Vogel, W. and Hong, U.: "Measurement and modeling of land mobile satellite

[Vog88]

- [Vog90] Vogel, W. and Goldhirsh, J.: "Mobile satellite system propagation measurements at L-band using MARECS-B2", *IEEE Transactions on Antennas and Propagation*, vol. 38, no.2, Feb.1990, pp.259-264
- [Vog95] Vogel, W.J. and Goldhirsh, J.: "Multipath Fading at L Band for Low Elevation Angle, Land Mobile Satellite Scenarios", *IEEE Journal on Selected Areas in Communications*, vol.13, no.2, Feb.1995, pp.197-204
- [Vuc92] Vucetic, B., and Du, J.: "Channel modeling and simulation in satellite mobile communication systems", *IEEE J. Sel. Areas Commun.*, Oct 1992, vol.10, no.8, pp. 1209-1218.
- [Wak97] Wakana, H.: "Propagation model for simulating shadowing and multipath fading in land mobile satellite channel." *IEE Electronics Letters*, Nov.1997, 33, (23), pp.1925-1926
- [Wal03] Wallace, J.W., Jensen, M.A., Swindlehurst, A. L. and Jeffs, B. D.: "Experimental characterization of the MIMO wireless channel: data acquisition and analysis", *IEEE Transactions on Wireless Communications*, vol.2, no.2, 2003, pp.335-343
- [Wei04] Weisstein, E.W.: "Point-Line Distance--3-Dimensional.", MathWorld—A Wolfram Web Resource.
- [Wim07] WiMax Forum Partners: "MIMO channel model for TWG RCT ad-hoc proposal, v16", Mar.07
- [Win87] Winters, J.H.: "On the Capacity of Radio Communication Systems with Diversity in a Rayleigh Fading Environment", *IEEE Journal on Selected Areas in Communications*, vol. SAC-5, no.5, Jun.1987, pp.871-878
- [Xu 01] Xu, H., Gans, M.J., Amitay, N. and Valenzuela, R.A.: "Experimental verification of MTMR system capacity in controlled propagation environment", *IEE Electronics Letters*, vol.37, no.15, July 2001, pp.936-937
- [Xu 02] Xu, H., Gans, M., Chizhik, D., Ling, J., Wolniansky, P. and Valenzuela, R.: "Spatial and Temporal Variations of MIMO Channels and Impacts on Capacity", *IEEE Conference on Communications*, 2002, pp.262-266
- [Yu 02a] Yu, K.: "Modeling of Multiple-Input Multiple-Output Radio Propagation Channels", Technical Licentiate report, KTH, Sweden. 2002
- [Yu 02b] Yu, K. and Ottersten, B.: "Models for MIMO Propagation Channels, A Review", Special Issue on Adaptive Antennas and MIMO Systems. IR-S3-SB-0223, KTH, Sweden. 2002

10 Appendix

Satellite frequency band terminology

The following frequency terminology originated during World War II as military radar bands, to keep the actual operating frequencies secret. After declassification, they were eventually adopted by the Institute of Electrical and Electronics Engineers (IEEE), and are widely used today in radar, satellite and terrestrial communications systems, both military and commercial.

Band	Frequency Range [MHz]	
HF	3 - 30	
VHF	30 - 300	
UHF	300 - 1000	
L	1000 - 2000	
S	2000 - 4000	
С	4000 - 8000	
X	8000 - 12000	
Ku	12000 - 18000	
K	18000 - 27000	
Ka	27000 - 40000	
mm	40000 - 300000	

Table 19 Frequency band terminology

		· · · · · · · · · · · · · · · · · · ·	
٠.			
		•	
	·		·